CARDIFF UNIVERSITY
PRIFYSGOL CAERDYDD

**Brian Cooke Dental Library**
***Llyfrgell Ddeintyddol Brian Cooke***

4th Floor
Dental School
Heath Park
Cardiff
CF14 4XY

*Llawr 4*
*Yr Ysgol Ddeintyddol*
*Parc y Mynydd Bychan*
*Caerdydd*
*CF14 4XY*

029 2074 2525
dentliby@cardiff.ac.uk

# Soft tissue modelling and facial movement simulation using the finite element method

Yongtao Lu

B.Eng (Hons.) M.Eng

Submitted for the degree of Doctor of Philosophy

Schools of Engineering and Dentistry

Cardiff University, UK

August 2010





ProQuest LLC
789 East Eisenhower Parkway
P.O. Box 1346
Ann Arbor, MI 48106-1346

# Abstract

This thesis presents a framework for soft tissue modelling, facial surgery simulation, and facial movement synthesis based on the volumetric finite element method.

Assessment of facial appearance pre- and post-surgery is of major concern for both patients and clinicians. Pre-surgical planning is a prerequisite for successful surgical procedures and outcomes. Early computer-assisted facial models have been geometrically based. They are computationally efficient, but cannot give an accurate prediction for facial surgery simulation. Therefore, in this thesis, the emphasis is placed on physically-based methods, especially the finite element technique.

To achieve realistic surgery simulation, soft tissue modelling is of crucial importance. Thus, in this thesis, considerable effort has been directed to develop constitutive equations for facial skeletal muscles. The skeletal muscle model subsequently developed is able to capture the complex mechanical properties of skeletal muscle, which are active, quasi-incompressible, fibre-reinforced and hyperelastic. In addition, to improve the characterisation of in-vivo muscle behaviour, a technique has been developed to visualise the internal fibre arrangement of skeletal muscle using the FEM-NURBS method, which is the combination of the finite element method and the non-uniform rational B-spline solid mathematical representation.

Another principal contribution made in this thesis is the three-dimensional finite element facial model, which can be used for the simulations of facial surgery and facial movement. The procedure of one cranio-facial surgery is simulated by using this facial model and the numerical predictions show a good agreement with the patient post-surgical data. In addition, it would be very helpful to also simulate the facial movement and facial expressions. In this thesis, two facial expressions (smile and disgust) and the mouth opening are simulated to assess the post-surgical appearance and test the muscle-driven facial movement simulation method.

# Acknowledgements

I would like to express my thanks to those people who have contributed to the completion of my PhD thesis.

Firstly, I would like to acknowledge Dr. Hanxing Zhu, Prof. Stephen Richmond and Prof. John Middleton for providing me with the financial support, their ideas and suggestions. Without their help, this thesis could not have been completed.

Secondly, I would like to thank Brian Walker and Liliana Beldie from Arup for providing the OASYS software, training, technical support and some valuable advice. The meetings with them proved to be invaluable. Also thanks to Advanced Research Computing @ Cardiff (ARCCA) for allowing me to access the Merlin supercomputer with appropriate training.

Finally, I would like to thank my family for their continual support and give special thanks to my girlfriend, Emily, who accompanied me in Cardiff during the last two years. Thanks very much for her love and encouragement.

# Contents

**Chapter 1 Introduction** ..... 1

1.1 Motivation and objectives ..... 1

1.2 Contributions ..... 3

1.3 Outline and organisation ..... 4

**Chapter 2 Background Knowledge** ..... 6

2.1 Facial anatomy ..... 6

2.1.1 Facial Skin ..... 7

2.1.2 Muscles of human head and neck ..... 7

2.1.3 Human Skull ..... 13

2.1.4 Temporomandibular Joint ..... 13

2.2 Skeletal muscles ..... 15

2.2.1 Skeletal muscle structure ..... 16

2.2.2 Skeletal muscle architecture ..... 18

2.2.3 Mechanical properties of skeletal muscle ..... 19

2.2.4 Contraction dynamics of skeletal muscle ..... 21

2.3 Basics of non-linear solid mechanics ..... 24

2.3.1 Basic notions ..... 24

2.3.2 General elastic constitutive relations ..... 30

**Chapter 3 Constitutive Skeletal Muscle Model** ..... 40

3.1 Introduction ..... 40

3.2 Literature reviews on constitutive muscle models ..... 41

3.2.1 Hill-type muscle models ..... 41
3.2.2 Huxley-type muscle models ..... 46
3.2.3 Other types of muscle models ..... 50
3.2.4 Reviews on muscle experimental data ..... 50
3.3 The constitutive skeletal muscle model ..... 53
3.3.1 Stress produced in the series elastic element ..... 54
3.3.2 Stress produced in the contractile element ..... 54
3.3.3 Stress produced in the parallel element ..... 61
3.4 LS-DYNA implementation of the skeletal muscle material model ..... 62
3.5 Validations and verifications of the developed skeletal muscle model. 69
3.5.1 Passive elongation ..... 73
3.5.2 Activated elongation ..... 74
3.5.3 Isometric contraction ..... 75
3.5.4 Isometric contraction followed by concentric contraction ..... 77
3.6 Parametric studies of the parameters ..... 80
3.7 Summary ..... 83

**Chapter 4 Three-Dimensional Finite Element Facial Model and Facial Movement Simulation ..... 84**

4.1 Introduction ..... 84
4.2 Overview of various facial simulation models ..... 85
4.2.1 Geometric models ..... 85
4.2.2 Mass-spring models ..... 85
4.2.3 Finite element models ..... 91
4.2.4 Other models ..... 97
4.3 Construction of the 3D finite element facial model ..... 97

4.3.1 Reconstruction of the facial geometry ..... 98
4.3.2 Creation of the 3D finite element facial model ..... 101
4.3.3 Description of the 3D finite element facial model ..... 108
4.4 Cranio-facial surgery simulation ..... 115
4.4.1 A clinical case report ..... 115
4.4.2 Finite element simulation results ..... 118
4.4.3 Validation of the finite element prediction ..... 120
4.5 Facial movement simulation ..... 122
4.5.1 Facial expression simulation ..... 122
4.5.2 Mouth opening simulation ..... 126
4.6 Discussion and conclusion ..... 127

**Chapter 5 Modelling the Fibre Arrangement of Skeletal Muscle Using the FEM– NURBS Method ..... 130**

5.1 Introduction ..... 130
5.2 Related work on muscle fibre representation ..... 131
5.3 Mathematical description of the NURBS ..... 136
5.3.1 NURBS Curve definition ..... 137
5.3.2 NURBS Surface definition ..... 139
5.3.3 NURBS solid definition ..... 141
5.3.4 NURBS solid construction ..... 141
5.4 FEM-NURBS method ..... 145
5.5 Muscle constitutive relation ..... 148
5.6 Numerical examples ..... 153
5.6.1 Example one: contraction of a cone ..... 154
5.6.2 Example two: contraction of a barrel shape muscle ..... 157

5.6.3 Example three: contraction of a whole torus ..... 159
5.6.4 Example four: contraction of a half torus ..... 161
5.6.5 Example five: contraction of the depressor anguli oris ..... 164
5.7 Summary ..... 169

**Chapter 6 Conclusions and Future Work ..... 171**
6.1 Summary and conclusions ..... 171
6.2 Directions for future work ..... 173

**References ..... 177**
**List of Publications ..... 192**

**Appendix A — Abbreviations ..... 193**
**Appendix B — Notation ..... 194**
**Appendix C — Hill's Force-Velocity Equation ..... 202**
**Appendix D — Geometry Relation in Hill's Three-Element Model 204**
**Appendix E — Fortran Codefor the Skeletal Muscle Model ..... 206**
**Appendix F — Makefile for Building LS971.exe on WindowsXP .... 216**
**Appendix G — Fortran Code for NURBS Solid Representation and its Derivatives ..... 217**

# Chapter 1

# Introduction

Since the development of modern medical imaging techniques, such as computer tomography (CT) and magnetic resonance imaging (MRI), computer assisted facial surgery has become a reality. Experimental limitations and difficulties are another drive for developing computer aided facial surgery simulation systems. The early facial models are parameterised, and just aim at the facial animation on a computer. More recent facial models are moving towards physically-based techniques, since they can give more realistic simulations. Methods for developing physically-based models include the mass-spring, the mass tensor and the finite element methods. The models developed in this thesis are finite element based.

## 1.1 Motivation and objectives

The motivations for the work presented in this thesis include the finite element modelling of facial soft tissues, the outcome prediction of the facial surgery and the simulation of facial movements.

- **Facial soft tissue modelling**

For the purpose of realistic surgery simulation, the soft tissue deformations under external forces are of crucial importance, and depend on the constitutive law of soft tissues. The more precise the physical properties of the soft tissues in the facial model, the more

realistic will be the simulation. More details about the response of soft tissues can be found in Fung's book (1981). Most of the current soft tissue models are based on the linear elastic approximation, because it is robust and efficient. However, this kind of model cannot accurately describe the mechanical properties of soft tissues, and is not suitable for large deformations. Thus a model with appropriate soft tissue constitutive relations is a prerequisite in providing a realistic facial surgery simulation.

- **Facial surgery simulation**

In modern society, personal looks are crucial in interpersonal relationships. For this reason, people with facial disharmony and diseases are more likely to seek facial surgery to normalise their facial appearance and to make them more attractive. From the patient's point of view, it would be of great benefit to be able to predict their post-surgery facial appearance. From the clinician's point of view, the post-surgical prediction could help plan the surgery and optimize the surgical procedures. Therefore, a reliable facial surgery simulation system would be considerably valuable for use by both clinicians and patients.

- **Facial movement simulation**

Patients may be unfamiliar with their facial appearance after surgery. Sometimes the patient and close family and friends are dissatisfied with the new appearance and would like to seek further corrections to achieve their goal. Therefore, prior to surgery, the patient should have the opportunity to preview the planned post-surgery facial appearance especially when the swelling has receded. The clinician could improve and adjust their surgical techniques to enhance the positive and minimize the negative facial effects. For these reasons, it would be very helpful to preview not only the post-surgical static face, but also the movement of the post-surgical face exhibited during facial expressions.

The arguments above have provided the motivation of this study. The objectives of this thesis are to develop reliable numerical soft tissue models and a facial model, which can give an accurate prediction of the facial surgery and can be used for the simulation of facial movements.

## 1.2 Contributions

The major contributions of this thesis are summarised as follows.

- **A validated three-dimensional constitutive skeletal muscle model**

Existing three-dimensional (3D) constitutive skeletal muscle models are mainly derived from either Hill-type three-element or Huxley-type cross-bridge models. Due to the lack of experimental data published on skeletal muscle mechanical properties, existing 3D constitutive skeletal muscle models are not reliable. The first contribution of this thesis is a validated 3D constitutive skeletal muscle material model. This model is able to characterise the skeletal muscle complex mechanical behaviour, including active, quasi-incompressible, fibre-reinforced and hyperelastic response. The model is validated by comparing the finite element (FE) simulation results with published experimental studies on the New Zealand white rabbit tibialis anterior muscle. The results show that the model is able to capture both the active and passive muscle tissue behaviour for strains below failure.

- **A three-dimensional finite element facial model**

Due to the complex facial anatomy, it is impossible for the clinician to predict the post-surgical soft tissue changes. Thus, a computer-aided facial surgery system is needed to assist with the prediction of the post-surgical appearance. The second contribution of this thesis is a three-dimensional finite element facial model which can be used for the prediction of facial surgical outcome and the simulation of facial movements. This facial model is an anatomy-based model, where the skull and facial skin are reconstructed from the patient specific Cone Beam Computerised Tomography (CBCT) scan data with the facial muscle geometry being taken from a standardised forensic database provided by the School of Life Sciences, University of Dundee.

- **Simulations of the cranio-facial surgery and facial movements**

The numerical facial model developed in this work can be used for many kinds of simulation. The third contribution is the simulation of cranio-facial surgery and muscle-based facial movements using the developed facial model. The simulation of a clinical case requiring cranio-facial surgery is presented. The result of the numerical prediction agrees with the patient's 6-month post-surgical data, showing the correction of the developed facial model. For the simulation of facial movements, a novel approach is proposed. In this approach, the muscles responsible for facial expressions are assigned by a 3D skeletal muscle material model specifically developed. Using this approach, two facial expressions and the mouth opening process are simulated.

- **FEM-NURBS method for modelling the fibre arrangement of skeletal muscle**

To accurately characterise the in vivo muscle behaviour, the internal features, such as the fibre arrangement, need to be visualised. The last contribution of this thesis is the proposed FEM-NURBS method, which is the combination of the finite element method (FEM) and the non-uniform rational B-spline (NURBS) solid mathematical representation. Several numerical examples demonstrate that this method is able to characterise both the fibre arrangement and the biomechanical response of skeletal muscle.

## 1.3 Outline and organisation

The structure of the present thesis consists of six chapters: 1) Introduction, 2) Background knowledge, 3) Constitutive skeletal muscle model, 4) Three-dimensional finite element facial model and facial movement simulation, 5) Modelling the fibre arrangement of skeletal muscles using the FEM-NURBS method, 6) Conclusions and future work.

Chapter 1 gives the motivation and objectives of this thesis, and the contributions to the science and technology.

Chapter 2 provides the background knowledge on which this thesis is based. Facial anatomy is briefly described. Information on the skeletal muscle structure, architecture and mechanical properties are then provided. Finally, basic notions and mathematics relevant to general elastic constitutive models are summarised and presented.

Chapter 3 concerns the mechanical description of constitutive skeletal muscle model. Firstly, a review is given on existing constitutive skeletal muscle models and experimental data published on skeletal muscle mechanical properties, which suggests a validated 3D constitutive skeletal muscle model is needed. Then the detailed description of the developed constitutive skeletal muscle model and the LS-DYNA implementation of this model are presented. Finally, the validation of the developed skeletal muscle model is provided through several numerical tests.

Chapter 4 focuses on the construction of a three-dimensional (3D) finite element facial model and the simulation of facial movements. After an overview of various facial models, including geometric models, mass-spring models, finite element models, etc., the procedure for constructing the 3D finite element facial model is detailed. Then the applications of this facial model, including the outcome prediction of a cranio-facial surgery and the simulation of muscle-based facial movements, are presented.

In Chapter 5, a FEM-NURBS method is presented to model the fibre arrangement of skeletal muscle. Firstly, the related work on muscle fibre arrangement representations is reviewed. Secondly, the background information on the NURBS mathematical description is summarised. Following this, a FEM-NURBS method using ABAQUS is introduced and the relevant muscle constitutive relation is provided. Finally, the validation of the proposed FEM-NURBS method is discussed.

Chapter 6 summarises the main results of this thesis and provides the guidelines for future improving work.

# Chapter 2

# Background Knowledge

The biomechanical modelling of the facial structure requires a comprehensive knowledge of three major fields: facial anatomy, facial physiology and continuum mechanics. Anatomy is the study of internal and external structure of the body and the physical relationships among body parts. In contrast, physiology is the study of how living organisms perform their vital functions. Anatomy and physiology are closely integrated both theoretically and practically. Anatomical information provides clues about functions, and physiological mechanisms can be explained in terms of the underlying anatomy. The knowledge of anatomy and physiology of the human face enables us to understand important mechanisms of the human face. The knowledge of continuum mechanics enables us to simulate the mechanisms of human facial movements, that is the biomechanics of the human face.

In this chapter, firstly the facial anatomy is described. Then, the focus is placed on the physiology and mechanical properties of human skeletal muscle. Finally, a basic knowledge of the non-linear solid mechanics is provided. These are the fundamental sections that form the basis of this thesis.

## 2.1 Facial anatomy

This section presents knowledge of the anatomy of the facial skin, facial muscles around the head and neck, and the skull.

## 2.1.1 Facial Skin

Facial skin provides the outermost covering of the face. The facial skin structure consists of three main layers: the epidermis, the dermis and the hypodermis (Maurel, Wu, Thalmann et al., 1998). The superficial layer, the epidermis, is a relatively thin layer of stratified epithelium. It is around 0.1 mm thick (Odland, 1991). The underlying dermis is mainly composed of collagen fibres, ground substance and elastic fibres. Since there is no sharp boundary between the dermis and the subcutaneous layer, the thickness of the dermis is hard to measure and varies over a range from 0.5 mm to 4.0 mm (Odland, 1991). The third layer, the hypodermis, is composed of loose fatty connective tissue. Thus it is also called the subcutaneous layer. A typical structure of human skin is shown in Figure 2.1.

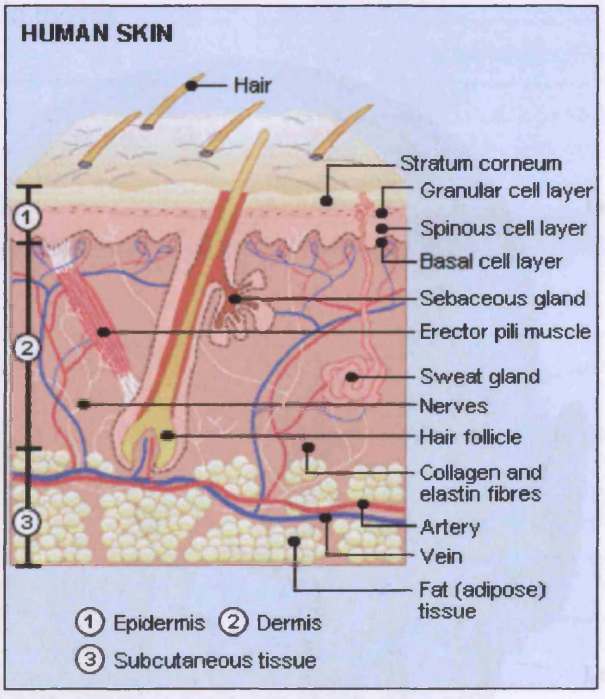


**Figure 2.1** Structure of human skin (Melbourne Dermatology, 2009)

## 2.1.2 Muscles of human head and neck

The muscular structure that connects the facial skin and the skull is extremely complex. A muscle in the muscular system shortens under neural control, causing the soft tissues and bony structures to move. Each muscle has two attachments to these structures, called origin and insertion according to their roles in the movement. The origin is the end of the muscle that is attached to the least movable structure and the insertion is the other end of the

muscle that is attached to the more movable structure. In general, the insertion of a muscle moves toward the origin when the muscle contracts.

The muscles of the human head and neck can be divided into several groups by functions. In this thesis, three groups of them are considered, i.e. muscles of facial expression, muscles of mastication and the hyoid muscles.

## • Muscles of Facial expression

The muscles of facial expression are paired muscles in the superficial fascia of the facial tissues, as shown in Figure 2.2. All the muscles of facial expression originate from the surface of the skull bone and insert into the dermis of the skin tissue. When the muscle contracts, the facial skin moves.

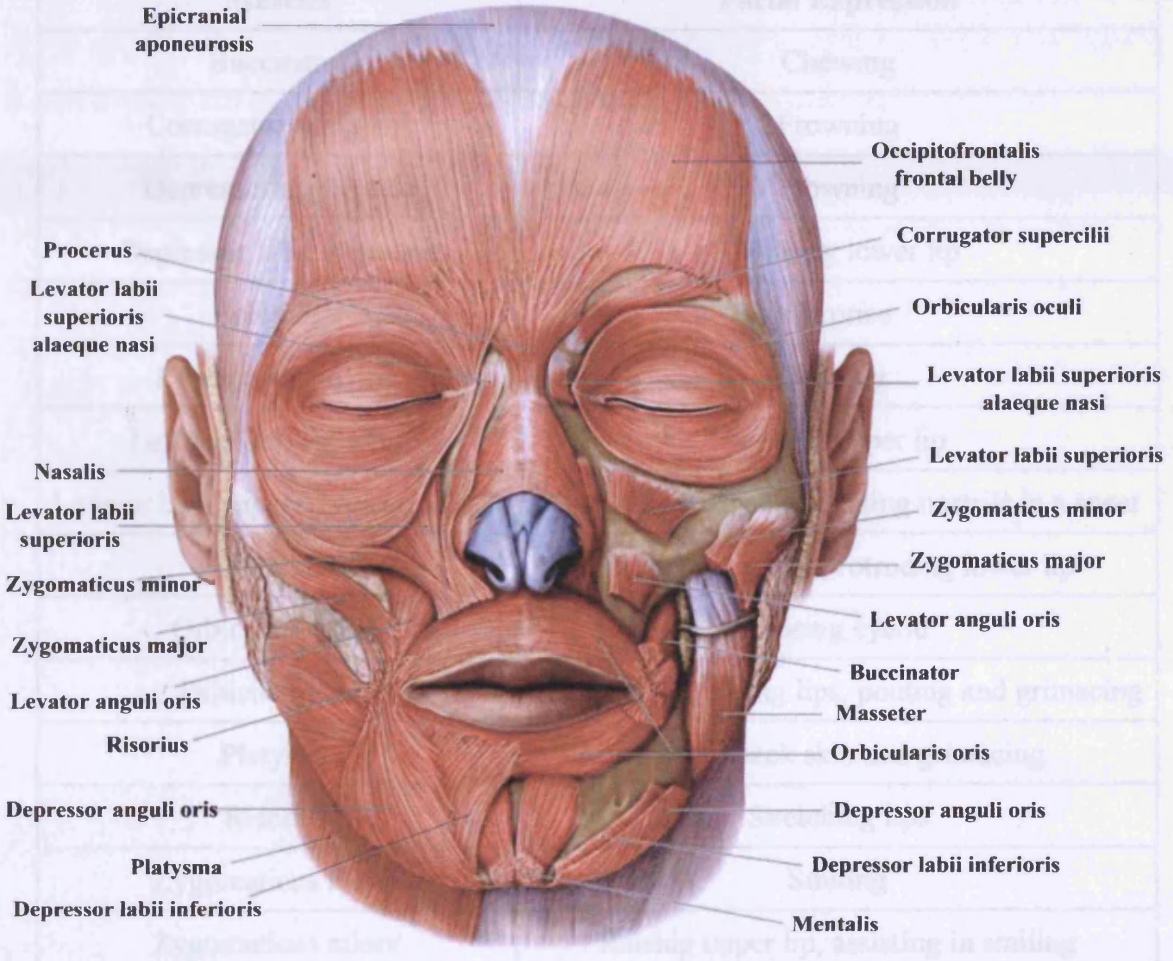


**Figure 2.2** Muscles of facial expression (Schuenke, Schulte, Schumacher et al., 2007)

During facial expression, the muscles act in various combinations to vary the appearance of the face (MaKinley and O'Loughlin, 2005; Martini, Ober, Garrison et al., 2006; Martini,Timmons and Tallitsch, 2008; Schuenke, Schulte, Schumacher et al., 2007), as summarised in Table 2.1. Examples of facial expressions by using some of these muscles are shown in Figure 2.3. In Figure 2.3A, the patient uses levator labii superioris muscle, levator anguli oris muscle, risorius muscle, zygomaticus minor and major muscles to provide a look of smile; In Figure 2.3B, the patient uses corrugator supercilii muscle, levator labii superioris alaeque nasi muscle and depressor anguli oris muscle to provide a look of disgust.

**Table 2.1** Muscles of facial expression and their associated facial expressions

| **Muscles** | **Facial Expression** |
|---|---|
| Buccinator | Chewing |
| Corrugator supercilii | Frowning |
| Depressor anguli oris | Frowning |
| Depressor labii inferioris | Lowering lower lip |
| Epicranial | Surprise |
| Levator anguli oris | Smiling |
| Levator labii superioris | Raising upper lip |
| Levator labii superoris alaeque nasi | Raising upper lip and dilating nostrils in a sneer |
| Mentalis | Raising chin and protruding lower lip |
| Orbicularis oculi | Closing eyelid |
| Orbicularis oris | Closing and pursing lips, pouting and grimacing |
| Platysma | Raising neck skin and grimacing |
| Risorius | Stretching lips |
| Zygomaticus major | Smiling |
| Zygomaticus minor | Raising upper lip, assisting in smiling |


**Figure 2.3** Examples of facial expressions, Left: smiling; Right: Disgusted (Schuenke, Schulte, Schumacher et al., 2007)

- **Muscles of mastication**

The muscles of mastication are four pairs of muscles attached to the mandible: the masseter, the temporalis, the medial pterygoid and the lateral pterygoid muscles (Figure 2.4).

The muscles of mastication are responsible for closing the jaws, moving the lower jaw forward or backward and shifting the jaw laterally. These jaw movements involve the movement of the mandible, while the rest of the skull remains relatively stable.

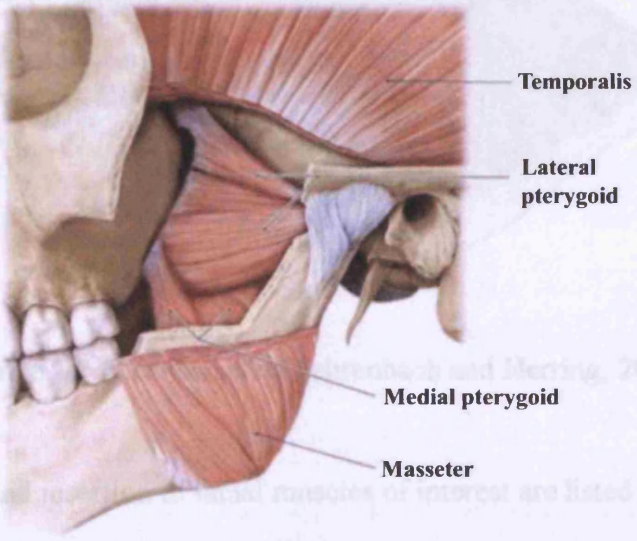


**Figure 2.4** Muscles of Mastication (Schuenke, Schulte, Schumacher et al., 2007)

- **Hyoid muscles**

The hyoid muscles assist in the actions of mastication, swallowing and opening of the mouth, etc. Most of these muscles are in a superficial position in the neck tissues. The hyoid muscles are attached in a complex way to the hyoid bone. Based on their relationship to the hyoid bone, they can be grouped to the suprahyoid muscles, which are above the hyoid bone, and the infrahyoid muscles, which are below the hyoid bone, as shown in Figure 2.5. The hyoid bone is a horseshoe-shaped bone suspended beneath the mandible, with the open end of the horseshoe pointed posteriorly. The hyoid bone does not articulate with any other bone and its only connection with other bones is through muscles and ligament attachment.

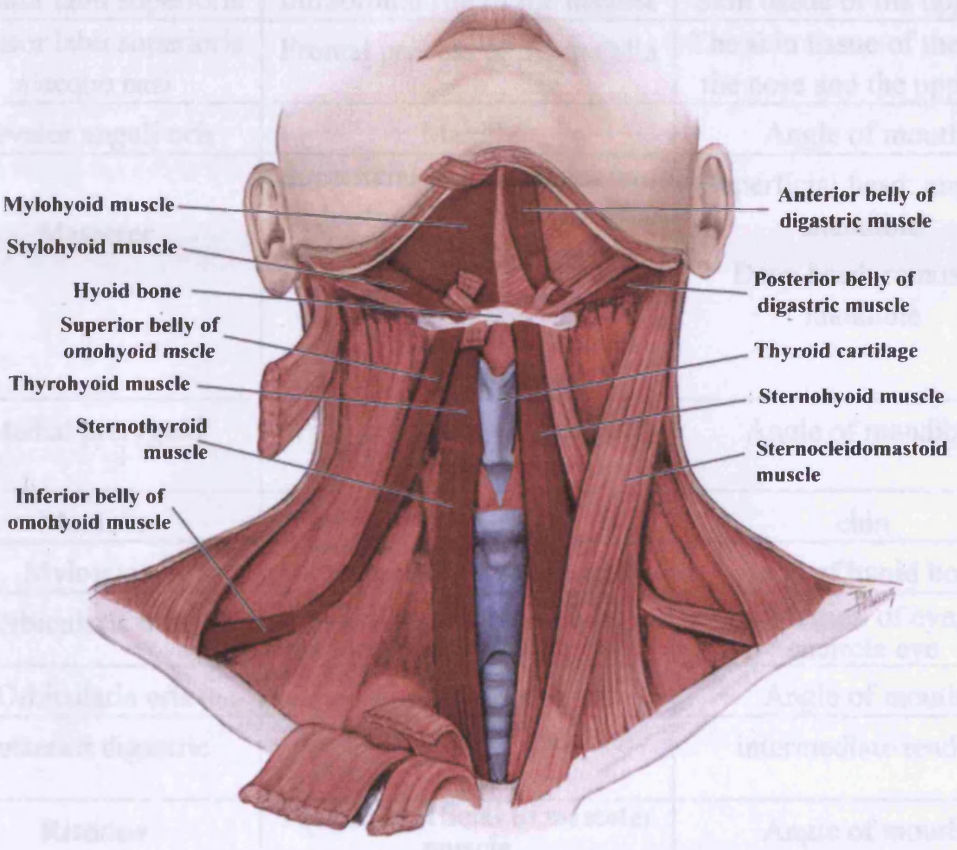


**Figure 2.5** Neck muscles (Fehrenbach and Herring, 2006)

The specific origin and insertion of facial muscles of interest are listed in Table 2.2.

**Table 2.2** Origin and insertion of facial muscles (Fehrenbach and Herring, 2006)

| Muscles | Origin | Insertion |
|---|---|---|
| Anterior digastric | intermediate tendon | medial surface of mandible |
| Buccinators | Maxilla, mandible and pterygomandibular raphe | Angle of mouth |
| Depressor anguli oris | Mandible | Angle of mouth |
| Depressor labii inferioris | Mandible | Lower lip |
| Geniohyoid | Genial tubercles of mandible | Body of hyoid bone |
| Lateral pterygoid | Superior head: greater wing of sphenoid bone<br>Inferior head: lateral pterygoid plate from sphenoid bone | Both heads: pterygoid fovea of mandible |
| Levator labii superioris | Infraorbital rim of the maxilla | Skin tissue of the upper lip |
| Levator labii superioris alaeque nasi | Frontal process of the maxilla | The skin tissue of the ala of the nose and the upper lip |
| Levator anguli oris | Maxilla | Angle of mouth |
| Masseter | Superficial head: anterior two thirds of lower border of zygomaticus arch<br>Deep head: posterior one third and medial surface of zygomaticus arch | Superficial head: angle of mandible<br>Deep head: ramus of mandible |
| Medial pterygoid | Pterygoid fossa of sphenoid bone | Angle of mandible |
| Mentalis | Mandible | chin |
| Mylohyoid | Mylohyoid line of mandible | Body of hyoid bone |
| Orbicularis oculi | Orbital rim, frontal and maxillary bones | Lateral region of eye, some encircle eye |
| Orbicularis oris | Encircle mouth | Angle of mouth |
| Posterior digastric | mastoid notch of temporal bone | intermediate tendon |
| Risorius | Fascia superficial to masseter muscle | Angle of mouth |
| Stylohyoid | Styloid process of temporal bone | Body of hyoid bone |
| Temporalis | Temporal fossa | Coronoid process of mandible |
| Zygomaticus major | Zygomatic bone | Angle of mouth |
| Zygomaticus minor | Zygomatic bone | Upper lip |

## 2.1.3 Human Skull

The human skull is the foundation for the soft tissues of the face and head. The bones of the skull play several different roles. They protect the brain, form the facial skeleton, and participate in jaw movement. The skull is composed of 22 bones which can be grouped into two categories based upon their roles. Eight bones make up the neurocranium, surrounding the brain and fourteen bones make up the viscerocranium, forming the face. Some of these bones are single, e.g. the frontal bone, mandible, etc., and some are paired bones, e.g. the maxilla, temporal bones, zygomatic bones, etc.

## 2.1.4 Temporomandibular Joint

The temporomandibular joint (TMJ) is a joint located on each side of the skull that allows for the movement of the mandible. As its name indicates, the TMJ is the articulation between the temporal bone and the mandible, as shown in Figure 2.6.

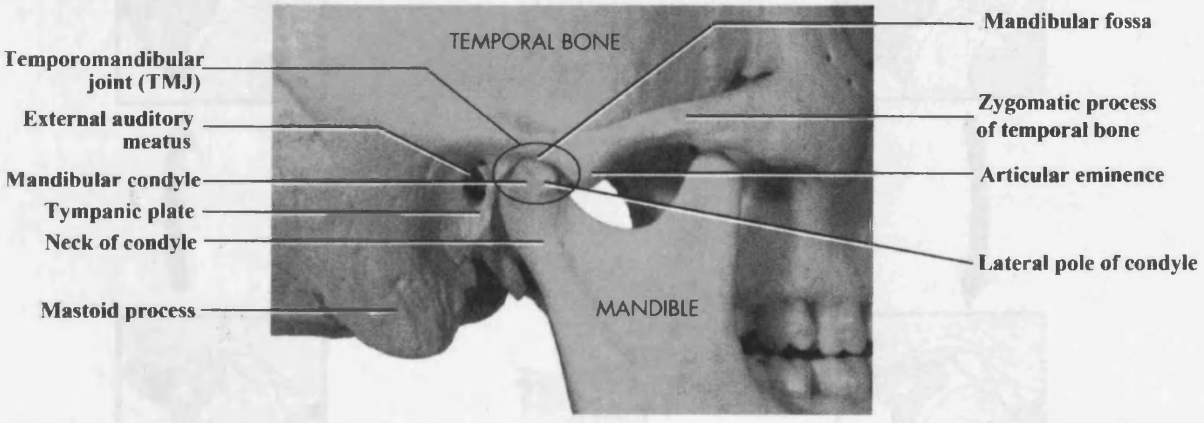


**Figure 2.6** Lateral view of the bones of the temporomandibular joint (Liebgott, 2001)

The TMJ has two distinct types of movement: a rotational movement and a gliding movement. The gliding movement allows the lower jaw to move forward (protrusion) and backward (retrusion). The protrusion involves the bilateral contraction of the lateral pterygoid muscles and the retrusion involves the contraction of the posterior portions of both temporalis muscles. The movements accomplished by TMJ rotation are the depression

and elevation of the mandible. The muscles involved in elevating the mandible are the bilateral masseter, temporalis, and medial pterygoid muscles, while the muscles involved in depressing the mandible are the inferior heads of the lateral pterygoid and the anterior suprahyoid muscles.

The various movements of the jaw during speech and mastication are accomplished by the combination of these two basic movements: gliding and rotation. For example, opening the mouth involves both depression and protrusion of the mandible and closing the mouth involves both elevation and retrusion of the mandible, as shown in Figure 2.7.

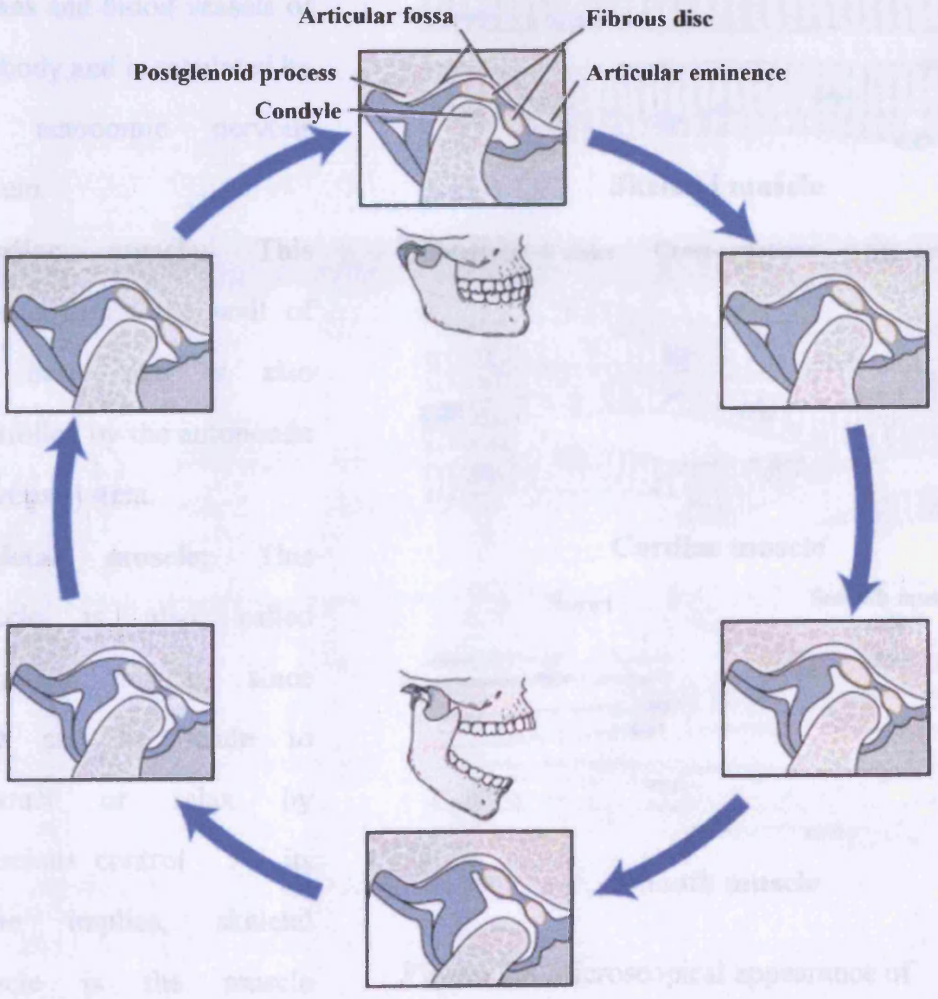


**Figure 2.7** Opening and closing of the mouth (Bath-Balogh,Fehrenbach and Thomas, 2006)

## 2.2 Skeletal muscles

In this section, the structure, architecture, mechanical properties and the contraction dynamics of the skeletal muscle tissue will be reviewed.

Muscles are distinguished from other soft tissues by their specific contractile properties. They can be classified into three types based on the functions they fulfil (Pocock and Richards, 2004; Widmaier, Raff and Strang, 2005):

- **Smooth muscle:** This muscle lies in the hollow organs and blood vessels of the body and is regulated by the autonomic nervous system.
- **Cardiac muscle:** This muscle forms the wall of the heart and is also controlled by the autonomic nervous system.
- **Skeletal muscle:** This muscle is also called voluntary muscle, since they can be made to contract or relax by conscious control. As its name implies, skeletal muscle is the muscle directly attached to the bones of the skeleton and its role is to maintain posture and move the limbs by contracting.

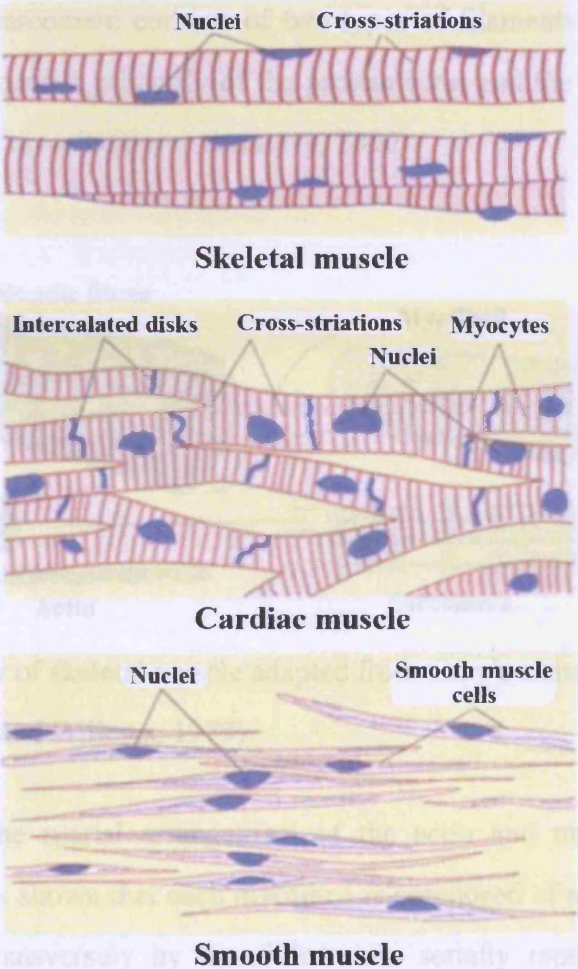


**Figure 2.8** Microscopical appearance of skeletal muscle, smooth and cardiac muscle (Pocock and Richards, 2004)

## 2.2.1 Skeletal muscle structure

A hierarchical structure of the skeletal muscle is shown in Figure 2.9. It can be seen that a muscle belly comprises a large number of fasciculi enclosed in a connective sheath, the epimysium. The fasciculi are formed by bundles of muscle fibres surrounded by a strong connective sheath, the perimysium. The spaces between the muscle fibres within a bundle are filled by a soft connective tissue called endomysium. Within a muscle fibre, there are a large number of myofibrils, whose diameter is approximately 1μm. The filaments of myofibrils are called myofilaments which are the formation of the smallest functional unit of muscle, termed the sarcomere. The sarcomere consists of two types of filaments: thin and thick filaments. The thin filaments consist primarily of the protein actin and the thick filaments consist primarily of the protein myosin (Berne and Levy, 2000).

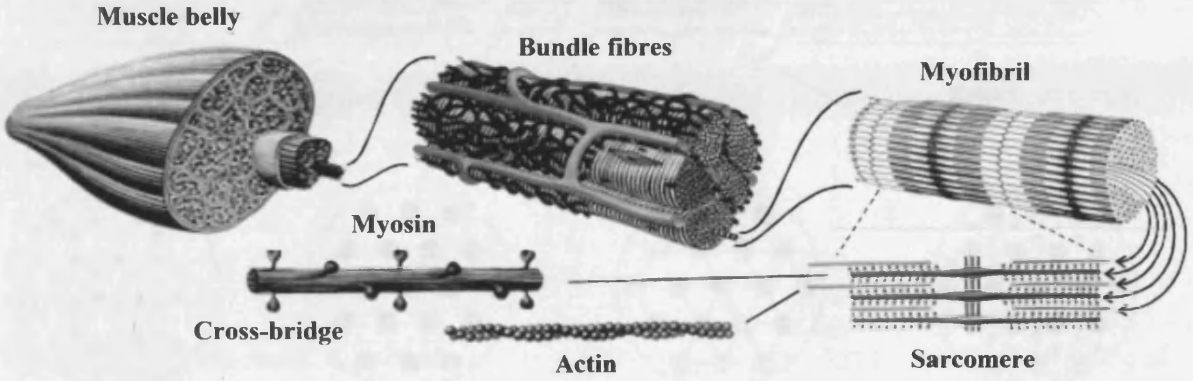


**Figure 2.9** The organisational hierarchy of skeletal muscle adapted from Gray's anatomy (Warwic and Willems, 1973)

The structure of a myofilament and the spatial arrangement of the actin and myosin molecules are shown in Figure 2.10. It is shown that each myofibril is composed of arrays of myofilaments, which are divided transversely by the Z-disk into serially repeating regions called sarcomere which is about 2.5 μm long. The area between the Z-disk is further divided into two bands: I band and A band, where the I band mainly contains thin actin filaments, whose diameter is about 5nm and the A band contains myosin filaments, whose diameter is around 12nm. Within the A band, the central region is called the H band, where there is no actin-myosin overlap when the muscle is in a relaxed state. Finally, the

line transversely across the H band is called the M-line. More information of the myofilament structure can be found in Carola, Wynsberghe et al.(1995), Silverthorn, Ober et al. (2009), Warwic and Willems (1973) and Widmaier, Raff et al. (2005).

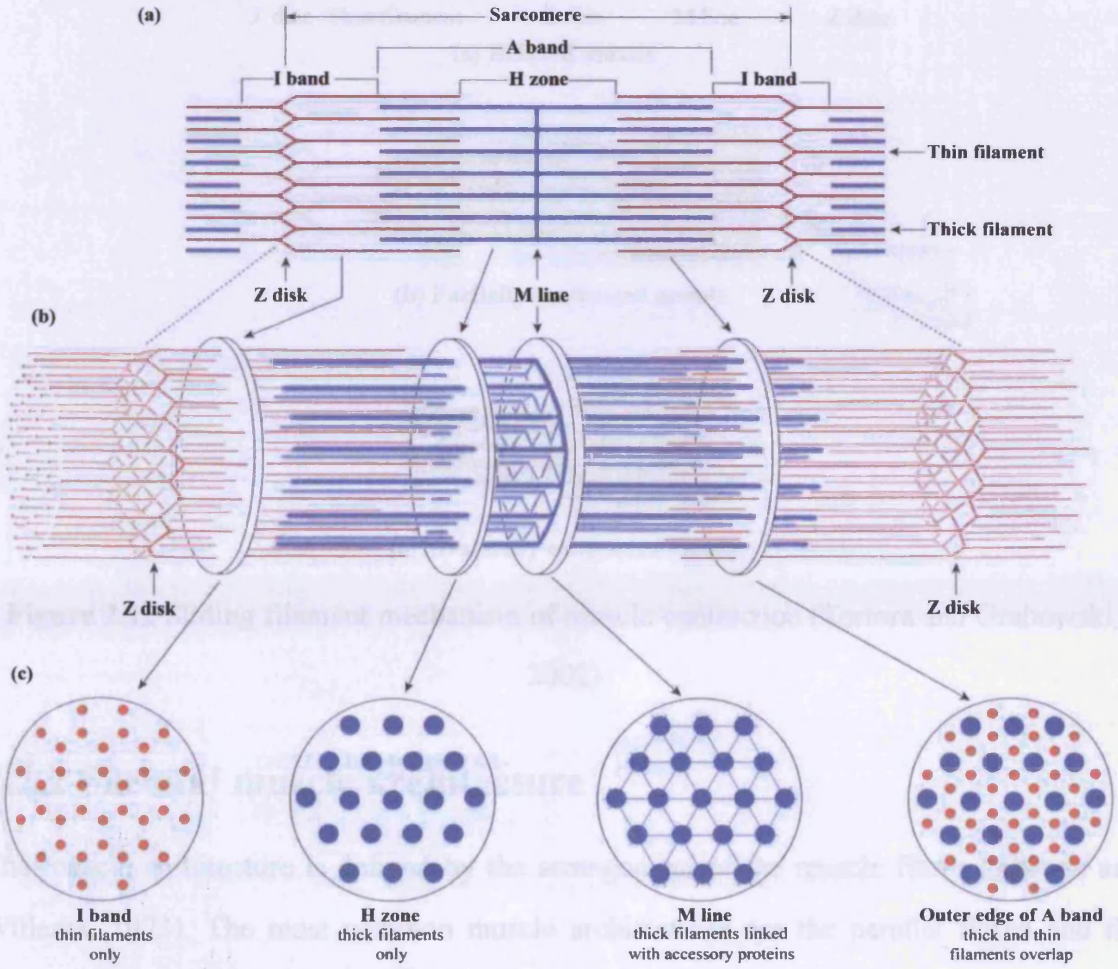


**Figure 2.10** Structure of a myofilament (Silverthorn, Ober, Garrison et al., 2009)

The actin filaments are attached at one end to the Z-line and are free at the other end to interact with the myosin filaments. When a muscle contracts, the actin is pulled along myosin toward the centre of the sarcomere until the actin and myosin filaments are completely overlapped. If the muscle contracts greatly, I- and H- bands may narrow to extinction, but the A-bands remain unaltered, as shown in Figure 2.11. This is called the sliding filament theory of muscle contraction (Tortora and Grabowski, 2002; Vander, Sherman and Luciano, 2003).

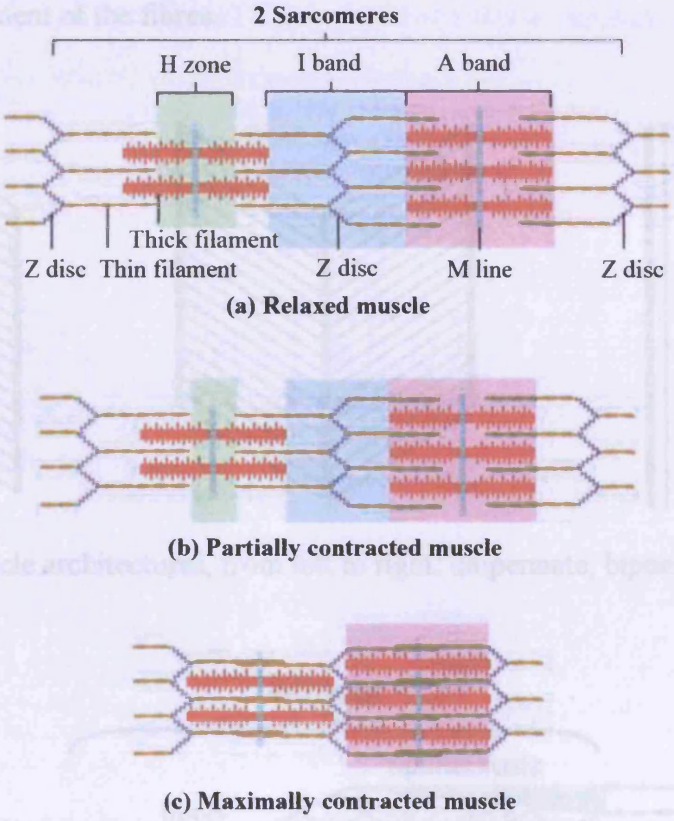


**Figure 2.11** Sliding filament mechanism of muscle contraction (Tortora and Grabowski, 2002)

## 2.2.2 Skeletal muscle architecture

The muscle architecture is defined by the arrangement of the muscle fibres (Warwic and Willems, 1973). The most common muscle architectures are the parallel fibred and the pennate, as shown in Figure 2.12. In a parallel fibred muscle, the fibres are arranged along the long muscle axis and have almost the same length as the muscle. In contrast, the pennate muscle fibres run obliquely to the long axis and are relatively short compared to the muscle length. The uni-pennate muscles have the tendon running along one side. In bi-pennate muscles, the tendon passes through the centre of the muscle and the fibres are attached to it on either side. In multi-pennate muscles, the fasciculi are arranged such that they converge on many tendons. The fibres of a pennate muscle are connected to the aponeurosis of the muscle, which is also called the internal portion of the tendon since its properties are the same as those of the external portion of the tendon. Figure 2.13 shows the

functional arrangement of the fibres.

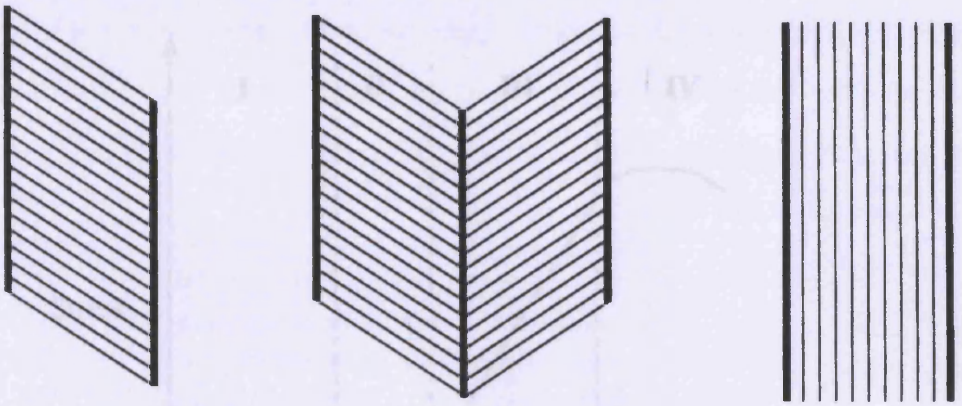

**Figure 2.12** Muscle architectures, from left to right: unipennate, bipennate and fusiform

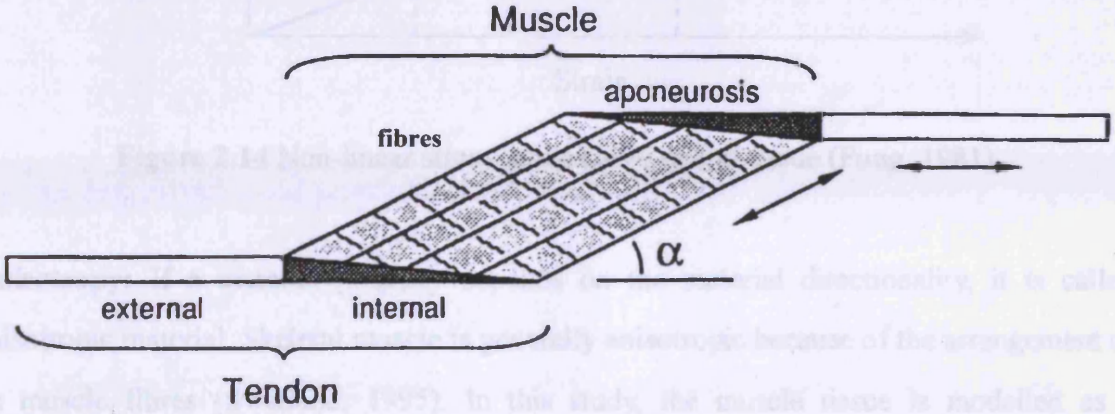


**Figure 2.13** Muscle-tendon architecture in a pennate muscle (Zajac, 1989)

## 2.2.3 Mechanical properties of skeletal muscle

In this section, the main mechanical properties of skeletal muscle will be discussed.

**Non-linearity:** The muscle tissue exhibits a non-linear stress-strain relationship which is characterised by four regions: in region I, the tissue is under low strains, its response is linear; in region II, the tangential modulus of the tissue increases due to the straightening of the collagen fibres; in region III, all the fibrils become taut and the tangential modulus of the tissue reaches a maximum value, thus the stress increases linearly with the strain in the

region; in region IV, groups of fibrils begin to fail and tissue destruction occurs, therefore the tangential modulus decreases, as shown in Figure 2.14.

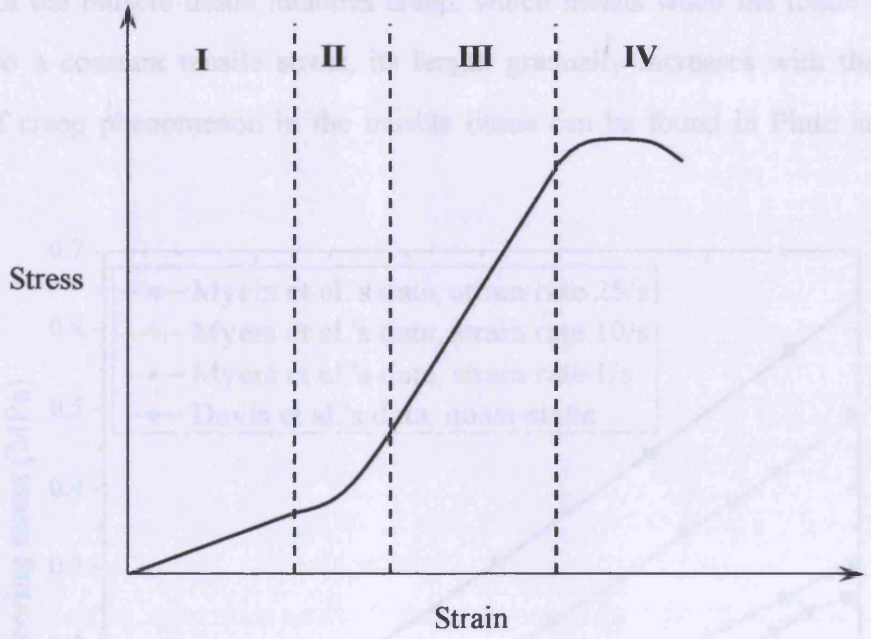


**Figure 2.14** Non-linear stress-strain curve of soft tissue (Fung, 1981)

**Anisotropy:** If a material property depends on the material directionality, it is called anisotropic material. Skeletal muscle is generally anisotropic because of the arrangement of its muscle fibres (Swatland, 1995). In this study, the muscle tissue is modelled as a transversely isotropic material by assuming the muscle is made of one branch of muscle fibres.

**Viscoelasticity:** The response of a viscoelastic material depends on the history of the deformation, i.e. the stress produced in the material is a function of not only the strain but also the strain rate and the strain history. The stress values appear higher at larger strain rate than those at a lower strain rate for the same strain, as shown in Figure 2.15 (Davis, Kaufman and Lieber, 2003; Myers, Wooley, Slotter et al., 1998). The stress relaxation behaviour of the muscle tissue has been demonstrated by the Van Loocke group (Van Loocke, Lyons and Simms, 2008). They performed compression tests in vitro on fresh porcine skeletal muscle at various rates and in different orientations of the tissue fibres.

The test results showed that when the muscle is compressed and maintained at its new length, the amplitude of the stress gradually drops with the time. Other time-dependent behaviour of the muscle tissue includes creep, which means when the tissue is suddenly submitted to a constant tensile stress, its length gradually increases with the time. The evidence of creep phenomenon in the muscle tissue can be found in Pinto and Patitucci (1977).

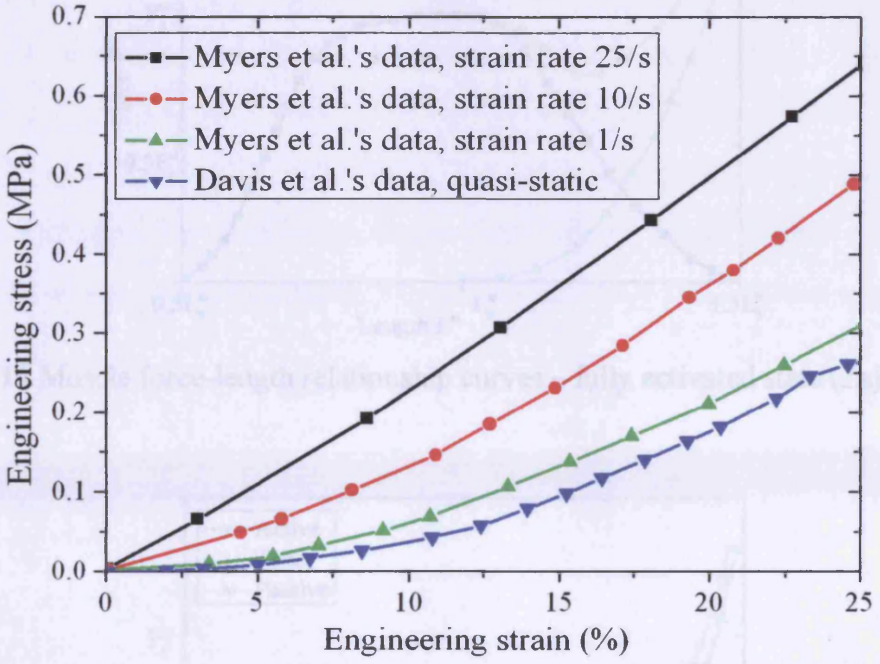


**Figure 2.15** Engineering stress versus strain curves for passive rabbit leg muscle

**Quasi-incompressible material:** Muscle tissue can be regarded as a quasi-incompressible material because it is made up of about 80% incompressible water, 3% fat and 10% collagenous tissues.

## 2.2.4 Contraction dynamics of skeletal muscle

Differing from other soft tissues, the skeletal muscle tissue has a unique feature of voluntary contraction. The contraction dynamics of the muscle is discussed below.

**Force-length relationship:** The force-length relationship provides an isometric contraction characteristic for the skeletal muscle tissue. This relationship is obtained from the static tests of muscle tissues (Edman, 1966; Gordon, Huxley and Julian, 1966). The muscle was

held at different lengths, and both the passive and the fully contracted muscle forces were recorded. The active force is the difference between the forces developed when muscle is activated and when muscle is passive.

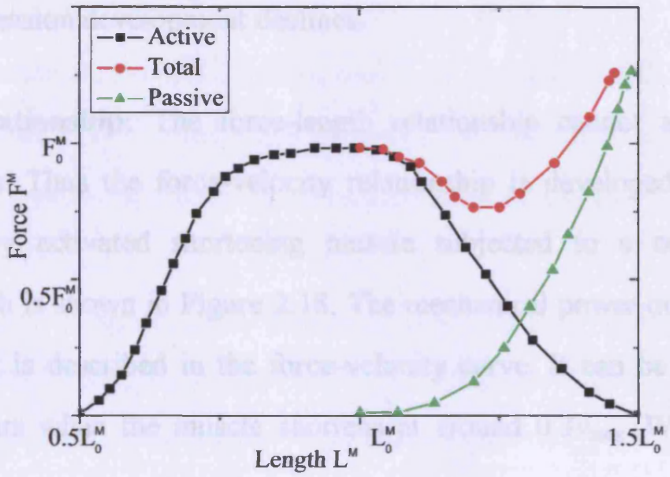


**Figure 2.16** Muscle force-length relationship curves – fully activated state (Zajac, 1989)

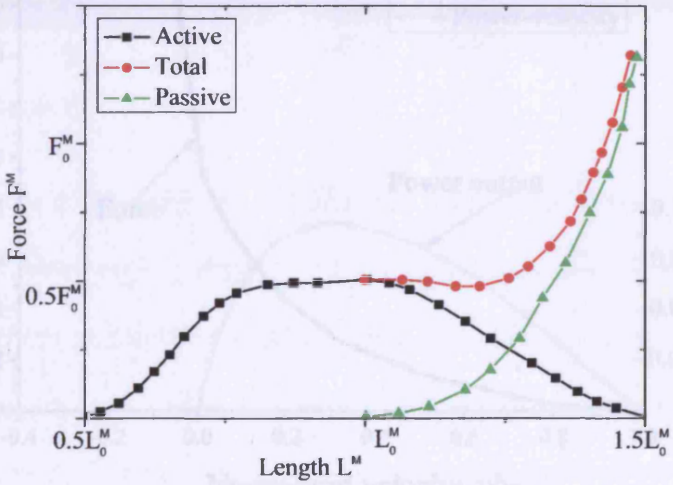


**Figure 2.17** Muscle force-length relationship curves – half activated state (Zajac, 1989)

The isometric active and passive force-length curves are shown in Figures 2.16 and 2.17, where in Figure 2.16, the muscle is fully activated and in Figure 2.17, the muscle is 50% activated. The sliding filament theory of muscle contraction provides a clear explanation for the skeletal muscle force-length relationship. When the muscle is at its resting length, there is a maximum tension, because the thin and thick filaments overlap optimally and

form a maximum number of cross-bridges. As the muscle lengthens, the filaments are pulled apart and the number of cross-bridges reduces. This leads to a decline in the ability of the muscle to generate tension. As the muscle shortens, the filaments from each end of the sarcomere touch in the centre of the A band and each interferes with the motion of the other. As a result, tension development declines.

**Force-velocity relationship:** The force-length relationship cannot account for muscle dynamic properties. Thus the force-velocity relationship is developed by measuring the velocity of a fully activated shortening muscle subjected to a constant tension. A force-velocity graph is shown in Figure 2.18. The mechanical power output that the active muscle can deliver is described in the force-velocity curve. It can be seen that the peak power output occurs when the muscle shortens at around $0.3v_{max}$ (Woledge, Curtin and Homsher, 1985).

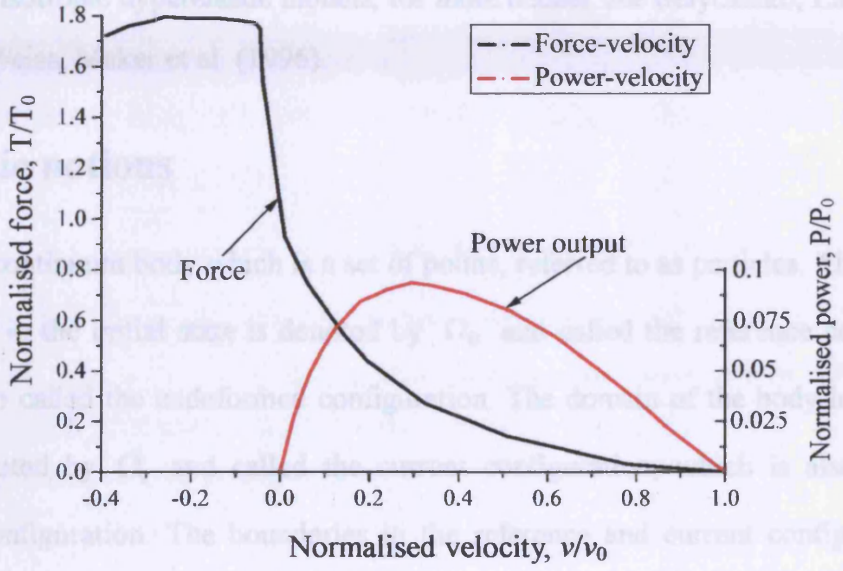


**Figure 2.18** Muscle force-velocity relationship curve (McMahon, 1984)

When a fully activated muscle is subjected to a constant tension, it will first shorten and then stop. The length where the shortening terminates corresponds to the length specified by force-length relation curve of the fully activated muscle. As a result of this, the mechanical properties of skeletal muscle can be described by a force-length-velocity relation (Gatto and Swannell, 1990).

## 2.3 Basics of non-linear solid mechanics

Skeletal muscle tissue is usually considered as an active, quasi-incompressible, transversely isotropic and hyperelastic material. There is currently no available software which presently describes these kinds of materials. However, ABAQUS and LS-DYNA provide the interfaces which allow the users to define their own material models. Before developing the constitutive models, it is worthwhile to revisit the basic notions and some general constitutive models within the framework of non-linear solid mechanics.

Summarised below in Chapter 2.3.1 are some basic notions, including definitions of deformation gradient, Cauchy stress, etc. for more details, see Belytschko, Liu and Moran (2000) and Shabana (2008); Summarised below in Chapter 2.3.2 are some general elastic constitutive models, including hyperelastic models, isotropic hyperelastic models and transversely isotropic hyperelastic models, for more details, see Belytschko, Liu and Moran (2000) and Weiss, Maker et al. (1996).

### 2.3.1 Basic notions

Let $B_y$ be a continuum body which is a set of points, referred to as particles. The domain of the body $B_y$ in the initial state is denoted by $\Omega_0$ and called the reference configuration, which is also called the undeformed configuration. The domain of the body in the current state is denoted by $\Omega_t$ and called the current configuration, which is also called the deformed configuration. The boundaries in the reference and current configurations are denoted by $\Gamma_0$ and $\Gamma_t$, respectively. The domain can be one-, two- or three-dimensional. Thus, the boundary corresponding to the two end-points is a line segment in one dimension, a curve in two dimensions and a surface in three dimensions. Two neighboring particles in the undeformed configuration are denoted by $P_0$ and $Q_0$ and the corresponding particles in the deformed configuration are denoted by $P_t$ and $Q_t$, as shown in Figure 2.19.

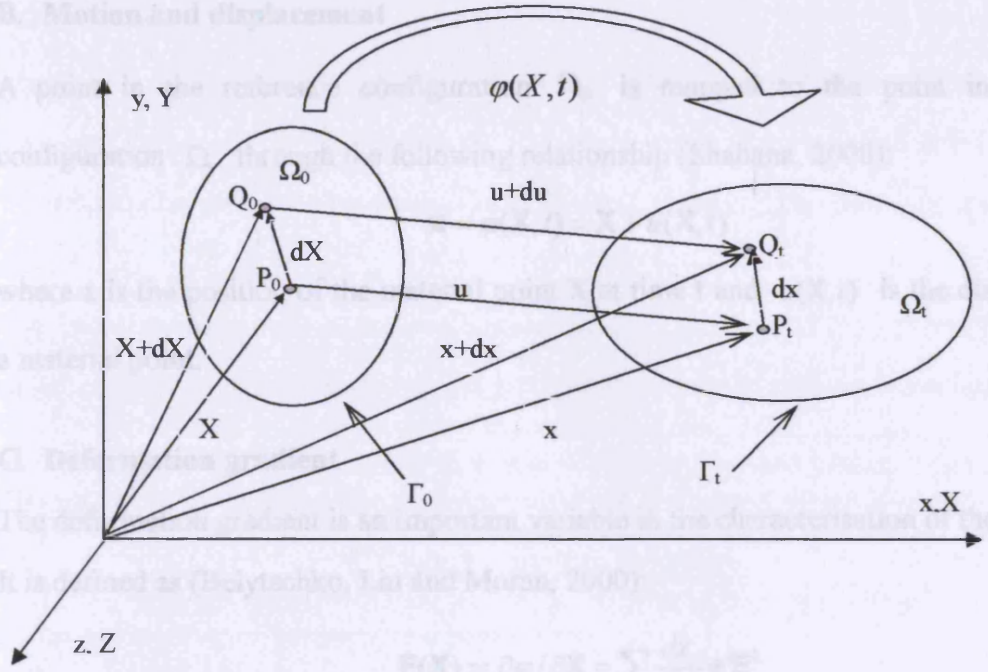


**Figure 2.19** Reference and current configurations of a continuum body

### A. Lagrangian and Eulerian coordinates

The position vector of a material point in the reference configuration is given by (Belytschko, Liu and Moran, 2000):

$$\mathbf{X} = X_I \mathbf{E}^I \tag{2.1}$$

where $X_I$ are the components of the position vector in the reference configuration and $\mathbf{E}^I$ are the unit base vectors of a rectangular Cartesian coordinate system in the reference configuration. The coordinates $X_I$ give the position of a material point, thus are called material coordinates or Lagrangian coordinates.

Correspondingly, the position vector of a point in the current configuration is given by (Belytschko, Liu and Moran, 2000):

$$\mathbf{x} = x_i \mathbf{e}^i \tag{2.2}$$

where $x_i$ are the components of the position vector in the current configuration and $\mathbf{e}^i$ are the unit base vectors in the current configuration. The coordinates $x_i$ give the spatial position and are called spatial coordinates or Eulerian coordinates. In this thesis, whenever indicial notation is employed, lower-case letters refer to the deformed configuration and upper case to the reference configuration.

**B. Motion and displacement**

A point in the reference configuration $\Omega_0$ is mapped to the point in the current configuration $\Omega_t$ through the following relationship (Shabana, 2008):

$$\mathbf{x} = \varphi(\mathbf{X}, t) = \mathbf{X} + u(\mathbf{X}, t) \tag{2.3}$$

where $\mathbf{x}$ is the position of the material point $\mathbf{X}$ at time t and $u(\mathbf{X}, t)$ is the displacement of a material point.

**C. Deformation gradient**

The deformation gradient is an important variable in the characterisation of the deformation. It is defined as (Belytschko, Liu and Moran, 2000):

$$\mathbf{F}(\mathbf{X}) := \partial\varphi / \partial\mathbf{X} = \sum \frac{dx_i}{dX_I} \mathbf{e}^i \mathbf{E}^I \tag{2.4}$$

It should be noted that, in the terminology of mathematics, the deformation gradient $\mathbf{F}$ is the Jacobian matrix of the mapping function $\varphi(\mathbf{X}, t)$. The determinant of $\mathbf{F}$ is called the Jacobian determinant or the determinant of the deformation gradient.

$$J := \det \mathbf{F} \tag{2.5}$$

Note that, $J$ is a scalar and for an incompressible material, it equals one.

A multiplicative decomposition of the deformation gradient is always applied to decouple the deviatoric and dilatational response (Flory, 1961):

$$\mathbf{F} := \mathbf{F}_{vol} \cdot \mathbf{F}_{dev} \tag{2.6}$$

where $\mathbf{F}_{vol} := J^{1/3}\mathbf{I}$ is the dilatational part, also called the volumetric response and $\mathbf{F}_{dev} := J^{-1/3}\mathbf{F}$ is the deviatoric part, sometimes called the isochoric response.

The determinant of the deviatoric deformation gradient is always unity, i.e. $\det(\mathbf{F}_{dev}) = 1$. Therefore, $\det(\mathbf{F}_{vol}) = \det \mathbf{F} = J$, which means only the volumetric deformation gradient $\mathbf{F}_{vol}$ contributes to the volume change of the material.

**D. Strain measures**

There are a number of different measures of strain used in non-linear continuum mechanics. The ones considered in this thesis are the Green strain, the right and left Cauchy-Green deformation tensors. In this section, the definitions of these strain measures are given.

The Green strain or Lagrangian strain measures the difference of the square of the length of an infinitesimal segment in the current configuration and the reference configuration.

The square of the length of the material vector dX in Figure 2.19 is given by:

$$(d\mathbf{X})^2 = dX_i dX_i = \delta_{ij} dX_i dX_j \tag{2.7}$$

In the deformed configuration, this is given by:

$$(d\mathbf{x})^2 = dx_i dx_i = \delta_{ij} dx_i dx_j \tag{2.8}$$

where $\delta_{ij}$ is the kronecker delta, with $\delta_{ij} = 1$ if i = j and $\delta_{ij} = 0$ if i ≠ j.

Then the difference of the square of the length is given by:

$$(d\mathbf{x})^2 - (d\mathbf{X})^2 = 2d\mathbf{X} \cdot \mathbf{E} \cdot d\mathbf{X} \tag{2.9}$$

where **E** is the Green strain tensor and given by

$$\mathbf{E} = \frac{1}{2}\left(\mathbf{F}^T\mathbf{F} - \mathbf{I}\right) \tag{2.10}$$

or

$$E_{ij} = \frac{1}{2}\left(F_{ik}^T F_{kj} - \delta_{ij}\right) \tag{2.11}$$

**I** is the second order unit tensor.

The right and left Cauchy-Green deformation tensors are defined respectively as (Weiss, Maker and Govindjee, 1996):

$$\mathbf{C} := \mathbf{F}^T\mathbf{F} = F_{iI} F_{iJ} \mathbf{E}^I \mathbf{E}^J \tag{2.12}$$

$$\mathbf{B} := \mathbf{F}\mathbf{F}^T = F_{iI} F_{jI} \mathbf{e}^i \mathbf{e}^j \tag{2.13}$$

The right and left Cauchy-Green deformation tensors can be used as a measure of the deformation because in the case of an arbitrary rigid-body displacement, they remain constant and are equal to the identity matrix.

Based on the multiplicative split of the deformation gradient, the right and left Cauchy-Green tensors can be decomposed as:

$$\mathbf{C} = \mathbf{F}^T\mathbf{F} = J^{2/3}\overline{\mathbf{C}} \tag{2.14}$$

$$\mathbf{B} = \mathbf{F}\mathbf{F}^T = J^{2/3}\overline{\mathbf{B}} \tag{2.15}$$

where $\overline{\mathbf{C}}$ and $\overline{\mathbf{B}}$ are the right and left Cauchy-Green tensors with the volume change eliminated.

**E. Stress measures**

In non-linear solid problems, various stress measures can be defined. However, in this thesis, only three of them are considered: the Cauchy stress $\boldsymbol{\sigma}$, the first Piola-Kirchhoff stress tensor **P** (nominal stress tensor) and the second Piola-Kirchhoff stress tensor **S**. Their definitions are given below.

A deformed body can be divided into two portions by a plane. Consider a surface element ds on the cross-section in the current configuration. Let vector **a** be the outward unit vector to this cross section. Correspondingly, let dS and **A** represent the surface element and the outward normal vector in the reference configuration, as shown in Figure 2.20.

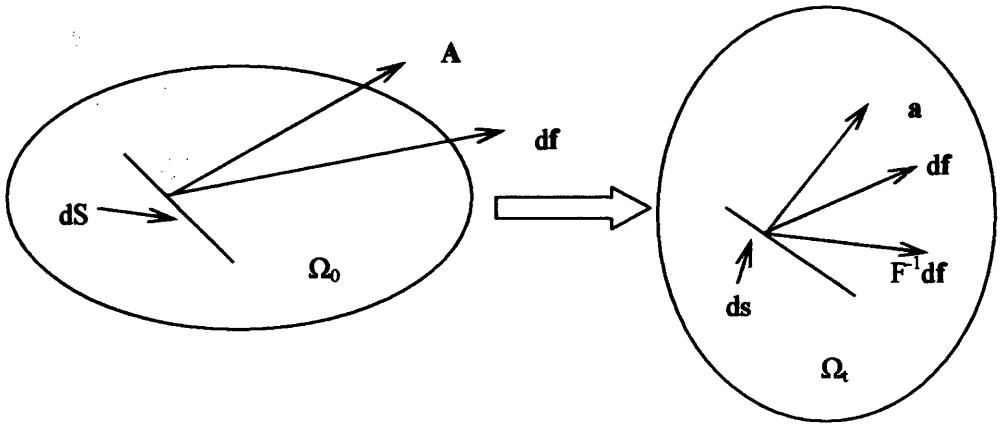


**Figure 2.20** Definition of the stress measures

The traction exerted on the surface element ds in the current configuration is called the Cauchy traction vector **t**. The corresponding traction exerted on dS in the reference configuration is called the first Piola-Kirchhoff traction vector $\mathbf{t}_0$.

According to Cauchy's law, the following relation exists (Marsden and Hughes, 1994):

$$\mathbf{a}\cdot\boldsymbol{\sigma}ds = d\mathbf{f} = \mathbf{t}ds \tag{2.16}$$

and in the reference configuration (Marsden and Hughes, 1994):

$$\mathbf{A}\cdot\mathbf{P}dS = d\mathbf{f} = \mathbf{t}_0 dS \tag{2.17}$$

where $\boldsymbol{\sigma}$ and $\mathbf{P}$ are the Cauchy stress tensor and the first Piola-Kirchhoff stress tensor, respectively.

The relation between these two stresses can be obtained by using the Nanson's relation (Malvern, 1969), which relates the current normal to the reference normal by:

$$\mathbf{a}ds = J\mathbf{A}\cdot\mathbf{F}^{-1}dS \tag{2.18}$$

Further using Equations (2.16) and (2.17), the following equation is obtained.

$$J\mathbf{A}\cdot\mathbf{F}^{-1}\cdot\boldsymbol{\sigma}dS = \mathbf{A}\cdot\mathbf{P}dS \tag{2.19}$$

Thus the Cauchy stress tensor can be related to the first Piola-Kirchhoff stress tensor by:

$$\mathbf{P} = J\mathbf{F}^{-1}\cdot\boldsymbol{\sigma} \tag{2.20}$$

The second Piola-Kirchhoff stress S is widely used for path-independent materials. It is defined by (Marsden and Hughes, 1994):

$$\mathbf{A}\cdot\mathbf{S}dS = \mathbf{F}^{-1}\cdot d\mathbf{f} = \mathbf{F}^{-1}\cdot\mathbf{t}_0 dS \tag{2.21}$$

Using Equations (2.17) and (2.21), the second Piola-Kirchhoff stress is related to the first Piola-Kirchhoff stress by:

$$\mathbf{P} = \mathbf{S}\cdot\mathbf{F}^{T} \tag{2.22}$$

Thus the Cauchy stress and the second Piola-Kirchhoff stress relate to each other by:

$$\boldsymbol{\sigma} = J^{-1}\mathbf{F}\cdot\mathbf{S}\cdot\mathbf{F}^{T} \tag{2.23}$$

It is worthy to note that: the Cauchy stress is expressed in terms of the area and normal of the deformed surface; the first and second Piola-Kirchhoff stresses are defined in terms of the area and normal of the undeformed surface; the Cauchy stress and the second Piola-Kirchhoff stress are symmetric, i.e. $\boldsymbol{\sigma} = \boldsymbol{\sigma}^{T}$ and $\mathbf{S} = \mathbf{S}^{T}$; the first Piola-Kirchhoff stress is not symmetric.

## 2.3.2 General elastic constitutive relations

The notions given in the preceding section are general, but they are not sufficient for describing the behaviour of non-linear solids. To complete the description of the mechanical properties of a material, a set of equations, called the constitutive equations, is needed. These equations should be objective and should not lead to any change in the energy of the stresses under an arbitrary rigid-body motion. Different constitutive equations allow us to distinguish between different materials.

If the constitutive equations of a material depend only on the current state of deformation, the behaviour is said to be elastic (Shabana, 2008). If the stresses can be derived from a strain energy function, the material is called hyperelastic or Green elastic material; if the stresses cannot be derived from a strain energy function, the material is called Cauchy elastic material (Ogden, 1997). In this section, some general hyperelastic constitutive relations are presented.

### A. Hyperelastic material

Hyperelastic material is a special case of elastic materials with the property that the work is independent of the load path. That is, the work done depends only on the initial and final states. Hyperelastic materials are characterised by the existence of a stored energy function or strain energy function (Belytschko, Liu and Moran, 2000; Ciarlet, 1988; Holzapfel, 2000). This strain energy function is also called the Helmholtz free-energy function and must obey the principle of Material Frame Indifference, which means that the constitutive equations must be invariant under changes of observer frame of reference.

For a hyperelastic material, the second Piola-Kirchhoff stress is derived from the strain energy as (Belytschko, Liu and Moran, 2000):

$$\mathbf{S} = 2\frac{\partial W(\mathbf{C})}{\partial \mathbf{C}} = \frac{\partial \psi(\mathbf{E})}{\partial \mathbf{E}} \tag{2.24}$$

where $W$ and $\psi$ are the strain energy functions; $\mathbf{C}$ and $\mathbf{E}$ are the right Cauchy-Green

deformation tensor and the Green strain, respectively. The relationship between these two tensors is $\mathbf{E}=\frac{1}{2}(\mathbf{C}-\mathbf{I})$, where **I** is the second order unit tensor. Thus, the relation between the two scalar functions is given as $W(\mathbf{C})=\psi(2\mathbf{E}+\mathbf{I})$.

According to Equation (2.23), the Cauchy stress for hyperelastic material can be written as:

$$\boldsymbol{\sigma}=2J^{-1}\mathbf{F}\cdot\frac{\partial W(\mathbf{C})}{\partial \mathbf{C}}\cdot\mathbf{F}^{T} \tag{2.25}$$

The material version of the second elasticity tensor $\hat{\mathbf{C}}$ is obtained by differentiating of the second Piola-Kirchhoff stress tensor S with respect to the deformation tensor C, as given below (Weiss,Maker and Govindjee, 1996):

$$\hat{\mathbf{C}}=4\frac{\partial^{2}W}{\partial \mathbf{C}\partial \mathbf{C}}=2\frac{\partial \mathbf{S}}{\partial \mathbf{C}}=2\frac{\partial S_{IJ}}{\partial C_{KL}}\mathbf{E}^{I}\otimes\mathbf{E}^{J}\otimes\mathbf{E}^{K}\otimes\mathbf{E}^{L} \tag{2.26}$$

The spatial version of the second elasticity tensor $\tilde{\mathbf{C}}$ is defined as the push-forward of the material elasticity tensor $\hat{\mathbf{C}}$ (Marsden and Hughes, 1994):

$$\tilde{\mathbf{C}}=\frac{1}{J}\mathbf{F}\mathbf{F}\cdot\hat{\mathbf{C}}\cdot\mathbf{F}^{T}\mathbf{F}^{T} \tag{2.27}$$

## B. Isotropic hyperelastic material

In the case of isotropic materials, the constitutive behaviour is the same in any material direction. Thus, the relation between the strain energy function W and the right Cauchy-Green deformation tensor C is independent of the chosen material axes. As a consequence, the strain energy function $W$ depends only on the invariants of the right Cauchy-Green deformation tensor C and can be written as a function of the principal invariants $(I_1,I_2,I_3)$ of the right Cauchy-Green deformation tensor C (Gurtin, 1981; Malvern, 1969; Truesdell and Noll, 1992):

$$W(\mathbf{C})=W(I_1,I_2,I_3) \tag{2.28}$$

The standard definitions of the principal invariants are given by (Spencer, 1984):

$$I_1 = tr\mathbf{C} = \lambda_1^2 + \lambda_2^2 + \lambda_3^2 \tag{2.29}$$

$$I_2 = \frac{1}{2}[(tr\mathbf{C})^2 - tr\mathbf{C}^2] = \lambda_1^2\lambda_2^2 + \lambda_2^2\lambda_3^2 + \lambda_3^2\lambda_1^2 \tag{2.30}$$

$$I_3 = \det\mathbf{C} = J^2 = \lambda_1^2\lambda_2^2\lambda_3^2 \tag{2.31}$$

where $\lambda_1^2$, $\lambda_2^2$ and $\lambda_3^2$ are the eigenvalues of the right Cauchy-Green tensor **C**; $\lambda_1$, $\lambda_2$ and $\lambda_3$ are the eigenvalues of the deformation gradient **F** and represent the principal stretches along the principal direction of **F**.

The invariants of the right Cauchy-Green tensor **C** have a clear physical meanings. For example, the first invariant $I_1$ is the sum of the square of the eigenvalues of the right Cauchy-Green deformation tensor **C**. It is an invariant that represents the multi-axial state of deformation within the material, specifically the ground substance. Therefore, it represents the isotropic shear and bulk behaviour of the matrix. The second invariant $I_2$ is less used than $I_1$ and can be omitted for biological soft tissues (Holzapfel, 2000). The third invariant $I_3$ characterises the volumetric response of the material and is directly related to the degree of compressibility. As biological soft tissues contain a large proportion of water (Fung, 1973), they can be assumed to be incompressible. In the case of incompressible materials, the third invariant $I_3$ can be set to 1 and does not appear in the equations. For more details about the physical interpretations of the above invariants, see Limbert and Middleton (2004), Shabana (2008) and Zhurov, Limbert et al. (2007).

The derivatives of these invariants with respect to the right Cauchy-Green tensor **C** are given as below:

$$\frac{\partial I_1}{\partial \mathbf{C}} = \mathbf{I},\ \frac{\partial I_2}{\partial \mathbf{C}} = I_1\mathbf{I} - \mathbf{C},\ \frac{\partial I_3}{\partial \mathbf{C}} = I_2\mathbf{I} - I_1\mathbf{C} + \mathbf{C}^2 = I_3\mathbf{C}^{-1} \tag{2.32}$$

Using these results and Equation (2.24), the second Piola-Kirchhoff stress for isotropic hyperelastic materials can be written as:

$$\mathbf{S} = 2\sum_{i=1}^{3} \frac{\partial W}{\partial I_i} \frac{\partial I_i}{\partial \mathbf{C}} = 2(W_1 + I_1 W_2)\mathbf{I} - 2W_2\mathbf{C} + 2I_3 W_3 \mathbf{C}^{-1} \tag{2.33}$$

where $W_\alpha = \partial W / \partial I_\alpha (\alpha = 1,2,\cdots)$ has been applied.

**Incompressible isotropic hyperelastic model:** When the material is incompressible, which means $I_3 = J^2 = 1$, $W$ is a function of only $I_1$ and $I_2$. However, another scalar called hydrostatic pressure enters into the expression of S as a reaction to the kinematic constraint in the deformation field. In this case, the second Piola-Kirchhoff stress is written as (Weiss, Maker and Govindjee, 1996):

$$\mathbf{S} = 2\sum_{\substack{i=1 \\ i\neq 3}}^{3} \frac{\partial W}{\partial I_i} \frac{\partial I_i}{\partial \mathbf{C}} + p\mathbf{C}^{-1} = 2\{(W_1 + I_1 W_2)\mathbf{I} - W_2\mathbf{C}\} + p\mathbf{C}^{-1} \tag{2.34}$$

where p is the hydrostatic pressure, $W_\alpha = \partial W / \partial I_\alpha (\alpha = 1,2,\cdots)$ has been applied.

Based on Equations (2.23) and (2.34), the Cauchy stress for incompressible isotropic hyperelastic material can be written as:

$$\boldsymbol{\sigma} = 2\{(W_1 + I_1 W_2)\mathbf{B} - W_2 \mathbf{B}^2\} + p\mathbf{I} \tag{2.35}$$

The following relations have been used to derive the above equation:

$$F_{iI} F_{jJ} \delta_{IJ} = F_{iI} F_{jI} = B_{ij} \tag{2.36}$$

$$F_{iI} F_{jJ} C_{IJ} = F_{iI} F_{jJ} F_{mI} F_{mJ} = (F_{iI} F_{mI})(F_{jJ} F_{mJ}) = B_{im} B_{jm} \tag{2.37}$$

$$F_{iI} F_{jJ} C^{-1}_{IJ} = F_{iI} F_{jJ} F^{-1}_{mJ} F^{-1}_{mI} = \delta^i_j \tag{2.38}$$

**Compressible isotropic hyperelastic model:** When the material is slightly compressible, the strain energy function can be split into the deviatoric and dilatational parts (Ogden, 1997):

$$W(\mathbf{C}) = W_{vol}(J) + W_{dev}(\bar{\mathbf{C}}) \tag{2.39}$$

where $W_{vol}(J)$ is the dilational component relating to the volume change and $W_{dev}(\bar{\mathbf{C}})$ is

the deviatoric component, which is a function of the right Cauchy-Green deformation tensor with volume change eliminated, $\bar{\mathbf{C}}$.

The corresponding second Piola-Kirchhoff stress can also be split into two parts:

$$\mathbf{S} = \mathbf{S}_{vol} + \mathbf{S}_{dev} \tag{2.40}$$

with

$$\mathbf{S}_{vol} = 2\frac{\partial W_{vol}}{\partial J}\frac{\partial J}{\partial \mathbf{C}} \quad \text{and} \quad \mathbf{S}_{dev} = 2\frac{\partial W_{dev}}{\partial \bar{\mathbf{C}}}\frac{\partial \bar{\mathbf{C}}}{\partial \mathbf{C}} \tag{2.41}$$

In order to obtain the second Piola-Kirchhoff stress, the following decoupled invariants are introduced (Holzapfel, 2000):

$$\bar{I}_1 = \mathrm{tr}\,\bar{\mathbf{C}} = J^{-2/3} I_1 \tag{2.42}$$

$$\bar{I}_2 = \frac{1}{2}[(tr\bar{\mathbf{C}})^2 - tr\bar{\mathbf{C}}^2] = J^{-4/3} I_2 \tag{2.43}$$

The derivatives of these decoupled invariants with respect to both the right Cauchy-Green tensor and the isochoric part of the right Cauchy-Green tensor are given below:

$$\frac{\partial \bar{I}_1}{\partial \mathbf{C}} = \frac{\partial}{\partial \mathbf{C}}(J^{-2/3} tr\mathbf{C}) = J^{-2/3}\mathbf{I} - \frac{1}{3}\bar{I}_1\mathbf{C}^{-1} \tag{2.44}$$

$$\frac{\partial \bar{I}_2}{\partial \mathbf{C}} = \frac{\partial}{\partial \mathbf{C}}\left(J^{-4/3} I_2\right) = -\frac{2}{3}J^{-4/3} I_2\mathbf{C}^{-1} + J^{-4/3}(I_1\mathbf{I} - \mathbf{C}) \tag{2.45}$$

$$\frac{\partial \bar{I}_1}{\partial \bar{\mathbf{C}}} = \mathbf{I}, \quad \frac{\partial \bar{I}_2}{\partial \bar{\mathbf{C}}} = \bar{I}_1\mathbf{I} - \bar{\mathbf{C}} \tag{2.46}$$

Further

$$\frac{\partial J}{\partial \mathbf{C}} = \frac{1}{2}J\mathbf{C}^{-1} \tag{2.47}$$

$$\frac{\partial \bar{\mathbf{C}}}{\partial \mathbf{C}} = \frac{\partial J^{-2/3}}{\partial \mathbf{C}} \otimes \mathbf{C} + J^{-2/3}\frac{\partial \mathbf{C}}{\partial \mathbf{C}} = -\frac{1}{3}J^{-2/3}\mathbf{C}^{-1} \otimes \mathbf{C} + J^{-2/3}\mathbf{L} \tag{2.48}$$

where **L** is the fourth order unit tensor.

Based on the above relations, the specific expression of the second Piola-Kirchhoff stress for a compressible isotropic hyperelastic material is given by:

$$\begin{aligned}\mathbf{S} &= \frac{\partial W_{vol}}{\partial J} J\mathbf{C}^{-1} + 2J^{-2/3}\left(\frac{\partial W_{dev}}{\partial \bar{\mathbf{C}}} - \frac{1}{3}\left(\frac{\partial W_{dev}}{\partial \bar{\mathbf{C}}} : \bar{\mathbf{C}}\right)\bar{\mathbf{C}}^{-1}\right) \\ &= \frac{\partial W_{vol}}{\partial J} J\mathbf{C}^{-1} + 2J^{-2/3}\left( \left(W^1_{dev} + W^2_{dev}\bar{I}_1\right)\mathbf{I} - W^2_{dev}\bar{\mathbf{C}} - \frac{1}{3}\left(W^1_{dev}\bar{I}_1 + 2W^2_{dev}\bar{I}_2\right)\bar{\mathbf{C}}^{-1}\right)\end{aligned} \tag{2.49}$$

where $W^1_{dev} = \partial W_{dev} / \partial \bar{I}_1$ and $W^2_{dev} = \partial W_{dev} / \partial \bar{I}_2$

Introducing an operator $DEV[\cdot]$, which is the deviatoric projection operator for stress-like quantities in the reference configuration:

$$\mathrm{DEV}[\cdot] = [\cdot] - \frac{1}{3}([\cdot] : \bar{\mathbf{C}})\bar{\mathbf{C}}^{-1} \tag{2.50}$$

Then Equation (2.49) can be rewritten as:

$$\mathbf{S} = \frac{\partial W_{vol}}{\partial J} J\mathbf{C}^{-1} + 2J^{-2/3} DEV\left[\frac{\partial W_{dev}}{\partial \bar{\mathbf{C}}}\right] \tag{2.51}$$

The above constitutive relations for a quasi-incompressible, isotropic hyperelastic material are apparently due to Simo, Taylor et al. (1985) and Weiss, Maker and Govindjee (1996).

It is worthwhile to note that there are some isotropic hyperelastic material models available in the existing commercial software ABAQUS and LS-DYNA, like the neo-Hookean model, the Mooney-Rivlin model, the Arruda-Boyce model, the Ogden model, etc. Isotropic hyperelastic models are widely used in modelling rubber-like material. When modelling fibre-reinforced materials, like skeletal muscle tissue, these models are shown to lead to unrealistic results.

## C. Transversely isotropic hyperelastic material

Transversely isotropic hyperelastic material can be regarded as isotropic hyperelastic material embedded by one set of fibres. Here, one unit vector **N** in the undeformed configuration is introduced to denote the principal direction of the fibres. After the material

undergoes deformation, the fibres will deform with the body as shown in Figure 2.21. Then, another unit vector **n** is introduced to describe the fibre direction in the deformed configuration. The relationship between the fibre direction in the undeformed configuration and that in the deformed configuration is given by (Martins, Pires, Salvado et al., 1998):

$$\lambda_f \mathbf{n} = \mathbf{F} \cdot \mathbf{N} \tag{2.52}$$

where $\lambda_f$ is the fibre stretch ratio in the direction of the undeformed fibre. Since **n** is a unit vector, $\lambda_f$ can be expressed as:

$$\lambda_f = \sqrt{\mathbf{C} : (\mathbf{N} \otimes \mathbf{N})} \tag{2.53}$$

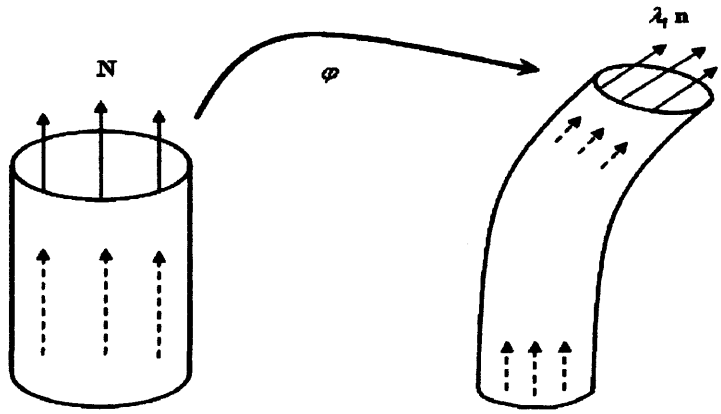


**Figure 2.21** Schematic representation of fibre direction (Limbert and Taylor, 2002)

In order to characterise the material behaviour induced by the reinforced fibres, two other invariants, namely $I_4$ and $I_5$, are introduced into the strain energy function (Spencer, 1984). In this case, the potential is expressed in terms of five invariants:

$$W(\mathbf{C}) = W(I_1, I_2, I_3, I_4, I_5) \tag{2.54}$$

where $I_4$ and $I_5$ are defined as (Spencer, 1984):

$$I_4 = (\mathbf{N} \otimes \mathbf{N}) : \mathbf{C} \quad \text{and} \quad I_5 = (\mathbf{N} \otimes \mathbf{N}) : \mathbf{C}^2 \tag{2.55}$$

From Equations (2.55), it can be seen that the invariant $I_4$ is the square of the stretch in the fibre direction which is the projection of the right Cauchy-Green deformation tensor **C** along the undeformed fibre direction **N**. It has a straightforward physical interpretation

that it characterises the directional mechanical properties of the soft tissues introduced by the presence of collagen fibres. The invariant $I_5$ has similar physical interpretation as $I_4$, but it involves the quadratic terms of the deformation tensor C. Since the effect of transverse isotropy has already been captured with $I_4$, the invariant $I_5$ is always omitted in the strain energy function W.

The derivatives of invariants $I_4$ and $I_5$ are given by:

$$\frac{\partial I_4}{\partial \mathbf{C}} = \mathbf{N} \otimes \mathbf{N} \quad \text{and} \quad \frac{\partial I_5}{\partial \mathbf{C}} = \mathbf{N} \otimes \mathbf{C} \bullet \mathbf{N} + \mathbf{N} \bullet \mathbf{C} \otimes \mathbf{N} \tag{2.56}$$

Using these results and Equation (2.54), the second Piola-Kirchhoff stress for transversely isotropic hyperelastic materials can be written as:

$$\begin{aligned} \mathbf{S} &= 2\sum_{i=1}^{5} \frac{\partial W}{\partial I_i} \frac{\partial I_i}{\partial \mathbf{C}} \\ &= 2(W_1 + I_1 W_2)\mathbf{I} - 2W_2 \mathbf{C} + 2I_3 W_3 \mathbf{C}^{-1} + W_4 \mathbf{N} \otimes \mathbf{N} + W_5 (\mathbf{N} \otimes \mathbf{C} \bullet \mathbf{N} + \mathbf{N} \bullet \mathbf{C} \otimes \mathbf{N}) \end{aligned} \tag{2.57}$$

where $W_\alpha = \partial W / \partial I_\alpha (\alpha = 1,2,\cdots)$ has been applied

**Incompressible transversely isotropic hyperelastic model:** With the strain energy Equation (2.54), the second Piola-Kirchhoff stress for an incompressible, transversely isotropic hyperelastic material can be written as:

$$\begin{aligned} \mathbf{S} &= 2\sum_{\substack{i=1 \\ i\neq 3}}^{5} \frac{\partial W}{\partial I_i} \frac{\partial I_i}{\partial C} + pC^{-1} \\ &= 2\{(W_1 + I_1 W_2)\mathbf{I} - W_2 \mathbf{C} + W_4 \mathbf{N} \otimes \mathbf{N} + W_5 (\mathbf{N} \otimes \mathbf{C} \bullet \mathbf{N} + \mathbf{N} \bullet \mathbf{C} \otimes \mathbf{N})\} + p\mathbf{C}^{-1} \end{aligned} \tag{2.58}$$

where $p$ is the hydrostatic pressure and $W_\alpha = \partial W / \partial I_\alpha (\alpha = 1,2,\cdots)$ has been applied.

The corresponding Cauchy stress is given as:

$$\boldsymbol{\sigma} = 2\{(W_1 + I_1 W_2)\mathbf{B} - W_2 \mathbf{B}^2 + I_4 W_4 \mathbf{n} \otimes \mathbf{n} + I_4 W_5 (\mathbf{n} \otimes \mathbf{B} \bullet \mathbf{n} + \mathbf{n} \bullet \mathbf{B} \otimes \mathbf{n})\} + p\mathbf{I} \tag{2.59}$$

The material elasticity tensor takes the form:

$$\hat{\mathbf{C}} = 4\{\mathbf{I}\otimes\frac{\partial W_1}{\partial \mathbf{C}} + \mathbf{I}\otimes W_2\frac{\partial I_1}{\partial \mathbf{C}} + \mathbf{I}\otimes I_1\frac{\partial W_2}{\partial \mathbf{C}} - \mathbf{C}\otimes\frac{\partial W_2}{\partial \mathbf{C}} - W_2\frac{\partial \mathbf{C}}{\partial \mathbf{C}} + \mathbf{N}\otimes\mathbf{N}\otimes\frac{\partial W_4}{\partial \mathbf{C}} + \frac{\partial I_5}{\partial \mathbf{C}}\otimes\frac{\partial W_5}{\partial \mathbf{C}} + W_5\frac{\partial^2 I_5}{\partial \mathbf{C}\partial \mathbf{C}}\} + p\frac{\partial \mathbf{C}^{-1}}{\partial \mathbf{C}} \tag{2.60}$$

Making use of the chain rule:

$$\frac{\partial W_\alpha}{\partial \mathbf{C}} = \frac{\partial W_\alpha}{\partial I_1}\frac{\partial I_1}{\partial \mathbf{C}} + \frac{\partial W_\alpha}{\partial I_2}\frac{\partial I_2}{\partial \mathbf{C}} + \frac{\partial W_\alpha}{\partial I_4}\frac{\partial I_4}{\partial \mathbf{C}} + \frac{\partial W_\alpha}{\partial I_5}\frac{\partial I_5}{\partial \mathbf{C}} (\alpha = 1,2,\cdots) \tag{2.61}$$

and further using the following relations (Marsden and Hughes, 1994):

$$(\mathbf{L})_{ijkl} = \left(\frac{\partial \mathbf{C}}{\partial \mathbf{C}}\right)_{ijkl} = \frac{1}{2}\left(\delta_{ik}\delta_{jl} + \delta_{il}\delta_{jk}\right) \tag{2.62}$$

$$\left(\mathbf{L}_{\mathbf{C}^{-1}}\right)_{ijkl} = \left(\frac{\partial \mathbf{C}^{-1}}{\partial \mathbf{C}}\right)_{ijkl} = \frac{\partial C_{ij}^{-1}}{\partial C_{kl}} = -\frac{1}{2}\left(C_{ik}^{-1}C_{jl}^{-1} + C_{il}^{-1}C_{jk}^{-1}\right) \tag{2.63}$$

The general form of material elasticity tensor for an incompressible, transversely isotropic hyperelastic material can be obtained as

$$\begin{aligned}\hat{\mathbf{C}} = 4\{&(W_{11} + 2W_{12}I_1 + W_{22}I_1^2 + W_2)\mathbf{I}\otimes\mathbf{I} - (W_{12} + W_{22}I_1)(\mathbf{I}\otimes\mathbf{C} + \mathbf{C}\otimes\mathbf{I}) + W_{22}\mathbf{C}\otimes\mathbf{C} - W_2\mathbf{L} \\ &+ (W_{14} + W_{24}I_1)(\mathbf{I}\otimes\mathbf{N}\otimes\mathbf{N} + \mathbf{N}\otimes\mathbf{N}\otimes\mathbf{I}) + W_5\frac{\partial^2 I_5}{\partial \mathbf{C}\partial \mathbf{C}} + (W_{25}I_1 + W_{15})(\mathbf{I}\otimes\frac{\partial I_5}{\partial \mathbf{C}} + \frac{\partial I_5}{\partial \mathbf{C}}\otimes\mathbf{I}) \\ &- W_{24}(\mathbf{C}\otimes\mathbf{N}\otimes\mathbf{N} + \mathbf{N}\otimes\mathbf{N}\otimes\mathbf{C}) - W_{25}(\mathbf{C}\otimes\frac{\partial I_5}{\partial \mathbf{C}} + \frac{\partial I_5}{\partial \mathbf{C}}\otimes\mathbf{C}) + W_{44}\mathbf{N}\otimes\mathbf{N}\otimes\mathbf{N}\otimes\mathbf{N} \\ &+ W_{45}(\mathbf{N}\otimes\mathbf{N}\otimes\frac{\partial I_5}{\partial \mathbf{C}} + \frac{\partial I_5}{\partial \mathbf{C}}\otimes\mathbf{N}\otimes\mathbf{N}) + W_{55}(\frac{\partial I_5}{\partial \mathbf{C}}\otimes\frac{\partial I_5}{\partial \mathbf{C}})\} + p\mathbf{L}_{\mathbf{C}^{-1}}\end{aligned} \tag{2.64}$$

where $\mathbf{L}$ is a fourth order unit tensor and $W_{\alpha\beta} = \partial^2 W / \partial I_\alpha \partial I_\beta (\alpha = 1,2,\cdots; \beta = 1,2,\cdots)$ has been introduced.

Using Equation (2.27), the spatial version of the second elasticity tensor can be obtained as:

$$\begin{aligned}\tilde{\mathbf{C}} = 4\{&(W_{11} + 2W_{12}I_1 + W_2 + W_{22}I_1^2)\mathbf{B}\otimes\mathbf{B} - (W_{12} + W_{22}I_1)(\mathbf{B}\otimes\mathbf{B}^2 + \mathbf{B}^2\otimes\mathbf{B}) + W_{22}\mathbf{B}^2\otimes\mathbf{B}^2 \\ &- W_2\mathbf{L}_{B^{-1}} + (W_{14} + W_{24}I_1)(\mathbf{B}\otimes\mathbf{n}\otimes\mathbf{n} + \mathbf{n}\otimes\mathbf{n}\otimes\mathbf{B}) + W_5\varphi^*\frac{\partial^2 I_5}{\partial \mathbf{C}\partial \mathbf{C}} + \\ &(W_{25}I_1 + W_{15})(\mathbf{B}\otimes\varphi^*\frac{\partial I_5}{\partial \mathbf{C}} + \varphi^*\frac{\partial I_5}{\partial \mathbf{C}}\otimes\mathbf{B}) - W_{24}(\mathbf{B}^2\otimes\mathbf{n}\otimes\mathbf{n} + \mathbf{n}\otimes\mathbf{n}\otimes\mathbf{B}^2) - \\ &W_{25}(\mathbf{B}^2\otimes\varphi^*\frac{\partial I_5}{\partial \mathbf{C}} + \varphi^*\frac{\partial I_5}{\partial \mathbf{C}}\otimes\mathbf{B}^2) + W_{44}\mathbf{n}\otimes\mathbf{n}\otimes\mathbf{n}\otimes\mathbf{n} + \\ &W_{45}(\mathbf{n}\otimes\mathbf{n}\otimes\varphi^*\frac{\partial I_5}{\partial \mathbf{C}} + \varphi^*\frac{\partial I_5}{\partial \mathbf{C}}\otimes\mathbf{n}\otimes\mathbf{n}) + W_{55}(\varphi^*\frac{\partial I_5}{\partial \mathbf{C}}\otimes\varphi^*\frac{\partial I_5}{\partial \mathbf{C}})\} - p\mathbf{L}\end{aligned} \tag{2.65}$$

where

$$\varphi^* \frac{\partial I_5}{\partial \mathbf{C}} = I_4(\mathbf{n}\otimes\mathbf{B}\cdot\mathbf{n}+\mathbf{n}\cdot\mathbf{B}\otimes\mathbf{n}) \tag{2.66}$$

To derive the spatial version of the second elasticity tensor, following relations have been used:

$$F_{il}F_{jJ}F_{kK}F_{lL}(\mathbf{I}\otimes\mathbf{I})_{IJKL} = (F_{il}F_{jJ}I_{IJ})\otimes(F_{kK}F_{lL}I_{KL}) = B_{ij}\otimes B_{kl} \tag{2.67}$$

$$F_{il}F_{jJ}F_{kK}F_{lL}(\mathbf{I}\otimes\mathbf{C})_{IJKL} = (F_{il}F_{jJ}I_{IJ})\otimes(F_{kK}F_{lL}C_{KL}) = B_{ij}\otimes(B_{km}B_{lm}) \tag{2.68}$$

$$F_{il}F_{jJ}F_{kK}F_{lL}(\mathbf{L}_{\mathbf{C}^{-1}})_{IJKL} = -\mathbf{L}_{ijkl} \tag{2.69}$$

$$(\mathbf{L}_{\mathbf{B}^{-1}})_{ijkl} = F_{il}F_{jJ}F_{kK}F_{lL}\mathbf{L}_{IJKL} = -(B^{-1}_{ik}B^{-1}_{jl}+B^{-1}_{il}B^{-1}_{jk})/2 \tag{2.70}$$

**Compressible transversely isotropic hyperelastic model:** If a material is slightly compressible, sometimes called quasi-incompressible, the strain energy function takes the uncoupled form:

$$W = W_{vol}(J)+W_{dev}(\bar{I}_1,\bar{I}_2,\bar{I}_4,\bar{I}_5) \tag{2.71}$$

The corresponding second Piola-Kirchhoff stress can be written as:

$$\mathbf{S} = \frac{\partial W_{vol}}{\partial J}J\mathbf{C}^{-1} + 2J^{-2/3}DEV[\frac{\partial W_{dev}}{\partial \bar{\mathbf{C}}}] \tag{2.72}$$

and the Cauchy stress takes the form:

$$\boldsymbol{\sigma} = \frac{\partial W_{vol}}{\partial J}\mathbf{I} + \frac{2}{J}dev\left[\bar{\mathbf{F}}\frac{\partial W_{dev}}{\partial \bar{\mathbf{C}}}\bar{\mathbf{F}}\right] \tag{2.73}$$

where the operator $dev[\cdot]$ is defined as (Weiss, Maker and Govindjee, 1996):

$$dev[\cdot] = [\cdot] - \frac{1}{3}([\cdot]:\mathbf{I})\mathbf{I} \tag{2.74}$$

# Chapter 3

# Constitutive Skeletal Muscle Model

## 3.1 Introduction

Skeletal muscle tissue plays an important role in the human body system and function. It can generate voluntary forces leading to human body motion and also provide protection to the upright skeleton. One way of studying the skeletal muscle tissue is through using the finite element method. With the rapid development of computer capacity, the finite element method has been used widely in studying the biomechanics of soft tissues and this method continues to expand across all areas of biomechanics.

Skeletal muscle exhibits very complex mechanical behaviour. It is active, incompressible, transversely isotropic because of the presence of a single muscle fibre direction, highly deformable and highly non-linear. The most important of all is that skeletal muscle fibres can be activated through neural stimulation. In this chapter, a three-dimensional (3D) finite element muscle model is developed to characterise the complex behaviour of the skeletal muscle tissue. The developed muscle material model is implemented into the finite element solver LS-DYNA by means of user-defined material (UMAT) subroutines. The performance of the developed muscle model is evaluated by comparing the finite element (FE) simulation results with the published experimental studies on the New Zealand white rabbit tibialis anterior (TA) muscle.

## 3.2 Literature reviews on constitutive muscle models

A number of mathematical skeletal muscle models have been developed over the past two decades. They can be classified into two commonly used skeletal muscle models: Hill-type and Huxley-type muscle models.

### 3.2.1 Hill-type muscle models

The first commonly used and phenomenologically based constitutive muscle model is originated from Hill's work (1938). The parameters involved in the Hill-type model are derived from the Fenn and Marsh's (1935) experiments. Hill's model is the basis for most of currently used muscle models and his model is composed of three elements, as depicted in Figure 3.1:

- **The contractile element (CE):** This is used to model the active part of the muscle. It can freely extend when the muscle is non-activated and it is responsible for force generation within the muscle when activated.
- **The series elastic element (SEE):** This is a non-linear spring arranged in series with the contractile element. It allows a rapid change of the muscle states from inactive to active and provides an energy storing mechanism.
- **The parallel element (PE):** This is a non-linear spring in parallel with CE and SEE. It is responsible for the passive behaviour of the muscle when stretched. It is related to the elasticity of the connective tissues.

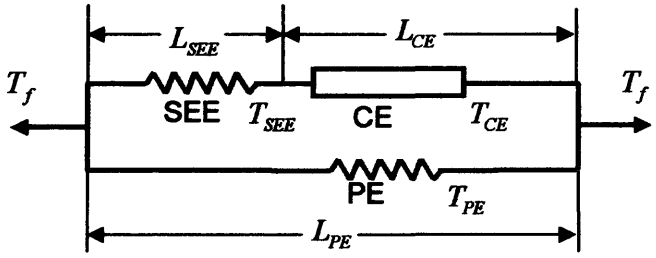


**Figure 3.1** Hill's three-element muscle model

In Hill's model, the contractile element generates a force with a magnitude that depends on the deformation velocity, the relative muscle length, and the activation degree over time. The generated force can be expressed as:

$$F_{CE} = F_{\max} \times f_t(t) \times f_v(v) \times f_\lambda(l) \tag{3.1}$$

where $F_{\max}$ is the maximal isometric force; $f_v$ is a function of the relative contraction velocity; $f_\lambda$ is a function of the relative muscle length and $f_t$ is the activation function.

From figure 3.1, it is clear that the total muscle force $F_f$ equals the sum of the force in the parallel element $F_{PE}$ and that in the contractile element $F_{CE}$:

$$F_f = F_{PE} + F_{CE} \tag{3.2}$$

The force in the contractile element $F_{CE}$ equals that in the series elastic element $F_{SEE}$:

$$F_{CE} = F_{SEE} \tag{3.3}$$

On the other hand, the muscle length $L_{PE}$ equals the sum of the length of the contractile element $L_{CE}$ and the length of the series elastic element $L_{SEE}$.

$$L_{PE} = L_{CE} + L_{SEE} \tag{3.4}$$

Hill's three-element model has been used in studying the mechanical behaviour of different muscle tissues (Audu and Davy, 1985; Pandy, Zajac, Sim et al., 1990; Winters, 1990; Zajac, Topp and Stevenson, 1986). However, Hill's model is only one-dimensional (1D). In order to investigate the complex three-dimensional geometry and the mechanical behaviour of skeletal muscle tissue, Hill's 1D model has been extended into the three-dimensional (3D) scope. The approach of extension, which has been employed by most researchers, is to add up the longitudinal stress from the muscle fibres $\sigma_{fibre}$, stress from the embedding matrix $\sigma_{matrix}$ and stress related to the incompressibility of the muscle $\sigma_{incomp}$. Thus, the Cauchy stress $\sigma$ produced in 3D muscle can be expressed as:

$$\sigma = \sigma_{fibre} + \sigma_{matrix} + \sigma_{incomp} \tag{3.5}$$

In the 3D Hill-type skeletal muscle model proposed by Kojic, Mijailovic et al. (1998), the contractile element and the series elastic element played the role of the active muscle fibre, and the parallel element played the role of the surrounding matrix which was assumed to be isotropic linear elastic. The incompressibility constraint was not taken into account. Thus from Equation (3.5), the total stress in their muscle model was expressed as:

$$\boldsymbol{\sigma} = \boldsymbol{\sigma}^{\mathrm{E}} \cdot (1-\phi) + \phi \cdot f_t(t) \cdot \boldsymbol{\sigma}^{\mathrm{S}} \tag{3.6}$$

where $\phi$ was the volume fraction of the muscle fibre; $f_t$ was the activation function; $\boldsymbol{\sigma}^{\mathrm{E}}$ was the stress produced in the surrounding matrix; $\boldsymbol{\sigma}^{\mathrm{S}}$ was the stress produced in the active muscle fibre which has a non-zero component only in the fibre direction.

Based on Kojic, Mijailovic et al.'s model, Tang, Stojanovic et al. (2005) and Tang, Tsui et al. (2007) incorporated muscle fatigue into the 3D skeletal muscle model. In their new model, the force developed in a fatigued muscle was described by a muscle fatigue formula which was a function of the time $t$, the activation $\alpha_a$ and the stretch $\lambda$. Stojanovic, Kojic et al. (2006) extended Kojic, Mijailovic et al.'s work by taking different fibre types into account. The model consisted of a number of different types of sarcomeres coupled in parallel with the connective tissue. Each sarcomere was modelled by one non-linear elastic element which was connected in series with one active contractile element, as shown in Figure 3.2.

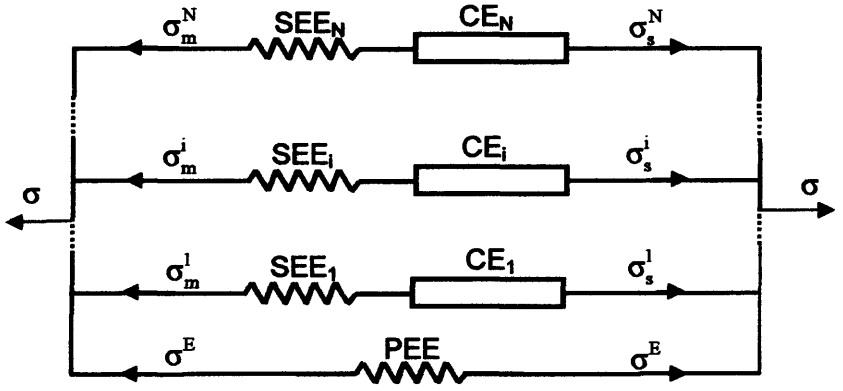


**Figure 3.2** Multi-fibre types muscle model (Stojanovic, Kojic, Rosic et al., 2006)

Martins, Pires et al. (1998) developed a 3D Hill-type skeletal muscle model based on the concept of a fibre-reinforced composite. This was a modified form of the constitutive equation proposed by Humphrey and Yin (1987) for cardiac tissue. The strain energy density per unit volume of the reference configuration was given by:

$$U = U_I(\bar{I}_1^C) + U_f(\bar{\lambda}_f, \xi^{CE}) + U_J(J) \tag{3.7}$$

where $U_I$ was the strain energy stored in the surrounding matrix; $U_J$ was the strain energy associated with volume change, which were the same as those used in Humphrey and Yin's model (1987); $U_f$ was the strain energy stored in the muscle fibre, which had the following form:

$$U_f(\bar{\lambda}_f, \xi^{CE}) = U_{PE}(\bar{\lambda}_f) + U_{SEE}(\bar{\lambda}_f, \xi^{CE}) \tag{3.8}$$

where $U_{PE}$ and $U_{SEE}$ were the strain energy stored in the parallel element and the series elastic element, respectively.

The Cauchy stress can be derived from the total strain energy Equation (3.7) by a standard routine (Belytschko, Liu and Moran et al., 2000). The same as the stress expression in Equation (3.5), the derived stress can also be divided into three parts: the first from the muscle fibre, the second from the matrix and the third due to the volume change.

Martins, Pires et al.'s (1998) 3D hyperelastic muscle model has been widely adopted and extended by other authors. Blemker, Pinsky et al. (2005) introduced two more strain invariants, namely $B_1$ and $B_2$ (Criscione, Douglas and Hunger, 2001), into the model to account for the shearing response along the muscle fibres and that transverse to the fibres. The biceps brachii was studied using this model and the analysis revealed that the variation in fascicle length within the muscle and the curvature of the fascicles were the primary factors contributing to the non-uniform strains. Martins, Pato et al. (2006) recently updated their previous model (1998) by multiplicative decomposition of the fibre stretch into contractile stretch and elastic stretch in the series elastic element. The stresses in the contractile element and the series elastic element can therefore be easily solved. Tang,

Zhang et al. (2009) extended Martins, Pires et al.'s (1998) model to considering concentric, eccentric, isometric and isotonic contractions of the skeletal muscle under either quasi-static or dynamic conditions. The proposed model has been used to simulate the dynamic response of a squid tentacle during a strike to catch prey.

In the 3D Hill-type skeletal muscle model proposed by Johansson, Meier et al. (2000), the Cauchy stress component in the active muscle fibre direction was described as the sum of an active part produced in the contractile element and a passive part developed in the parallel element. The series elastic element was not considered in this model. Therefore, it was mainly appropriate for the dynamic analysis of the muscle behaviour.

In the 3D Hill-type muscle model proposed by Hedenstierna, Halldin et al. (2008), the super-positioned muscle finite element (SMFE), which is the combination of the passive, non-linear, visco-hyperelastic solid elements with the active Hill-type truss elements (Figure 3.3), has been first evaluated. An asymmetric model of a rabbit tibialis anterior muscle was used for the model validation. The model was tested under different strain rates and in both active and passive states. The analysis showed the SMFE muscle model was capable of simulating tensile experiments for quasi-static and dynamic loadings (1, 10, 25 $s^{-1}$), in both passive and active states.

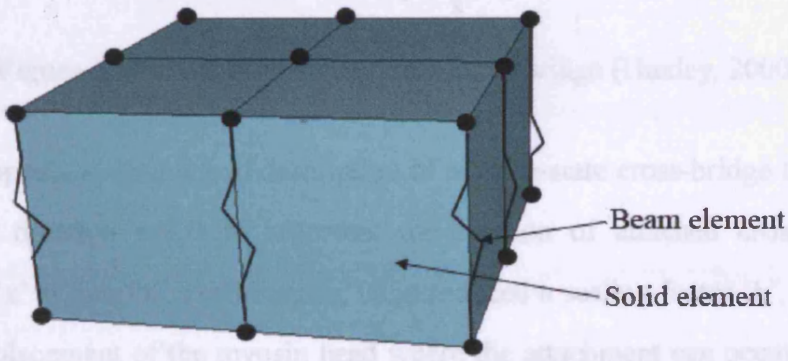


**Figure 3.3** SMFE element (Hedenstierna, Halldin and Brolin 2008)

## 3.2.2 Huxley-type muscle models

The second most commonly used constitutive muscle model is based on the biophysical 1D cross-bridge model proposed by Huxley (1957). Huxley's model focuses on an ensemble of myosin heads, which are always referred to as cross-bridges. It is assumed that each myosin head is capable of binding to an actin binding site and acts independently of other cross-bridges. It is further assumed that at any given time instant a cross-bridge can only bond to its nearest actin site. The mechanical model of Huxley's cross-bridge model is shown in Figure 3.4, where 'x' is the displacement of the myosin head relative to the equilibrium position. Huxley's original theory also assumes that a cross-bridge could exist in two biochemical states: attached and detached. In the attached state, the cross-bridge generates a force proportional to its displacement 'x'.

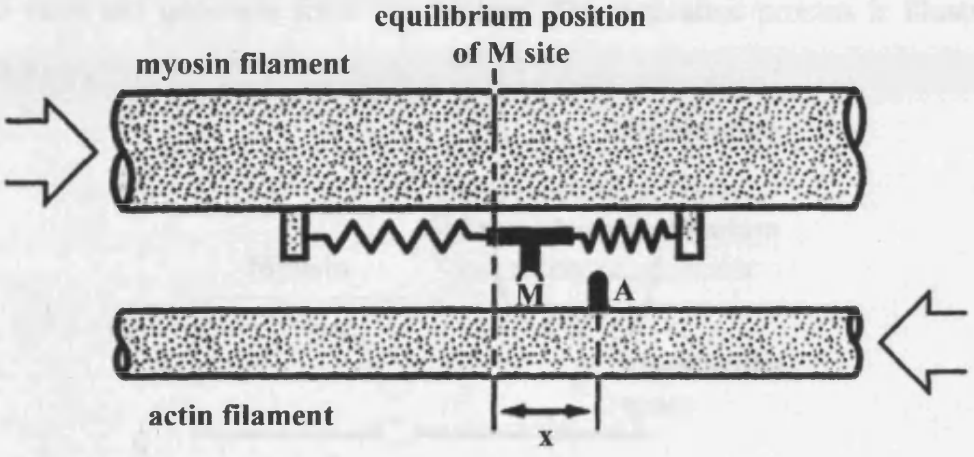


**Figure 3.4** Schematic diagram of a cross-bridge (Huxley, 2000)

Huxley developed a mathematical description of his two-state cross-bridge theory. He used a distribution function n(x,t) to represent the fraction of attached cross-bridges with displacement 'x' at time 't'. Furthermore, he introduced a scaling factor 'h', which was the maximum displacement of the myosin head where the attachment can occur. Then the rate of change of this distribution function can be expressed by a partial differential equation:

$$\frac{dn(\xi,t)}{dt} = \frac{\partial n(\xi,t)}{\partial t} - u(t)\frac{\partial n(\xi,t)}{\partial \xi} = f(\xi)[1-n(\xi,t)] - g(\xi)n(\xi,t) \qquad (3.9)$$

where $\xi = x/h$; u(t) is the scaled shortening velocity of a half sarcomere; $f(\xi)$ and $g(\xi)$ represent the attachment rate function and the detachment rate function respectively.

A number of researchers have extended Huxley's work. Zahalak and Ma (1990) broadened the basic Huxley model to taking account of the role of calcium in activating the contractile machinery. They employed the consensus of opinion among biophysicists and biochemists concerning how calcium induces muscular contraction: (1) an action potential depolarises the sarcoplasmic reticulum (SR), causing a transient increase in the permeability of the SR to $Ca^{++}$ ions; (2) the calcium ions diffuse rapidly out of the SR, which is driven by a calcium concentration difference between the interior and exterior of the SR; (3) the calcium ions bind to specific receptor sites on troponin molecules located at intervals along the thin actin filaments; (4) the troponin molecules with bound calcium, release an inhibition which they impose in their calcium-free state on actin sites, permits myosin to bond to actin and generates force and motion. This activation process is illustrated in Figure 3.5.

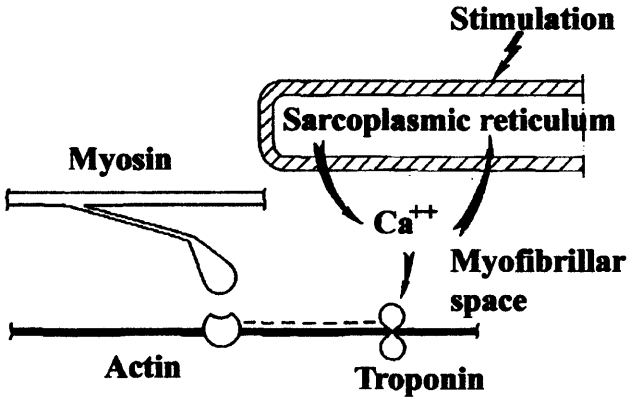


**Figure 3.5** Schematic diagram of the activation-contraction coupling (Zahalak and Ma, 1990)

Based on this activation-contraction mechanism, they introduced a parameter 'r', which was referred to as the activation factor and given by:

$$r([Ca]) = \frac{[TCa_2]}{[T]+[TCa]+[TCa_2]} \tag{3.10}$$

where 'T' stands for troponin; 'Ca' for the free $Ca^{2+}$ ions; 'TCa' for troponin bound to one calcium ion and '$TCa_2$' for troponin bound to two calcium ions.

Incorporating the activation factor 'r' into Huxley's original rate Equation (3.9), a modified two state Huxley equation can be obtained:

$$\frac{\partial n}{\partial t} - u(t) \cdot \frac{\partial n}{\partial \xi} = f \cdot r \cdot [\varphi - n] - g \cdot n \tag{3.11}$$

where $\varphi$ represents the fraction of participating myosin heads; 'r' is the activation factor given in Equation (3.10).

Huxley's theory requires a solution for the bond distribution function $n(\xi,t)$. However, for describing the macroscopic muscle behaviour, only certain moments of the distribution function are needed. In order to avoid the solution of the partial differential equations, Zahalak (1981) developed a 'distributed-moment (DM) approximation' method, which can give the direct approximation of these moments. Applying his DM approximation to Equation (3.11) yields (Zahalak and Ma, 1990):

$$\frac{dQ_\theta}{dt} = \varphi \cdot r \cdot \beta_\theta - r\phi_{1\theta} - \phi_{2\theta} - \theta \cdot u(t) \cdot Q_{\theta-1} \tag{3.12}$$

where $\varphi$ represents the fraction of participating myosin heads; 'r' is the activation factor and $Q_\theta$ is the θ-th normalised moment of the bond distribution function:

$$Q_\theta = \int_{-\infty}^{\infty} \xi^\theta n(\xi,t) d\xi \tag{3.13}$$

and

$$\beta_\theta = \int_{-\infty}^{\infty} \xi^\theta \cdot f(\xi) d\xi \tag{3.14}$$

$$\phi_{1\theta} = \int_{-\infty}^{\infty} \xi^\theta \cdot f(\xi) \cdot n(\xi,t) d\xi \tag{3.15}$$

$$\phi_{2\theta} = \int_{-\infty}^{\infty} \xi^\theta \cdot g(\xi) \cdot n(\xi,t) d\xi \tag{3.16}$$

It can be seen that, through Zahalak's DM method, Huxley's partial differential equation has been transformed into a system of ordinary differential equations, which are computationally much simpler. Furthermore, the three lowest order moments, as described in Equation (3.13), have direct physical meanings: $Q_0$ is proportional to the instantaneous stiffness of the contractile tissue; $Q_1$ is proportional to the instantaneous muscle force and

$Q_2$ is proportional to the total elastic energy stored in the cross-bridges.

In applications, Gielen, Oomens et al. (2000) proposed a geometrically and physically non-linear continuum muscle model which has been used to study the mechanical behaviour of both passive and active skeletal muscles. In their model, the total stress $\boldsymbol{\sigma}$ in the muscle tissue was defined as a superposition of the active stress $\sigma_a$ and the passive stress $\boldsymbol{\sigma}_p$. The active stress $\sigma_a$ was derived from Huxley's cross-bridge theory and had the following form.

$$\sigma_a(t) = \sigma_0 \lambda \int \xi \cdot n(\xi, t) \cdot d\xi = \sigma_0 \lambda \cdot Q_1(t) \tag{3.17}$$

where $\sigma_0$ was a material constant, which represented the maximal isometric stress with the maximum number of cross-bridges attached and $\lambda$ was the extension ratio in the fibre direction.

The analysis of the rat TA muscle behaviour has been performed with Gielen, Oomens et al.'s model for the aim of future validation work. As far as we know, Gielen, Oomens et al.'s continuum skeletal muscle model is the first model that incorporates Huxley's contraction model for the active behaviour of the muscle.

Based on Gielen, Oomens et al.'s work, Oomens, Maenhout et al. (2003) used the same continuum muscle model for describing the mechanical behaviour of rat TA muscle. The results were compared with the experimentally determined strains at the surface of the muscle. Qualitatively there was good agreement between the measured and the calculated strains.

In summary, Hill-type and Huxley-type models are both phenomenological models, but are based at different architectural levels. Hill-type models account for the force-velocity and force-length relationship of the muscle, thus are based at the macroscopic level. Huxley-type models describe the muscle behaviour at the molecular level. They are mainly used to understand the properties of the microscopic contractile element.

## 3.2.3 Other types of muscle models

Besides Hill-type and Huxley-type muscle models, there are various other kinds of muscle models. For example, in order to gain insight into the complex biomechanical phenomena related to skeletal muscle modelling, Böl and Reese (2008) formulated a novel micromechanically-based skeletal muscle model which split the Helmholtz free energy into passive and active parts. The passive part was represented by an assembly of tetrahedral and non-linear truss elements, and the active behaviour was implemented into 3D truss elements. The stimulus rate dependence on the muscle contraction, the influence of muscle fibre type and fibre recruitment on the muscle activation were incorporated into the 3D model.

Van Loocke, Lyons et al. (2006) adapted Li, Guo et al.'s (2001) strain dependent Young's moduli model to represent the compressive behaviour of skeletal muscle tissue. The model gave a good prediction for the muscle behaviour when it was compressed at various angles from the fibre direction. Van Loocke, Lyons et al. (2008) extended their previous model with Prony series to represent the skeletal muscle viscoelastic behaviour. This model successfully predicted the muscle stress-relaxation behaviour at 60° from the fibre direction and the muscle behaviour at compression rates of 0.05% $s^{-1}$ and 5% $s^{-1}$.

## 3.2.4 Reviews on muscle experimental data

It is worthy to review the experimental data available for studying 3D muscle models. The published data can be divided into two groups according to the experiment types: data from compression tests and data from tensile tests.

There has been some published experimental data on the compressive behaviour of passive skeletal muscle. Grieve and Armstrong (1988) performed in vitro unconfined compression tests on aged porcine samples in their transverse direction. Zhang, Mak et al. (1999) developed an ultrasound indentation system with a pen-size hand-held probe and used it to carry out manual indentation tests on the in vivo human forearm. Bosboom, Thomassen et

al. (2001) performed indentation experiments on an excised muscle of a rat to determine the passive transverse mechanical properties of skeletal muscle. Later on, Bosboom, Hesselink et al. (2001) performed the compression tests on four rat TA muscles in vivo and employed an incompressible viscoelastic Ogden model to describe the passive muscle behaviour. The results showed that the measured behaviour can be accurately simulated with the Ogden model. Van Loocke, Lyons et al. (2006) conducted uniaxial, unconstrained compression experiments on both aged and fresh animal muscle samples oriented at various angles from the fibre direction. They compared their experimental results with other available published data, as shown in Figure 3.6, which serves as a short summary of the published data from the compressive type of experiments. Besides, Palevski, Glaich et al. (2006) performed rapid indentation tests on fresh porcine gluteus muscle in vitro to measure the transient shear modulus of the tissue in the transverse direction. In 2008, Van Loocke, Lyons et al. complemented their previous study by investigating the time-dependent properties of passive skeletal muscle. They performed uniaxial ramp and hold compression tests in vitro on fresh porcine skeletal muscle at various rates and orientations of the tissue fibres. The results showed that the viscoelastic component plays a significant role in muscle mechanical properties

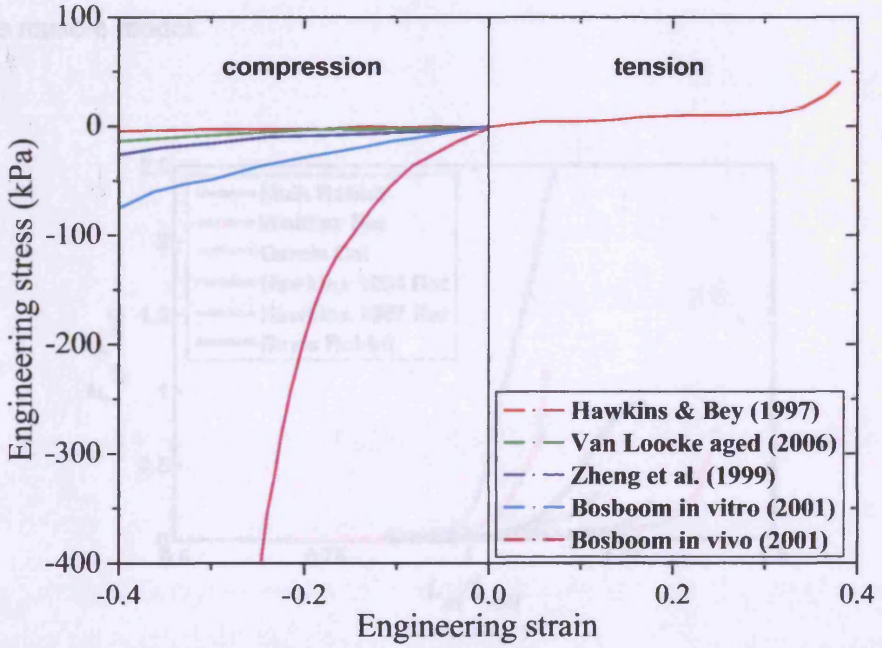


**Figure 3.6** Published muscle tissue data from compression tests (VanLoocke,Lyons and Simms, 2006)

A number of authors have conducted tensile tests on animal muscles to study skeletal muscle behaviour. Muhl (1982) determined the active length-tension relation for the left digastric muscle of seven New Zealand White rabbits. Gareis, Solomonow et al. (1992) determined experimentally the muscle length-force relations by using nine different skeletal muscles in the hindlimb of the cat. Hawkins and Bey (1994) developed a comprehensive approach for studying the mechanics of partially intact muscle-tendon and this approach was applied to study a rat tibialis anterior muscle. They (1997) also investigated the force-length properties of the rat TA muscle and tendon by determining the lengths occurred in the rat body during the ankle joint motion ranging from 20° to 90° of flexion. Davis, Kaufman et al. (2003) performed length-tension experiments on the isolated TA of the New Zealand White rabbit to quantify the relationship between the intramuscular pressure and muscle force during isometric contraction. Van Loocke (2007) summarised the test data obtained by these authors in his thesis, as shown in Figure 3.7. In addition, Myers, Wooley et al. (1998) measured the passive and stimulated engineering stress-strain mechanical properties of skeletal muscle at the mid-belly of the rabbit tibialis anterior. They also measured the effect of the strain rate on these responses and obtained good data for active muscle behaviour, which will be used in this study for validating the developed constitutive muscle model.

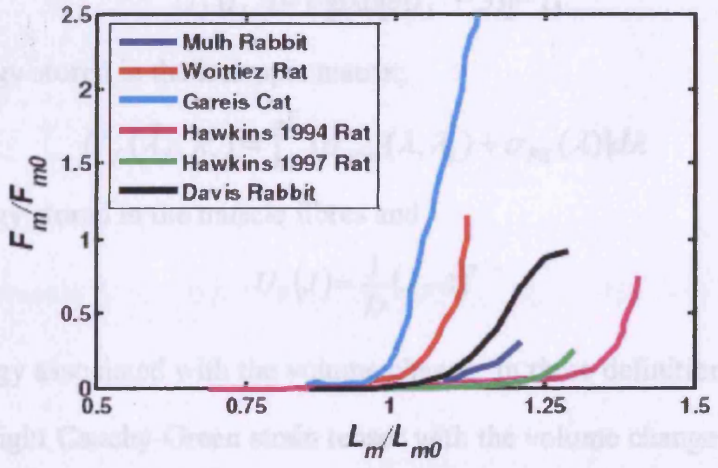


**Figure 3.7** Published muscle tissue data from tensile tests (Van Loocke, 2007)

## 3.3 The constitutive skeletal muscle model

The skeletal muscle model developed in this chapter is based on the Hill-type model. The constitutive relation is derived through the total strain energy and the formulations are within the framework of non-linear solid mechanics (Truesdell and Noll, 2004).

The muscle is regarded as a fibre-reinforced composite comprising a ground substance matrix and the muscle fibres (Figure 3.8). The fibres are assumed to be distributed in parallel and have a single direction.

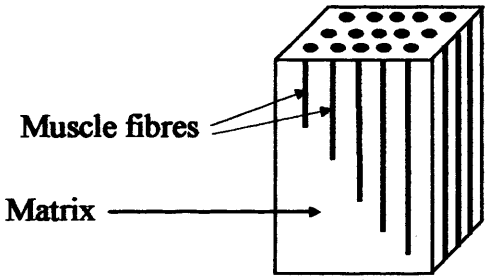


**Figure 3.8** Diagram illustration of a parallel-fibred muscle

The total strain energy in the muscle is given by:

$$U = U_I(\bar{I}_1^C) + U_f(\bar{\lambda}_f, \lambda_s) + U_J(J) \tag{3.18}$$

where

$$U_I(\bar{I}_1^C) = c\{\exp[b(\bar{I}_1^C - 3)] - 1\} \tag{3.19}$$

is the strain energy stored in the isotropic matrix;

$$U_f(\bar{\lambda}_f, \lambda_s) = \int_1^{\bar{\lambda}_f} [\sigma_{SEE}(\lambda, \lambda_s) + \sigma_{PE}(\lambda)] d\lambda \tag{3.20}$$

is the strain energy stored in the muscle fibres and

$$U_J(J) = \frac{1}{D}(J-1)^2 \tag{3.21}$$

is the strain energy associated with the volume change. In these definitions, $\bar{I}_1^C$ is the first invariant of the right Cauchy-Green strain tensor with the volume change eliminated; $b$ and $c$ are material parameters; $\bar{\lambda}_f$ is the fibre stretch ratio with the volume change eliminated; $\lambda_s$ is the stretch ratio in SEE; $\lambda$ is the fibre stretch ratio; $\sigma_{SEE}(\lambda, \lambda_s)$ is the stress

produced in SEE; $\sigma_{PE}(\lambda)$ is the stress produced in PE; $J$ is the Jacobian of the deformation gradient; and $D$ is the compressibility constant.

## 3.3.1 Stress produced in the series elastic element

Based on the experiments of Pinto and Fung (1973) on the papillary muscle of a rabbit heart, a recurrence relation is proposed to express the stress produced in SEE (Fung, 1981):

$$^{t+\Delta t}\sigma_{SEE} = e^{\alpha\Delta\lambda_s}\left(^{t}\sigma_{SEE} + \beta\right) - \beta \tag{3.22}$$

with

$$^{t}\sigma_{SEE} = \beta[e^{\alpha(^{t}\lambda_s - 1)} - 1] \tag{3.23}$$

where $\alpha$, $\beta$ are material constants

Equation (3.22) contains one unknown, namely $\Delta\lambda_s$, and this can be solved using the method proposed by Kojic, Mijailovic et al. (1998). The idea is to set up a non-linear equation with the unknown $\Delta\lambda_s$ by utilizing the stresses relationship between CE and SEE, i.e. the stress in CE is equal to the stress in SEE at any moment.

$$^{t+\Delta t}\sigma_{CE} = {}^{t+\Delta t}\sigma_{SEE} \tag{3.24}$$

## 3.3.2 Stress produced in the contractile element

The stress produced in CE is given by:

$$^{t+\Delta t}\sigma_{CE} = \sigma_0 \cdot f_t(t+\Delta t) \cdot f_\lambda(\bar{\lambda}_f) \cdot f_v(\dot{\lambda}_m) \tag{3.25}$$

where $\sigma_0$ is the maximal isometric stress; $f_t(t+\Delta t)$ is the muscle activation function; $f_\lambda(\bar{\lambda}_f)$ is the muscle force-stretch function; and $f_v(\dot{\lambda}_m)$ is the muscle force-velocity function.

### (a) The activation function

The activation behaviour of the muscle is quite complex and still under research. In the model developed in this thesis, an exponential function, which has also been used by Meier and Blickhan (2000), is adopted:

$$f_t(t) = \begin{cases} n_1, & \text{if } t < t_0 \\ n_1 + (n_2 - n_1) \cdot h_t(t, t_0), & \text{if } t_0 < t < t_1 \\ n_1 + (n_2 - n_1) \cdot h_t(t_1, t_0) - [(n_2 - n_1) \cdot h_t(t_1, t_0)] \cdot h_t(t, t_1), & \text{if } t > t_1 \end{cases} \quad (3.26)$$

with

$$h_t(t_i, t_b) = \{1 - \exp[-S \cdot (t_i - t_b)]\} \quad (3.27)$$

where $n_1$ is the activation level before and after the activation; $n_2$ is the activation level during the activation; $t_0$ is the activation time; $t_1$ is the deactivation time; and $S$ is the exponential factor. When modelling single muscle fibres, the magnitude of parameter $S$ is related to the rate of the chemical processes. For modelling large muscles, $S$ represents the time dependent recruitment of different motor units.

Figure 3.9 shows the activation function curves for $t_0 = 0.1\,\text{s}$, $t_1 = 0.4\,\text{s}$, $n_1 = 0.0$ and $n_2 = 1.0$, where the solid curve is with $S$ = 50 and the dotted curve is with $S$ = 100. The diagram shows that the bigger the value of $S$, the faster the activation process.

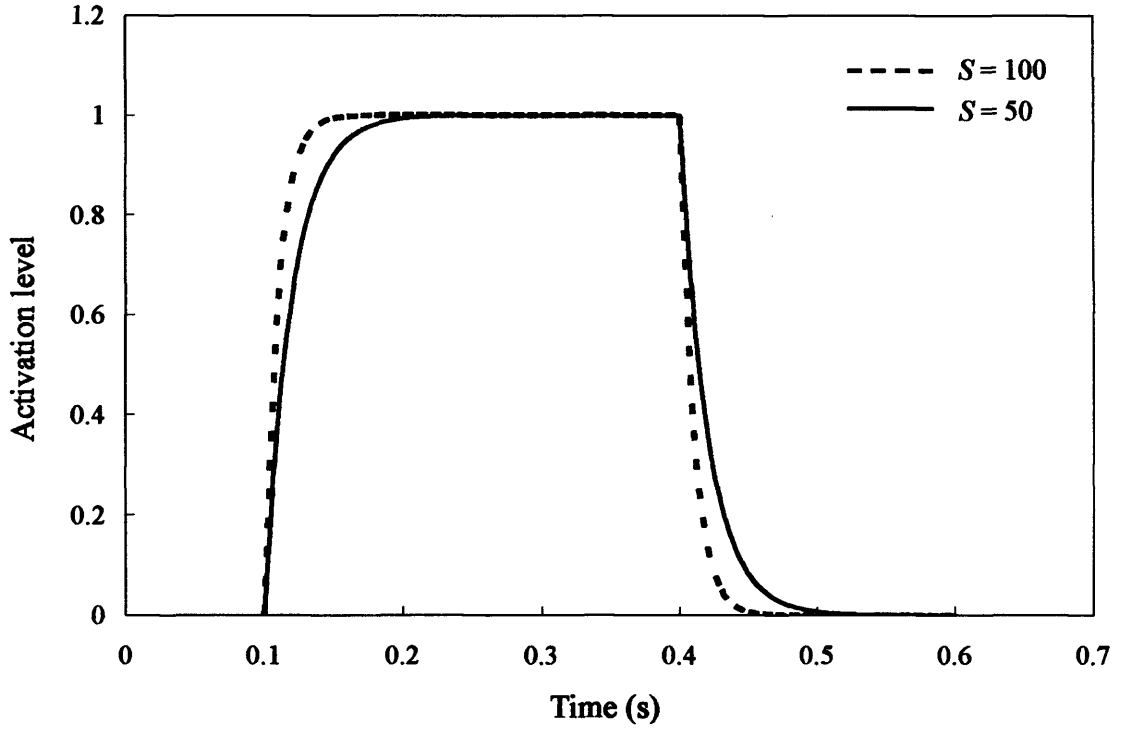


**Figure 3.9** Activation function curve

## (b) The force-stretch function

The force developed in a muscle depends on its sarcomere length. In order to find the relationship between the isometric tension and the sarcomere length, Gordon, Huxley et al. (1966) conducted a series of experiments on a single fibre of frog skeletal muscle and found a piecewise linear isometric tension versus length dependency, as shown in Figure 3.10, where the slack sarcomere length is $2.1\,\mu m$. By definition, the slack sarcomere length is the one when the extension ratio is 1.0. It can be seen from the Figure 3.10 that when the sarcomere length is too small or too large, the maximum tension will drop to zero. When the sarcomere length falls in the range of $2.0 - 2.2\,\mu m$, the tension is maximal.

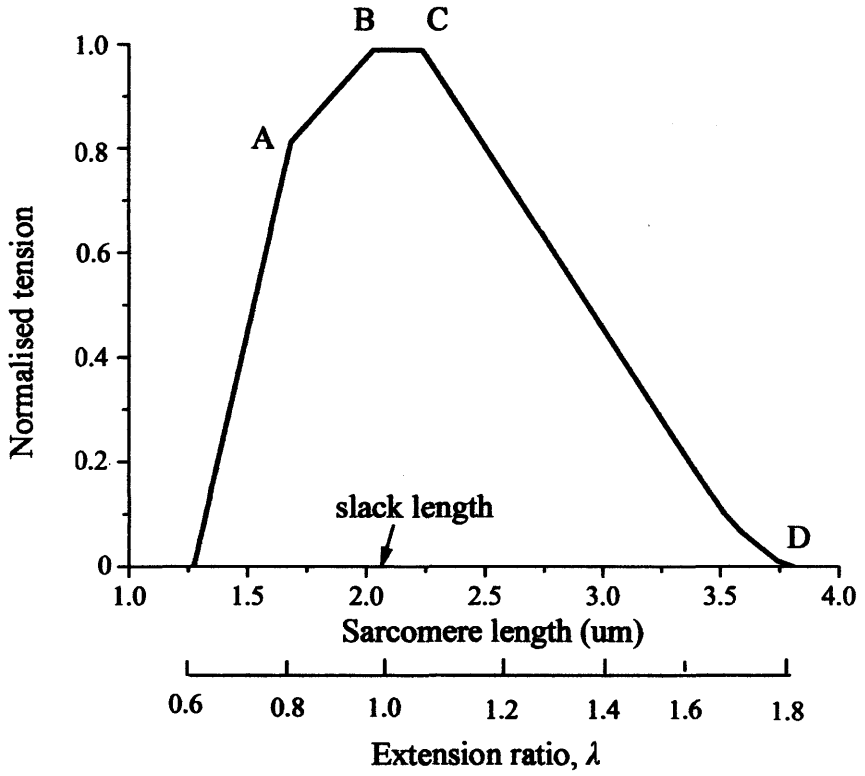


**Figure 3.10** Isometric tension versus length curve (Gordon, Huxley and Julian, 1966)

In the muscle model developed in this thesis, a smooth quadratic function proposed by Blemker, Pinsky and Delp (2005) is used to approximate Gordon's experimental curve. This quadratic function has also been used by Böl and Reese (2008) and it has the following form:

$$f_\lambda({}^t\bar{\lambda}_f)=\begin{cases}0, & if \quad {}^t\bar{\lambda}_f/\lambda_{opt}<0.4\\ 9({}^t\bar{\lambda}_f/\lambda_{opt}-0.4)^2, & if \quad 0.4\le{}^t\bar{\lambda}_f/\lambda_{opt}<0.6\\ 1-4(1-{}^t\bar{\lambda}_f/\lambda_{opt})^2, & if \quad 0.6\le{}^t\bar{\lambda}_f/\lambda_{opt}<1.4\\ 9({}^t\bar{\lambda}_f/\lambda_{opt}-1.6)^2, & if \quad 1.4\le{}^t\bar{\lambda}_f/\lambda_{opt}<1.6\\ 0, & if \quad {}^t\bar{\lambda}_f/\lambda_{opt}\ge1.6\end{cases} \tag{3.28}$$

where $\lambda_{opt}$ is the optimal fibre stretch.

The smooth force against stretch function for $\lambda_{opt}$ = 1.05 is plotted in Figure 3.11. Compared to the piecewise linear function used by Tang, Zhang et al. (2009), this smooth function has the big advantage that it reduces the parameter inputs from five to one.

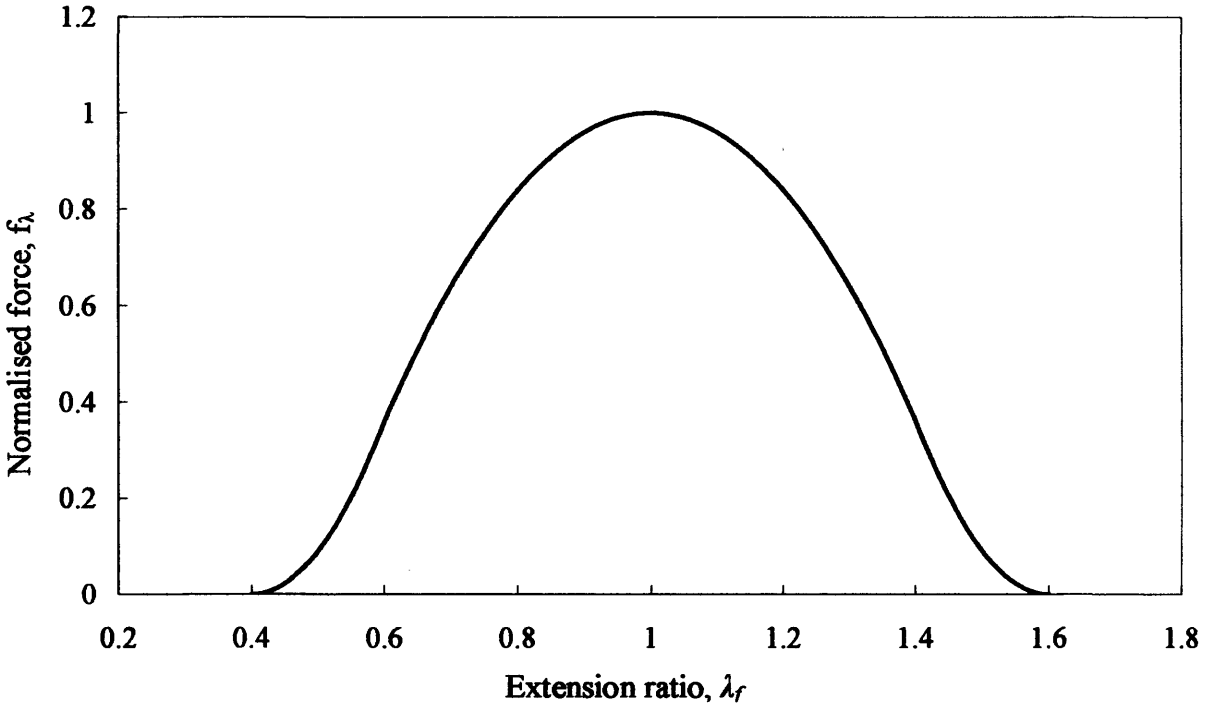


**Figure 3.11** Normalised force versus extension ratio curve

## (c) The force-velocity function

It is well-known that the force generated in the muscle during contraction is highly dependent on its velocity of contraction (Hill, 1970). In 1938, Hill proposed a hyperbolic relation between the muscle force and the velocity, which is still used by scientists today (Hill, 1938), see Appendix C for more detail.

However, Hill's force-velocity equation is restricted to the concentric and isometric contraction of the muscle. The tension-velocity relation for muscle lengthening was first characterised in the form of an equation by Otten (1987). Later, this hyperbolic equation was used by Van Leeuwen (1991).

The force-velocity function, which is incorporated into the muscle model developed here, is derived from the following equation:

$$f_v(\dot{\lambda}_m)=\begin{cases}\dfrac{1-\dot{\lambda}_m/\dot{\lambda}_m^{\min}}{1+k_c\,\dot{\lambda}_m/\dot{\lambda}_m^{\min}}, & if \quad \dot{\lambda}_m \le 0\\ d-(d-1)\dfrac{1+\dot{\lambda}_m/\dot{\lambda}_m^{\min}}{1-k_c k_e\,\dot{\lambda}_m/\dot{\lambda}_m^{\min}}, & if \quad \dot{\lambda}_m > 0\end{cases} \tag{3.29}$$

where $k_c$ and $k_e$ are shape parameters of the hyperbolic curves, which control the curvature of the curve; $d$ is the offset of the eccentric function; $\dot{\lambda}_m$ is the stretch rate in the CE and $\dot{\lambda}_m^{\min}$ is the minimum stretch rate.

The effect of $k_c$ on the force-velocity function is shown in Figure 3.12 and the effect of $k_e$ on the eccentric contraction part of the force-velocity function is presented in Figure 3.13. The two diagrams indicate that: during eccentric contraction, the force increases as $k_c$ and $k_e$ increase; however, the force decreases as $k_c$ increases during concentric contraction.

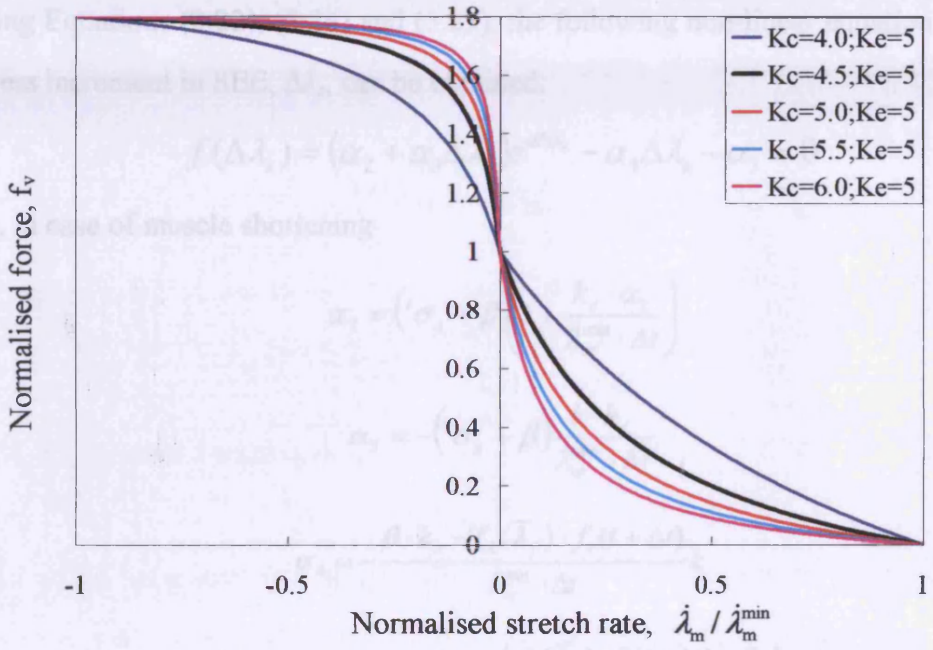


**Figure 3.12** Effect of $k_c$ on the normalised force versus velocity curve

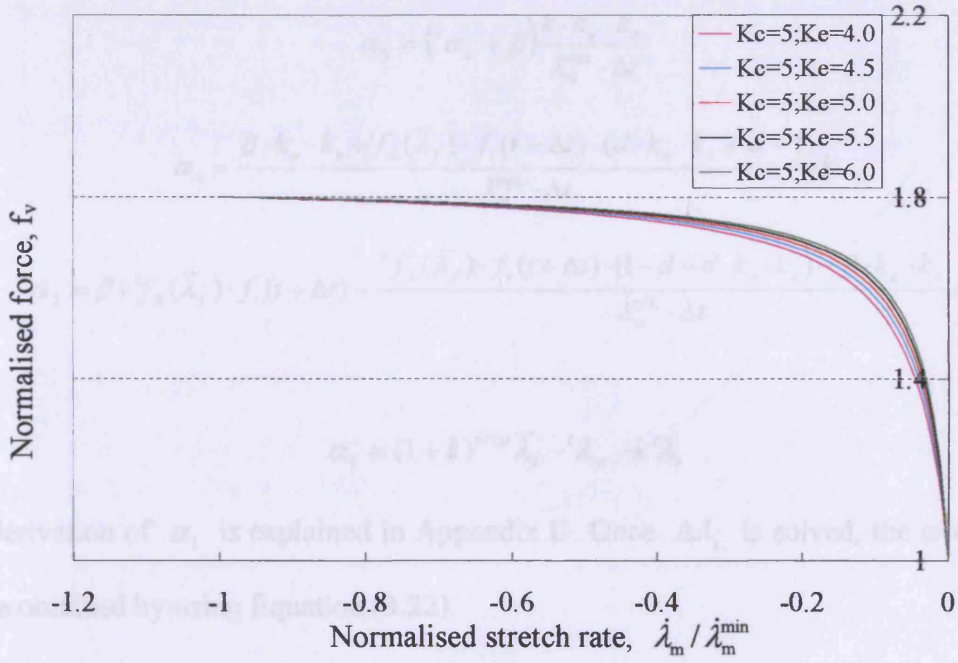


**Figure 3.13** Effect of $k_e$ on the normalised force versus velocity curve

By using Equations (3.22), (3.24) and (3.25), the following non-linear equation for solving the stress increment in SEE, $\Delta\lambda_s$, can be obtained:

$$f(\Delta\lambda_s) = (\alpha_2 + \alpha_3 \Delta\lambda_s) e^{\alpha \Delta\lambda_s} - \alpha_4 \Delta\lambda_s - \alpha_5 = 0 \tag{3.30}$$

where, in case of muscle shortening

$$\alpha_2 = \left({}^t\sigma_s + \beta\right)\left(1 + \frac{k_c \cdot \alpha_1}{\dot{\lambda}_m^{min} \cdot \Delta t}\right) \tag{3.31}$$

$$\alpha_3 = -\left({}^t\sigma_s + \beta\right)\frac{k \cdot k_c}{\dot{\lambda}_m^{min} \cdot \Delta t} \tag{3.32}$$

$$\alpha_4 = -\frac{\beta \cdot k_c - {}^t f_\lambda(\bar{\lambda}_f) \cdot f_t(t + \Delta t)}{\dot{\lambda}_m^{min} \cdot \Delta t} k \tag{3.33}$$

$$\alpha_5 = \beta + {}^t f_\lambda(\bar{\lambda}_f) \cdot f_t(t + \Delta t) - \frac{{}^t f_\lambda(\bar{\lambda}_f) \cdot f_t(t + \Delta t) - \beta \cdot k_c}{\dot{\lambda}_m^{min} \cdot \Delta t} \alpha_1 \tag{3.34}$$

and in case of muscle lengthening

$$\alpha_2 = \left({}^t\sigma_s + \beta\right)\left(1 - \frac{k_e \cdot k_c \cdot \alpha_1}{\dot{\lambda}_m^{min} \cdot \Delta t}\right) \tag{3.35}$$

$$\alpha_3 = \left({}^t\sigma_s + \beta\right)\frac{k \cdot k_e \cdot k_c}{\dot{\lambda}_m^{\min} \cdot \Delta t} \tag{3.36}$$

$$\alpha_4 = \frac{\beta \cdot k_e \cdot k_c + {}^t f_\lambda(\bar{\lambda}_f) \cdot f_t(t+\Delta t) \cdot (d \cdot k_e \cdot k_c + d - 1)}{\dot{\lambda}_m^{\min} \cdot \Delta t} k \tag{3.37}$$

$$\alpha_5 = \beta + {}^t f_\lambda(\bar{\lambda}_f) \cdot f_t(t+\Delta t) - \frac{{}^t f_\lambda(\bar{\lambda}_f) \cdot f_t(t+\Delta t) \cdot (1 - d - d \cdot k_e \cdot k_c) - \beta \cdot k_e \cdot k_c}{\dot{\lambda}_m^{\min} \cdot \Delta t} \alpha_1 \tag{3.38}$$

with

$$\alpha_1 = (1+k)^{t+\Delta t}\bar{\lambda}_f - {}^t\lambda_m - k\,{}^t\lambda_s \tag{3.39}$$

The derivation of $\alpha_1$ is explained in Appendix D. Once $\Delta\lambda_s$ is solved, the stress in SEE can be obtained by using Equation (3.22).

## 3.3.3 Stress produced in the parallel element

When a muscle is not activated, the forces in CE and SEE are zero. The force in PE is positive when a muscle is stretched and null when it is compressed. Based on the experimental test (Chen and Zeltzer, 1992), the stress in PE can be expressed as:

$${}^{t+\Delta t}\sigma_{PE} = \sigma_0 f_{PE}\left({}^{t+\Delta t}\bar{\lambda}_f\right) \tag{3.40}$$

with

$$f_{PE}\left({}^{t+\Delta t}\bar{\lambda}_f\right) = \begin{cases} A \cdot ({}^{t+\Delta t}\bar{\lambda}_f - 1)^2, & if \quad {}^{t+\Delta t}\bar{\lambda}_f > 1 \\ 0, & otherwise \end{cases} \tag{3.41}$$

where $A$ is a material parameter.

Figure 3.14 shows an example of the normalised axial force against the muscle fibre stretch ratio with $A$ = 4.0. It should be noted that since the muscle fibre cannot resist any axially compressive load, the force developed in the muscle fibre is null when the stretch ratio is less than 1.0.

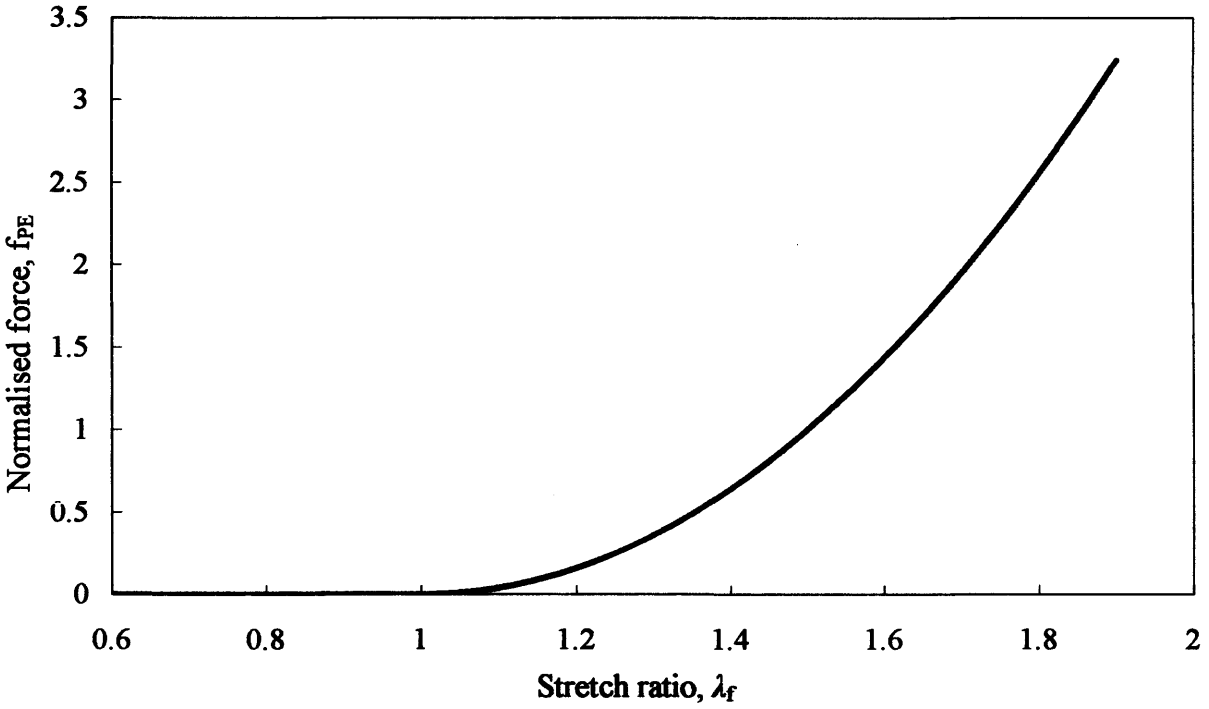


**Figure 3.14** Normalised force in PE versus stretch ratio curve

With the stress expressions of Equations (3.22) and (3.40), the strain energy produced in the muscle fibres can now be obtained from Equation (3.20). Then the strain energy in the whole composite can be solved by using Equation (3.18). The Cauchy stress tensor can be derived from the strain energy following the procedure stated in Chapter 2.3.

## 3.4 LS-DYNA implementation of the skeletal muscle material model

The software LS-DYNA (LSTC, Livermore, 2007) gives the possibility of defining up to 10 Fortran-routines. Thus a user can implement his or her own material model into the software through the use of a user-defined material (UMAT) subroutine. There are two formats of user routines: scalar or vector. In the scalar case, the user routine is sequentially called for each element. In the vector case, the routine is called with a block of elements and the size of this block depends on the type of machine. The scalar routines are called umat41, umat42, ..., umat50 and the vector routines are called umat41v, umat42v, ... ,

umat50v. The material subroutine used in this thesis is scalar.

The structure of the skeletal muscle material subroutine developed in this thesis is shown in Figure 3.15. The LS-DYNA code calculates the strain increments for a time step and passes them to the UMAT subroutine at the beginning of each time step. The material constants are read from the LS-DYNA input file by the subroutine. The history variables can be used to store the accumulated variables. By using the history variables, the subroutine is able to calculate the stresses at the end of the time step by using an incremental form of the constitutive equations. The skeletal muscle material subroutine code developed in this thesis is given in Appendix E.

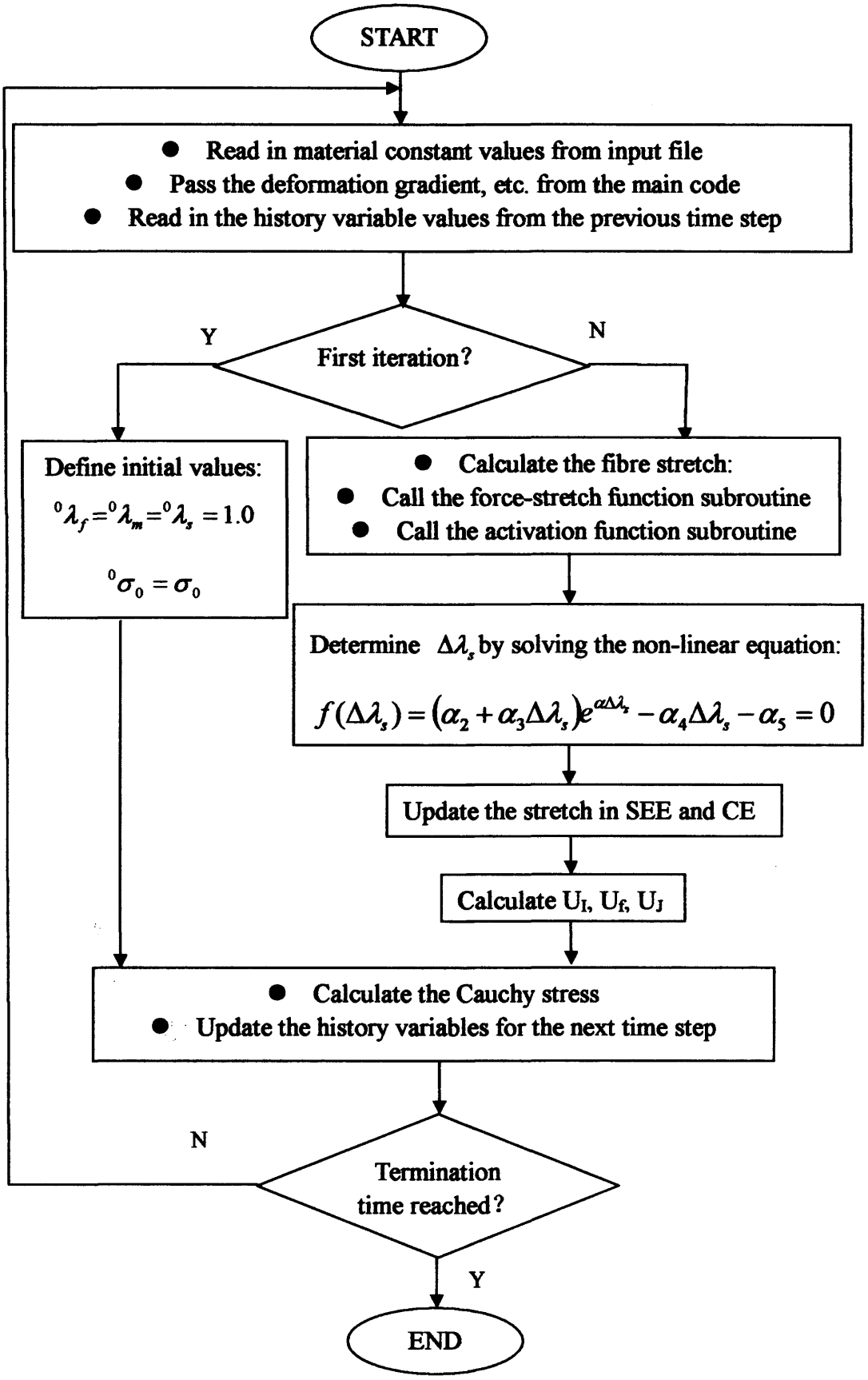


**Figure 3.15** Flowchart for the implementation of the user defined material in LS-DYNA

The user-defined material routine is invoked by LS-DYNA user material interface through a LS-DYNA Keyword input deck which uses the keyword '*MAT_USER_DEFINED_MATERIAL_MODELS'. The input parameter cards associated with this keyword, which are needed for the skeletal muscle routine developed in this thesis, are listed from Table 3.1 to Table 3.6 and the variables are explained in Table 3.7.

Eight history variables are defined in the developed skeletal muscle model. The first four of them store the stress in the matrix, the stress in PE, the stress in SE and the stress due to the volume change, respectively. These variables are stored for the purpose of validation and verification. The last four of them are for calculating the Cauchy Stresses, updated at the end of the routine and passed to the next time step iteration. All user-defined material models require a bulk modulus and a shear modulus for transmitting boundaries, contact interfaces, rigid body constraints and time step calculations. The bulk modulus K and shear modulus G used in the developed skeletal muscle model are given as:

$$K = \frac{E}{3(1-2\nu)} \tag{3.42}$$

$$G = \frac{E}{2(1+\nu)} \tag{3.43}$$

where $E$ and $\nu$ are the Young's modulus and Poisson's ratio of the skeletal muscle, respectively. Based on the measurements of Duck (1990), a stiffness value of $E$ = 6.2 KPa is used for Young's modulus of the muscle at rest. The Poisson's ratio $\nu$ is set as 0.499999, since the skeletal muscle tissue is incompressible. Thus, $K = 1.03\text{x}10^3$ MPa, $G = 2.07$ KPa.

An example of the input file for the developed skeletal muscle material routine is given in Figure 3.16.

**Table 3.1** User defined material model card 1 (LS-DYNA, 2007)

| Variable | MID | RO | MT | LMC | NHV | IORTHO | IBULK | IG |
|---|---|---|---|---|---|---|---|---|
| Type | A8 | F | I | I | I | I | I | I |

**Table 3.2** User defined material model card 2 (LS-DYNA, 2007)

| Variable | IVECT | IFAIL | ITHERM | IHYPER | IEOS | | | |
|---|---|---|---|---|---|---|---|---|
| Type | I | I | I | I | I | | | |

**Table 3.3** Define LMC material parameters using 8 parameters per card (a)

| Variable | P1 | P2 | P3 | P4 | P5 | P6 | P7 | P8 |
|---|---|---|---|---|---|---|---|---|
| Type | F | F | F | F | F | F | F | F |

**Table 3.4** Define LMC material parameters using 8 parameters per card (b)

| Variable | P9 | P10 | P11 | P12 | P13 | P14 | P15 | P16 |
|---|---|---|---|---|---|---|---|---|
| Type | F | F | F | F | F | F | F | F |

**Table 3.5** Define LMC material parameters using 8 parameters per card (c)

| Variable | P17 | P18 | P19 | P20 | P21 | P22 | P23 | P24 |
|---|---|---|---|---|---|---|---|---|
| Type | F | F | F | F | F | F | F | F |

**Table 3.6** Define LMC material parameters using 8 parameters per card (d)

| Variable | P25 | P26 | P27 | P28 | P29 | P30 | P31 | P32 |
|---|---|---|---|---|---|---|---|---|
| Type | F | F | F | F | F | F | F | F |

**Table 3.7** Variable description

| VARIABLE | DESCRIPTION |
|---|---|
| MID | Material identification |
| RO | Mass density, 1060.0 kg/m$^3$ for muscle material. |
| MT | User material type (41-50 inclusive). |
| LMC | Length of material constant array. |
| NHV | Number of history variables to be stored. |
| IORTHO | Set to 1 if the material is orthotropic |
| IBULK | Address of bulk modulus in material constants array |
| IG | Address of shear modulus in material constants array |
| IVECT | Vectorisation flag (on = 1) |
| IFAIL | Failure flag (on = 1) |
| ITHERM | Temperature flag (on =1) |
| IHYPER | Deformation gradient flag (on =1 or -1) |
| IEOS | Equation of state (on =1) |
| P1- P2 | Material constants b and c for determining the stress in matrix |
| P3 | Material constant $\sigma_0$, the maximal isometric stress |
| P4 | Material constant D, the compressibility constant |
| P5 | Material constant k, the length ratio between SEE and CE |
| P6, P7 | Material constants $\alpha$ and $\beta$ for determining the stress in SEE |
| P8 | Material constant $\lambda_c^{min}$, the minimum stretch rate |
| P9,P10,P11 | Material constants $k_c$, $k_e$ and d for the force-velocity function |
| P12, P13 | Bulk modulus and shear modulus, respectively |
| P14, P15 | Activation time and deactivation time, respectively |
| P16 | Material constant S, the rate of the chemical process |
| P17 | Material constant A for determining the stress in PE |
| P18 | Activation level before and after the activation |
| P19 | Activation level during the activation |
| P20 | The optimal fibre stretch |
| P21-P24 | Reserved for future development |
| P25,P26,P27 | Coordinates of muscle origin point P |
| P28,P29,P30 | Coordinates of muscle insertion point Q |

| *MAT_USER_DEFINED_MATERIAL_MODELS | | | | | | | |
|---|---|---|---|---|---|---|---|
| 17 | 1060.0 | 43 | 32 | 8 | 0 | 12 | 13 |
| 0 | 0.0 | 0 | 1 | 0 | | | |
| 23.46 | 379.0 | 1.6e5 | 1.0e-9 | 0.3 | 10.0 | 1.0e5 | -17.0 |
| 5.0 | 5.0 | 1.8 | 1.033e9 | 2.07e3 | 0.0 | 0.49 | 50.0 |
| 4.0 | 0.0 | 1.0 | 1.05 | 0.0 | 0.0 | 0.0 | 0.0 |
| 0.0 | 0.0 | 0.0 | 0.0 | 0.0 | 1.0 | 0.0 | 0.0 |

**Figure 3.16** Example of skeletal muscle material definition in LS-DYNA

In order to create the LS-DYNA executable file used for the developed skeletal muscle model, the following is needed:

- Fortran user material subroutine
- Intel@ Fortran 10.1 Compiler
- Makefile (Appendix F)
- The Fortran file dyn21.f
- Object code files

The last three items are supplied by LS-DYNA distributor and they will need the specifications for the operating system (OS) to be used. The systems used in this thesis are described in Table 3.8.

**Table 3.8** System specifications

| **Computer Type** | Personal computer | Merlin cluster |
|---|---|---|
| **Computer OS** | Window XP V2002 SP2 | RHEL 5 |
| **Processor** | Intel(R) Core(TM) 2 CPU 6320 @1.86GHz, 1.97 GB of RAM | 2×Xeon E5472 3.0 GHz, 1600FSB, 16GB of RAM |
| **Compiler** | Intel@ Fortran Compiler 10.1 for windowsXP | Intel@ Fortran Compiler 10.1 for Linux |
| **Pre-processor** | Oasys Primer 9.3 | Oasys Primer 9.3 |
| **LS-DYNA version** | LS-DYNA 971R3 | LS-DYNA 971R3 |
| **Post-processor** | Oasys D3plot 9.3 | Oasys D3plot 9.3 |

In the file dyn21.f, all the available subroutines for user material routines can be found. There are two ways to link the user routine to the compilation, either adding the code in the dyn21.f file or commenting out a call in the dyn21.f and placing the user routine in a separate file. When having done so and having the Makefile and the object code files in the same directory, the user can execute the compilation and link the files by typing 'nmake' on a command line. Now a new executable file should be generated.

In this thesis, two versions of executable files are generated: SMP and MPP. The SMP version of executable file is used in the personal computer and the MPP version, which enables the user to execute one LS-DYNA simulation on multiple processors, is used in the cluster – Merlin.

## 3.5 Validations and verifications of the developed skeletal muscle model

The muscle model described in Section 3.3 is active, quasi-incompressible, fibre-reinforced and hyperelastic. This model was implemented into LS-DYNA by means of user-defined

material (UMAT) subroutines. There are 14 material parameters in this muscle model, as listed in Table 3.9.

**Table 3.9** Material parameters

| Stress in the matrix | | Stress in SEE | | Stress in PE | | Stress in CE | | | | | | | Compressibility constant |
|---|---|---|---|---|---|---|---|---|---|---|---|---|---|
| | | | | | | $f_t(t)$ | $f_v(\dot{\lambda}_m)$ | | | | $f_l(\bar{\lambda}_f)$ | | |
| $b$ | $c$ | $\alpha$ | $\beta$ | $A$ | $\sigma_0$ | $S$ | $k_c$ | $k_e$ | $d$ | $\dot{\lambda}_m^{min}$ | $\lambda_{opt}$ | $k$ | $D$ |

Parameters $b$ and $c$ are used to characterise the stress produced in the isotropic matrix and they first appeared in an exponential form expression proposed by Humphrey and Yin (1987). In their work, the values of $b$ and $c$ were determined in a least-squared sense from the experimental data. However, it was pointed out that the best-fit material parameters varied with the experimental protocol. In this thesis, the data set $b = 23.46$ and $c = 379.0$ Pa is chosen, as it has also been used in Martins et al.'s study (2006, 2007).

To determine the stress in the SEE, Pinto and Fung (1973) performed experiments on the papillary muscle of a rabbit heart and it was found that the derivative of stress with respect to strain is a linearly increasing function of the stress. From their experimental work, it is found that $\alpha = 10.0$ and $\beta = 1.0\text{x}10^3$ Pa.

Chen and Zelter (1992) performed the tension-length experiment on frog muscle to measure the force for the passive muscle. To express the experimental tension-length curve, they subsequently proposed a quadratic function, as shown in Equation (3.41), where the parameter $A$ was set to 4.0 to best fit the experimental curve. With regard to the maximum isometric stress $\sigma_0$, it is reported that $\sigma_0$ ranges from 0.16 MPa to 1.0 MPa (Zajac, 1989).

There is only one parameter $S$ used to define the muscle activation function. Parameter $S$ is an exponential factor. When modelling single muscle fibres, the magnitude of $S$ is related to the rate of the chemical processes and when modelling large muscle compartments, $S$

represents the time-dependent recruitment of different motor units. In this thesis, $S$ is set as 50.0 to mimic the muscle activation process (Meier and Blickhan, 2000).

Four parameters $k_c$, $k_e$, $d$ and $\dot{\lambda}_m^{min}$ are used to describe the muscle force-velocity relationship. It is reported that the value of $k_c$ for slow muscle fibres is 5.88 and its value for fast muscle fibres is 4.0 (Close, 1964; Otten, 1987). The value of $k_e$ varies in the literature. In Van Leeuwen's work (Van Leeuwen, 1991), it was chosen as 7.56. In Böl and Reese's work (Böl and Reese, 2008), it was 5 and in Tang et al.'s work (Tang, Zhang and Tsui, 2009), it was set to 3.14 for frog gastrocenemius muscle and 7.56 for squid tentacle. The dimensionless constant $d$ is the offset of the function due to the eccentric movement. It is seen from Equation (3.29) that the maximum eccentric stress at time $t+\Delta t$ is dominated by the parameter $d$. The ultimate tension that a muscle can sustain is limited from $1.1\sigma_0$ to $1.8\sigma_0$ (Zajac, 1989). Therefore, the value range for $d$ is from 1.1 to 1.8. It is reported that the minimum stretch rate $\dot{\lambda}_m^{min}$ is -17 $s^{-1}$, although this cannot be reached due to the inertia of muscle (Meier and Blickhan, 2000). In this thesis, the muscle inertia is not taken into account. Therefore, $\dot{\lambda}_m^{min}$ is chosen as -17 $s^{-1}$.

In the developed muscle model, the muscle force-stretch relationship is characterised by one parameter, namely $\lambda_{opt}$. In this thesis, the value of $\lambda_{opt}$ is set as 1.05 in order to fit Gordon's isometric tension-length curve obtained from the experiments on a single fibre of frog skeletal muscle (Gordon, Huxley and Julian, 1966). Parameter $k$ is the ratio of the length of the contractile element to that of the series elastic element and is always assumed to be 0.3 (Fung, 1981; Kojic, Mijailovic and Zdravkovic, 1998).

Parameter $D$ is a compressibility constant and it can be best understood as a penalty parameter which is used to penalise the volume change. Therefore, the value of $D$ is chosen on the condition that the object volume is preserved during the deformation.

From the above analysis, it is seen that the parameters $b$, $c$, $\alpha$, $\beta$ and $A$ have been determined by best fitting with the corresponding experimental data. Parameters $\sigma_0$, $S$,

$\dot{\lambda}_m^{min}$ and $\lambda_{opt}$ have their physical meanings. Parameters $k_c$, $k_e$ and $d$ are for characterising the muscle force-velocity curves. The analysis also shows that parameters $\sigma_0$, $k_c$, $k_e$ and $d$ have their own value ranges. In this thesis, the investigations are performed to test if the developed muscle constitutive model can predict some experimental data by tuning the parameters within their value ranges. To do so, the experimental data from the New Zealand white rabbit hind leg muscle tibialis anterior (Davis, Kaufman and Lieber, 2003; Myers, Wooley, Slotter et al., 1998) are used. Passive and activated elongation simulations are performed and the simulation results are compared with the experimental data. The values of the parameters $\sigma_0$, $D$, $k_e$, $k_c$ and $d$ were tuned to make the numerical results fit with the experimental data. Finally, a good set of parameter values were found, as listed in Table 3.10.

**Table 3.10 Material parameters**

| Description | | Parameter | Value | Source |
|---|---|---|---|---|
| Stress in Matrix | | $b$ | 23.46 | Humphrey and Yin (1987) |
| | | $c$ (N/m$^2$) | 379.0 | |
| Stress in SEE | | $\alpha$ | 10 | Pinto and Fung (1973) |
| | | $\beta$ ( N/m$^2$) | 1.0e3 | |
| Stress in PE | | $A$ | 4.0 | Chen and Zelter (1992) |
| | | $\sigma_0$ ( N/m$^2$) | 7.0e5 | Zajac (1989) |
| Stress in CE | $f_t(t)$ | $S$(s$^{-1}$) | 50 | Meier and Blickhan (2000) |
| | $f_v(\dot{\lambda}_m)$ | $k_c$ | 5 | Close (1964)<br>Böl and Reese (2008)<br>Tang et al. (2009) |
| | | $k_e$ | 5 | |
| | | $d$ | 1.5 | |
| | | $\dot{\lambda}_m^{min}$ | -17 | |
| | $f_\lambda(\bar{\lambda}_f)$ | $\lambda_{opt}$ | 1.05 | Gordon (1966) |
| | | $k$ | 0.3 | Fung (1981) |
| Compressibility constant | | $D$ (m$^2$/ N) | 1.0e-9 | |

Aother two tests, isometric contraction and isometric contraction followed by concentric contraction, are performed for the purpose of model verification, even though no test data is available.

A simple muscle model shown in Figure 3.17 is used for the validations and verifications. The length of the muscle is 5.0 cm. The diameter is 0.9 cm for the smallest cross section and 1.75 cm for the largest cross section. The initial direction of the parallel distributed fibre is chosen to be along the Z direction.

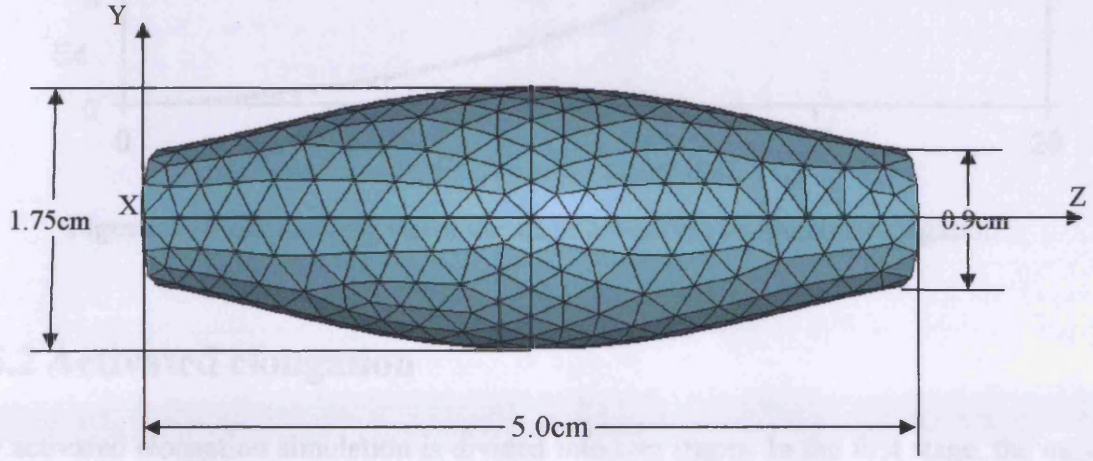


**Figure 3.17** Finite element mesh of the muscle

## 3.5.1 Passive elongation

In the passive elongation test, one end of the muscle was fully fixed and the other end of the muscle was pulled quasi-statically at a controlled velocity of 5.0 mm/s from its rest length, while the muscle was not activated. The engineering stress versus strain relationship was obtained from the simulation results and plotted in Figure 3.18, with the available experimental results included for comparison. Figure 3.18 shows a reasonably good agreement between the experimental data and the passive elongation simulation results.

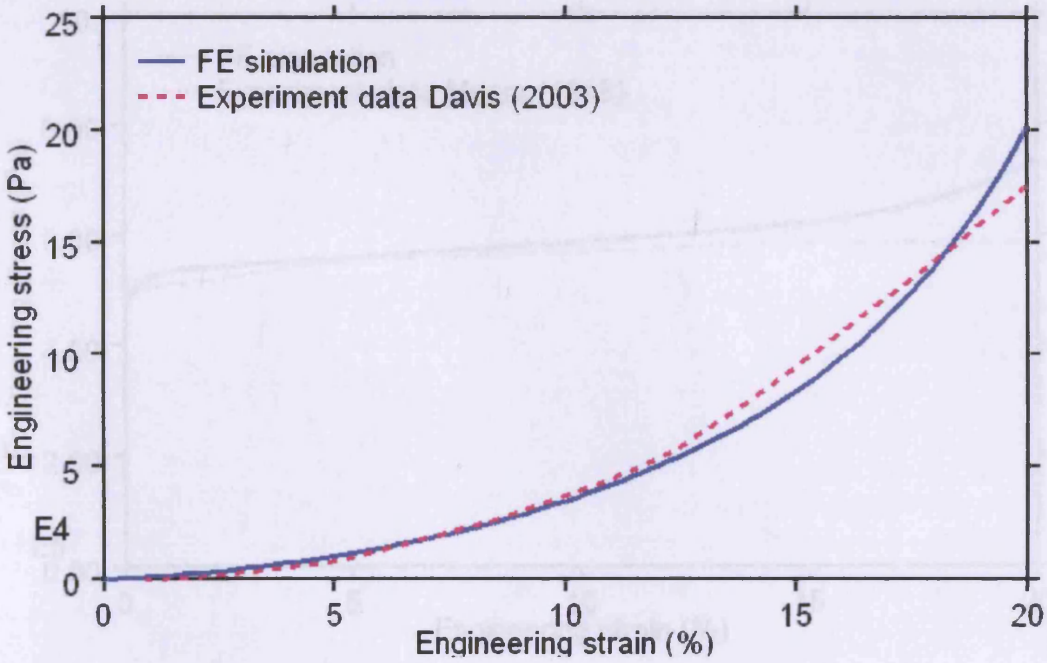


**Figure 3.18** Engineering stress versus strain curves for passive elongation

## 3.5.2 Activated elongation

The activated elongation simulation is divided into two stages. In the first stage, the muscle was held constant in length while being stimulated for 0.5 s, at the end of which the muscle reached full activation. In the second stage, while one end of the muscle was still fully fixed, the other end of the muscle was released and pulled quasi-statically at a controlled velocity of 5.0 mm/s. In this stage, the full activation was maintained. The stress response predicted by the developed model is in accordance with the experimental data up to 15% engineering strain (Figure 3.19).

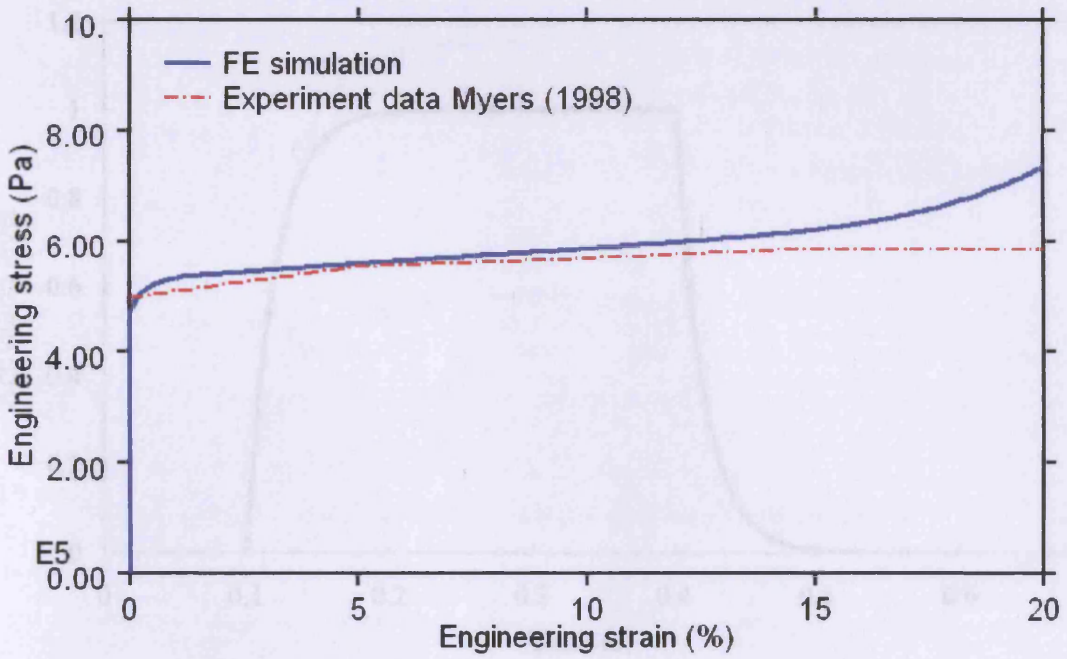


**Figure 3.19** Engineering stress versus strain curves for activated elongation

## 3.5.3 Isometric contraction

In this example, the muscle was subjected to an isometric contraction, thus its two ends were fully fixed during the simulation. A neural excitation with the amplitude of 1.0 was applied at 0.1 s and kept constant for 0.3 s, after which the neural excitation was gradually dropped to zero. Thus, the parameters in the activation function are set as: $n_1 = 0.0$; $n_2 = 1.0$; $t_0 = 0.1$; $t_1 = 0.4$. The activation curve is shown in Figure 3.20.

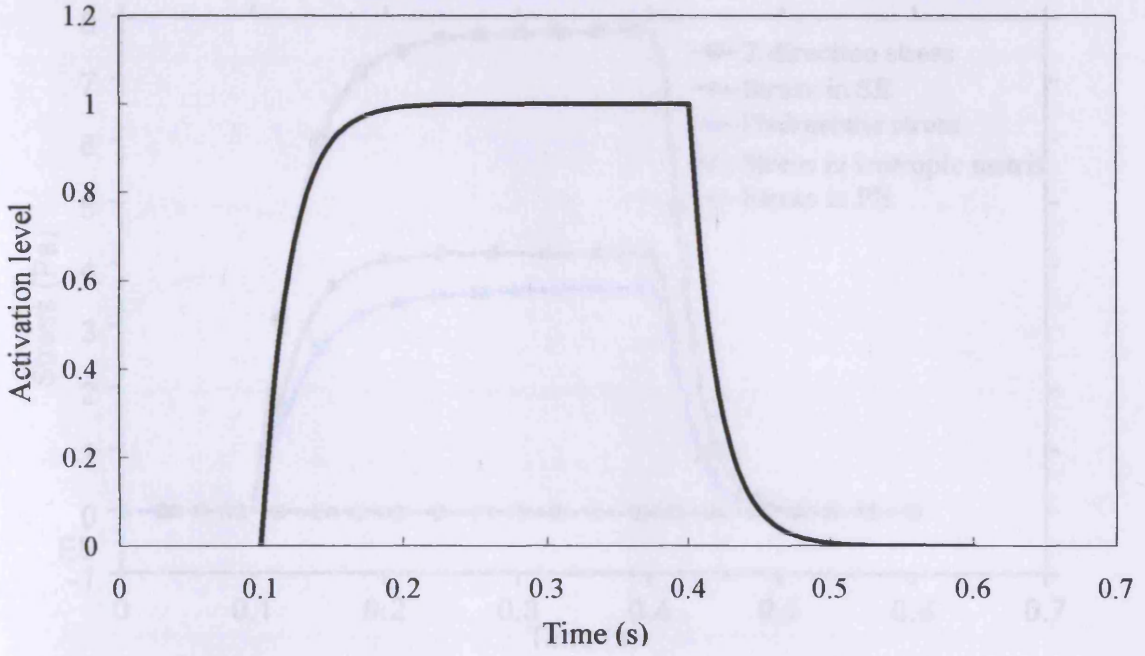


**Figure 3.20** Activation curve for the isometric contraction simulation

The Cauchy stress components in the z axis direction have the following relation:

$$\sigma_{33} = \sigma_{CE33} + \sigma_{VOL33} + \sigma_{I33} + \sigma_{PE33} \tag{3.44}$$

where $\sigma_{33}$ is the Z direction Cauchy stress component; $\sigma_{CE33}$ is the component produced in CE; $\sigma_{VOL33}$ is the hydrostatic stress component; $\sigma_{I33}$ is the component produced in the matrix; and $\sigma_{PE33}$ is the component produced in PE .

The five stress components versus time at a node located in the middle part of the muscle are plotted in Figure 3.21. Since the length of the muscle is held constant during the simulation, the stresses produced in the parallel element and the isotropic substance matrix are zero, as expected. The variation of the other three stresses with time reflects the evolution of the activation function, i.e. they have the same shape as the activation function. Those theoretical predictions are verified by the numerical results shown in Figure 3.21.

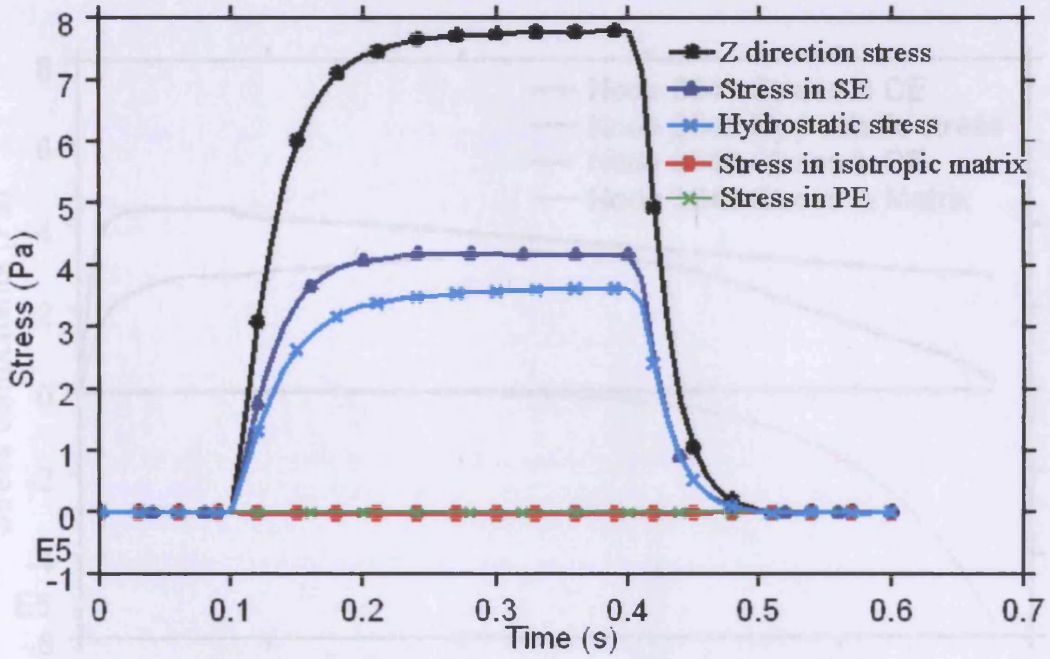


**Figure 3.21** Z-direction stress verse time curves at a node in the centre of muscle for the isometric contraction simulation

## 3.5.4 Isometric contraction followed by concentric contraction

This test is divided into two stages. In the first stage, the muscle was subjected to an isometric contraction. Its two ends were fixed and the muscle was stimulated until the tetanised state was reached. The stimulus was kept for 0.4 s in this example. In the second stage, one end of the muscle was released and the muscle was contracting quasi-statically at a controlled velocity of 5.0 mm/s, while the full activation was maintained.

The four stress components from a node located in the middle part of the muscle versus time are plotted, as shown in Figure 3.22. From time 0.0 s to 0.4 s, the muscle was contracting isometrically and from 0.4 s to 2.4 s, the muscle was contracting concentrically and quasi-statically. Since in reality the muscle fibre cannot resist a compressive force along the fibre, the stress in the parallel element is zero in this simulation. The total length of the muscle does not change during the isometric stage, thus the stress produced in the isometric matrix is zero. In the concentric contraction stage, the matrix is producing a resistant force. Thus the stress in the matrix is negative during concentric contraction. These theoretical predictions are verified by the numerical results (Figure 3.22).

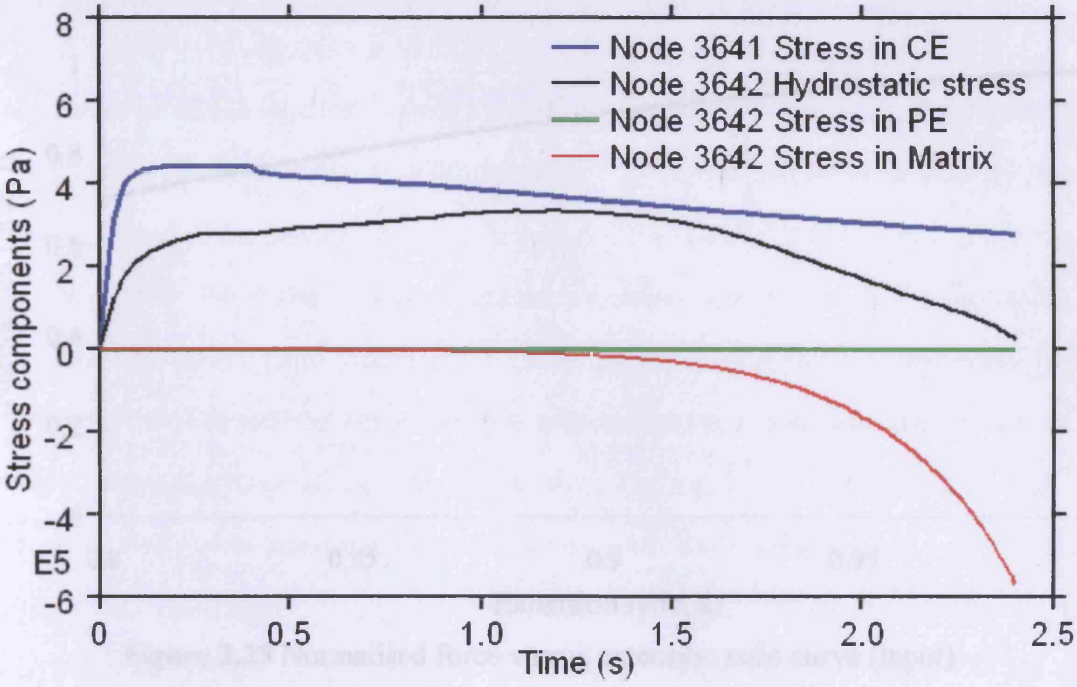


**Figure 3.22** Stress components versus time curves

Furthermore, the variation of the stress in the contractile element during the controlled concentric contraction stage is discussed. The stress in CE is defined in Equation (3.25), and given once more as below:

$$^{t+\Delta t}\sigma_m = \sigma_0 \cdot f_t(t+\Delta t) \cdot f_\lambda(\bar{\lambda}_f) \cdot f_v(\dot{\lambda}_m) \tag{3.45}$$

During the concentric contraction, the activation function $f_t(t+\Delta t)$ is a constant, since the muscle was kept in a tetanised state. The muscle was contracting at a constant velocity, thus the force-velocity function $f_v(\dot{\lambda}_m)$ did not change in this stage. Therefore, the stress in CE depends on the force-stretch function $f_\lambda(\bar{\lambda}_f)$. In this simulation, the force against extension ratio curve as shown in Figure 3.23 was input into the model. The variation of the normalised stress produced in CE against the extension ratio (Figure 3.24) reflects the relationship between the input force and extension ratio, thus verifies the stress expression in CE.

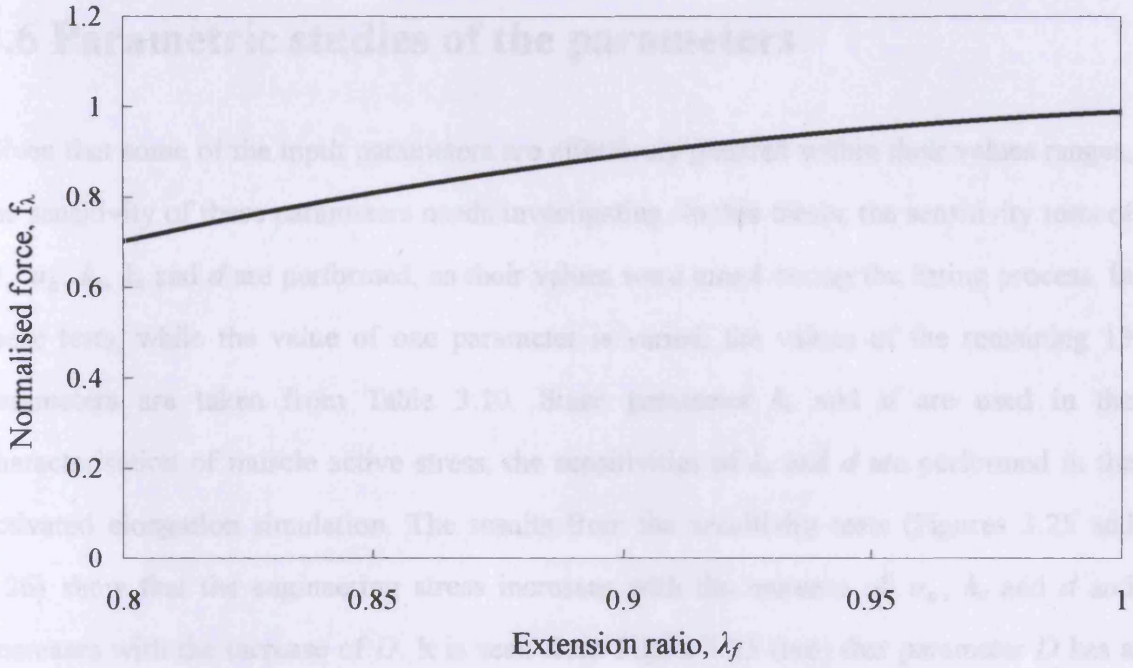


**Figure 3.23** Normalised force versus extension ratio curve (input)

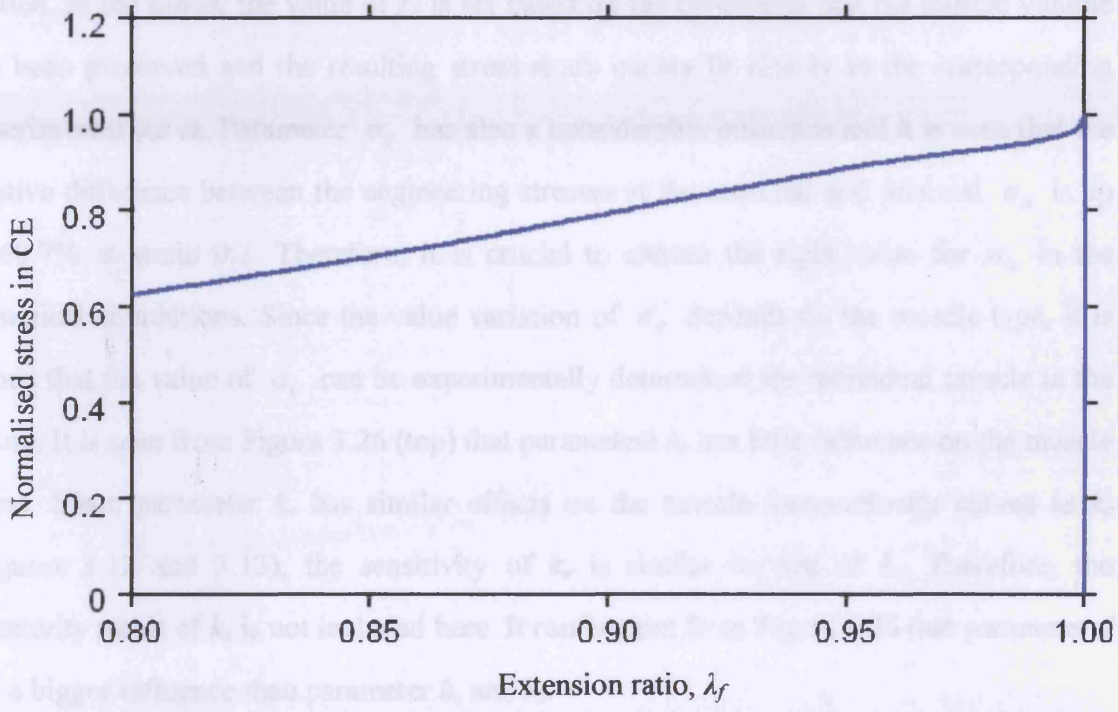


**Figure 3.24** Normalised stress in CE versus extension ratio curve (output)

## 3.6 Parametric studies of the parameters

Given that some of the input parameters are effectively guessed within their values ranges, the sensitivity of these parameters needs investigating. In this thesis, the sensitivity tests of $D$, $\sigma_0$, $k_c$, $k_e$ and $d$ are performed, as their values were tuned during the fitting process. In these tests, while the value of one parameter is varied, the values of the remaining 13 parameters are taken from Table 3.10. Since parameter $k_c$ and $d$ are used in the characterisation of muscle active stress, the sensitivities of $k_c$ and $d$ are performed in the activated elongation simulation. The results from the sensitivity tests (Figures 3.25 and 3.26) show that the engineering stress increases with the increase of $\sigma_0$, $k_c$ and $d$ and decreases with the increase of $D$. It is seen from Figure 3.25 (top) that parameter $D$ has a considerable influence on the total engineering stress and so its value should be carefully chosen. In the thesis, the value of $D$ is set based on the conditions that the muscle volume has been preserved and the resulting stress-strain curves fit closely to the corresponding experimental curve. Parameter $\sigma_0$ has also a considerable influence and it is seen that the relative difference between the engineering stresses at the maximal and minimal $\sigma_0$ is up to 60.7% at strain 0.2. Therefore, it is crucial to choose the right value for $\sigma_0$ in the numerical simulations. Since the value variation of $\sigma_0$ depends on the muscle type, it is hoped that the value of $\sigma_0$ can be experimentally determined for individual muscle in the future. It is seen from Figure 3.26 (top) that parameters $k_c$ has little influence on the muscle stress. Since parameter $k_e$ has similar effects on the muscle force-velocity curves as $k_c$ (Figures 3.12 and 3.13), the sensitivity of $k_e$ is similar to that of $k_c$. Therefore, the sensitivity result of $k_e$ is not included here. It can be seen from Figure 3.26 that parameter $d$ has a bigger influence than parameter $k_c$ and $k_e$.

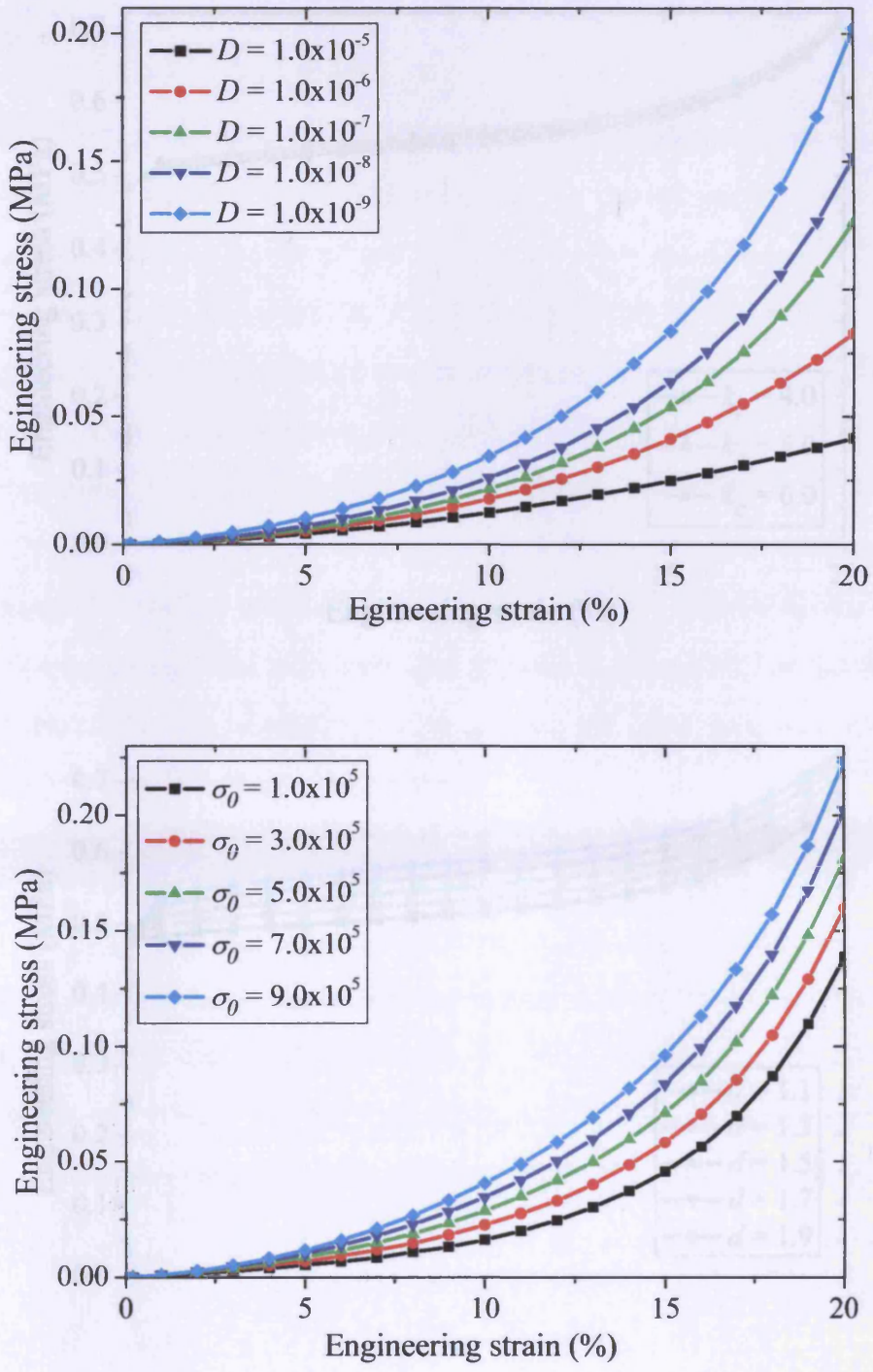


**Figure 3.25** Sensitivities of parameters $D$ and $\sigma_0$ in the passive elongation simulation.

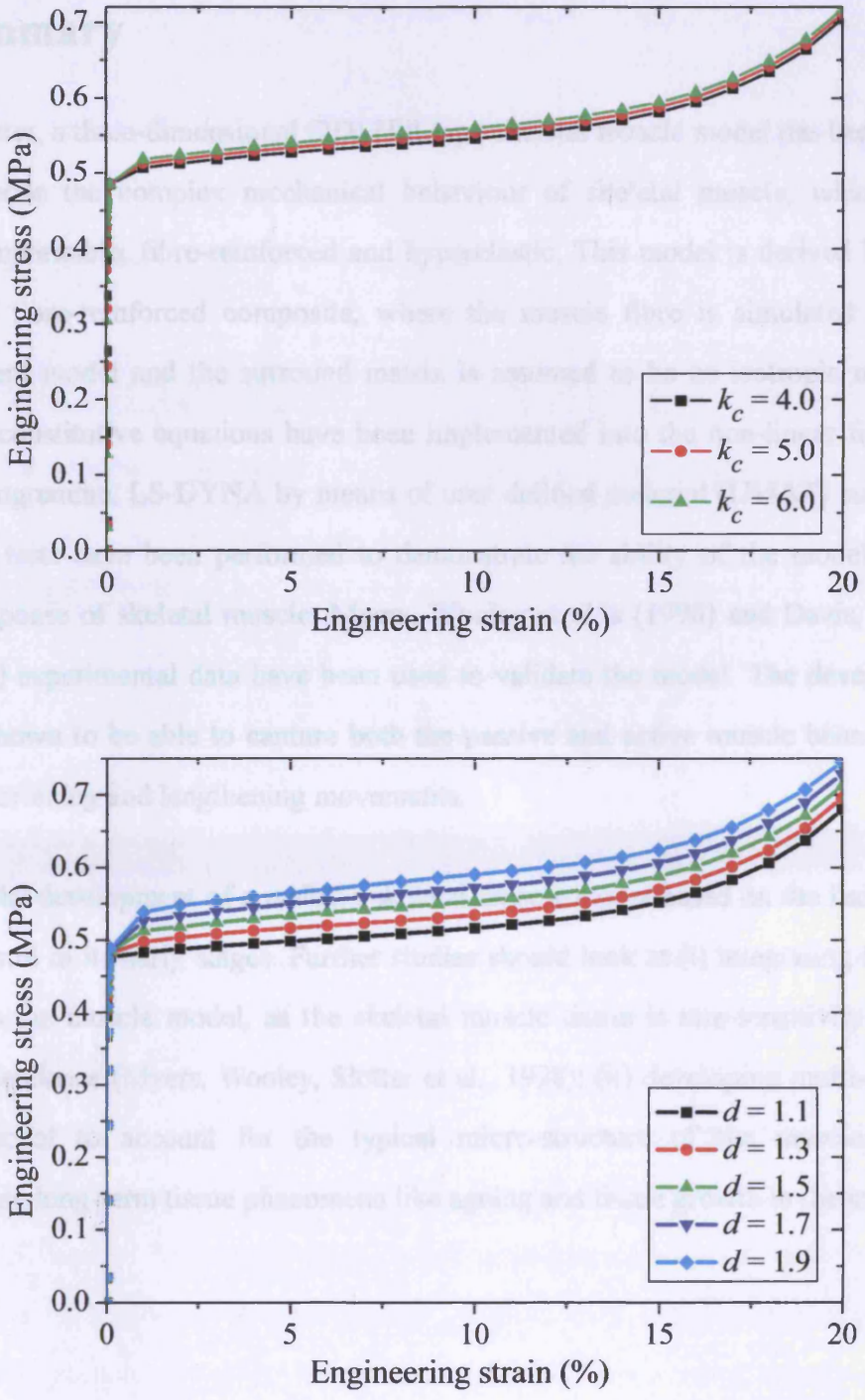


**Figure 3.26** Sensitivities of parameters $k_c$ and $d$ in the activated elongation simulation

## 3.7 Summary

In this chapter, a three-dimensional (3D) Hill-type skeletal muscle model has been developed to characterise the complex mechanical behaviour of skeletal muscle, which is active, quasi-incompressible, fibre-reinforced and hyperelastic. This model is derived based on the concept of fibre-reinforced composite, where the muscle fibre is simulated using Hill's three-element model and the surround matrix is assumed to be an isotropic material. The developed constitutive equations have been implemented into the non-linear finite element analysis programme, LS-DYNA by means of user defined material (UMAT) subroutines. A number of tests have been performed to demonstrate the ability of the model to simulate various response of skeletal muscle. Myers, Wooley et al.'s (1998) and Davis, Kaufman et al.'s (2003) experimental data have been used to validate the model. The developed model has been shown to be able to capture both the passive and active muscle behaviour during both the shortening and lengthening movements.

However, the development of a realistic skeletal muscle model based on the finite element method is still in its early stages. Further studies should look at (i) integrating the viscous effects into the muscle model, as the skeletal muscle tissue is rate-sensitivity and strain history dependence (Myers, Wooley, Slotter et al., 1998); (ii) developing multi-scale finite element model to account for the typical micro-structure of the muscle; and (iii) incorporating long-term tissue phenomena like ageing and tissue growth in the model.

# Chapter 4

# Three-Dimensional Finite Element Facial Model and Facial Movement Simulation

## 4.1 Introduction

This chapter begins with a review of various facial models developed for the simulations of facial animation and facial surgery, followed by a detailed introduction to the procedure of constructing the three-dimensional (3D) finite element facial model. The construction work involves the usage of patient specific Cone Beam Computerised Tomography (CBCT) scan data of the facial bones and facial surface together with the adjusted generic facial muscles which are taken from a standardised forensic database in the School of Life Sciences, University of Dundee. The simulation of patient specific cranio-facial surgery is performed and subsequently validated with the patient's post-surgical CBCT and surface scanning data. Finally, a muscle-controlled facial movement simulation method is proposed. In this method, the facial movement is created by activating the responsible muscles and the muscle activation-contraction process is modelled by the developed muscle material model which is described in Chapter 3. The facial movements, including two facial expressions (smile and disgust) and the mouth opening process, are simulated by using the developed finite element facial model.

## 4.2 Overview of various facial simulation models

This section gives an overview of various facial simulation models. Special attention is placed on the simulations of facial surgery and facial movement.

### 4.2.1 Geometric models

The first facial models were geometrically based and aimed just at facial animations. For example, Parke (1982) proposed an early parameterised facial model, in which the head was represented by polygons. Platt and Badler (1981) proposed a muscle-controlled facial expression model, in which the skin was the outermost level represented by a set of 3D points defining a movable surface and muscles are groups of elastic arcs underneath the skin surface. Waters (1987) developed a parameterised muscle-controlled facial model for creating realistic facial expressions. DiPaola (1992) developed a parametric facial animation system, in which the facial expressions were accomplished by modifying the parameters that define the facial model. A survey for parameterised facial models and facial animation is provided in Parke and Waters' (2008) book.

The geometric models are computationally efficient. However, they do not reflect the physical properties of the face, thus they are mainly used in computer-aided design. As a consequence of the demand for accuracy in the facial surgery simulation, physically-based models are needed. In the following sections, several physically-based facial models are reviewed with the focus on mass-spring models (MSM) and finite element models (FEM).

### 4.2.2 Mass-spring models

Mass-spring systems are also called mass-spring-damper (MSD) systems. In these systems, an object is modelled as a collection of point masses connected by springs in a lattice structure as shown in Figure 4.1. The spring forces are often linear (Hookean law), but non-linear springs can be used to model complex tissues such as human skin.

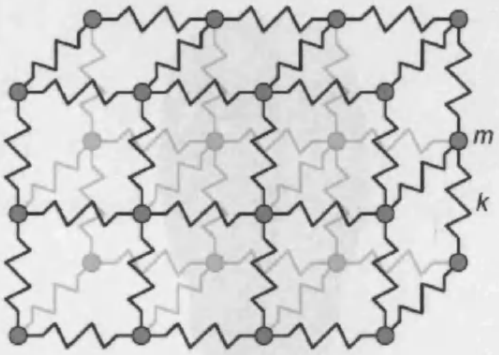


**Figure 4.1** Mass-spring model (Gibson and Mirtich, 1997)

Mass-spring systems were first exploited by Miller (1988). Now, mass-spring systems have been widely applied to a variety of problems, such as cloth motion, facial animation and surgery simulation. The research interest herein lies in their applications into the simulations of facial animation and facial surgery.

In facial animation, Terzopoulos and Waters (1990) proposed a 3D hierarchical model of the human face. This model consisted of three layers of elements representing the cutaneous tissue, subcutaneous tissue and muscle layer. The springs in each layer had different stiffness parameters in accordance with the non-homogeneity of real facial tissue. A set of anatomically-motivated facial muscle actuators was incorporated into the model. Thus the facial animations were produced as a result of the muscle contractions. Examples of some of their produced facial animations are shown in Figure 4.2. Following their work, Lee, Terzopoulos and Waters (1993; 1995) proposed a more accurate biomechanical model for facial animation. The basic element used in their model is shown in Figure 4.3. The epidermal surface is defined by nodes 1, 2 and 3, which are connected by epidermal springs. The fascia surface is defined by nodes 4, 5 and 6, which are interconnected by fascia springs. Nodes 7, 8 and 9 define the skull surface.

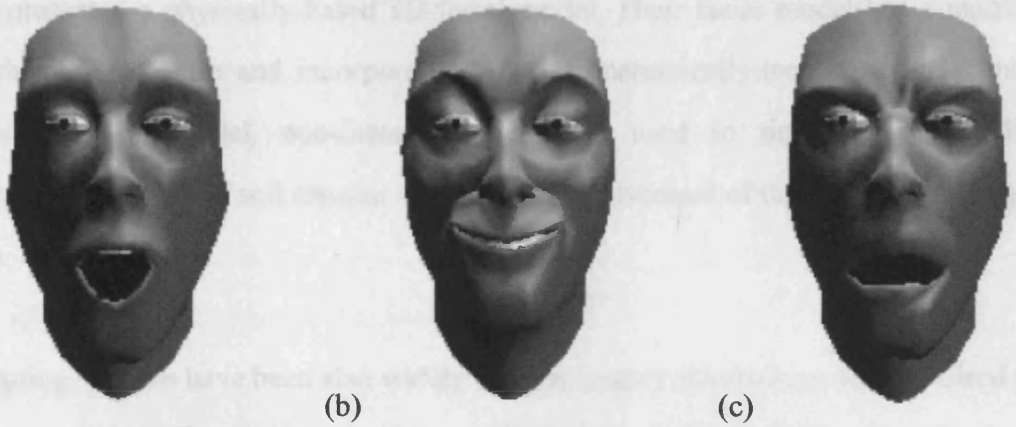

(a) (b) (c)

**Figure 4.2** Facial animations: (a) Jaw rotated; (b) Smile; (c) Anger (Terzopoulos and Waters, 1990)

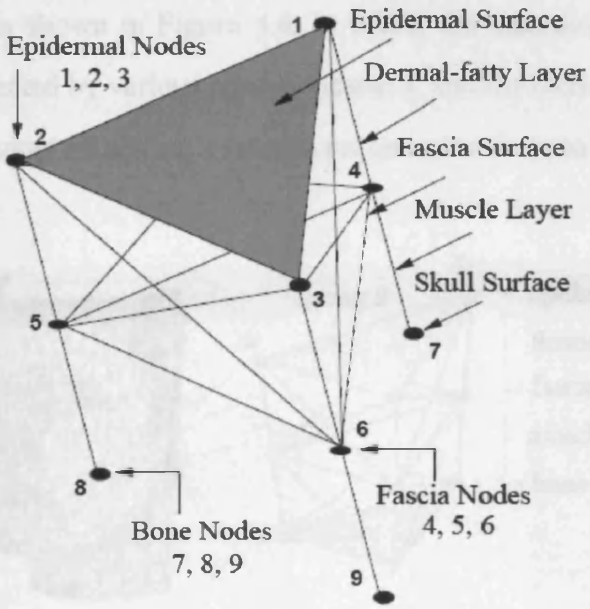


**Figure 4.3** Triangular skin tissue prism element (Lee, Terzopoulos and Walters, 1995; Lee, Terzopoulos and Waters, 1993)

In addition, Kahler, Haber et al. (2001) proposed a muscle-based model for facial animation using a three-layer mass-spring system to connect the skull, muscle and the skin. Pitermann and Munhall (2001) presented a dynamic inversion of a muscle-based model that allows the facial animation to be created from the kinematical recordings of facial movements. In this model, the facial tissue was modelled as a three-layered mesh: the epidermis layer, the fascia layer and the skull layer. More recently, Zhang, Prakash et al.

(2004) presented a physically-based 3D facial model. Their facial model had a multilayer biomechanical structure and incorporated a set of anatomically-motivated facial muscle actuators. In this model, non-linear springs were used to simulate the non-linear viscoelastic behaviour of soft tissues, which is an improvement of the previous mass-spring models.

Mass-spring systems have been also widely used in surgery simulations. Keeve, Girod et al. (Keeve, Girod and Girod 1996a, b; Keeve, Girod, Kikinis et al., 1998) adopted a layered mass-spring tissue model (Lee, Terzopoulos and Walters, 1995; Lee, Terzopoulos and Waters, 1993) for simulating cranio-facial surgery. The basic tissue element used in Keeve, Girod et al.'s model is shown in Figure 4.4, in which the mechanical properties of each tissue layer are represented by various spring constants, and the incompressibility of human tissue is taken into account by adding a volume preservation force to each node.

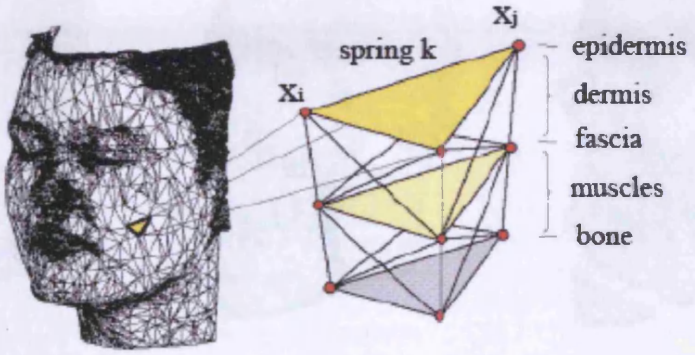


**Figure 4.4** Basic tissue element (Keeve, Girod, Kikinis et al., 1998)

Teschner, Girod et al. (1999) developed a system for interactive, 3D cranio-facial surgery simulations. The system was based on the multi-layer soft tissue model, in which the layer springs represented the soft tissue layers, the bone springs represented connections between the bones and the soft tissues, and the boundary springs prevented the soft tissues from any global transformation, as shown in Figure 4.5. This system was able to simulate bimaxillary osteotomies and physiological jaw movement. Later, Teschner, Girod et al. (2000) improved their mass-spring system to model patient individual soft tissue deformation. In

the new system, the non-linear deformation and incompressibility of soft tissues were taken into account. Furthermore, the mass and skin turgors were integrated into the proposed soft tissue model. The developed methods have been tested for soft tissue deformation using cuttings of six individual patient data. Figure 4.6 shows one of the test results showing the soft tissue deformation for two different surgery options: the simulated realignment of a part of the lower jaw and that of the chin.

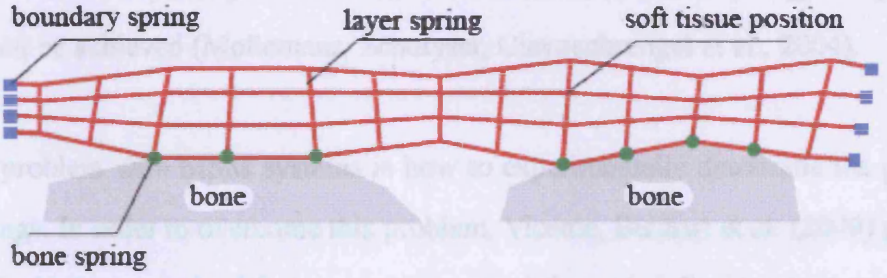


**Figure 4.5** Multi-layer soft tissue model (Teschner, Girod and Girod, 1999)

(a)

(b)

**Figure 4.6** Surgery simulation: (a) Simulated bone realignment; (b) The corresponding soft tissue changes (Teschner, Girod and Girod, 2000)

Mollemans, Schutyser et al. (2003) proposed a tetrahedral-based Mass-Spring Model (MSM) for a surgery planning system to predict soft tissue changes caused by the skeletal changes. In contrast to traditional MSM, their extended model consisted of three types of elements: mass points, springs and tetrahedrons. The tetrahedrons were extracted from the 3D tetrahedral mesh. The mass points were set on the mesh nodes and the linear springs on the mesh edges. This MSM was quantitatively validated by measuring distances between the predicted and the post-operative facial surface for three patients, suggesting that good results could be achieved (Mollemans, Schutyser, Cleynenbreugel et al., 2004).

The main problem with MSM systems is how to experimentally determine the parameters of the springs. In order to overcome this problem, Vicente, Buchart et al. (2009) proposed a new MSM which was derived from a continuum and the scaled displacement method. With the scaled displacement technique, neither re-meshing nor removing of elements was required during the simulation of maxillofacial surgery. Therefore, a more reliable description of the post-surgical displacement of soft tissues was achieved.

From the above, it can be seen that mass-spring systems have been widely used in the simulations of facial animation and facial surgery. Mass-spring models are easy to construct and allow for both interactive and real-time simulations. In addition, they are efficient in dealing with large deformation problems.

However, mass-spring systems have several significant drawbacks. First of all, mass-spring models give an insufficient approximation of true physics, because they only offer a coarse approximation of true material properties. That means this system cannot provide required accuracy for some complex composite materials such as soft tissues. Secondly, the material behaviour relies on the spring constants, but accurate values for these constants are very difficult to obtain from experiments. Furthermore, some material properties, such as incompressibility and anisotropy, cannot be modelled in this system. In addition, mass-spring systems are also weak in modelling thin surfaces, which resist bending. Last

but not least, when modelling nearly rigid objects, large constants are needed. In this case the mass-spring systems behave stiffly because of their poor stability resulting from a large number of spring constants.

As a consequence, for simulations of complex objects such as human face, or complex materials such as soft tissues, or accurate simulations such as surgical operations, other methods should be employed, such as the finite element method, the finite difference method, etc.

### 4.2.3 Finite element models

Mass-spring systems typically model an object in a discrete manner. In contrast, the finite element method (FEM) is capable of modelling deformable objects as a continuum system. Thus, a more realistic and accurate solution can be achieved by using the FEM. In addition, the finite element technique is superior to other techniques when modelling deformable objects, since it allows arbitrary geometries. However, the main limitation of the finite element method lies in the computational costs. The more elements that are used, the more computer resources are needed. Regardless of this limitation, the finite element method is still widely used in many applications, such as soft tissue modelling and surgery simulations.

Koch, Gross et al. (1996) proposed a surface based finite element model for the simulation of facial surgery. In their approach, the facial surface was represented by $C^1$-continuous thin plate finite elements and connected to the skull by springs, as shown in Figure 4.7. The spring stiffness parameters were computed according to the segmentation of the underlying CT data. This model has been successfully used in the simulation of facial surgery and emotion editing (Koch, Gross and Bosshard, 1998). However, the model lacked true volumetric physics and therefore was unable to account for some effects, such as volume preservation. For volumetric soft tissue modelling, Koch (2000) extended the surface based model towards volumetric finite element modelling. The material incompressibility was incorporated into the model by means of linear elasto-mechanics. In this approach, instead

of connecting top and bottom triangles with a spring, they established prism elements during the set-up of the facial model. Koch, Roth et al. (2002) presented a framework for the simulation of facial surgery based on volumetric finite element modelling. However, their model was restricted to linear elastic theory, which could not deal with large deformations. To achieve both volumetric and non-linear soft tissue modelling, Roth, Gross et al. (1998) developed the tetrahedral Bernstein-Bezier elements by combining the finite element method with Bernstein-Bezier representations. Although higher order interpolations and incompressible, non-linear material behaviour were incorporated, it was restricted to $C^0$-continuous interpolation across element boundaries. To overcome this shortcoming, Roth (2002) proposed a tetrahedral $C^1$-continuous Bernstein-Bezier finite element model, whose simulation results were better than the $C^0$ solution.

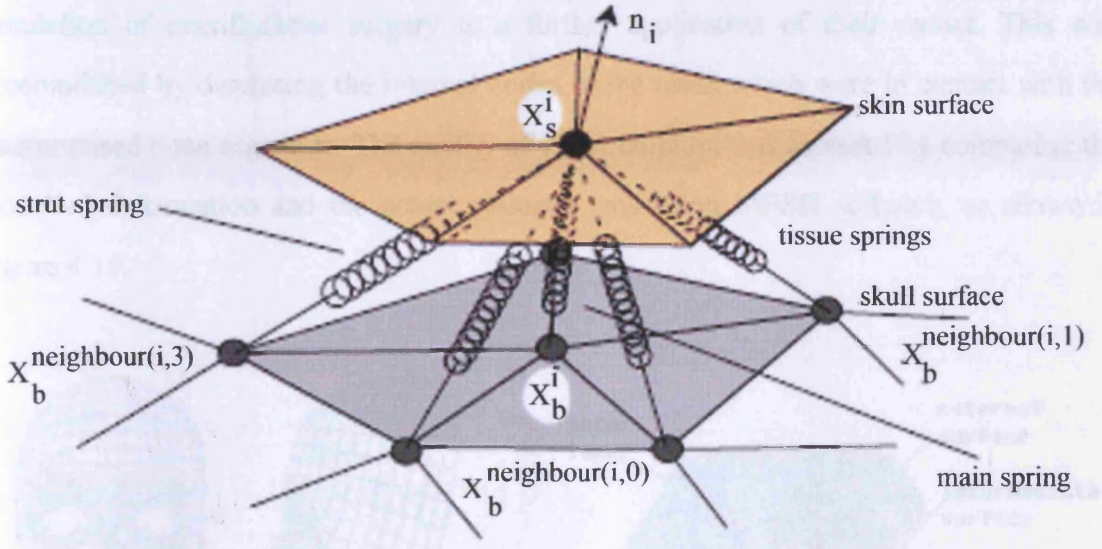


**Figure 4.7** Spring mesh for soft tissue modelling (Koch, Gross, Carls et al., 1996)

Chabanas, Payan et al. have worked on the simulation of maxillo-facial surgery (Chabanas, Luboz and Payan, 2003; Chabanas, Marecaux, Chouly et al., 2004; Chabanas, Marecaux, Payan et al., 2002; Chabanas and Payan, 2000; Chabanas, Payan, Marecaux et al., 2004; Luboz, Chabanas, Swider et al., 2005) by using the finite element method. They developed a 3D mesh of a generic human face by using three surface meshes: the external surface mesh represents the facial skin, the internal surface mesh corresponds to the projection of

the external surface onto a standard skull and the intermediate surface mesh lies at the interface between the dermis and the hypodermis. Two layers of hexahedral elements were created by connecting the nodes of these surfaces, see Figure 4.8 (right). The facial muscles were represented by labelling the corresponding elements inside the outer layer of the 3D mesh, so that they can be prescribed with specific mechanical properties. Figure 4.8 (left and middle) shows the final 3D mesh of a generic human face. Finally, patient specific model can be quasi-automatically built up by adapting the generic mesh to an individual patient's morphology using the Mesh-Matching algorithm. The simulation of facial expression is one application of their facial model. In their simulation, facial expressions were created by muscular contractions which were modelled by a low-level force generator applying forces on nodes located between the two extremities of the muscle. Figure 4.9 shows one example of the facial deformation caused by the muscle activation. The simulation of maxillofacial surgery is a further application of their model. This was accomplished by displacing the internal nodes of the mesh which were in contact with the osteotomised bone segments. The quality of the simulation was assessed by comparing the modelled deformation and the actual patient's data using MESH software, as shown in Figure 4.10.

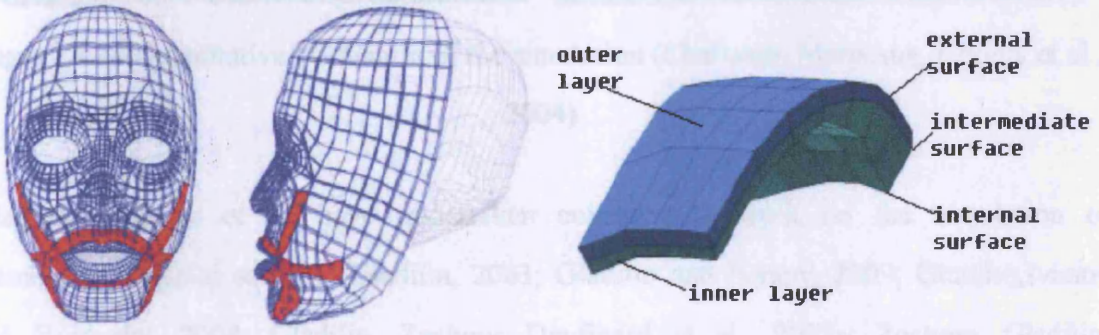


**Figure 4.8** The generic 3D mesh with embedded main facial muscles (Chabanas, Marecaux, Payan et al., 2002)

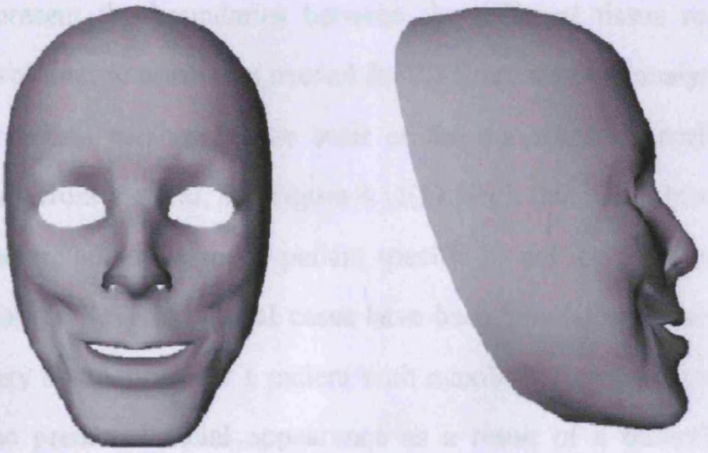

**Figure 4.9** Face deformation due to the activation of the zygomaticus muscles (Chabanas, Luboz and Payan, 2003)

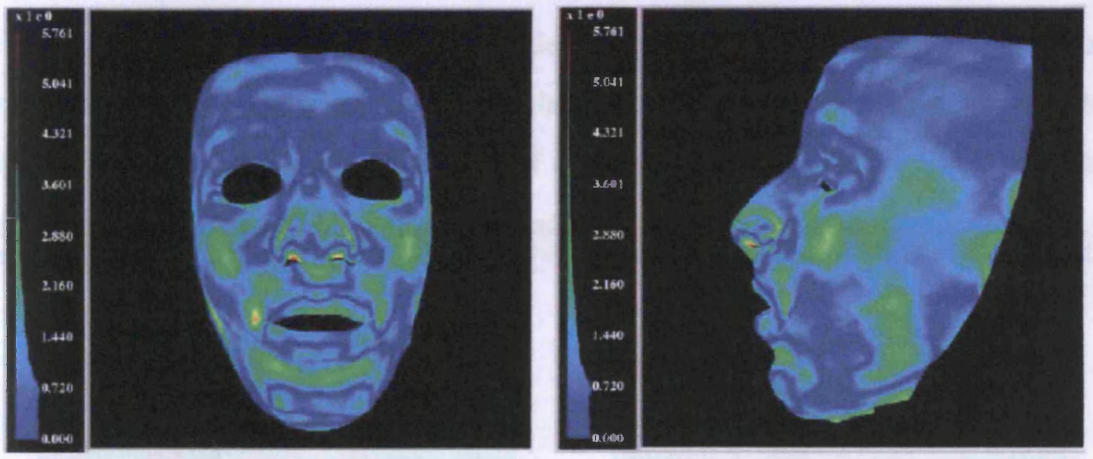


**Figure 4.10** Quantitative evaluation of the simulation (Chabanas, Marecaux, Chouly et al., 2004)

Gladilin, Zachow et al. have undertaken considerable work on the simulation of cranio-maxillofacial surgery (Gladilin, 2003; Gladilin and Ivanov, 2009; Gladilin,Ivanov and Roginsky, 2004; Gladilin, Zachow, Deuflhard et al., 2003a; Zachow, Gladilin, Zeilhofer et al., 2001; Zachow, Hege and Deuflhard, 2006) and the simulation of individual facial expression (Gladilin, 2003; Gladilin, Zachow, Deuflhard et al., 2002a; Gladilin, Zachow, Deuflhard et al., 2002b, 2003b; Gladilin, Zachow, Deuflhard et al., 2004) using the finite element method. In their simulations, the individual geometrical models of patients' anatomy were generated from CT data and the triangulated surfaces were

generated to represent the boundaries between the different tissue regions, see Figure 4.11(a). Since a volumetric mesh was needed for the finite element analysis, they generated unstructured tetrahedral meshes on the basis of the non-manifold surface triangulations with the advancing front method, see Figure 4.11(b). With this reconstructing method, they were able to generate an adequate 3D patient specific model for the surgical planning and soft tissue simulation. Several clinical cases have been simulated. Figure 4.12 shows one case of the surgery simulations for a patient with maxillary retrognathism and mandibular prognathism. The predicted facial appearance as a result of a bimaxillary operation is shown in Figure 4.12(b). In their facial animation simulation approach, the individual facial expressions were estimated by the superpositioning of pre-computed single muscle actions. Some of the simulated expressions are shown in Figure 4.13, where happiness was generated by superimpositioning of single muscle actions of zygomaticus major, zygomaticus minor, risorius and orbicularis oris; and disgust was created by superpositioning of single muscle actions of depressor angularis oris left, depressor labii left, mentalis left, levator labii right and orbicularis oris left and right.

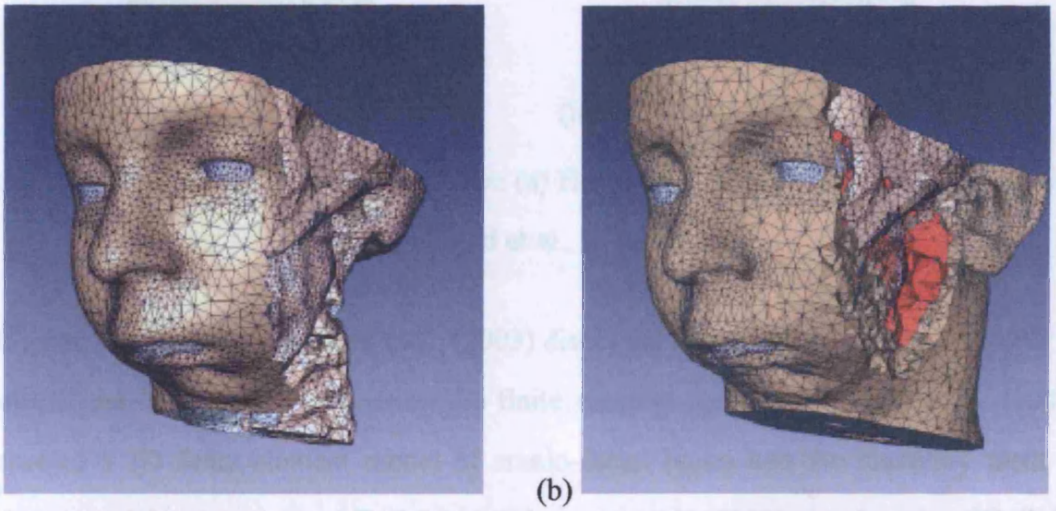

(a) (b)

**Figure 4.11** Facial model: (a) Simplified surface model; (b) Tetrahedral mesh (Zachow, Gladilin, Zeilhofer et al., 2001)

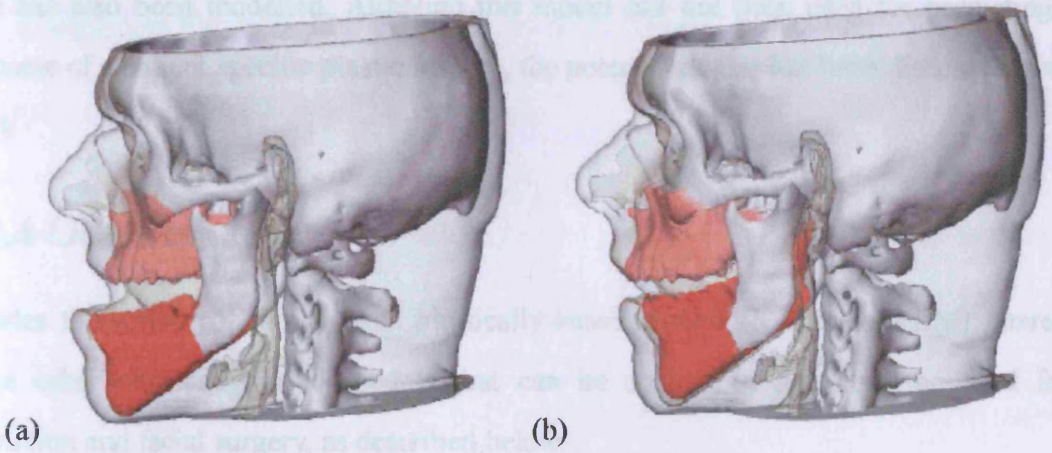


**Figure 4.12** Simulation of the cranio-maxillofacial surgery: (a) Pre-surgery; (b) Post-surgery (Gladilin, 2003)

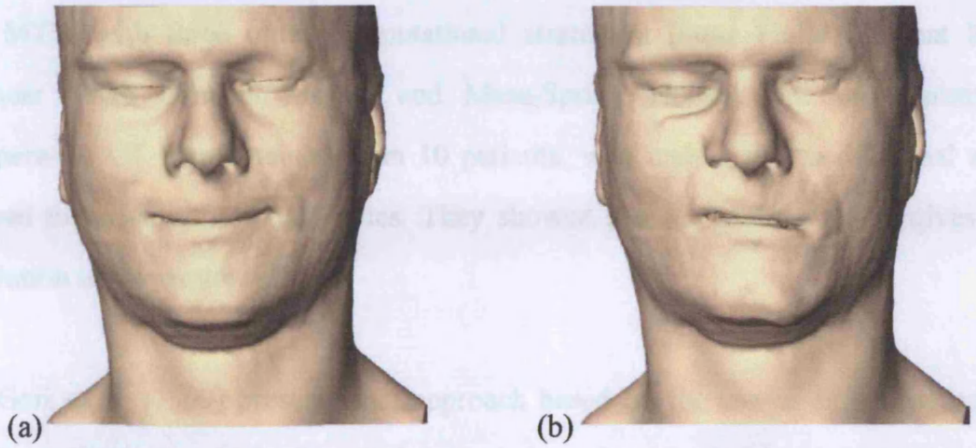


**Figure 4.13** Simulation of facial expressions: (a) Happiness; (b) Disgust (Gladilin, Zachow, Deuflhard et al., 2004)

In addition, Vandewalle, Schutyser et al. (2003) discussed the modelling of tissue growth as a result of maxillofacial surgery using the finite element method. Yu, Baik et al. (2007) constructed a 3D finite element model of cranio-facial bones and the maxillary teeth to simulate actual bone reactions. Barbarino, Jabareen et al. (2008) developed a 3D finite element model of the face aiming at improving the design of medical devices used for plastic surgery on the human face. Later, they (Barbarino, Jabareen, Trzewik et al., 2009) validated the response of their facial model to gravity loads, and to the applications of a pressure inside the oral cavity and of an imposed displacement. The ageing response of the

face has also been modelled. Although this model has not been used for predicting the outcome of a patient specific plastic surgery, the potential of this has been discussed in their work.

### 4.2.4 Other models

Besides these two commonly used physically-based models (MSM and FEM), there are some other physically-based models that can be applied in the simulations of facial animation and facial surgery, as described below.

Mollemans, Schutyer et al. (2005) presented a Mass Tensor Model (MTM) to simulate soft tissue deformations after maxillofacial surgery. They (2007) subsequently compared the novel MTM with three other computational strategies: linear Finite Element Models, non-linear Finite Element Models and Mass-Spring Models. The pre-operative and post-operative CT data obtained from 10 patients, who underwent maxillofacial surgery, was used to validate these techniques. They showed that the MTM strategy gives both a fast solution and accurate results.

Sarti, Gori et al. (1999) presented an approach based on the use of embedded boundary condition techniques, which allowed the simulation of cranio-facial surgery directly on the grid of 3D CT images of the patient. However, their method demanded a large amount of data and the simulation has to been implemented on a supercomputer, which is a considerable drawback.

## 4.3 Construction of the 3D finite element facial model

Building a three-dimensional (3D) finite element model of the human face is a complex task. It involves a multi-disciplined knowledge base and a considerable understanding of typical anatomy is required. This section presents the procedure for building a 3D finite element mesh which is capable of accurately capturing facial geometry.

## 4.3.1 Reconstruction of the facial geometry

Accurate data acquisition is an important step in this procedure. In this thesis, the facial skin and skull structures were based on the available patient specific data. The geometry of the patient specific face was re-visualised by using the cone-beam computer tomography (CBCT) scanning. The scanned images in the DCM format were manipulated, and triangulated surfaces in an STL format were obtained for the reconstruction of the facial geometry. In this project, the scanning and image manipulation were done by the technical staff in the School of Dentistry, Cardiff University. Finally, the patient specific STL files of the facial skin and skull were provided. The muscles were obtained from a standardised forensic database (Wilkinson, Rynn, et al. 2006) with each muscle being simulated separately and stored as an STL file, which contains the original geometric data. The STL files for the muscles used in the thesis were provided by Caroline Wilkinson at the School of Life Sciences, University of Dundee.

The second step in this procedure is to reconstruct the geometric surfaces from the patient STL files. The resulting triangulated mesh surface data, which is stored as STL files, can be quite coarse due to holes, noise points, sharp edges, etc. If finite element models were constructed using these raw data, meshes with sharp angles are likely to induce inaccuracies in the resulting analysis. Therefore, the triangulated mesh of an STL model needs to be converted into a parametric surface so that the geometrical parameters of the 3D objects' outer surfaces can be controlled. This work is difficult to implement in common computer-aided design (CAD) software, even in the powerful CAD packages such as UG and Pro/Engineer. However, the reverse engineering software, RapidForm, provides the ability to solve this problem.

Reverse engineering is a modelling process which translates original data to a concise geometric model which is exportable to CAD/CAM/FE packages. RapidForm is a software based solution system that allows users to go from 3D scan data to a fully parametric CAD model. It possesses automated methods for creating optimised polygon mesh models and

also has functions to remove disparate geometries such as holes and noise points.

Therefore, in this thesis, RapidForm (INUS Technology Inc. & Rapidform Inc. 2006) was used to process the raw data. The dense point clouds were cleaned, holes were filled-in and sharp edges were smoothed using standardised algorithms. Non-Uniform Rational Basis Spline (NURBS) surface were employed to mathematically represent the exterior anatomical structures. Three examples are given to show the differences before and after the process. Figures 4.14 (a), (c) and (e) show the raw triangulated mesh models which are stored in the format of STL files. Figures 4.14 (b), (d) and (f) show the corresponding NURBS surface models after the smoothing process was applied.

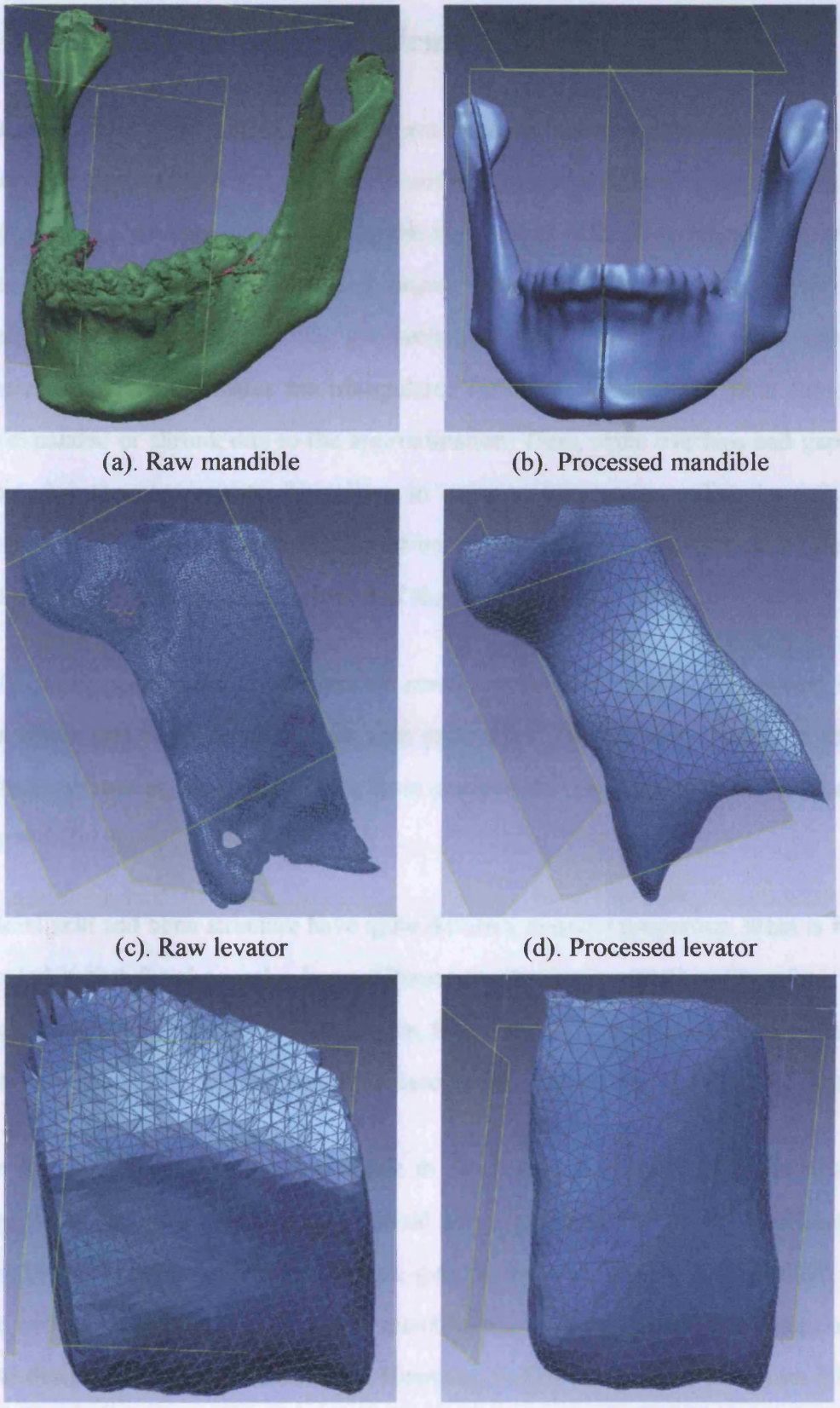

(a). Raw mandible (b). Processed mandible

(c). Raw levator (d). Processed levator

(e). Raw mentalis (f). Processed mentalis

**Figure 4.14** Data process. Left: triangulated mesh models; Right: NURBS surface models

## 4.3.2 Creation of the 3D finite element facial model

Constructing a three-dimensional finite element model of the human face is a complicated task. First of all, human face is a complex structure. Even in a simplified form, human face has approximate 27 components, including the skull, facial skin, 20 facial muscles, etc. For the finite element computation, these components should be correctly connected within the continuum system. However, in the geometry reconstruction process, when using the parametric surface approximates the triangulated mesh, the geometry of each component may be expanded or shrunk due to the approximation. Thus, some overlaps and gaps may occur between the components. Therefore, in order to accurately predict the soft tissue deformation, any overlapped sections should be removed and the gaps should be replaced or filled to provide an accurate description of the facial construct.

Secondly, either rigid node constraints or contact constraints should be applied to the surfaces where two components contact with each other. The difficulty here is to identify the contact surfaces or nodes and furthermore geometrical irregularity makes this process even more difficult.

Also, facial skin and bone structure have quite different material properties. What is further complicated is that facial muscles have different mechanical properties. Therefore, while building a finite element model of human face, the nodes and elements should be classified such that corresponding components can be described within elemental and nodal data sets.

Because of the difficulties mentioned above in developing a finite element facial model, choosing the appropriate software is a critical process. ABAQUS (Hibbit, Karlsson and Sorensen Inc. 2006) is a highly sophisticated, general purpose finite element analysis (FEA) package and is widely used in many research areas, such as mechanical engineering, structural design and biomedical analysis. However, in this application, it is quite difficult for ABAQUS to automatically detect the contact surfaces. MSC Corporation developed MSC/PATRAN (MSC.Software Corporation, 2008) which is the world leading

pre/post-processing software for finite element analysis and MSC/PATRAN provids solid modelling, meshing, and analysis setup for ABAQUS, LS-DYNA, ANSYS, etc. Unfortunately, MSC/PATRAN still has the problem of identifying the contact surfaces.

To overcome some of these problems, the Simpleware software package (Simpleware Ltd., 2008) +ScanCAD, ScanIP and +ScanFE and the Oasys.PRIMER (Oasys Ltd & Arup, 2009) were chosen as the pre-processing software for building the finite element facial model.

Simpleware is a well developed software solution for the conversion of 3D images into CAD/STL files, rapid prototyping applications and finite element meshes. Simpleware offers three software options for processing and meshing 3D image data: +ScanCAD, ScanIP and +ScanFE. The +ScanCAD module is mainly used for working with implants and allows importing CAD models, positioning them interactively and generating a ScanIP mask of the combined data. The ScanIP module provides an extensive selection of image processing tools to assist the user in visualizing and segmenting regions of interest from any volumetric 3D data (e.g. MRI, CT, Micro CT). Segmented images can be exported as STL files for CAD analysis or RP manufacturing. The +ScanFE module generates volume and/or surface meshes, contact surfaces and material properties from segmented data. The relationship between these modules is shown in Figure 4.15.

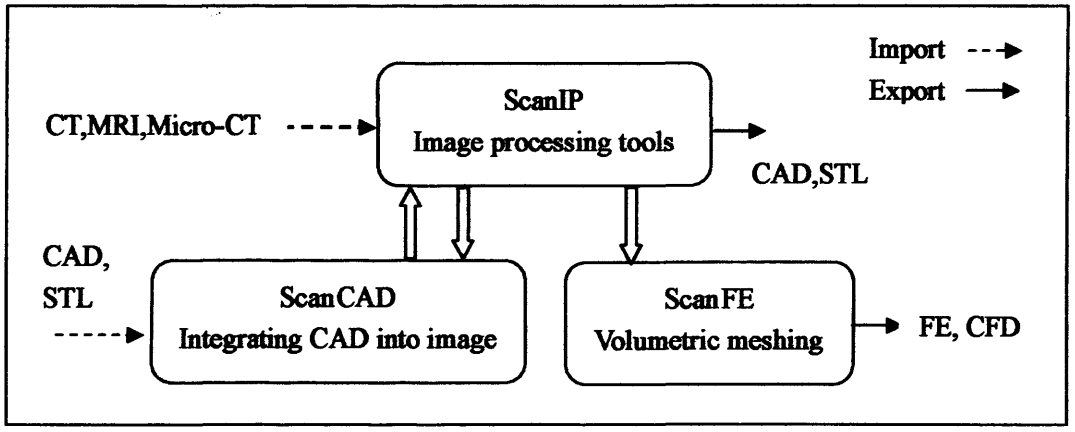


**Figure 4.15** Simpleware software products

In this thesis, 27 STL files, which are geometrical data of the 27 facial components, were imported into +ScanCAD. In +ScanCAD, 27 masks were created by using the 'CAD to Mask' method and all the muscles were placed as accurately as possible according to their anatomic positions. Then all the masks were exported into ScanIP, in which the subcutaneous tissue was created. In ScanIP, the overlapped sections were automatically identified and were fixed by using 'Boolean' operations. Finally the facial model was exported into +ScanFE for generating the volumetric meshes. An important component in the facial model is the subcutaneous tissue, which fills the gaps among the facial skin, the bones and the facial muscles. It is worthy to mention that the subcutaneous tissue is created by using ScanIP and the creation process is shown in Figures 4.16.

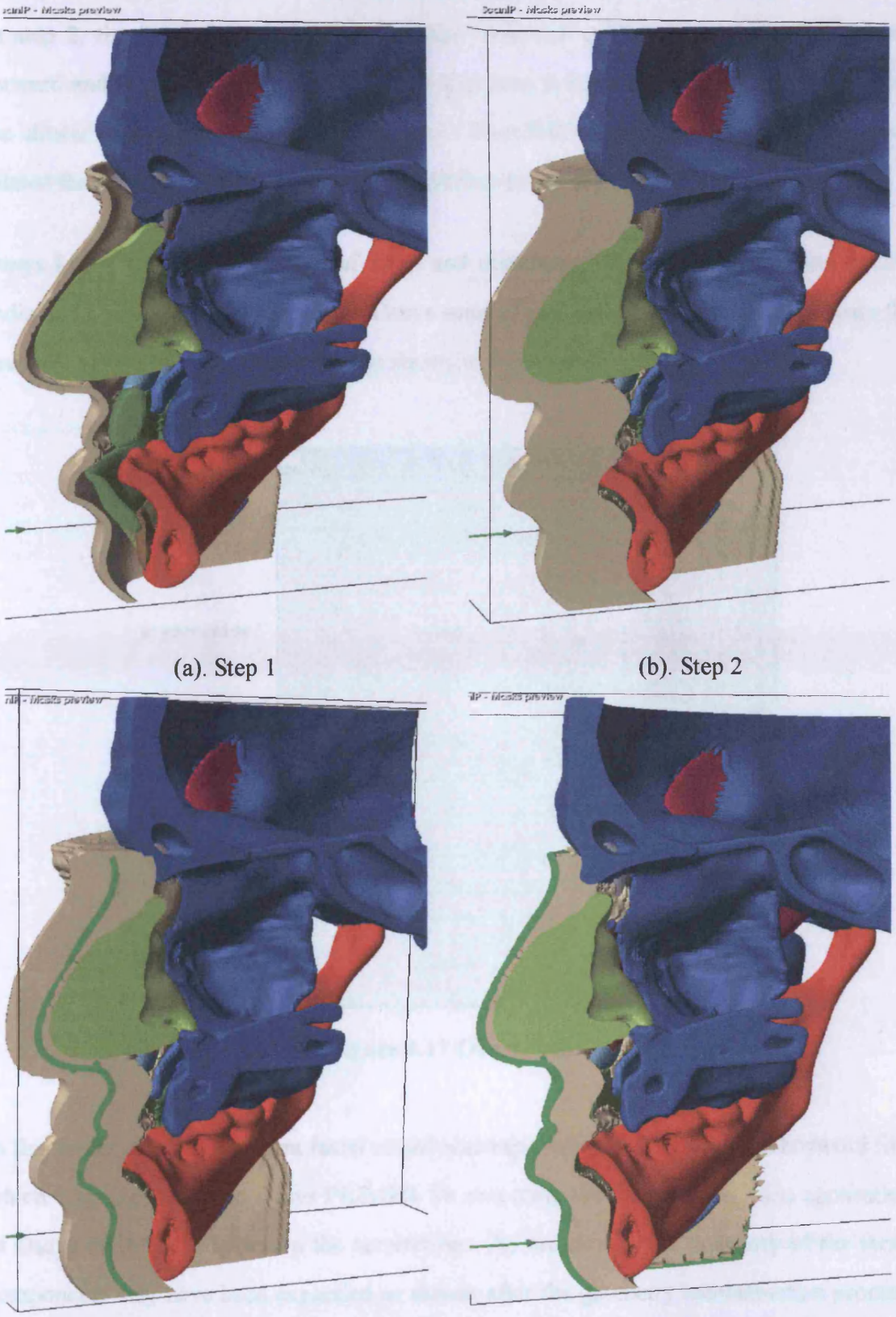

(a). Step 1 (b). Step 2

(c). Step 3 (d). Step 4

**Figure 4.16** Procedure for the creation of the subcutaneous tissue

In step 1, a duplicated face was created and the nose, eye and mouth openings were filled. In step 2, the 'Morphological filter & Dilate' tool was used to expand the face 10mm forward and backward. In step 3, Boolean operations were used to subtract the face from the dilated face. In step 4, 'Segementation', 'FloodFill' tools were used with the inner dilated face retained and the rest of the dilated face being deleted.

Oasys Ltd is the software house of Arup and distributor of LS-DYNA software in UK, India and China. Arup developed the Oasys suite of pre- and post- processing software for use with LS-DYNA. The Oasys shell is shown in Figure 4.17.

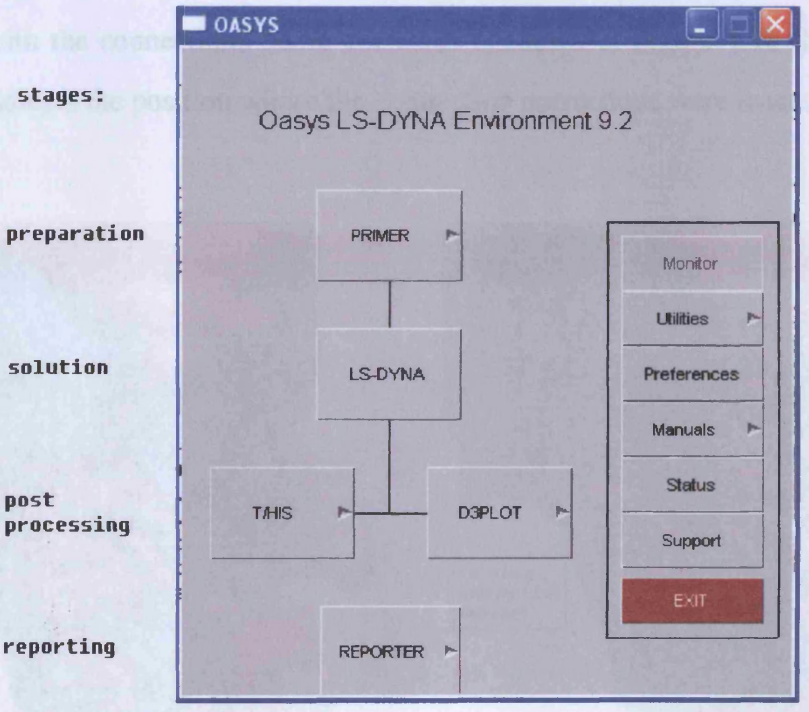


**Figure 4.17** Oasys shell

In this thesis, the finite element facial model was exported from $^{+}$ScanFE as a keyword file, which was later read into Oasys PRIMER for preparing the facial model. One application of Oasys PRIMER is to set up the connections. As mentioned, the geometry of the facial components may have been expanded or shrunk after the geometry reconstruction process. The geometrical expansion is likely to induce wrong connections which are automatically defined in ScanIP, and these connections are redundant. The geometrical shrinkage is likely

to induce the missing of some connections. For example, the top left corner of the masseter muscle should connect with the maxilla from the anatomy point of view. However, in the reconstructed model, there is a gap between them, as indicated in Figure 4.18 (a). In order to define this missing connection, prescribed nodes from the maxilla were connected with prescribed nodes from the masseter, as shown in Figure 4.18 (b). Through studying the facial anatomy and using expertise within the Department of Anatomy at Cardiff University, the redundant connections generated in the facial model were detected and detached using the 'clipboard' tool in Oasys PRIMER; the missing connections were detected and defined by using the 'node_rigid_body' keyword for defining attachments between two deformable bodies and using the 'extra_nodes' keyword for defining attachments to the rigid body. The facial model with the connections being corrected is shown in Figure 4.18 (b), where the dense points indicate the position where the connection corrections were made.

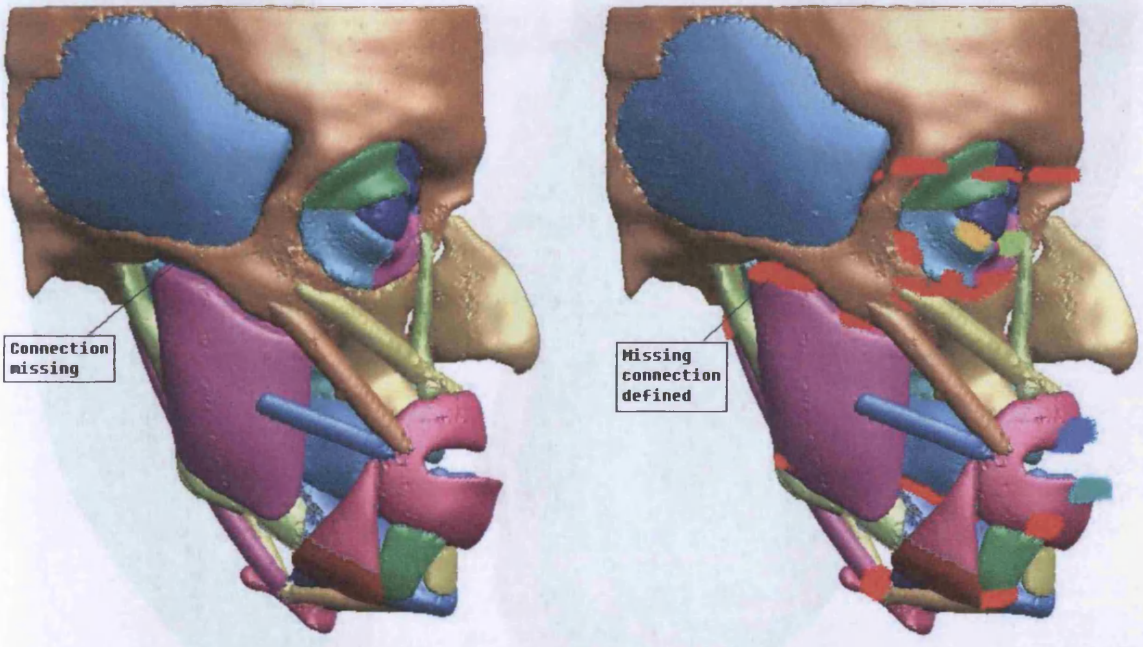


(a) Model from +ScanFE (b) Model with the connections corrected

**Figure 4.18** Correcting the connections in the finite element facial model

The second application of Oasys PRIMER is to define the boundary conditions. The assumption of facial symmetry was introduced to allow the development of a half-facial

model, which reduced both the size of the finite element model and the computational time considerably. Plane symmetry was assumed in the facial structure and plane symmetrical boundary conditions were applied to the symmetry plane, as shown in Figure 4.19. Because of the symmetrical boundary conditions, the nodes located in the symmetrical plane are fixed and cannot move left or right. However, for the cases when the loading and constraint conditions are not symmetrical to the middle plane, the symmetrical boundary condition should be removed and the half model should be mirrored to build the whole facial model. In the following two applications, the loading and constraint conditions are both symmetrical to the symmetrical plane. So using a half-facial model is appropriate in this case.

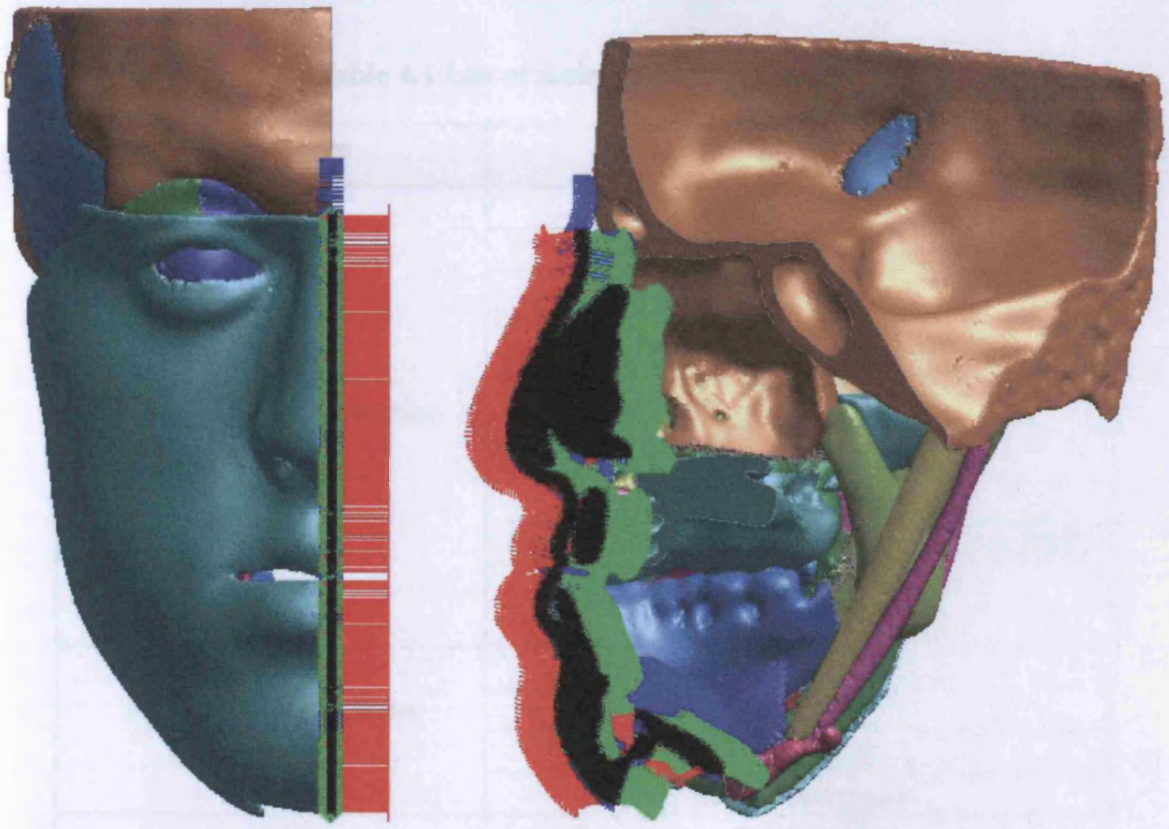

(a) front view (b) Side view

**Figure 4.19** Symmetry boundary conditions in the finite element facial model

Other applications of Oasys PRIMER include defining the temporomandibular joint, and

assigning the material properties. In the facial model developed in this thesis, the revolute joint is used to simulate the human temporomandibular joint (TMJ). A revolute joint (also called hinge joint) is a one degree of freedom kinematic pair used in mechanisms. Revolute joints provide single-axis rotation function used in many places such as door hinges, folding mechanisms, etc. In this thesis, the revolute joint is used to define the TMJ, where the maxilla stands still and the mandible rotates along a horizontal axis which is located at the maxilla-mandible connection. The material properties for the individual component are detailed in the following section.

### 4.3.3 Description of the 3D finite element facial model

In the finite element facial model, 20 muscles are simulated as listed in Table 4.1.

**Table 4.1** List of facial muscles modelled

| Muscle type | Muscles |
|---|---|
| Muscle of facial expression | Buccinator |
| | Zygomaticus major |
| | Zygomaticus minor |
| | Risorius |
| | Depressor anguli oris |
| | Orbicularis oculi |
| | Orbicularis oris |
| | Mentalis |
| | Levator labii superioris alaeque nasi (LLSAN) |
| | Depressor labii inferioris |
| | Levator labii superioris |
| Muscles of mastication | Temporalis |
| | Masseter |
| | Lateral pterygoid |
| | Medial pterygoid |
| Hyoid muscles | Stylohyoid |
| | Posterior digastric |
| | Mylohyoid |
| | Anterior digastric |
| | Geniohyoid |

The 20 facial muscles are illustrated in Figure 4.20.

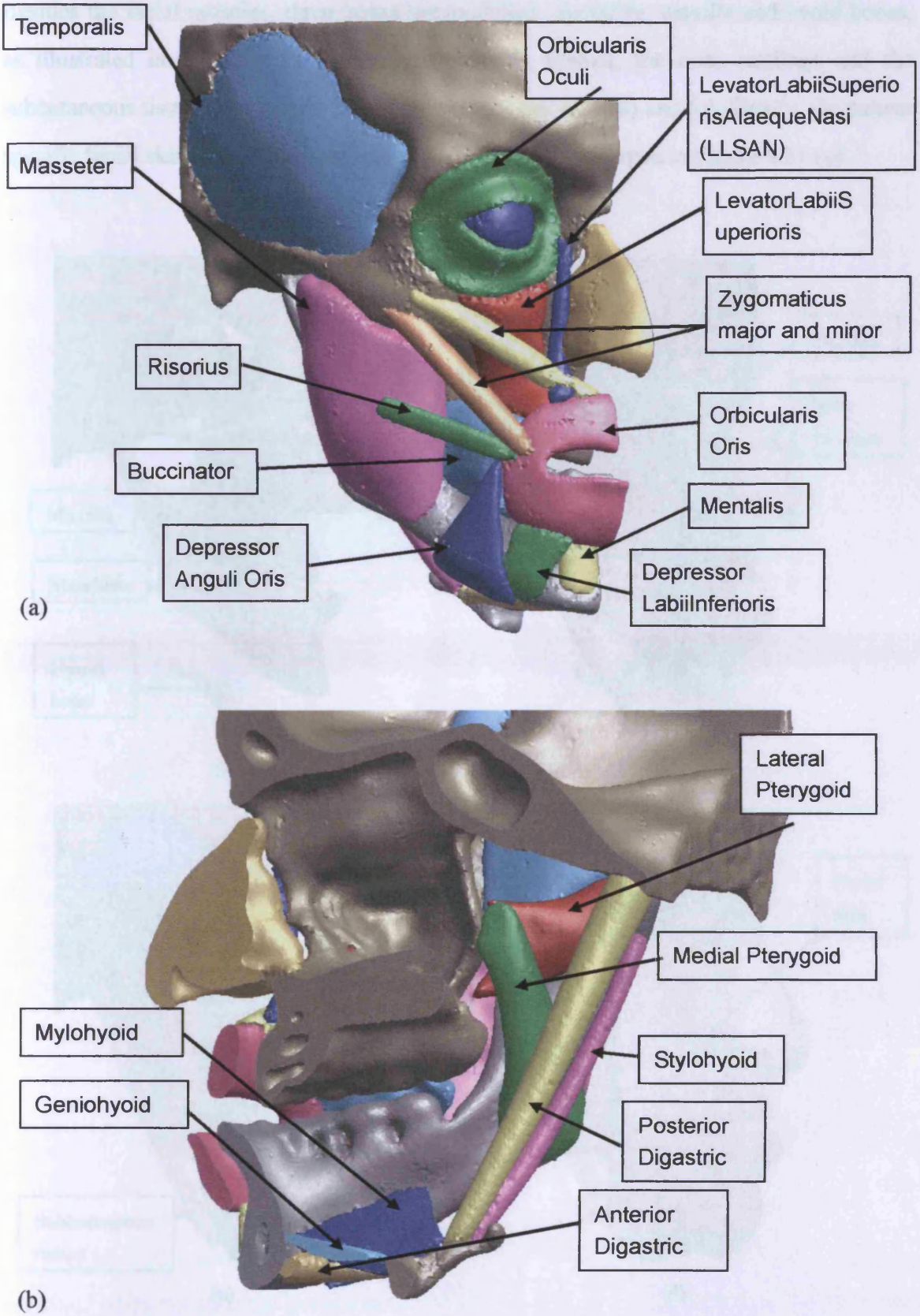


**Figure 4.20** Finite element facial model - muscle illustration: Top: Lateral view (external); Bottom: Lateral view (internal)

Besides the facial muscles, three bones are modelled: mandible, maxilla and hyoid bones, as illustrated in Figure 4.21 (a). In addition, the eyeball, the nose cartilage and the subcutaneous tissue are modelled, as shown in Figures 4.21 (b) and (c). Finally, the patient specific facial skin is implemented into the facial model, as shown in Figure 4.21 (d).

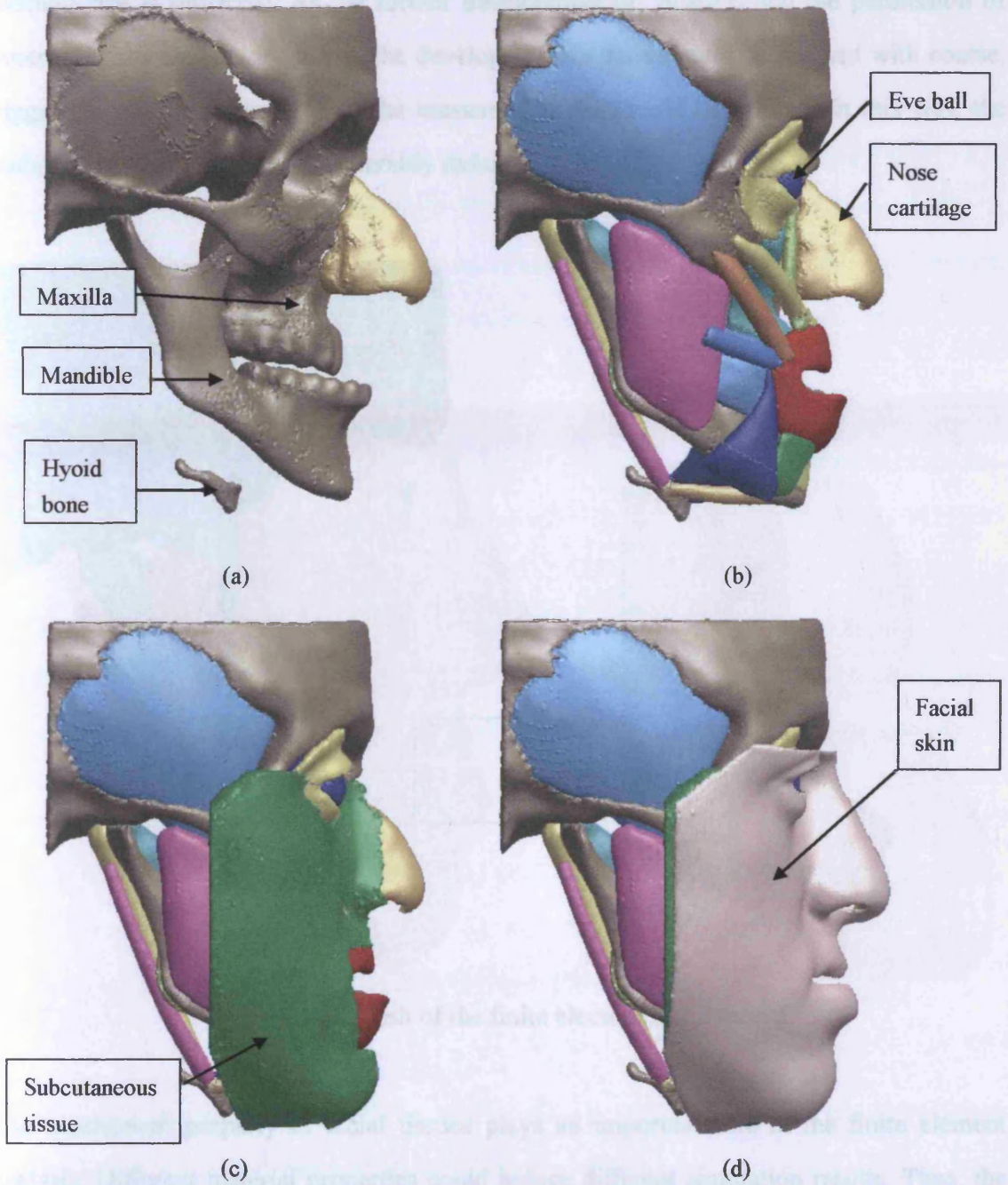


**Figure 4.21** Finite element facial model illustration

The 3D finite element model of the half face is meshed with approximately 2 million tetrahedral solid elements and the element size is approximately 1 mm, as shown in Figure 4.22, where the left figure shows the whole facial mesh and the right figure shows the enlarged mesh around the mouth. It should be noted that the finite element mesh was generated in $^{+}$ScanFE and in the current version of $^{+}$ScanFE (version 3.1), the control of the element size is restricted. As the further development of $^{+}$ScanFE and the permission of controlling the element is gained, the developed facial face should be meshed with coarse, bigger elements and the mesh in the concerned zones should be refined. In this way, the computational time will be considerably reduced.

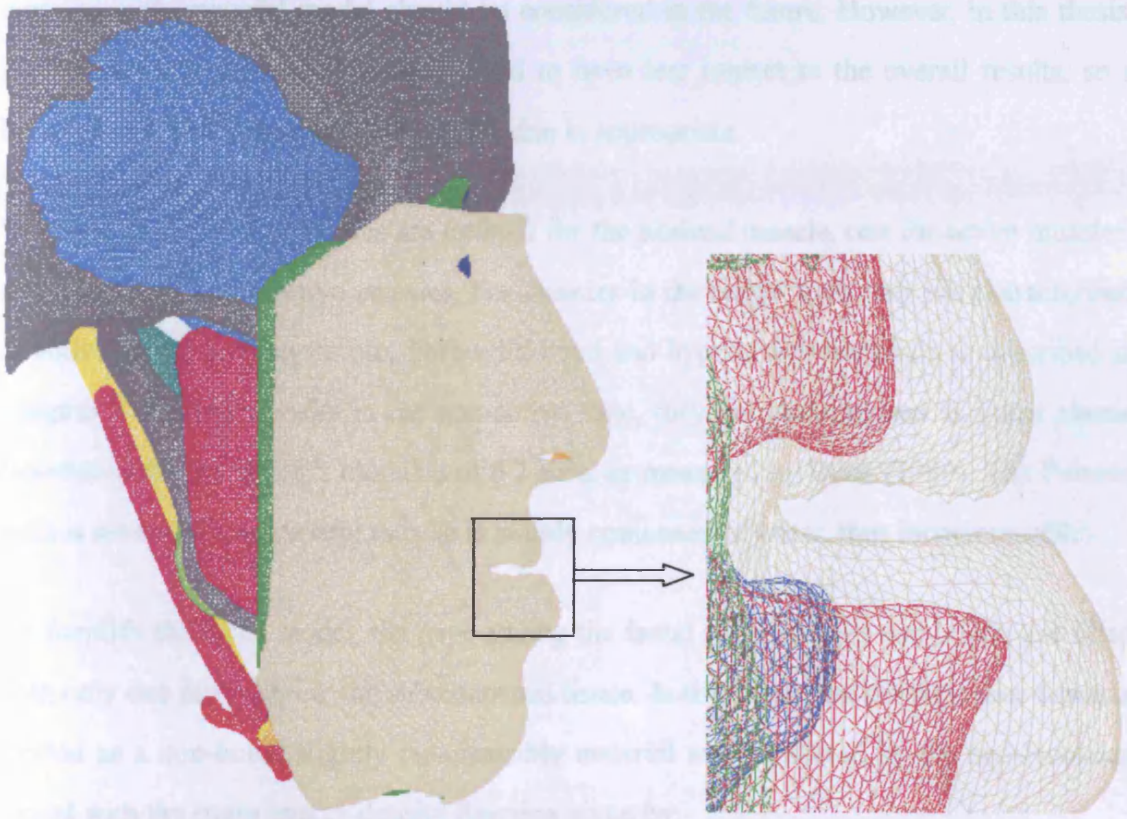

**Figure 4.22** Mesh of the finite element facial model

The mechanical property of facial tissues plays an important role in the finite element analysis. Different material properties could induce different simulation results. Thus, the most accurate choice for the soft tissue materials is critical for achieving accurate simulations. In this work, various facial tissue models have been explored. Then the

material models for different facial tissues are selected or developed on the consideration of both the model simplicity and the simulation accuracy.

The mechanical properties of facial skin are complex because of its intricate structure. Extensive experiments have shown that facial skin is an inhomogeneous, anisotropic, multi-layered and viscoelastic material (Fung, 1981; Tran, Charleux, Rachik et al., 2007). In the developed facial model, the facial skin is modelled as an isotropic linear elastic material with two independent material constants, Poisson ratio and Young's modulus. The Poisson ratio is chosen as 0.49 in order to simulate the quasi-incompressibility of the skin tissue. The Young's modulus is set to 15 KPa , according to Fung's work (Fung, 1981). A more accurate material model should be considered in the future. However, in this thesis, the influence of facial skin is considered to have less impact to the overall results, so a linear elastic approximation to the facial skin is appropriate.

Two sets of material properties are defined for the skeletal muscle, one for active muscles, and the other for non-active muscles. For muscles in the active state, they are characterised as active, quasi-incompressible, fibre-reinforced and hyperelastic materials as described in Chapter 3. For the muscles in the non-active state, they are characterised as linear elastic materials with the Young's modulus of 6.2 KPa, as measured by Duck (1990). The Poisson ratio is set to 0.49, as skeletal muscle is mainly composed of water, thus incompressible.

To simplify the facial model, the gaps among the facial skin, muscles and bones, are filled with only one material, i.e. the subcutaneous tissue. In this work, the subcutaneous tissue is treated as a non-linear slightly compressible material and simulated by the neo-Hookean model with the strain energy density function given by:

$$U = C_{10}(I_1 - 3) + 0.5K(J-1)^2 \tag{4.1}$$

where $I_1$ is the first invariant of the strain tensor, $J$ is the Jacobian of the deformation gradient, $C_{10}$ and $K$ are material parameters. The values of $C_{10}$ and $K$ are taken from Tran et.al.'s indentation tests: $C_{10}$= 0.42 KPa and $K$ = 36 KPa (Tran, Charleux, Rachik et al., 2007).

The mechanical properties of bones vary a lot, depending upon the age, anatomical location, liquid content, etc. In the model developed in this thesis, the bones are assumed to be rigid elastic material, since the main focus in this work is the deformation of the soft tissues. The material parameter values for the bones are taken from Sarkar, Majumder et al.'s (2004) work, i.e. density = 1412 $Kg/m^3$, Young's Modulus = 6.5e3 MPa and Poisson's ratio = 0.22. The nose cartilage and the eyeball were modelled as a linear elastic material with the Young's modulus of 6.1 MPa and Poisson's ratio of 0.2 (Protsenko and Wong, 2007).

Figure 4.23 shows the material models used for different facial tissues.

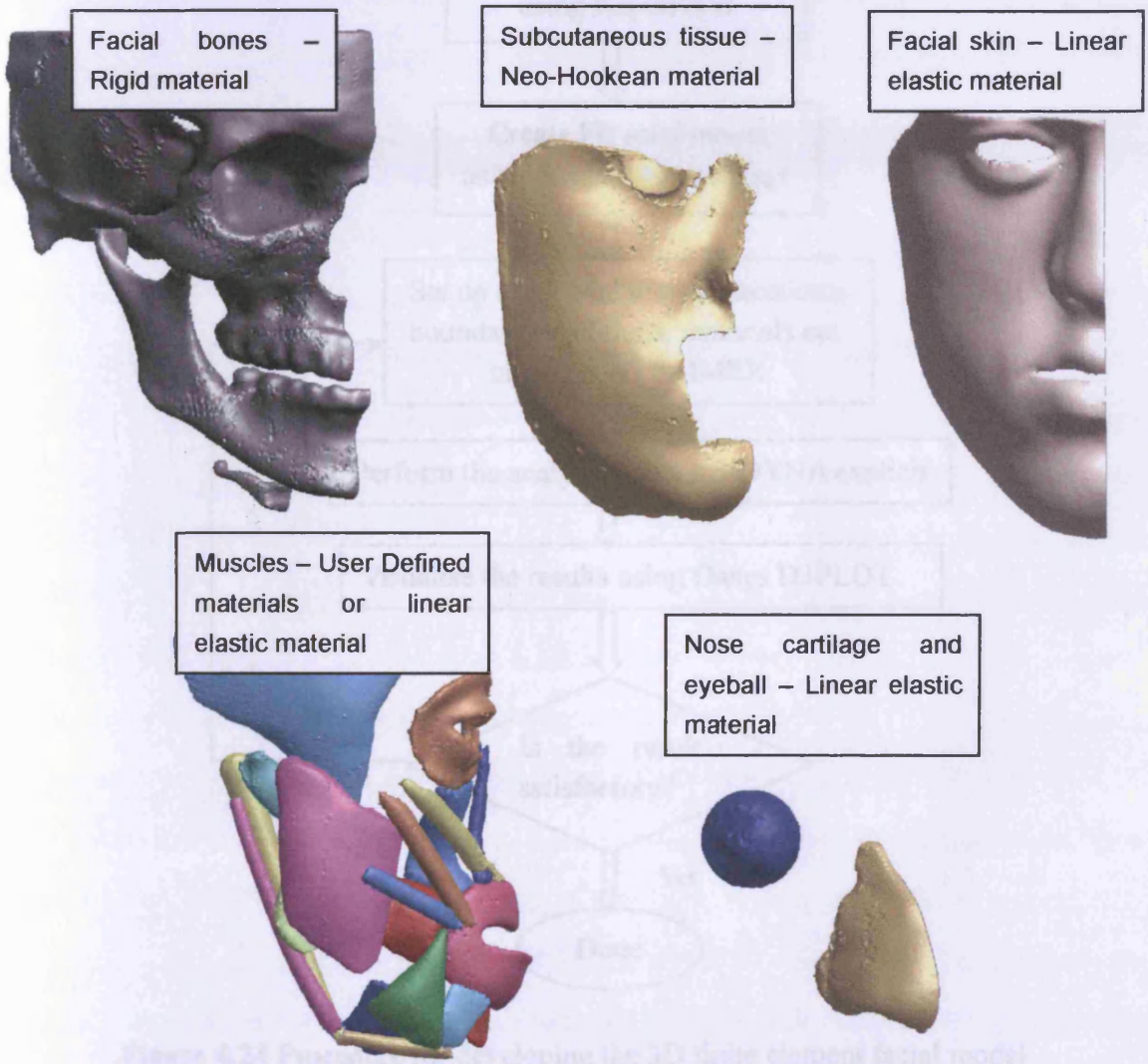


**Figure 4.23** Materials for the finite element facial components

This concludes the review of how the 3D finite element facial model was formed. The non-linear finite element analysis programme LS-DYNA is employed as the computational analysis tool and Oasys D3PLOT 9.3 is used for post-processing, i.e. the visualisation of results, animations, viewing the displacement and stress, etc. The procedure for developing the facial model is summarised in Figure 4.24.

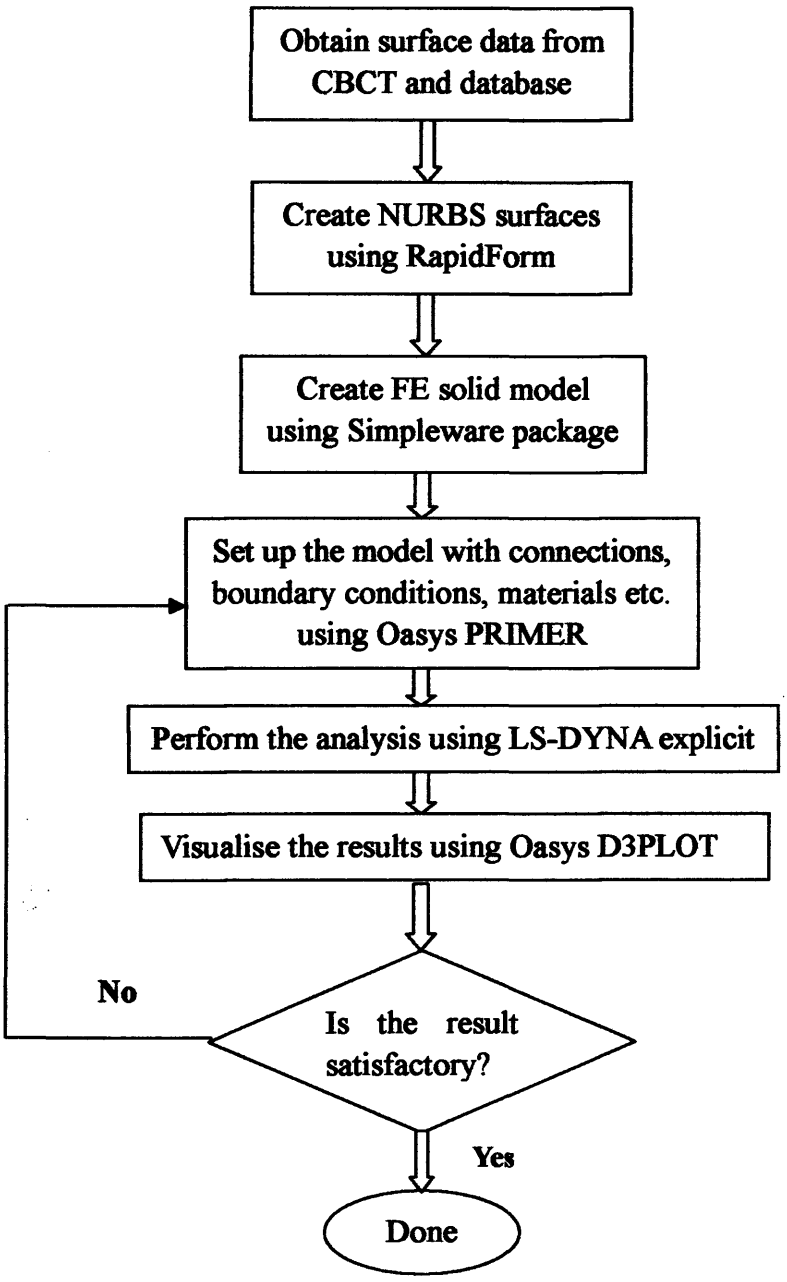


**Figure 4.24** Procedure for developing the 3D finite element facial model

# 4.4 Cranio-facial surgery simulation

One application of the facial model is the outcome prediction of facial surgery. In this section, a cranio-facial surgical procedure is simulated and the accuracy of the simulation is discussed.

## 4.4.1 A clinical case report

A male student was referred to the University Hospital of Wales with the lower jaw anterior to the upper (Class III and skeletal 3 malocclusion). The permission was obtained from this patient to use his data for research. The sequence of the surgical procedures is outlined in Figure 4.25. His 3D facial surface was captured using two Konica Minolta Vivid 910 laser cameras. The surface scan and the skeletal structures were placed in the correct spatial relationship and then aligned to the horizontal plane based on the inner canthi and mid-sagittal planes, as shown in Figure 4.25 (a). In order to determine the soft tissue discrepancies for this patient, an average facial template matched for age and sex was fitted to the individual's face. The details of the discrepancies were quantified using a colour deviation map, as shown in Figure 4.25 (b), which clearly highlighted a mid-face insufficiency and that the lower lip was prominent. The 'cut-away' approach was used whereby the half facial shell was removed to reveal the underlying skeletal structure, as shown in Figure 4.25 (c). As the individual's face was long by 4mm, a bi-maxillary surgical procedure was planned. The maxilla and mandible were removed from the computerised model just leaving the cranial base, as shown in Figure 4.25 (d). A Le fort 1 procedure was proposed to move the maxilla upward 4mm and forward by 5mm, as shown in Figure 4.25 (e). The upper and lower dental casts were scanned in a best-fit occlusion and then superimposed on the maxillary dentition, as shown in Figure 4.25 (f). A sagittal split procedure was performed, the anterior part of the mandible was aligned and fitted to the mandibular dental cast and the posterior fragment left in its original position, as shown in Figure 4.25 (g). Finally, the individual's surface laser scan was repeated post-operatively, aligned and fitted to the original facial surface, as shown in Figure 4.25 (h).

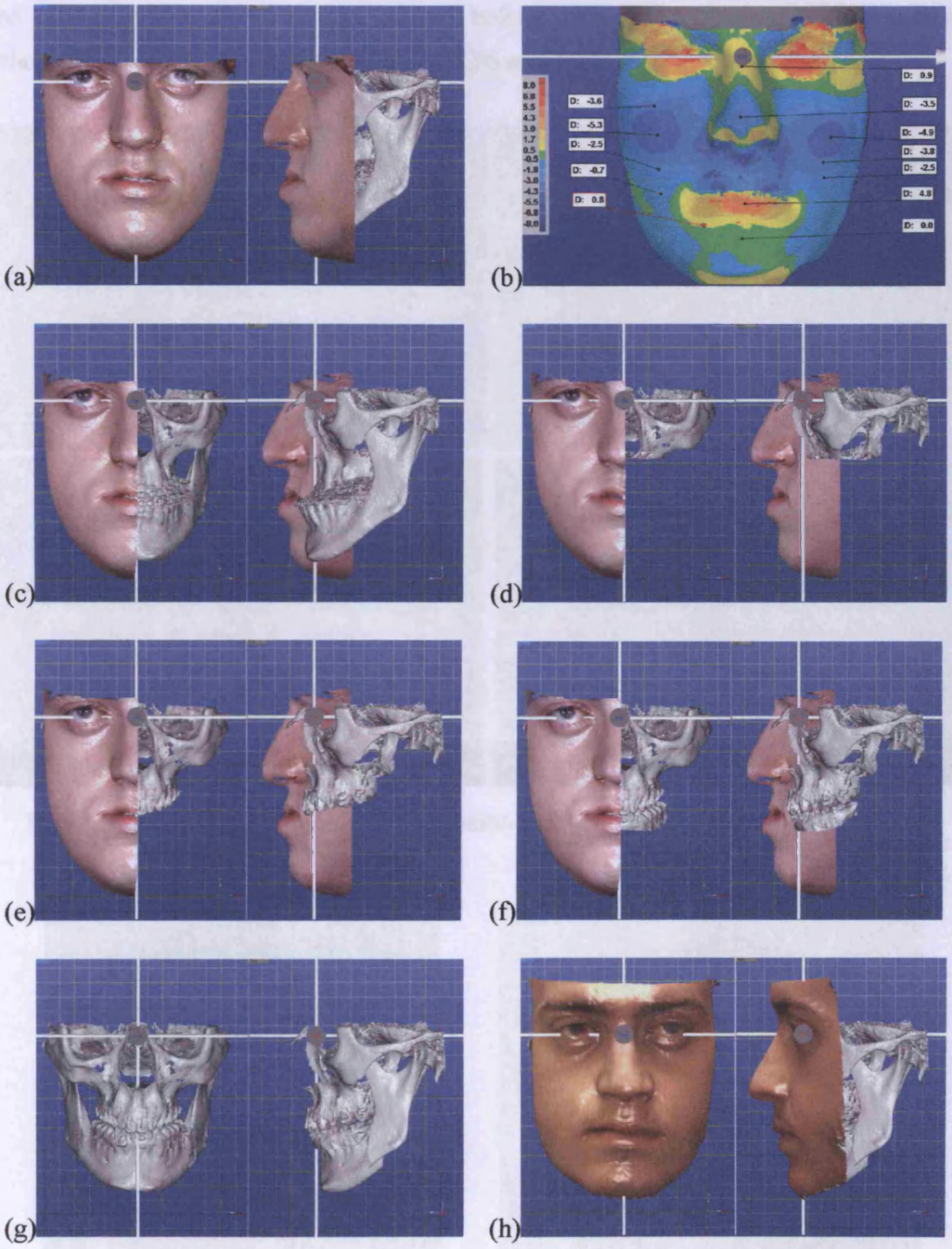


**Figure 4.25** Procedure of the cranio-facial surgery (Richmond, Beldie, Lu et al., 2010)

The clinical photographs of the patient before and after orthodontic alignment and orthognathic surgery are shown in Figures 4.26 and 4.27.

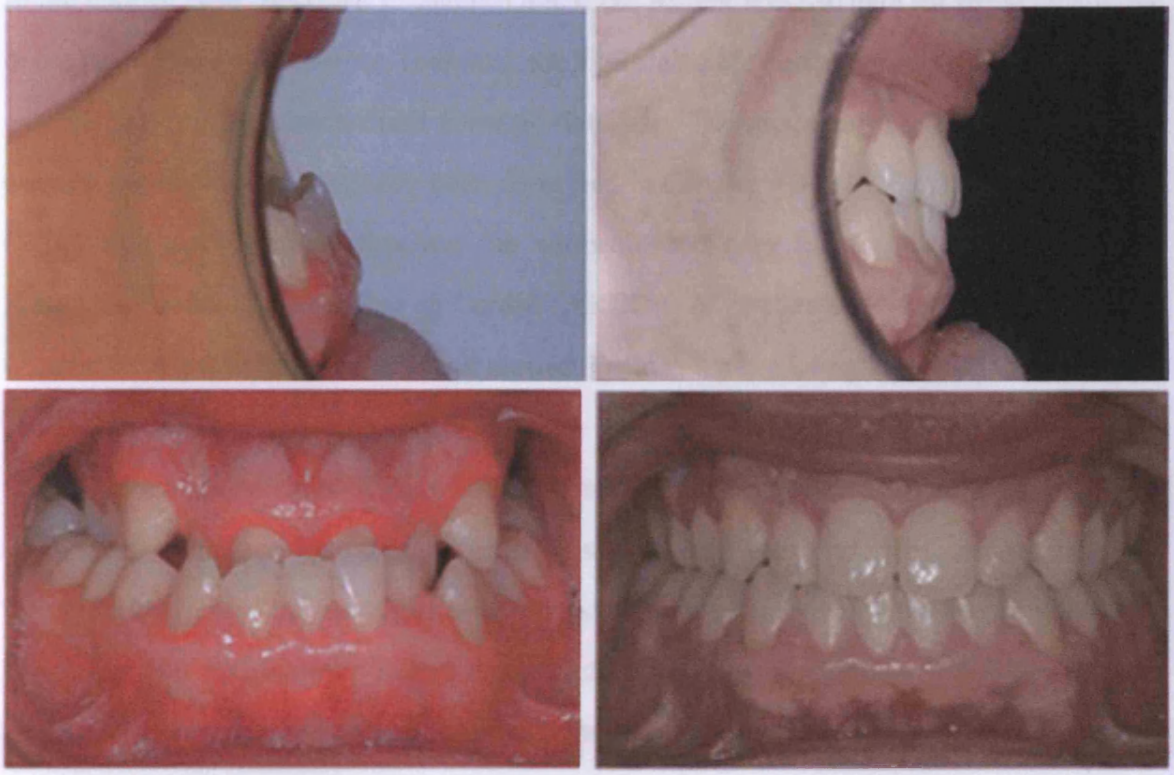

**Figure 4.26** Changes of the dental occlusion before (left) and after (right) operation

**Figure 4.27** Changes of the patient appearance before (left) and after (right) operation

## 4.4.2 Finite element simulation results

In the clinical case described in Section 4.4.1, the patient specific data for the skull and the outer facial shell was used to construct the finite element facial model, while the muscle data came from the standardised forensic database. The procedure for building the finite element facial model has already been described in Chapter 4.3. The finite element analysis (FEA) was performed to simulate the surgical procedure listed in Figure 4.24 in the Advanced Research Computing @ Cardiff (ARCCA) High-Performance Computing (HPC) Cluster - Merlin. The simulation took around 3 minutes when using 8 processors.

In the finite element simulation, a Le Fort 1 was performed with the maxilla being moved upwards by 4mm and forwards by 5mm. A sagittal split was performed on the mandible. The anterior part of the mandible was moved to create the best fit (occlusal fit) with the upper jaw and the posterior fragment was left in its original position. The finite element simulation is outlined in Figure 4.28, where the left column shows the facial features before the surgery, the middle column shows the facial features in the middle of the simulation and the right column shows the facial features after the surgery.

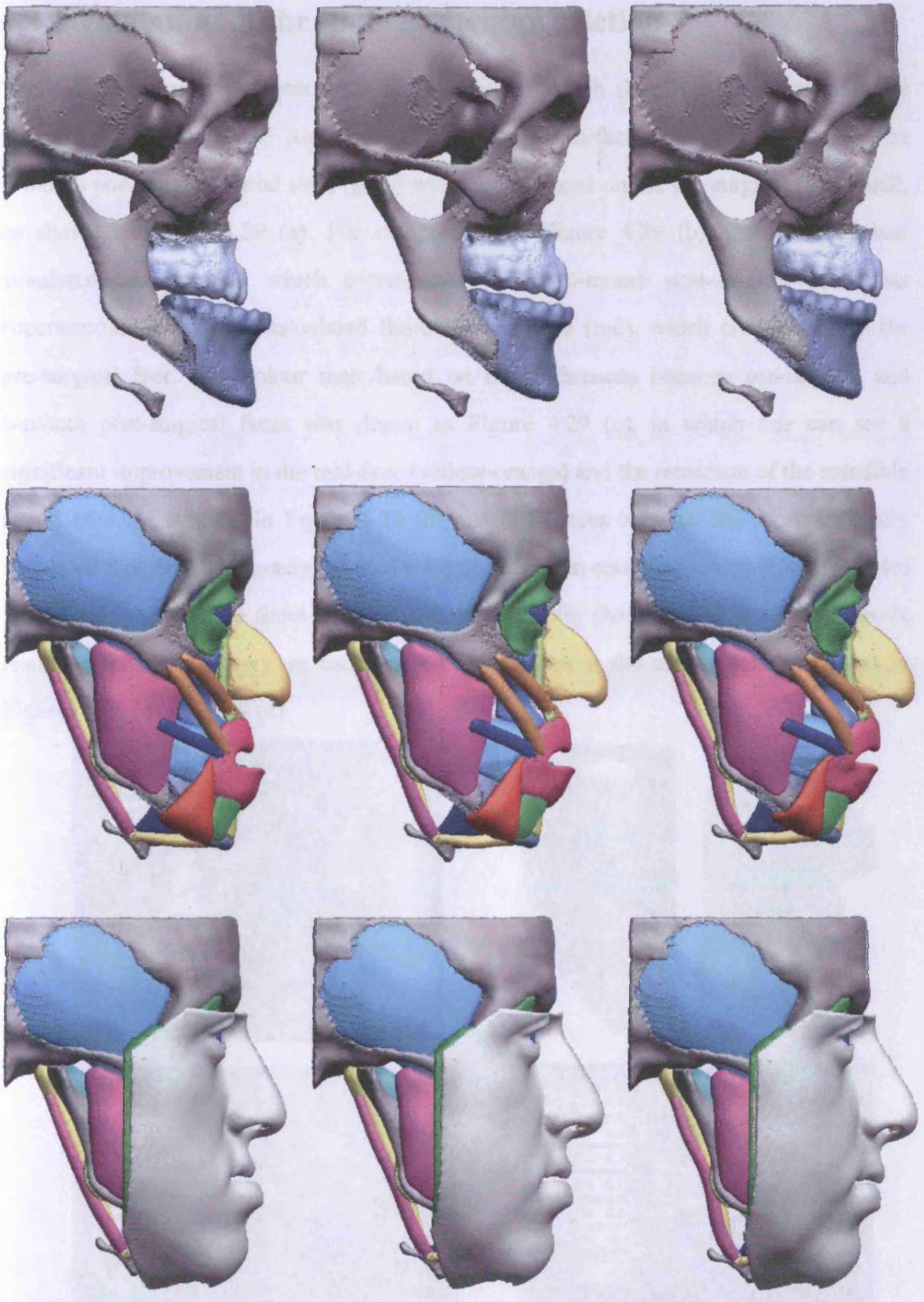

**Figure 4.28** Finite element simulation of the cranio-facial surgery

### 4.4.3 Validation of the finite element prediction

The patient returned 6-month after the surgery, at which time the facial swelling has reduced (Kau, Cronin and Richmond, 2007) and the surface scans were repeated. The 6-month post-surgical facial shell (gray) was superimposed on the pre-surgical facial shell, as shown in Figure 4.29 (a). For comparison, in Figure 4.29 (b), the finite element simulated face (green), which corresponds to the 6-month post-surgical face, was superimposed on the pre-calculated finite element face (red), which corresponds to the pre-surgical face. The colour map based on the differences between pre-surgical and 6-month post-surgical faces was drawn in Figure 4.29 (c), in which one can see a significant improvement in the mid-face (yellow-orange) and the retraction of the mandible (blue) after the surgery. In Figure 4.29 (d), the differences between the computationally simulated face and the pre-surgical face were quantified in comparison with Figure 4.29 (c). The clinic data and the finite element simulated results show similar facial movements resulting from the surgery, as can be seen by comparing the colour deviation maps in Figures 4.29 (c) and 4.29 (d).

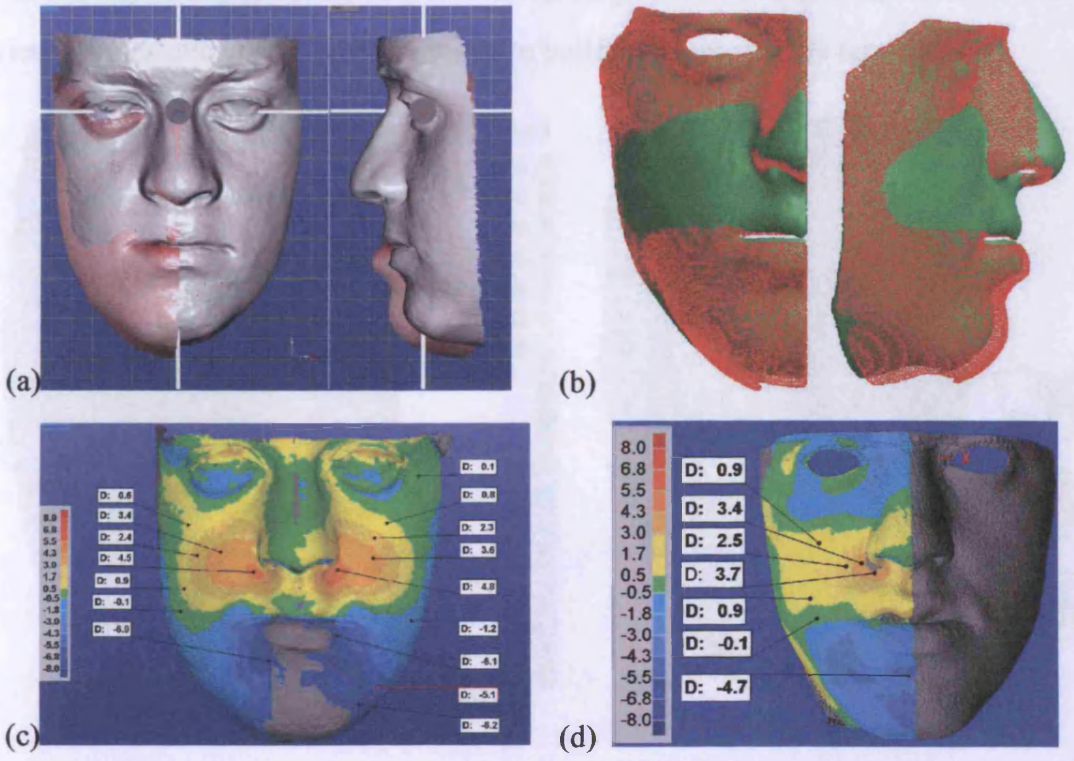


**Figure 4.29** Superimposition of the pre-surgical and 6-month post-surgical faces. Left: clinic data, Right: finite element results

The finite element simulated face after the cranio-facial surgery was also superimposed on the patient's face at 6-month post-surgery using Geomagic Qualify 10 (Raindrop Geomagic, Inc., 2008), as shown in Figure 4.30 (a). The differences are highlighted using a colour deviation map, as shown in Figure 4.30 (b), where the green represents a tolerance level of ± 2.0 mm, which is the acceptable mean surface error (Kaipatur and Flores-Mir 2009), the yellow area (the bridge of the nose and the lower lip) represents the prominence of the simulated face and the blue area (the chin) represents the less prominence of the simulated face. The superimposition shows that the finite element prediction of the face after surgery is in good agreement with the patient's surgical outcome, with an overall agreement of 85% while the error was generally contained within a ± 2.0 mm threshold. That means 85% of the points from the finite element prediction model are within the tolerance of ± 2.0 mm with the patient's 6-month surgical outcome. The areas which show less accuracy are the lower lip and a localised area of the lower cheek. The results are promising, especially showing that the use of generic facial muscles does not compromise the predicted results. However, more development work is needed before the proposed method can be used as a tool in the day-to-day planning of cranio-facial surgery. For example, the need of a more efficient segmentation technique is required to build a patient specific facial model.

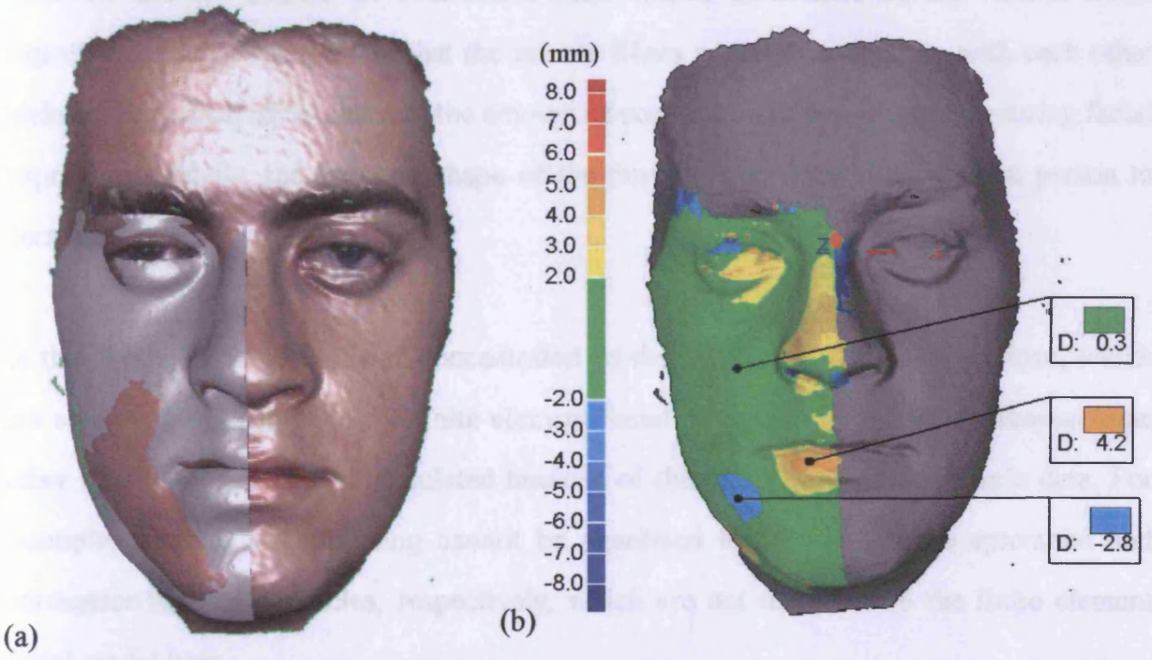


**Figure 4.30** Superimposition of facial finite element simulation with patient data at 6-month post-surgery

# 4.5 Facial movement simulation

The other application of the facial model is the simulation of facial movement. Two facial expressions (smile and disgust) and mouth opening process are simulated. The simulations were performed with 8 processors in the ARCCA HPC cluster - Merlin. The simulation times for each analysis are listed in Table 4.2

**Table 4.2** Simulation times for each analysis

| **Simulation type** | Pre-surgery smile | Pre-surgery disgust | Post-surgery Smile | Post-surgery disgust | Mouth opening |
|---|---|---|---|---|---|
| **Simulation time** | 5 hours 38 minutes | 5 hours 48 minutes | 3 hours 43 minutes | 3 hours 52 minutes | 3 hours 50 minutes |

## 4.5.1 Facial expression simulation

Simulating facial expressions is challenging, since there is little knowledge of the muscles involved and the amount of contraction each muscle undertakes during various facial expressions. Secondly, the fact that the muscle fibres generally intertwine with each other makes it very difficult to measure the amount of contraction of active muscles during facial expression. Finally, the size and shape of the muscles may vary slightly from person to person.

In this thesis, research has been concentrated on the simulation of two expressions, which are smile and disgust. With the finite element facial model developed in this thesis, some other expressions cannot be simulated because of the shortage of facial muscle data. For example, surprise and frowning cannot be simulated since they require epicranial and corrugator supercilii muscles, respectively, which are not modelled in the finite element facial model here.

The developed constitutive muscle model, described in Chapter 3, is applied to the half facial model to simulate the facial expressions. During the simulation of facial expressions, the active muscles are assigned with the developed muscle material model and the activation function used for the simulation of facial expressions is defined as follows: the activation levels before and after the stimulation are set to zero to simulate the rest state of facial muscle; the activation level during the stimulation is set to one to simulate the fully contracted state of facial muscle; the activation is set to start from time zero and the deactivation time is set to infinity so that the simulated facial expression is maintained. Please refer to Chapter 3.3.2 for the detail of the activation function applied.

According to Fehrenbach and Herring's (2006) work, for the expression of smile, the muscles activated are the Zygomaticus Major, the Risorius and the Orbicularis Oculi muscles; and for the expression of disgust, the muscles activated are the Levator Labii Superioris Alaeque Nasi, the Orbicularis Oculi and the Depressor Anguli Oris muscles.

The smile and disgust expressions were first simulated in the pre-surgical facial model, as shown in Figure 4.31.

**Figure 4.31** Facial expressions in the pre-surgical facial model - smile (first row) and disgust (second row). Left: at simulation time zero; Middle: in the middle of the simulation; Right: at the end of the simulation

The smile and disgust expressions were then simulated in the post-surgical facial model, as shown in Figure 4.32. The simulations of facial expressions in the post-surgical facial model can be used as an additional virtual tool to give more information about the outcome of the surgery, to assist the clinician to study various surgery plans, and to help the patient understand the suggested outcomes.

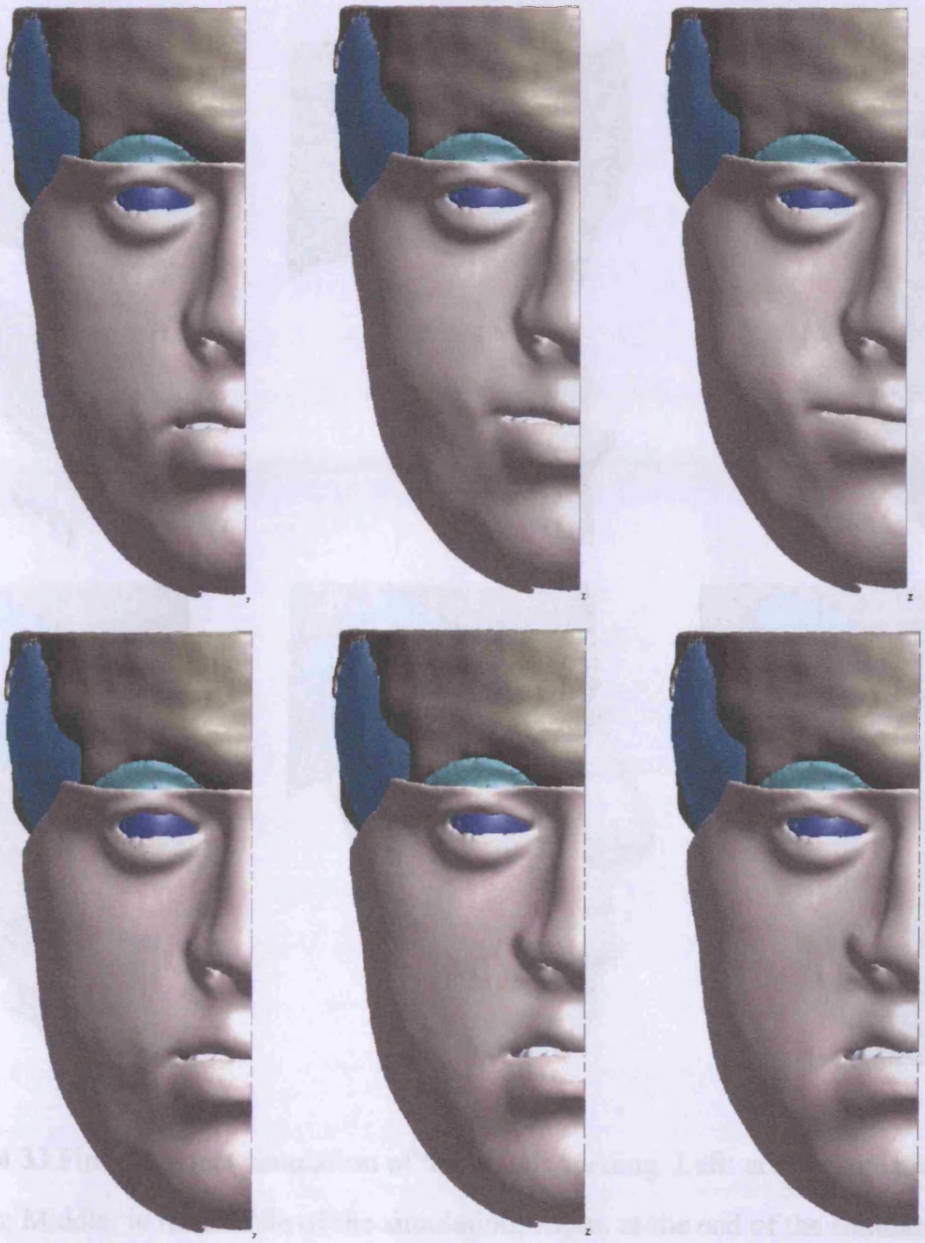

**Figure 4.32** Facial expressions in the post-surgical facial model - smile (first row) and disgust (second row). Left: at simulation time zero; Middle: in the middle of the simulation; Right: at the end of the simulation

## 4.5.2 Mouth opening simulation

A simulation of the mouth opening process was performed in the pre-surgical facial model by activating Anterior Digastric and Mylohyoid muscles. The results are shown in Figure 4.33. The work is still at its early stages and development. The ultimate goal of this is to simulate the facial movement during speech.

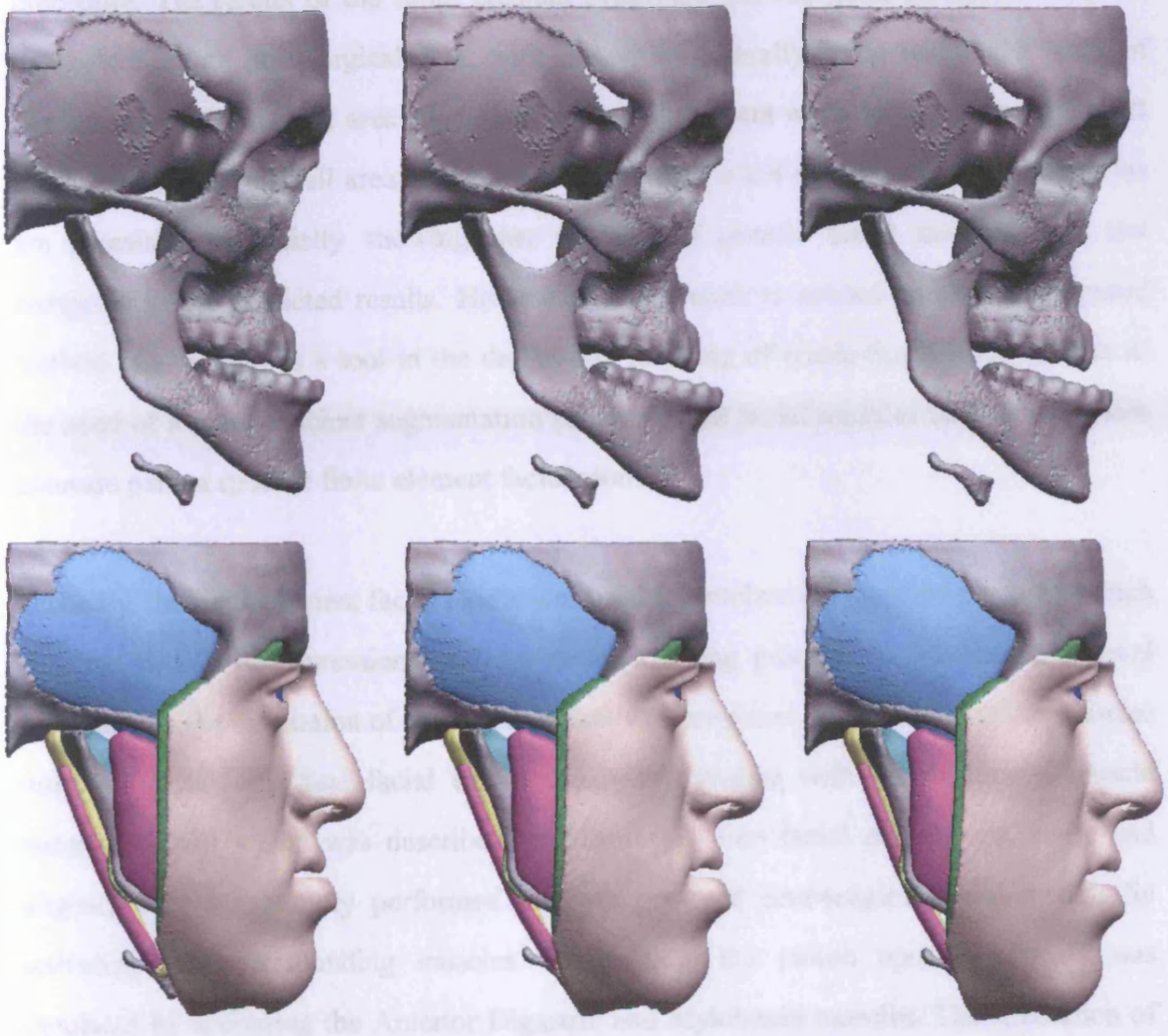

**Figure 4.33** Finite element simulation of the mouth opening. Left: at the simulation time zero; Middle: in the middle of the simulation; Right: at the end of the simulation

## 4.6 Discussion and conclusion

In this chapter, a finite element facial model was created based on the patient specific facial skin, skull data and the generic muscles. The Simpleware package and Oasys PRIMER were employed in the procedure of developing the finite element facial model. The developed finite element facial model was firstly used to simulate a cranio-facial surgical procedure. The results of the finite element prediction showed good agreement with the patient's 6-month post-surgical data, with the errors generally being within the range of -2.0 mm to +2.0 mm. The areas that showed least agreement were the lower lip with a 4.2 mm variation and a small area of the lower cheek with a 2.8 mm deviation. These results are promising, especially showing that the use of generic facial muscles does not compromise the predicted results. However, further work is needed before the proposed method can be used as a tool in the day-to-day planning of cranio-facial surgery, such as the need of a more efficient segmentation process of the facial muscles leading to a more accurate patient specific finite element facial model.

Secondly, the finite element facial model was used to simulate the facial movements, which includes two facial expressions and the mouth opening process. In this thesis, a novel approach for the simulation of facial movement was proposed. In this method, the muscles responsible for individual facial expression were assigned with the developed muscle material model, which was described in Chapter 3. Two facial expressions, smile and disgust, were successfully performed on both pre- and post-surgical facial models by activating the corresponding muscles. In addition, the mouth opening process was simulated by activating the Anterior Digastric and Mylohyoid muscles. The simulation of the aforementioned facial movements showed promising results of the proposed simulation method. Furthermore, the simulation of the facial expressions post-surgery can be included in the process of planning the maxillofacial surgery, as a virtual tool to help predict the outcome of facial surgery and help the surgeon exploring various different surgery scenarios. A more quantitative comparison of the simulation of the facial expressions with

the actual patient expressions would have been beneficial, however not enough data post surgery was available in order to accommodate this. Work is currently being undertaken to establish a three-dimensional database for normal facial movement and compare and contrast facial movement of patients with facial disharmony with this normative group prior to surgery and post-operatively. We hope to use this as one of the measures to quantify movement and success of surgery.

The potential for this work to provide a virtual training tool is enormous. It has been demonstrated in this chapter that the computational tool can provide detailed three-dimensional anatomy of the human face. Different surgical scenarios can be demonstrated. With the development of force-feedback haptic technology, computational models could potentially deliver the same 'hands on' feeling as the dummy simulators. However, to use the computational models for educational purposes, significant research and development are required and the researchers need to overcome the limitation of the current modelling frameworks and liaise with clinical experts to identify their needs.

In order for the models to be clinically useful, several factor need to be addressed, such as the computational speed, reliability and user friendliness of the software tools. The solution procedure of current model is too slow and sometimes unstable, which precludes real-time clinical application. The inclusion of detailed anatomical information will require more computational power and efficiency to cope with the complexity of the models. In order to overcome the speed issue, advanced numerical methods are required to handle the increased nonlinearities and computational demand. Besides, the model reliability needs to be improved by quantitatively validating the predictions against experimental data and/or clinical measurements. To data, little work has been done using such models as clinical tools. The next stage of model development should be carried out in collaboration with clinicians to assess their needs and requirements. In general, a clinical/educational tool should have the following features: a quick and easy interface with reasonable precision and accuracy; a clear display; the capacity to store, search, and quickly retrieve patient

information; and the ability to connect to an online database for cross-reference and diagnosis.

In the finite element modelling, a finer mesh typically results in a more accurate solution. However, as a mesh is made finer, the computational time increases. Therefore, a mesh convergence study should be preformed to get a mesh that satisfactorily balances accuracy and computing resources. As the version of Simpleware we used (version 3.1) does not allow the user to change the element size, the convergence study was not performed in this thesis. The newly released Simpleware (version 4.0) has enabled the user to refine the mesh. Therefore, a convergence analysis of the developed facial model is highly recommended in the future to determine a proper mesh density.

More future development work concerns (i) improvement of the accuracy of the finite element facial model by constructing the patient face using patient specific muscle data instead of generic muscle data and by modelling a variety of muscle fibre arrangements; (ii) development of better models for the facial skin instead of the linear elastic model used in this thesis. The skin shows a non-linear stress-strain relationship, behaves time-dependent, incompressible, anisotropic and inhomogeneous. Besides, the skin has a wrinkling phenomenon. Incorporating these features into the FE facial model will lead to a realistically simulated appearance of the face; (iii) quantitative validation of the simulated facial movements by comparing the results with the actual patient facial movements through collection of post-operative patient data; and (iv) using the developed finite element facial model to simulate speech and other facial actions.

# Chapter 5

# Modelling the Fibre Arrangement of Skeletal Muscle Using the FEM–NURBS Method

## 5.1 Introduction

Skeletal muscle is responsible for the movement of human body. In contrast to other biological tissues, they display the ability of active contraction and when activated, they contract along their fibre directions. In order to more precisely characterise their in vivo behaviour, it is very important to visualise their internal features such as the fibre orientation arrangements.

Skeletal muscle has a complex fibre orientation arrangement and this makes the creation of an accurate finite element (FE) muscle model a difficult task. In general, each change in the fibre orientation requires a new material to be defined in ABAQUS. As a result, it is nearly impossible to simulate the complex fibre arrangement using existing techniques. In this chapter, a FEM-NURBS method, which is the combination of the finite element method and the non-uniform rational B-spline (NURBS) solid mathematical representation, is proposed. With the introduction of this method, only one ABAQUS material per muscle is needed to be prescribed. The initial direction of the muscle fibre is specified as the tangent direction of the NURBS curve which the fibre lies on. The direction at each Gauss point is

calculated from the NURBS mathematical formulation and passed into the finite element software as the initial fibre direction. In the subsequent calculation, the fibre directions are updated using the initial fibre directions, the deformation gradients and the fibre stretches. Several numerical examples are used to demonstrate the ability of the proposed FEM-NURBS method.

## 5.2 Related work on muscle fibre representation

One way of simulating the muscle fibre arrangement is through using a series of line segments (Chao, Lynch and Vanderploeg, 1993; Delp, Loan, Hoy et al., 1990; Hoy, Zajac and Gordon, 1990; Jensen and Davy, 1975; Nedel and Thalmann, 1998). In Hoy, Zajac et al.'s (1990) approach, the musculotendon actuators (lliopsoas, hamstrings and vasti) were modelled as a single straight line from the origin to the insertion, as shown in Figure 5.1. In Nedel and Thalmann's (1998) work, the Biceps Brachii muscle was represented by two action lines running from the insertion points to the origin points (Figure 5.2). In this method, the line segments pass through the approximate centroidal path of the muscle and represent the muscle action lines. This fact makes it very challenging to define a series of line segments for muscles with complex geometries and muscles wrapping around the underlying structures. In addition, the line segment muscle representation method assumes that all fibres within a muscle have the same length and moment arm (Zajac, 1989). However, studies (Herzog and Keurs, 1988) show that the variations in fibre lengths and moment arms could greatly affect the muscle force, especially for muscles with complex geometries. Thus the line segment method cannot accurately represent in vivo muscle behaviour.

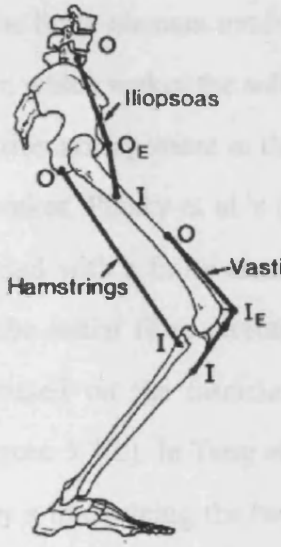


**Figure 5.1** Straight-line approximation for musculotendon actuators(Hoy, Zajac and Gordon, 1990)

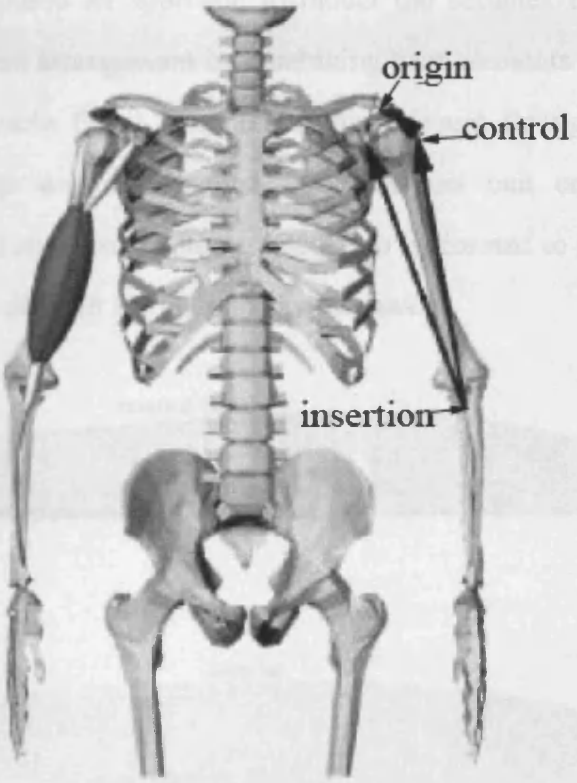


**Figure 5.2** The biceps Brachi muscle and its action line (Nedel and Thalmann, 1998)

Considerable research has been reported in the use of the finite element method for simulating the muscle behaviour (Blemker and Delp, 2005; Blemker, Pinsky and Delp,

2005; Chen and Zeltzer, 1992). The finite element model is usually created by considering the volumetric shape of the muscle, which makes the solution more accurate. However, it is difficult to define the fibre orientation arrangement in the finite element muscle model due to the complex geometries. In Blemker, Pinsky et al.'s (2005) model, the long head of the biceps muscle tissue was represented with a finite element hexahedral mesh, as shown in Figure 5.3(a). In order to define the initial fibre direction vector for each element in the mesh, a fibre map was created based on the fascicle arrangement measurements from ultrasound images, as shown in Figure 5.3(b). In Tang et al.'s (2009) FE muscle model, the fibre orientation was determined by a line joining the two central points of the two surfaces of a hexahedron (Figure 5.4). This method restricted its application to muscle models meshed only with regularly arranged hexahedrons. In the presence of a complex geometrical model meshed with tetrahedrons, this method could lose its applicability. Ből and Reese (2008) proposed an approach to model the complex muscle structures with arbitrary fibre orientation arrangement by combining truss elements with tetrahedrons. The orientations of the muscle fibres were taken into account through 3D truss elements. However, in their approach, a so-called finite element unit cell, consisting of one tetrahedral element and six truss elements, needed to be formed to mesh the object which made their model quite difficult for general applications.

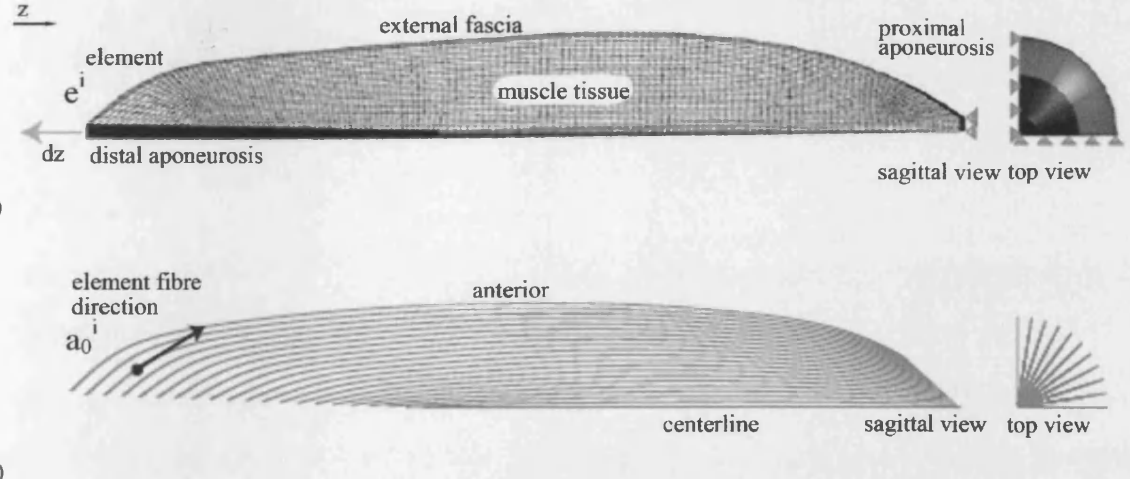


**Figure 5.3** Finite element model of biceps brachii: (A) muscle tissue mesh; (B) muscle fibre map (Blemker, Pinsky and Delp, 2005)

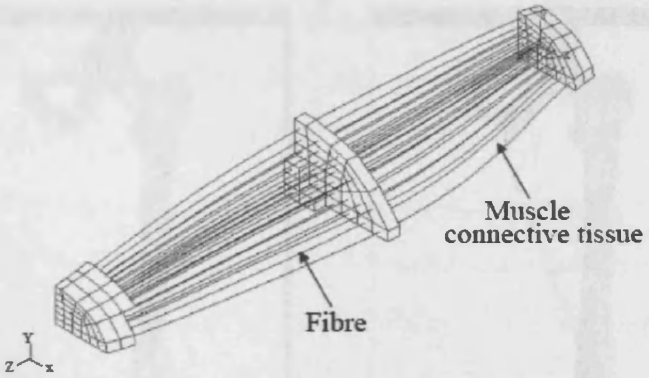


**Figure 5.4** Schematic diagram of muscle architecture (Tang, Zhang and Tsui, 2009)

It has been demonstrated that a B-spline solid model can be used to represent a large variety of muscle shapes (Ng-Thow-Hing and Fiume, 1997). The B-spline solid model allows the internal structures to be specified over the entire domain of the solid. A framework of how to create different B-spline muscle solids from the contour curves, which are extracted from medical images, has been proposed in Ng-Thow-Hing and Fiume (2002), as shown in Figure 5.5. However, a B-spline solid representation is just a geometric description and it cannot be used to capture the biomechanical behaviour of skeletal muscle. In order to do this, Teran et al. (2003) proposed a finite volume method to simulate the skeletal muscle, where the B-spline solids were used to model the fibre directions.

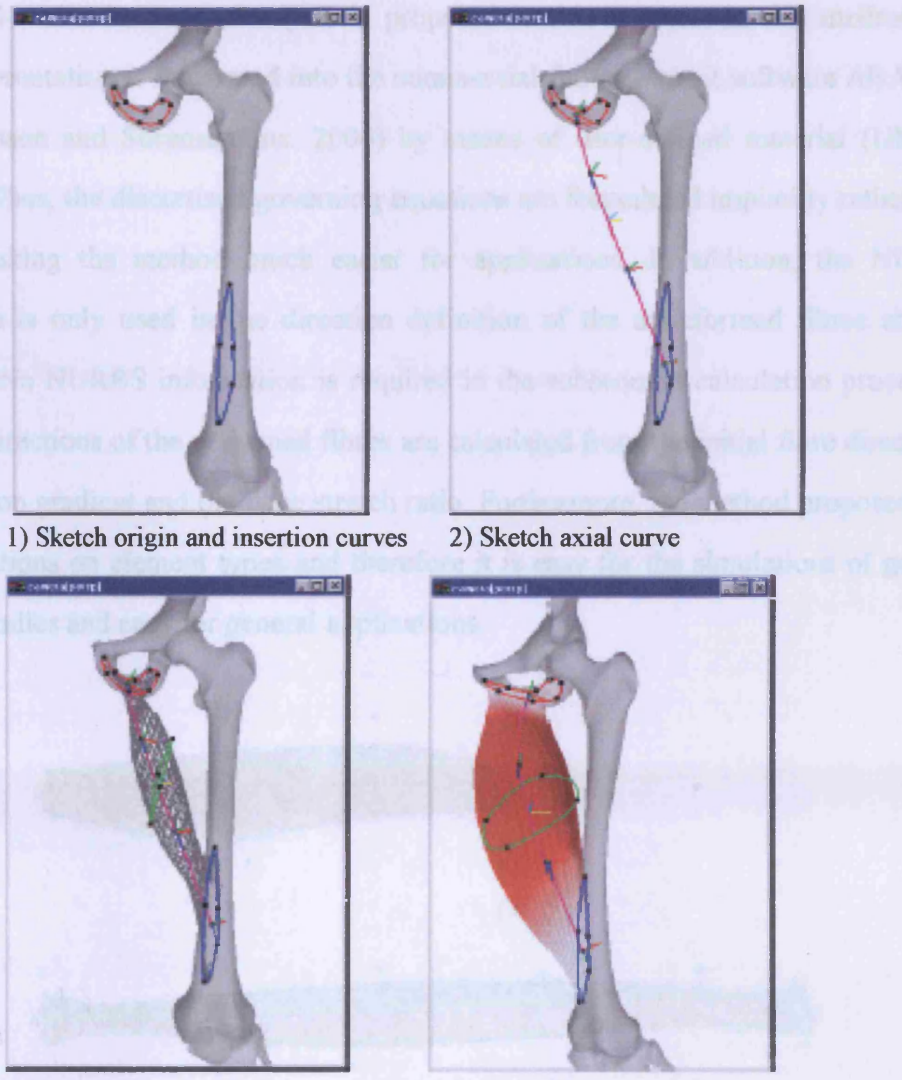


**Figure 5.5** Stages of development of B-spline solids for representing muscle (Ng-Thow-Hing and Fiume, 2002)

By combining the merits of the Non-Uniform Rational B-spline (NURBS) geometric representation and the Galerkin finite element method, a FEM-NURBS method for modelling skeletal muscle was first proposed by Zhou and Lu in 2005. In this method, the finite element equations were derived directly from the existing NURBS geometric description, and so no finite elements needed to be generated. The passive stretch of one muscle was simulated using their FEM-NURBS method, as shown in Figure 5.6, where the dots represented the control points of the NURBS solid. Following Zhou and Lu's idea, a

FEM-NURBS method using ABAQUS is proposed in this chapter. In this method, the NURBS representation is integrated into the commercial finite element software ABAQUS (Hibbit, Karlsson and Sorensen Inc. 2006) by means of user-defined material (UMAT) subroutines. Thus, the discretised governing equations are formulated implicitly rather than explicitly, making the method much easier for applications. In addition, the NURBS representation is only used in the direction definition of the undeformed fibres at each Gauss point. No NURBS information is required in the subsequent calculation procedure, because the directions of the deformed fibres are calculated from the initial fibre directions, the deformation gradient and the fibre stretch ratio. Furthermore, the method proposed here has no restrictions on element types and therefore it is easy for the simulations of general deformable bodies and easy for general applications.

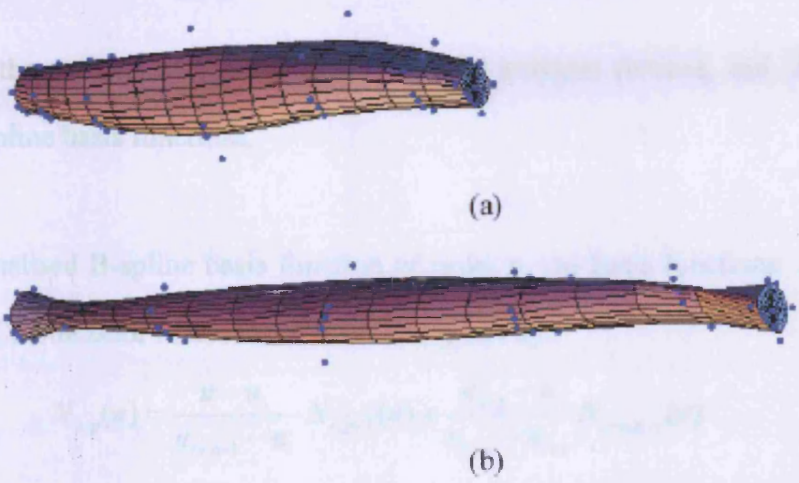


**Figure 5.6** Passive stretch of a muscle: (a) Initial shape; (b) Deformation (Zhou and Lu, 2005)

## 5.3 Mathematical description of the NURBS

Before introducing the proposed FEM-NURBS method, it is worthwhile to give a brief mathematical description of the NURBS. The non-Uniform Rational B-Splines, or NURBS, was first studied in the 1950s for the aim of mathematically precise representation of freeform surfaces. The pioneering work was undertaken by Pierre Bézier and Paul de

Casteljau in the late 1960s and early 1970s. The first personal computer NURBS modeller was developed in 1985 for the creation of ships and workboats. Today, NURBS are the standard for describing objects in computer aided design and computer graphics and are widely used in areas from automobile bodies to animated characters in films. In this section, the mathematical definitions of NURBS curve, surface and solid are presented.

## 5.3.1 NURBS Curve definition (Rogers, 2001)

A B-spline curve is a curve generated by using the vertices of a control polygon. Letting $\mathbf{P}(t)$ be the position vector along the curve as a function of the parameter $t$, a B-spline curve is given by:

$$\mathbf{P}(t) = \sum_{i=1}^{n+1} \mathbf{B}_i N_{i,p}(t), t_{\min} \le t < t_{\max}, 2 \le k \le n+1 \tag{5.1}$$

where $\mathbf{B}_i$ are the position vectors of the n+1 control polygon vertices, and $N_{i,p}$ are the normalised B-spline basis functions.

For the i[th] normalised B-spline basis function of order $p$, the basis functions $N_{i,p}(u)$ are defined by the Cox de Boor recursion relation and given by:

$$N_{i,p}(u) = \frac{u - u_i}{u_{i+p-1} - u_i} N_{i,p-1}(u) + \frac{u_{i+p} - u}{u_{i+p} - u_{i+1}} N_{i+1,p-1}(u) \tag{5.2}$$

with

$$N_{i,0}(u) = \begin{cases} 1, & u_i \le u < u_{i+1} \\ 0, & otherwise \end{cases} \tag{5.3}$$

where $u_i$ and $u_{i+1}$ are the elements of the knot vectors.

A NURBS curve is the generalisation of a B-spline curve. It is defined by its basis functions and a set of weighted control points. A NURBS curve in four-dimensional (4D) homogeneous coordinate space is given as:

$$\mathbf{P}(t) = \sum_{i=1}^{n+1} \mathbf{B}_i^h N_{i,p}(t) \tag{5.4}$$

where $\mathbf{B}_i^h$ are the 4D homogeneous control polygon vertices; $N_{i,p}$ are the non-rational B-spline basis functions previous given in Equations (5.2) and (5.3).

Projecting Equation (5.4) back into 3D space by dividing through the homogeneous coordinate yields the rational B-spline curve

$$\mathbf{P}(t) = \frac{\sum_{i=1}^{n+1} \mathbf{B}_i w_i N_{i,p}(t)}{\sum_{i=1}^{n+1} w_i N_{i,p}(t)} = \sum_{i=1}^{n+1} \mathbf{B}_i R_{i,p}(t) \tag{5.5}$$

where $\mathbf{B}_i$ are the 3D control polygon vertices for the rational B-spline curve; $w_i$ are the homogeneous coordinates, which are also called the homogeneous weighting factors or just weights, and

$$R_{i,p}(t) = \frac{w_i N_{i,p}(t)}{\sum_{i1=1}^{n+1} w_{i1} N_{i1,p}(t)} \tag{5.6}$$

are the rational B-spline basis functions.

From the definitions, it can be seen that the non-rational B-spline curves are a special case of rational B-spline curves. The primary difference is the weighting of the control points which makes the NURBS curves rational. One example of NURBS curve and its control points are shown in Figure 5.7.

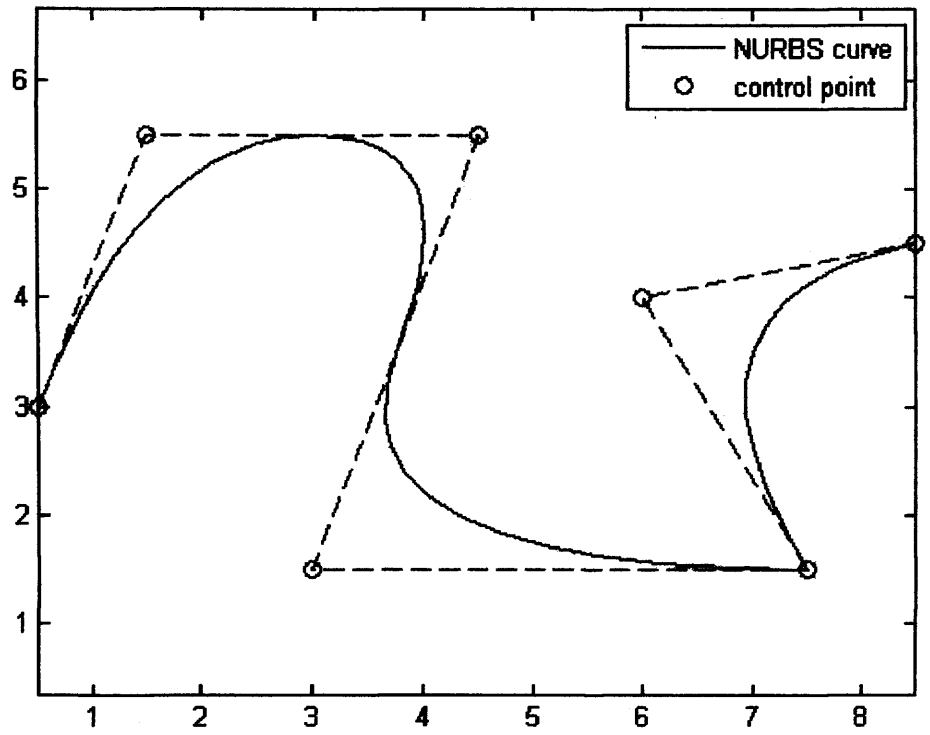


**Figure 5.7** A NURBS curve (blue line) and its control polygon (red dot)

## 5.3.2 NURBS Surface definition (Rogers, 2001)

Since non-rational B-splines are a special case of rational B-splines, as stated in Chapter 5.3.1, only rational B-spline surface and solid definitions are presented in the sections to follow.

A Cartesian product rational B-spline surface in 4D homogeneous coordinate space is given by:

$$\mathbf{Q}(u,v) = \sum_{i=1}^{n+1}\sum_{j=1}^{m+1}\mathbf{B}_{i,j}^{h}N_{i,p}(u)N_{j,q}(v) \tag{5.7}$$

where $\mathbf{B}_{i,j}^{h}$ are the 4D homogeneous polygonal control vertices, and $N_{i,p}(u)$ and $N_{j,q}(v)$ are the non-rational B-spline basis functions which have been previously defined in Equations (5.2) and (5.3).

Projecting back into 3D space by dividing through the homogeneous coordinate gives the rational B-spline surface:

$$\mathbf{Q}(u,v)=\frac{\sum_{i=1}^{n+1}\sum_{j=1}^{m+1}w_{i,j}\mathbf{B}_{i,j}N_{i,p}(u)N_{j,q}(v)}{\sum_{i=1}^{n+1}\sum_{j=1}^{m+1}w_{i,j}N_{i,p}(u)N_{j,q}(v)}=\sum_{i=1}^{n+1}\sum_{j=1}^{m+1}\mathbf{B}_{i,j}S_{i,j}(u,v) \tag{5.8}$$

where $\mathbf{B}_{i,j}$ are the 3D control net vertices; $w_{i,j}$ are the weight factors associated with the vertices; and $S_{i,j}(u,v)$ are the rational B-spline surface basis functions which are defined as:

$$S_{i,j}(u,v)=\frac{w_{i,j}N_{i,p}(u)N_{j,q}(v)}{\sum_{i1=1}^{n+1}\sum_{j1=1}^{m+1}w_{i1,j1}N_{i1,p}(u)N_{j1,q}(v)}=\frac{w_{i,j}N_{i,p}(u)N_{j,q}(v)}{Sum(u,v)} \tag{5.9}$$

One example of NURBS surface and its control points can be seen in Figure 5.8.

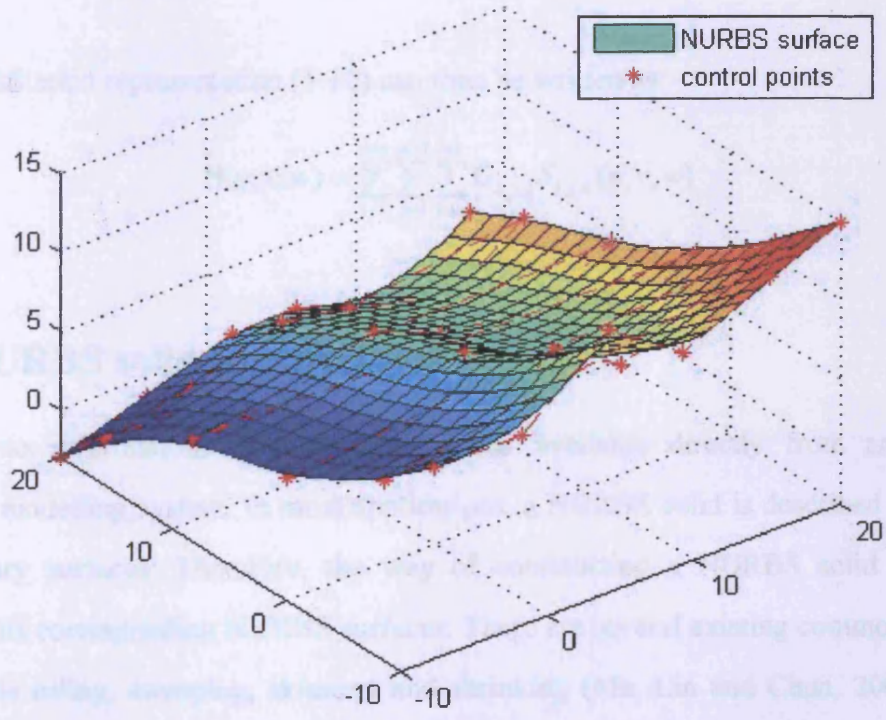


**Figure 5.8** A NURBS surface (colour area) and its control points (red stars)

## 5.3.3 NURBS solid definition (Hoschek and Lasser, 1993)

A NURBS solid representation is the generalisation of NURBS representation of curves and surfaces. A position of a generic point in the solid is defined as:

$$\mathbf{H}(u,v,w)=\frac{\sum_{i=1}^{n+1}\sum_{j=1}^{m+1}\sum_{k=1}^{l+1}w_{i,j,k}\mathbf{B}_{i,j,k}N_{i,p}(u)N_{j,q}(v)N_{k,r}(w)}{\sum_{i=1}^{n+1}\sum_{j=1}^{m+1}\sum_{k=1}^{l+1}w_{i,j,k}N_{i,p}(u)N_{j,q}(v)N_{k,r}(w)} \tag{5.10}$$

where $\mathbf{B}_{i,j,k}$ are the control point position vectors; $w_{i,j,k}$ are the weights associated with the control points; and $N_{i,p}(u)$, $N_{j,q}(v)$, $N_{k,r}(w)$ are the basis functions previously defined in Equations (5.2) and (5.3).

Giving the rational B-spline solid basis functions:

$$S_{i,j,k}(u,v,w)=\frac{w_{i,j,k}N_{i,p}(u)N_{j,q}(v)N_{k,r}(w)}{\sum_{i1=1}^{n+1}\sum_{j1=1}^{m+1}\sum_{k1=1}^{l+1}w_{i1,j1,k1}N_{i1,p}(u)N_{j1,q}(v)N_{k1,r}(w)}=\frac{w_{i,j,k}N_{i,p}(u)N_{j,q}(v)N_{k,r}(w)}{Sum(u,v,w)} \tag{5.11}$$

The NURBS solid representation (5.10) can then be written as:

$$\mathbf{H}(u,v,w)=\sum_{i=1}^{n+1}\sum_{j=1}^{m+1}\sum_{k=1}^{l+1}\mathbf{C}_{i,j,k}S_{i,j,k}(u,v,w) \tag{5.12}$$

## 5.3.4 NURBS solid construction

There is no information about NURBS solids available directly from any existing geometric modelling system. In most applications, a NURBS solid is described in terms of its boundary surfaces. Therefore, the way of constructing a NURBS solid is through extending its corresponding NURBS surfaces. There are several existing common methods, for example ruling, sweeping, skinning and shrinking (Ma, Lin and Chua, 2001). In this application, the shrinking method proposed by Ma, Lin and chua (2001) is used for constructing the NURBS solid. The shrinking method has been frequently used to deal with

close or periodic NURBS surfaces. For example, by shrinking a sphere to its centre point, a spheroid is derived and by shrinking a cylinder surface to its centreline, a cylinder volume is obtained. The NURBS solids presented in this chapter are derived by shrinking their boundary surfaces to their centrelines.

It is assumed that the centreline of the NURBS solid lies in the v direction. Therefore, the mathematical description of the NURBS solid can be written as (Ma, Lin and Chua, 2001):

$$\mathbf{H}(u,v,w)=\sum_{i=1}^{n+1}\sum_{j=1}^{m+1}\sum_{k=1}^{l+1}\mathbf{C}_{i,j,k}^{h}N_{i,p}(u)N_{j,q}(v)N_{k,r}(w) \tag{5.13}$$

where $\mathbf{C}_{i,j,0}^{h}=\mathbf{B}_{i,j}^{h}$ and $\mathbf{C}_{i,j,l}^{h}=\mathbf{D}_{j}$; $\mathbf{D}_{j}$ are the control point vectors of the centreline and given as (Ma, Lin and Chua, 2001):

$$\mathbf{D}_{j}=\frac{1}{n+1}\sum_{i=1}^{n+1}\mathbf{B}_{i,j}^{h} \tag{5.14}$$

Projecting back into 3D space by dividing through by the homogeneous coordinate gives the NURBS solid:

$$\mathbf{H}(u,v,w)=\frac{\sum_{i=1}^{n+1}\sum_{j=1}^{m+1}\sum_{k=1}^{l+1}w_{i,j,k}\mathbf{C}_{i,j,k}N_{i,p}(u)N_{j,q}(v)N_{k,r}(w)}{\sum_{i=1}^{n+1}\sum_{j=1}^{m+1}\sum_{k=1}^{l+1}w_{i,j,k}N_{i,p}(u)N_{j,q}(v)N_{k,r}(w)}=\sum_{i=1}^{n+1}\sum_{j=1}^{m+1}\sum_{k=1}^{l+1}\mathbf{C}_{i,j,k}S_{i,j,k}(u,v,w) \tag{5.15}$$

where $S_{i,j,k}(u,v,w)$ is defined in Equation (5.11).

The derivatives of the NURBS solid are obtained by formal differentiation of Equation (5.15) and given as:

$$\mathbf{H}_{u}=\frac{\overline{\mathbf{N}}^{H}}{\overline{D}}\left(\frac{\overline{\mathbf{N}}_{u}^{H}}{\overline{\mathbf{N}}^{H}}-\frac{\overline{D}_{u}}{\overline{D}}\right) \tag{5.16}$$

$$\mathbf{H}_{v}=\frac{\overline{\mathbf{N}}^{H}}{\overline{D}}\left(\frac{\overline{\mathbf{N}}_{v}^{H}}{\overline{\mathbf{N}}^{H}}-\frac{\overline{D}_{v}}{\overline{D}}\right) \tag{5.17}$$

$$\mathbf{H}_w = \frac{\overline{\mathbf{N}}^H}{\overline{D}}\left(\frac{\overline{\mathbf{N}}_w^H}{\overline{\mathbf{N}}^H} - \frac{\overline{D}_w}{\overline{D}}\right) \tag{5.18}$$

where $\overline{\mathbf{N}}^H$ and $\overline{D}^H$ are the numerator and denominator of Equation (5.15), respectively.

$$\overline{\mathbf{N}}^H = \sum_{i=1}^{n+1}\sum_{j=1}^{m+1}\sum_{k=1}^{l+1} w_{i,j,k}\mathbf{C}_{i,j,k}N_{i,p}(u)N_{j,q}(v)N_{k,r}(w) \tag{5.19}$$

$$\overline{D}^H = \sum_{i=1}^{n+1}\sum_{j=1}^{m+1}\sum_{k=1}^{l+1} w_{i,j,k}N_{i,p}(u)N_{j,q}(v)N_{k,r}(w) \tag{5.20}$$

Their derivatives are given as:

$$\overline{\mathbf{N}}_u^H = \sum_{i=1}^{n+1}\sum_{j=1}^{m+1}\sum_{k=1}^{l+1} w_{i,j,k}\mathbf{C}_{i,j,k}N'_{i,p}(u)N_{j,q}(v)N_{k,r}(w) \tag{5.21}$$

$$\overline{\mathbf{N}}_v^H = \sum_{i=1}^{n+1}\sum_{j=1}^{m+1}\sum_{k=1}^{l+1} w_{i,j,k}\mathbf{C}_{i,j,k}N_{i,p}(u)N'_{j,q}(v)N_{k,r}(w) \tag{5.22}$$

$$\overline{\mathbf{N}}_w^H = \sum_{i=1}^{n+1}\sum_{j=1}^{m+1}\sum_{k=1}^{l+1} w_{i,j,k}\mathbf{C}_{i,j,k}N_{i,p}(u)N_{j,q}(v)N'_{k,r}(w) \tag{5.23}$$

$$\overline{D}_u^H = \sum_{i=1}^{n+1}\sum_{j=1}^{m+1}\sum_{k=1}^{l+1} w_{i,j,k}N'_{i,p}(u)N_{j,q}(v)N_{k,r}(w) \tag{5.24}$$

$$\overline{D}_v^H = \sum_{i=1}^{n+1}\sum_{j=1}^{m+1}\sum_{k=1}^{l+1} w_{i,j,k}N'_{i,p}(u)N'_{j,q}(v)N_{k,r}(w) \tag{5.25}$$

$$\overline{D}_w^H = \sum_{i=1}^{n+1}\sum_{j=1}^{m+1}\sum_{k=1}^{l+1} w_{i,j,k}N'_{i,p}(u)N_{j,q}(v)N'_{k,r}(w) \tag{5.26}$$

From the definition of a NURBS solid, it can be seen that the NURBS solid is able to describe not only the exterior surface of an object but also the interior. In this thesis, the mathematic description of NURBS solid is applied to the finite element muscle model to characterise the muscle fibre orientation arrangement.

In order to formulise the NURBS solid, the information on its boundary surface is required. There are two different ways to construct the boundary NURBS surfaces for a solid. In the first approach, the boundary surfaces are obtained directly form the Visible Human Data.

Firstly, the contours lines are extracted from Data Slices. Then the boundary NURBS surfaces are created by using these contour lines. This approach is illustrated in Figure 5.9.

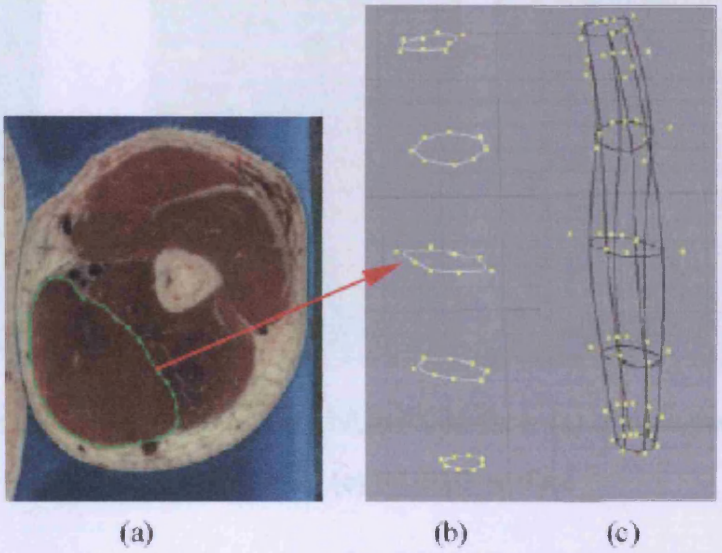


**Figure 5.9** 3D reconstruction of muscle shape with NURBS: (a) Contour of muscle boundary in one slice; (b) Stacks of contour curves; (c) NURBS surface by skinning the NURBS contours (Zhou and Lu, 2005)

In the second approach, the boundary NURBS surfaces are created from the muscle geometry. Taking the depressor anguli oris muscle as an example to illustrate this method, Figure 5.10 (a) shows the geometry of this muscle. First, the corresponding contour lines, as shown in Figure 5.10 (b), are extracted from the geometric model by using the pre-processing tool, ANSA (BETA CAE Systems S.A., 2009). Then the boundary NURBS surfaces, as shown in Figure 5.10 (c), are generated by blending the contour lines in the CAD package software Pro/ENGINEER (Parametric Technology Corp, 2004). Finally, these NURBS surfaces are exported as an IGS file, from which the corresponding information is extracted for creating the NURBS solid model.

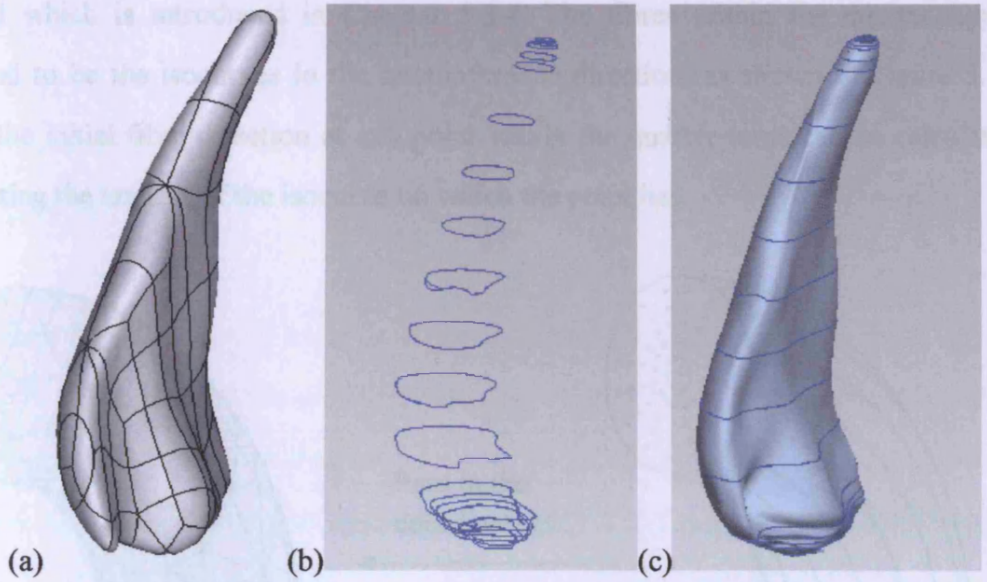


**Figure 5.10** Procedure of creating boundary NURBS surface: (a) Muscle geometry; (b) Muscle contour lines; (c) NURBS surface

In the applications presented in this chapter, the second method of creating NURBS boundary surfaces is used. The NURBS solids are created by shrinking the boundary NURBS surfaces to their centrelines. This step is accomplished by writing a FORTRAN code. The corresponding programme is given in Appendix G.

## 5.4 FEM-NURBS method

Characterising the complex interior fibre orientation arrangement of skeletal muscle is the motivation for developing the FEM-NURBS method. The basic idea of the FEM-NURBS method proposed in this chapter is to use the NURBS solid for representing the muscle fibre orientation arrangement, and pass the fibre directions at each Gauss point into the finite element model as the initial fibre directions.

A quarter of a torus is created as an example to illustrate the FEM-NURBS method. Figure 5.11 (a) shows a finite element torus model meshed with tetrahedrons. A NURBS solid of the same size, as shown in Figure 5.11(b), is constructed by using the shrinking

method which is introduced in Chapter 5.3.4. The fibres within the quarter torus are assumed to be the isocurves in the circumference direction, as shown in Figure 5.11(b). Thus, the initial fibre direction at any point within the quarter torus can be calculated by computing the tangent of the isocurve on which the point lies.

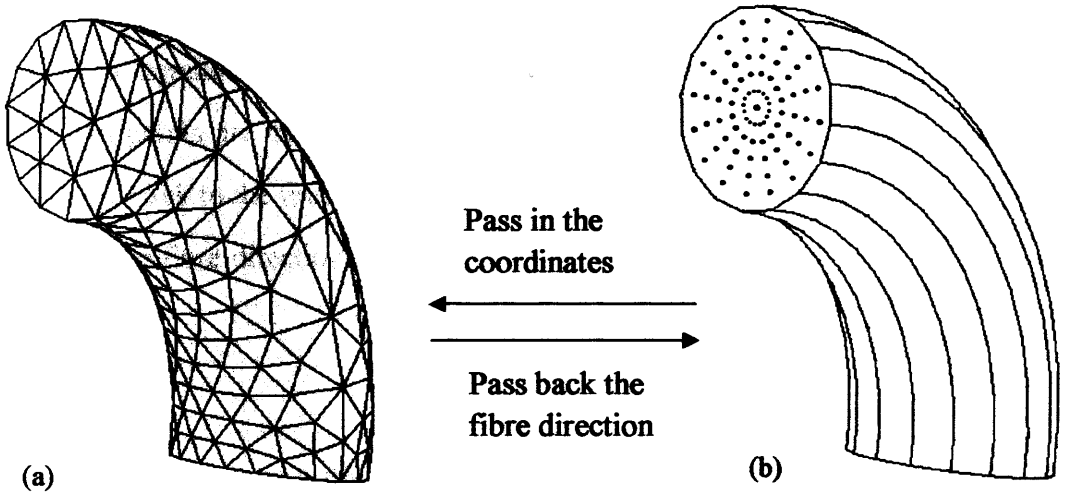


**Figure 5.11** Illustration of the FEM-NURBS method: (a) FE model with tetrahedrons; (b) NURBS solid model with the fibre orientation arrangement indicated

As an example, assuming a fibre lies on an isocurve P and the fibre direction is along the u-direction, then on this isocurve P, the values of the other two directions are constant, i.e. $\{v,w\} = \{v_0,w_0\}$. This isocurve can be expressed mathematically as:

$$\mathbf{H}(u,v_0,w_0)=\sum_{i=0}^{l}\sum_{j=0}^{m}\sum_{k=0}^{n}\mathbf{C}_{i,j,k}S_{i,j,k}(u,v_0,w_0) \tag{5.27}$$

The tangent vector of this isocurve can be obtained by taking the derivative of Equation (5.27) with respect to $u$. The normalised form can be expressed as:

$$\mathbf{A}(u,v_0,w_0)=\frac{\partial\mathbf{H}(u,v_0,w_0)/\partial u}{\left|\partial\mathbf{H}(u,v_0,w_0)/\partial u\right|} \tag{5.28}$$

The fibre direction at a point, which lies on the isocurve **P** and has the coordinate of $\{u_0,v_0,w_0\}$, is given by:

$$\mathbf{A}(u_0, v_0, w_0) = \frac{\partial \mathbf{H}(u, v_0, w_0)/\partial u}{\left|\partial \mathbf{H}(u, v_0, w_0)/\partial u\right|_{u_0}} \tag{5.29}$$

where the derivative of the isocurve $\mathbf{P} = \mathbf{H}(u, v_0, w_0)$ with respect to $u$ is given in Equation (5.16).

In the first iteration of the finite element calculation, the fibre directions at all Gauss integration points are calculated using Equation (5.29). These fibre direction vectors are then passed back to the finite element solver as the initial fibre directions. In the subsequent iterations, the fibre directions at each Gauss integration point are updated by (Weiss et al. 1996):

$$\mathbf{a} = \frac{\mathbf{F} \cdot \mathbf{A}}{\lambda_f} \tag{5.30}$$

where **a** is the deformed fibre direction; **A** is the undeformed fibre direction; **F** is the deformation gradient and $\lambda_f$ is the fibre stretch ratio. The process of how the FEM-NURBS method is implemented into ABAQUS is shown in Figure 5.12.

```
do i=1, steps
    do j=0, increments in each step
        do m=0, iterations in each increment
            do n=1, elements in the model
                do p=1, integration points in each element
                    if((i .eq. 1) and. (j .eq. 0) .and. (m .eq.0))  then
                      call the FEM-NURBS method to assign the fibre directions
                    else
                      use Equation (5.30) to update the fibre directions
                    endif
                    ......
                enddo
            enddo
        enddo
    enddo
enddo
```

**Figure 5.12** Fibre direction assignment process in ABAQUS

Finally, it should be noted that the FEM-NURBS method can be implemented into any commercial finite element software, as long as enough information is passed to the user-defined material subroutines. The specific information needed for the FEM-NURBS method is the coordinates of each Gauss point. The user-defined material subroutine interface in ABAQUS is shown in Figure 5.13, where COORDS is an array containing the coordinates of current Gauss integration point.

```
SUBROUTINE UMAT(STRESS,STATEV,DDSDDE,SSE,SPD,SCD,
    1 RPL,DDSDDT,DRPLDE,DRPLDT,
    2 STRAN,DSTRAN,TIME,DTIME,TEMP,DTEMP,PREDEF,DPRED,CMNAME,
    3 NDI,NSHR,NTENS,NSTATV,PROPS,NPROPS,COORDS,DROT,PNEWDT,
    4 CELENT,DFGRD0,DFGRD1,NOEL,NPT,LAYER,KSPT,KSTEP,KINC)
```

**Figure 5.13** User subroutine interface in ABAQUS

The FEM-NURBS method cannot be implemented into LS-DYNA at this stage, because the coordinates of each Gauss point is not available from the LS-DYNA user subroutine interface. Figure 5.14 shows the user-defined material subroutine interface in LS-DYNA. It is seen the information in the LS-DYNA user subroutine interface is less than that in the ABAQUS user subroutine interface and it is restricted at the moment.

```
SUBROUTINE UMAT43 (CM, EPS, SIG, EPSP, HSV, DT1, CAPA, ETYPE, TIME,
     1   TEMP, FAILEL, CRV)
```

**Figure 5.14** User subtoutine interface in LS-DYNA

## 5.5 Muscle constitutive relation

Since the FEM-NURBS method cannot be implemented into LS-DYNA at this stage and the validated three-dimensional (3D) finite element (FE) skeletal muscle model presented in Chapter 3 was developed in LS-DYNA, this model cannot be used for the calculations undertaken in this chapter.

In this chapter, a 3D FE skeletal muscle model was developed in ABAQUS (Hibbit, Karlsson and Sorensen Inc. 2006). The muscle constitutive relation is proposed by Tang et al. (2009) and this model has been validated through several scenarios in their work. The model is able to capture the complex behaviour of skeletal muscle, which is active, quasi-incompressible, transversely isotropic and hyperelastic (Herzog, 2000; Oomens, Maenhout, Drost et al., 2003). Different from that in LS-DYNA, the material constitutive model in ABAQUS requires the spatial form of the material tensor to be defined. Thus it is worthwhile to give an overview of Tang et al.'s 3D skeletal muscle constitutive relation.

Tang et al.'s model is an extension of the Hill-type muscle model (Figure 5.15), consisting of a contractile element in series with a series elastic element (SEE) and in parallel with a parallel elastic element (PE).

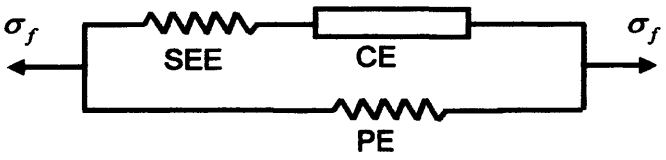


**Figure 5.15** Hill's three-element muscle model

The strain energy function used in their model has the following form:

$$U = U_I(\bar{I}_1^C) + U_f(\bar{\lambda}_f, \alpha_a, \Delta\lambda_s) + U_J(J) \tag{5.31}$$

where $U_I$, $U_f$ are the strain energy stored in the isotropic matrix and the muscle fibre structures, respectively; and $U_J$ is the portion of strain energy associated with the volume change.

The ground substance consists of the connective tissue and the water. In Tang et al.'s (2009) model, the ground substance is modelled as an isotropic material with the following strain energy form:

$$U_I(\bar{I}_1^C) = c\{\exp[b(\bar{I}_1^C - 3)] - 1\} \tag{5.32}$$

where $b$ and $c$ are material constants; $\bar{I}_1^C$ is the first invariant of the right Cauchy-Green strain tensor with the volume change eliminated.

In order to preserve the volume during the deformation, an additional item $U_J(J)$ is added into the total strain energy:

$$U_J(J)=\frac{1}{D}(J-1)^2 \tag{5.33}$$

where $J$ is the Jacobian of the deformation gradient; the constant $D$ can be best understood as a penalty parameter for incompressibility. Thus, nearly incompressibility can be modelled with a rather small value of $D$.

The muscle fibre strain energy has the following form:

$$U_f(\bar{\lambda}_f,\alpha_a,\Delta\lambda_s)=U_{PE}(\bar{\lambda}_f)+U_{SE}(\bar{\lambda}_f,\alpha_a,\Delta\lambda_s) \tag{5.34}$$

where $\bar{\lambda}_f$ is the stretch ratio in the muscle with the volume change eliminated; $\alpha_a$ is the activation function and $\Delta\lambda_s$ is the stretch increment in the series elastic element; $U_{PE}$, $U_{SE}$ are the energy stored in the parallel element (PE) and series elastic element (SEE), respectively. They can be expressed as the integral form of stress in PE ($\sigma_{PE}$) and stress in SEE ($\sigma_{SE}$) over the muscle stretch $\lambda$:

$$U_{PE}(\bar{\lambda}_f)=\int_1^{\bar{\lambda}_f}\sigma_{PE}(\lambda)d\lambda \tag{5.35}$$

$$U_{SE}(\bar{\lambda}_f,\alpha_a,\Delta\lambda_s)=\int_1^{\bar{\lambda}_f}\sigma_{SE}(\lambda,\alpha_a,\Delta\lambda_s)d\lambda \tag{5.36}$$

where

$$\sigma_{PE}(\bar{\lambda}_f)=\sigma_0\begin{cases}4(\bar{\lambda}_f-1)^2, & if \quad \bar{\lambda}_f>1\\ 0, & otherwise\end{cases} \tag{5.37}$$

$$\sigma_{SE}(\bar{\lambda}_f,\alpha_a,\Delta\lambda_s)=\beta\{\exp[\alpha(\lambda_s-1)]-1\} \tag{5.38}$$

where $\sigma_0$ is the maximal isometric stress and $\alpha$, $\beta$ are material constants.

The process of updating $\lambda_s$ has been given in Chapter 3.3, where the stress relationship

between CE and SEE is used, i.e. the stress in CE equals to the stress in SEE. Since the stress expression in CE here is different from that in Chapter 3.3, it is worthwhile to give the expression of the stress in CE at time t + Δt :

$$ {}^{t+\Delta t}\sigma_{CE}(\Delta\lambda_m) = {}^{t}\sigma_0 \, {}^{t+\Delta t}\alpha_a \begin{cases} \dfrac{1+\Delta\lambda_m/\Delta\lambda_{m0}}{1-k_c\,\Delta\lambda_m/\Delta\lambda_{m0}} & ,if \quad \Delta\lambda_m \le 0 \\ d-(d-1)\dfrac{1-\Delta\lambda_m/\Delta\lambda_{m0}}{1+k_c k_e\,\Delta\lambda_m/\Delta\lambda_{m0}} & ,if \quad \Delta\lambda_m > 0 \end{cases} \tag{5.39} $$

where ${}^{t}\sigma_0$ is the stress corresponding to the fibre stretch ${}^{t}\lambda_f$; $k_c = {}^{t}\sigma_0 / a_v$ and $k_e$ are the shape parameters of the hyperbolic tension force-velocity curve of the contractile element.

The 2nd Piola-Kirchhoff stress tensor **S** can be obtained from the strain energy density given in Equation (5.31) (Belytschko, Liu and Moran et al., 2000):

$$ \mathbf{S} = \frac{\partial U}{\partial \mathbf{E}} = U_I'\left(2J^{-2/3}\mathbf{I} - \frac{2}{3}\bar{I}_1^C\mathbf{C}^{-1}\right) + U_f'\left(J^{-2/3}\bar{\lambda}_f^{-1}(\mathbf{N}\otimes\mathbf{N}) - \frac{1}{3}\bar{\lambda}_f\mathbf{C}^{-1}\right) + JU_J'\mathbf{C}^{-1} \tag{5.40} $$

The Cauchy stress is defined by the push-forward of S (Marsden and Hughes, 1994):

$$ \boldsymbol{\sigma} := \frac{1}{J}\left[U_I'\left(2\bar{\mathbf{B}} - \frac{2}{3}\bar{I}_1^C\mathbf{I}\right) + U_f'\left(\bar{\lambda}_f(\mathbf{n}\otimes\mathbf{n}) - \frac{1}{3}\bar{\lambda}_f\mathbf{I}\right)\right] + U_J'\mathbf{I} \tag{5.41} $$

where

$$ U_I' = \frac{\partial U_I}{\partial \bar{I}_1^C} = bc\exp\left[b\left(\bar{I}_1^C - 3\right)\right] \tag{5.42} $$

$$ U'_f = U'_{PE}(\bar{\lambda}_f) + U'_{SE}(\bar{\lambda}_f, \alpha_a, \Delta\lambda_s) \tag{5.43} $$

$$ U_J' = \frac{\partial U_J}{\partial J} = \frac{2}{D}(J-1) \tag{5.44} $$

with

$$ U'_{PE}(\bar{\lambda}_f) = \sigma_{PE}(\bar{\lambda}_f) \tag{5.45} $$

$$ U'_{SE}(\bar{\lambda}_f, \alpha_a, \Delta\lambda_s) = \sigma_{SE}(\bar{\lambda}_f, \alpha_a, \Delta\lambda_s) \tag{5.46} $$

For the hyperelastic material specified by a strain energy function U, the material elasticity tensor is given by:

$$\begin{aligned}\mathbf{H} &:= 4\frac{\partial^2 U}{\partial \mathbf{C}\partial \mathbf{C}} = 2\frac{\partial \mathbf{S}}{\partial \mathbf{C}} \\ &= 4J^{-4/3}U_I''(\mathbf{I}\otimes\mathbf{I}) - \frac{4}{3}J^{-2/3}(U_I' + \bar{I}_1^C U_I'')(\mathbf{I}\otimes\mathbf{C}^{-1} + \mathbf{C}^{-1}\otimes\mathbf{I}) \\ &+ \left[\frac{4}{9}\bar{I}_1^C(U_I' + \bar{I}_1^C U_I'') + \frac{1}{9}\bar{\lambda}_f(U_f' + \bar{\lambda}_f U_f'') + J(U_J' + JU_J'')\right](\mathbf{C}^{-1}\otimes\mathbf{C}^{-1}) \\ &+ J^{-4/3}\bar{\lambda}_f^{-2}(U_f'' + \bar{\lambda}_f^{-1}U_f')(\mathbf{N}\otimes\mathbf{N}\otimes\mathbf{N}\otimes\mathbf{N}) \\ &- \frac{1}{3}J^{-2/3}(U_f'' + \bar{\lambda}_f^{-1}U_f')(\mathbf{N}\otimes\mathbf{N}\otimes\mathbf{C}^{-1} + \mathbf{C}^{-1}\otimes\mathbf{N}\otimes\mathbf{N}) \\ &- 2\left(\frac{2}{3}\bar{I}_1^C U_I' + \frac{1}{3}\bar{\lambda}_f U_f' - JU_J'\right)\mathbf{L}_{\mathbf{C}^{-1}}\end{aligned} \tag{5.47}$$

where

$$(\mathbf{L}_{C^{-1}})_{ijkl} = \left(\frac{\partial \mathbf{C}^{-1}}{\partial \mathbf{C}}\right)_{ijkl} = -\frac{1}{2}\left(C_{ik}^{-1}C_{jl}^{-1} + C_{il}^{-1}C_{jk}^{-1}\right) \tag{5.48}$$

The spatial form of the material tensor is again defined as the push-forward of the material elasticity tensor H (Marsden and Hughes, 1994):

$$\begin{aligned}\mathbf{h} &:= \frac{1}{J}\mathbf{F}\mathbf{F}\cdot\mathbf{H}\cdot\mathbf{F}^T\mathbf{F}^T \\ &= \frac{4}{J}U_I''\bar{\mathbf{B}}\otimes\bar{\mathbf{B}} - \frac{4}{3}J^{-1}(U_I' + \bar{I}_1^C U_I'')(\bar{\mathbf{B}}\otimes\mathbf{I} + \mathbf{I}\otimes\bar{\mathbf{B}}) \\ &+ \frac{1}{J}\left[\frac{4}{9}\bar{I}_1^C(U_I' + \bar{I}_1^C U_I'') + \frac{1}{9}\bar{\lambda}_f(U_f' + \bar{\lambda}_f U_f'') + J(U_J' + JU_J'')\right](\mathbf{I}\otimes\mathbf{I}) \\ &+ \frac{\bar{\lambda}_f^2}{J}(U_f'' - \bar{\lambda}_f^{-1}U_f')(\mathbf{n}\otimes\mathbf{n}\otimes\mathbf{n}\otimes\mathbf{n}) \\ &- \frac{1}{3}\frac{\bar{\lambda}_f^2}{J}(U_f'' + \bar{\lambda}_f^{-1}U_f')(\mathbf{n}\otimes\mathbf{n}\otimes\mathbf{I} + \mathbf{I}\otimes\mathbf{n}\otimes\mathbf{n}) \\ &+ \frac{2}{J}\left(\frac{2}{3}\bar{I}_1^C U_I' + \frac{1}{3}\bar{\lambda}_f U_f' - JU_J'\right)\mathbf{L}\end{aligned} \tag{5.49}$$

where **L** is the symmetric 4th order unit tensor

$$L_{ijkl} = \frac{1}{2}\left(\delta_{ik}\delta_{jl} + \delta_{il}\delta_{jk}\right) \tag{5.50}$$

and

$$U_I'' = b^2 c\exp\left[b\left(\bar{I}_1^C - 3\right)\right] \tag{5.51}$$

$$U^{"}_{f} = U^{"}_{PE}(\bar{\lambda}_f) + U^{"}_{SE}(\bar{\lambda}_f, \alpha_a, \Delta\lambda_s) \tag{5.52}$$

$$U^{"}_{PE}(\bar{\lambda}_f) = {}^{t}\sigma_0 \begin{cases} 8(\lambda_f - 1), & for \quad \lambda_f > 1 \\ 0 & otherwise \end{cases} \tag{5.53}$$

$$U^{"}_{SE}(\bar{\lambda}_f, \alpha_a, \Delta\lambda_s) = \alpha\beta \frac{1+k}{k} \exp[\alpha(\lambda_s - 1)] \tag{5.54}$$

$$U^{"}_{J} = \frac{2}{D} \tag{5.55}$$

where $k$ is the ratio of the length of contractile element to that of series elastic element.

The material parameter values are adopted from Tang et al. (2009) and given in Table 5.1.

**Table 5.1** Muscle material model parameters

| $b$ | $c$ (N/m$^2$) | $D$ (m$^2$/N) | $\alpha$ | $\beta$ (N/m$^2$) | $d$ | $k_e$ | $\dot{\lambda}_{m0}$ (s$^{-1}$) | $\sigma_0$ (N/m$^2$) | $a_v$ (N/m$^2$) | $k$ |
|---|---|---|---|---|---|---|---|---|---|---|
| 1.79 | 821 | 1.0e-9 | 100 | 0.1 | 1.65 | 3.14 | 2 | 2.2e5 | 7.0e4 | 0.3 |

# 5.6 Numerical examples

The proposed FEM-NURBS method and the muscle constitutive equations outlined in Chapter 5.5 were implemented into ABAQUS (Hibbit, Karlsson and Sorensen Inc. 2006) by programming user-defined material (UMAT) subroutines. The ability of the proposed FEM-NURBS method is demonstrated through the examples presented below.

The muscle response can be classified as active or passive. The active muscle response is induced by the brain signal. The active muscle force is generated by the contraction of muscle fibres and the contraction magnitude is controlled by the neural input, which is represented by the activation function $\alpha_a$ in the constitutive model. In the following five numerical examples, only the active responses of several different muscles are simulated

and the muscles are stimulated from time zero. It is assumed that the muscles take 0.005 s to reach the fully activated level and then the fully activated muscle is maintained in this state until the end of the simulation. The total activation time is defined as 0.2 s. This muscle activation function is shown in Figure 5.16.

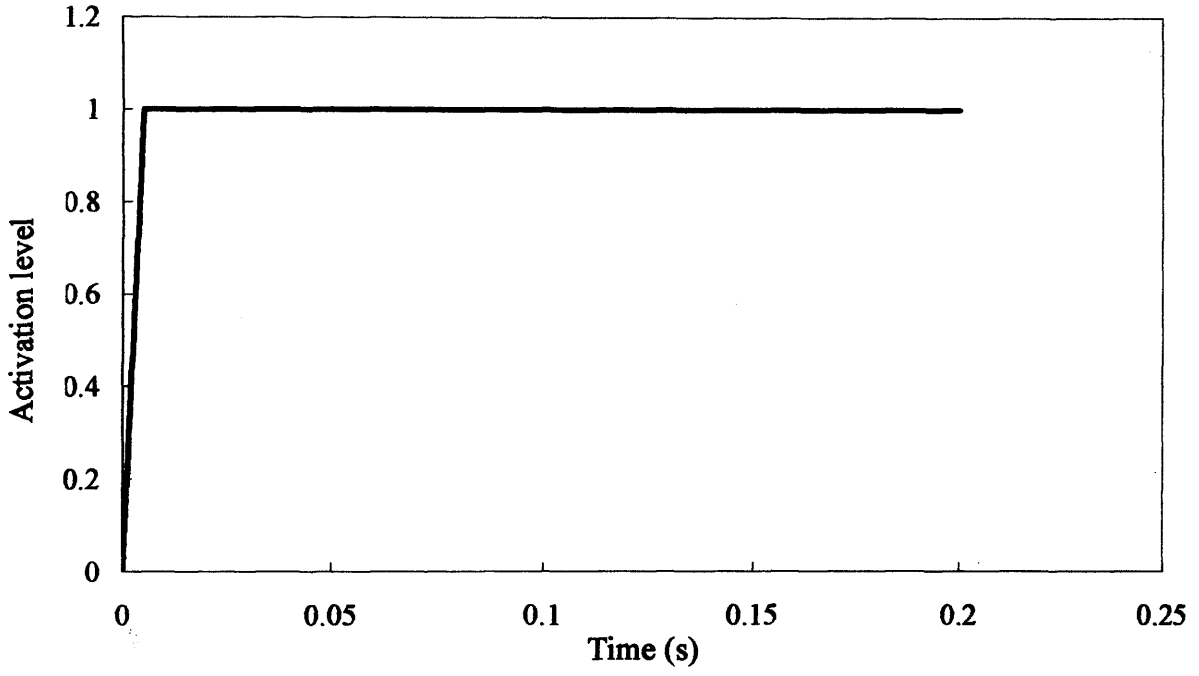


**Figure 5.16** The muscle activation function for the simulations

In the following five examples, only one boundary NURBS surface is generated for each muscle. The orders of the two basis functions, which are used for defining the NURBS surface, are set to 4. Each NURBS solid is created by shrinking its corresponding boundary NURBS surface to its centreline. The control points in the centreline are obtained using Equation (5.14). The order of basis function in the shrinking direction is set to 2. The weight at each control point is set to 1. The knot vector and control point values are fetched from the IGS files, which contain the NURBS surface information.

## 5.6.1 Example one: contraction of a cone

A muscle with a conical shape is considered for the test in this example. The top diameter of the cone is 0.8 cm, the bottom diameter is 4.0 cm and the height is 5.0 cm (Figure 5.17).

The bottom face of the cone is fully fixed during the simulation (Figure 5.18). The fibres within the cone are assumed to be arranged in the way described in Figure 5.19.

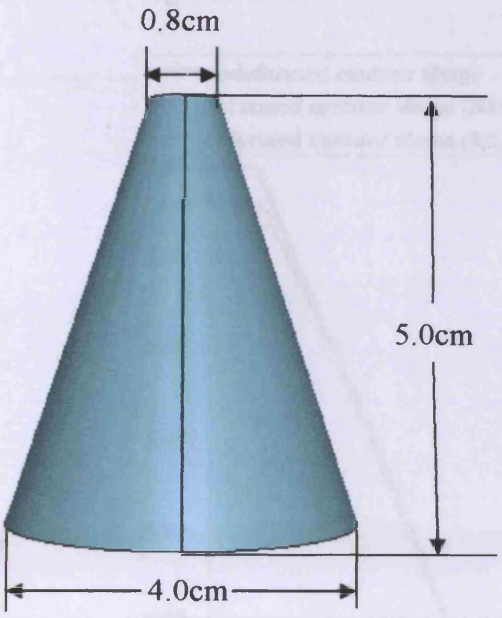


**Figure 5.17** Geometry of the cone

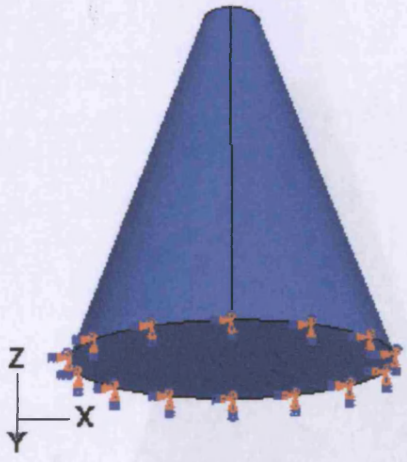


**Figure 5.18** Boundary condition on the cone

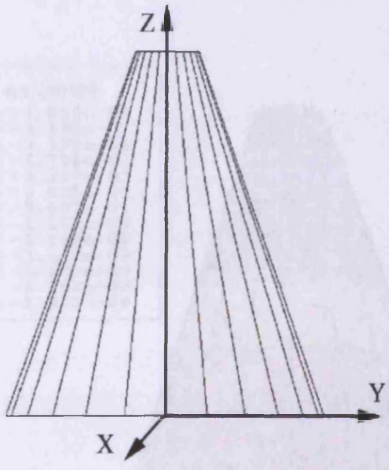


**Figure 5.19** Fibre arrangement in the cone

Two methods are used for simulating the fibre arrangement within this cone. In the first approach, the fibre directions are approximated as being along the z-direction. In the second approach, the fibre arrangement is simulated using the NURBS method. The deformed contour lines from these two methods, together with the undeformed contour

lines, are plotted in Figure 5.20. From this figure, it can be seen that the deformations from the two methods are almost identical. The deformation of the cone and the Z-directional displacement distribution are presented in Figure 5.21.

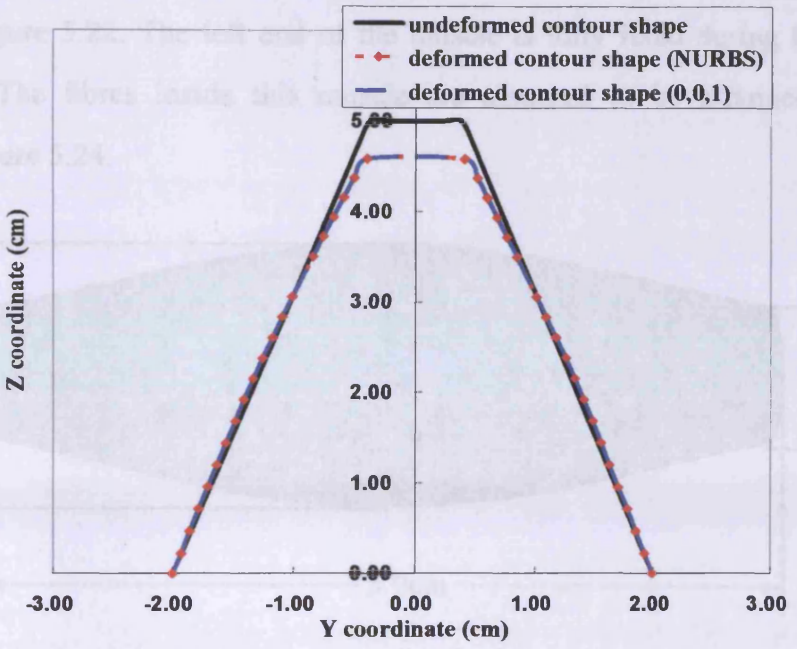


**Figure 5.20** The undeformed and deformed contour lines of the cone

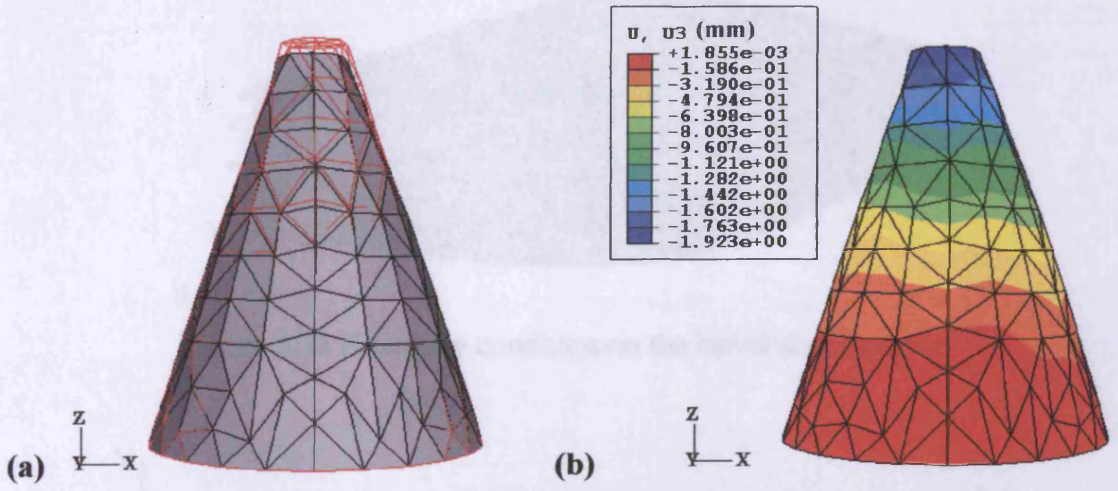


**Figure 5.21** (a) Deformation of the cone: Shaded area represents the deformed shape and the red lines represent the undeformed shape; (b) Z-directional displacement distribution

## 5.6.2 Example two: contraction of a barrel shape muscle

In this case, a barrel shape muscle is constructed for the test. The length of this muscle is 5.0 cm, the diameter at the two ends is 0.9 cm, and the diameter in the middle is 1.75 cm, as shown in Figure 5.22. The left end of the muscle is fully fixed during the simulation (Figure 5.23). The fibres inside this muscle are assumed to be arranged in the way described in Figure 5.24.

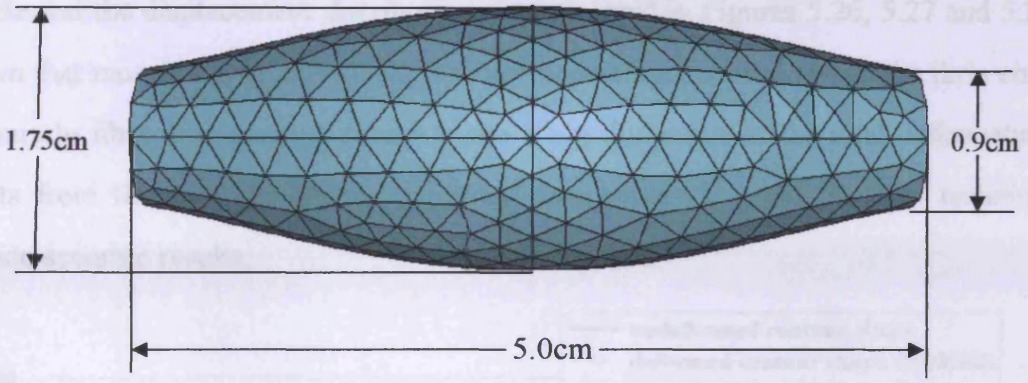


**Figure 5.22** Geometry of the barrel shape muscle

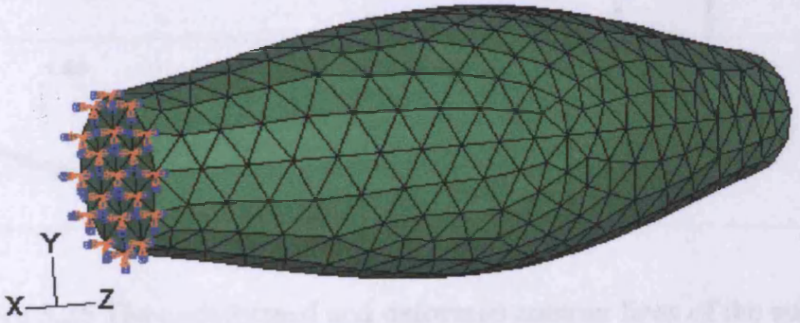


**Figure 5.23** Boundary condition on the barrel shape muscle

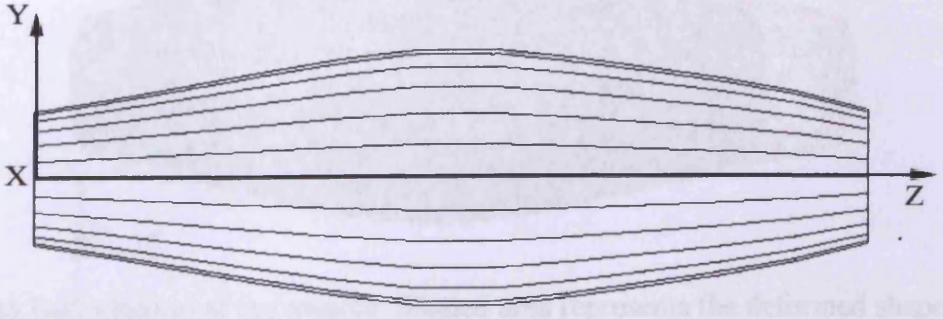


**Figure 5.24** Fibre arrangement in the barrel shape muscle

Two methods are used to model the fibre arrangement in this barrel shape muscle. In the first approach, it is assumed the muscle fibres are arranged parallel in a single direction (Z-direction). In the second approach, the fibre arrangement shown in Figure 5.24 is simulated using the NURBS technique. The deformed contour lines from the two methods, together with the undeformed contour lines, are plotted in Figure 5.25. From the resulting configurations, it can be concluded that the muscle deformations from these two methods are almost identical, which agrees with that from the first example. The deformation of this muscle and the displacement distribution are presented in Figures 5.26, 5.27 and 5.28. It is known that muscle tissue is basically an incompressible material. Thus, the little change in the muscle fibre arrangement cannot make a big difference in the total deformation. The results from the two approaches therefore demonstrate that the NURBS technique can provide accurate results.

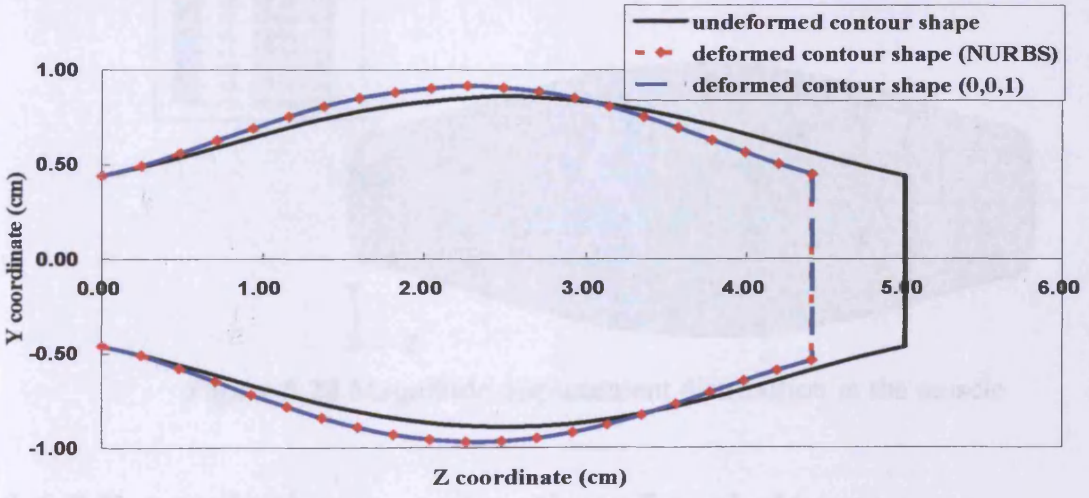


**Figure 5.25** The undeformed and deformed contour lines of the muscle

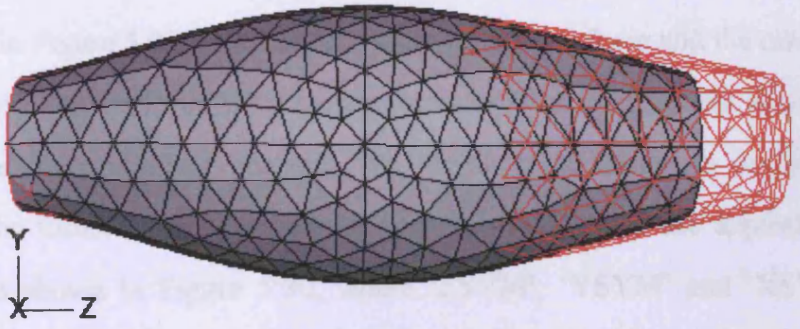


**Figure 5.26** Deformation of the muscle: Shaded area represents the deformed shape and the red lines represent the undeformed shape

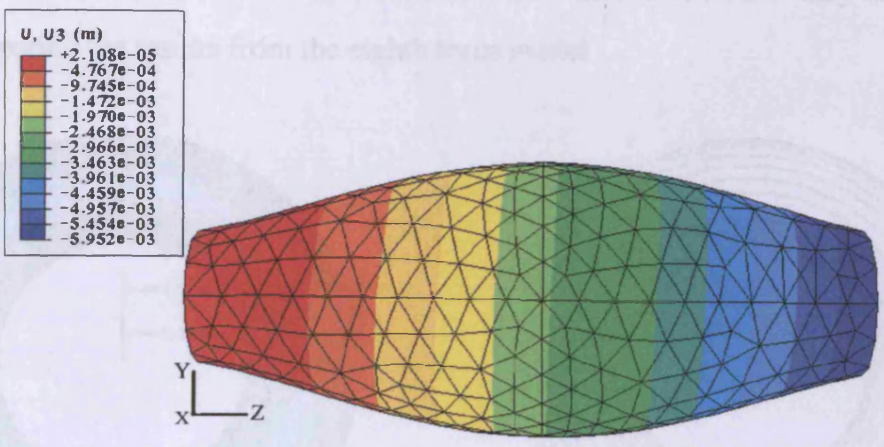


**Figure 5.27** Z-directional displacement distribution in the muscle

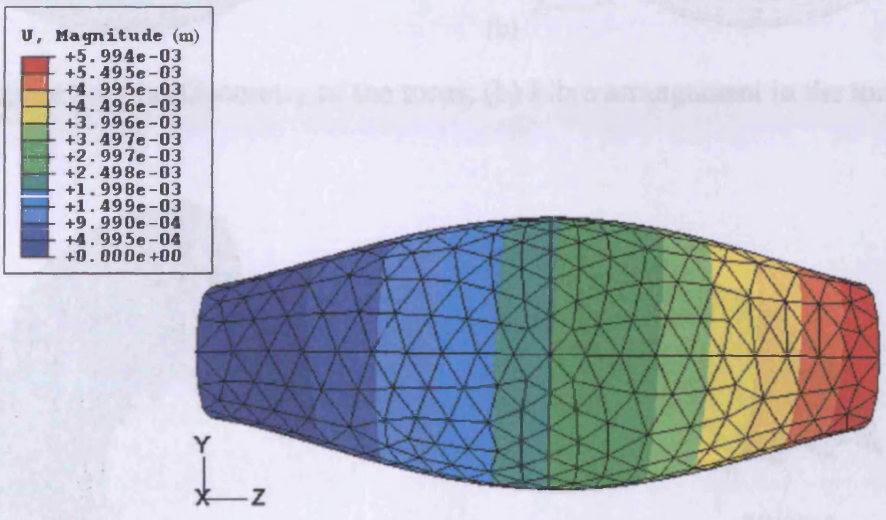


**Figure 5.28** Magnitude displacement distribution in the muscle

## 5.6.3 Example three: contraction of a whole torus

In this example, a whole torus is considered for the demonstration. The geometry of the torus is shown in Figure 5.29(a), where the inner radius is 0.9 cm and the outer radius is 1.7 cm. It is assumed that the torus has a parallel circular fibre arrangement as shown in Figure 5.29(b). In the finite element analysis, the eighth torus model is utilised due to the symmetry of the torus. Plane symmetrical boundary conditions are applied to the eighth torus model, as shown in Figure 5.30, where 'ZSYM', 'YSYM' and 'XSYM' represent Z-plane, Y-plane and X-plane symmetrical conditions, respectively. However, the eighth torus model is only used in the finite element calculation. To better visualise the

deformation of the torus, the results on the whole torus are used and they are obtained through mirroring the results from the eighth torus model.

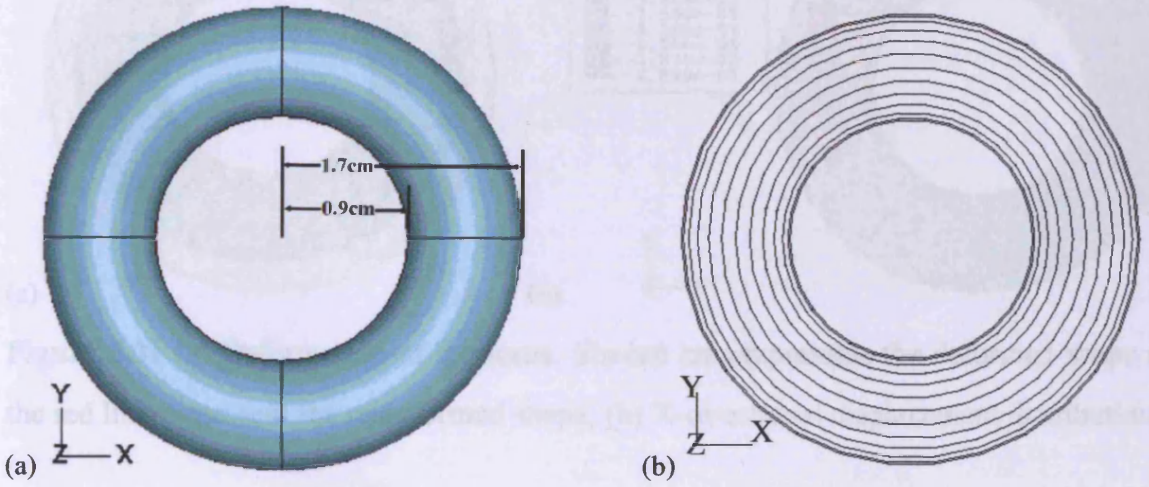


**Figure 5.29** (a) Geometry of the torus; (b) Fibre arrangement in the torus

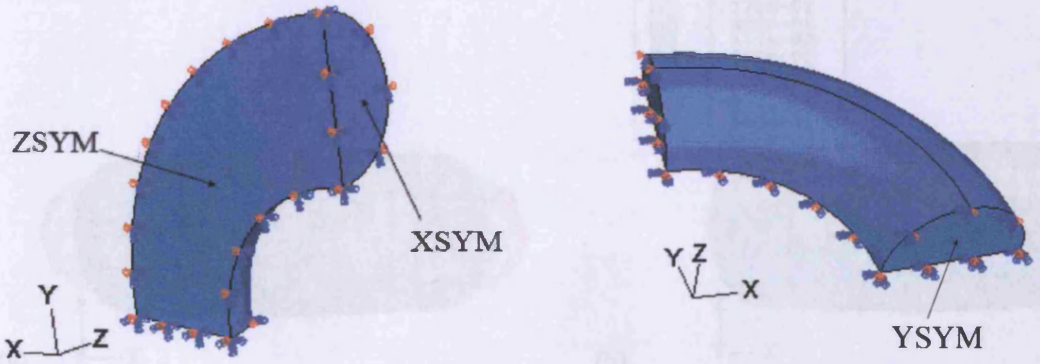


**Figure 5.30** Boundary conditions on the eighth torus

In practice, when the torus is stimulated, it would contract along its circular fibres. Then the circular fibres will shrink towards the centre of the torus after the deformation. On the other hand, since the torus is modelled as an incompressible material, it will become thicker in Z-direction. These theoretical predictions are matched by the finite element results presented in Figures 5.31 and 5.32, where 'U1' and 'U3' represent X-directional and Z-directional displacements, respectively. It should be noted that the aim of this example is towards the realistic simulation of the orbicularis oris muscle which also has circularly arranged fibres.

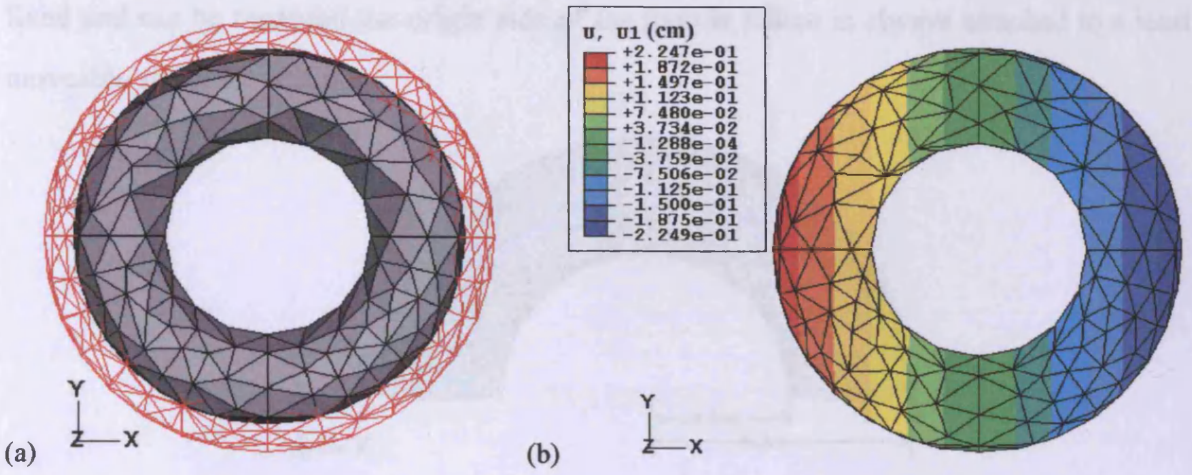


**Figure 5.31** (a) Deformation of the torus: Shaded area represents the deformed shape and the red lines represent the undeformed shape; (b) X-directional displacement distribution

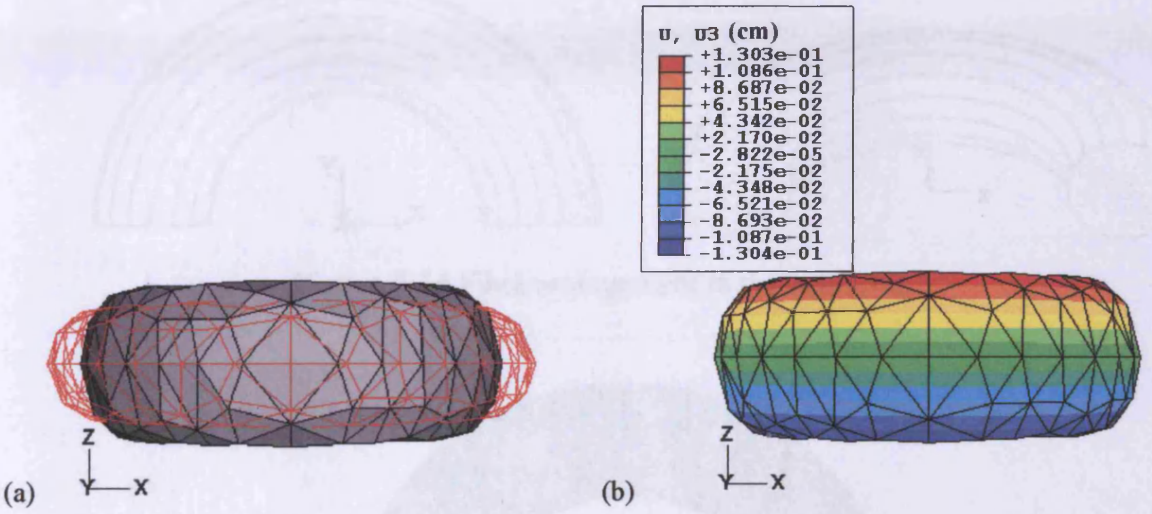


**Figure 5.32** (a) Deformation of the torus: Shaded area represents the deformed shape and the red lines represent the undeformed shape; (b) Z-directional displacement distribution

## 5.6.4 Example four: contraction of a half torus

In this example, a half torus is built with the inner radius of 0.7 cm and the outer radius of 1.3 cm (Figure 5.33). The fibres within this half torus are assumed to be arranged circumferentially, as shown in Figure 5.34. During the simulation, one end of the half torus is fully fixed, as shown in Figure 5.35. If the half torus is regarded as a muscle, this fully

fixed end can be regarded the origin side of the muscle which is always attached to a least moveable structure.

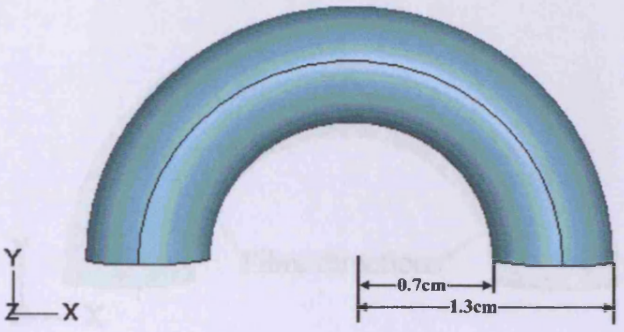


**Figure 5.33** Geometry of the half torus

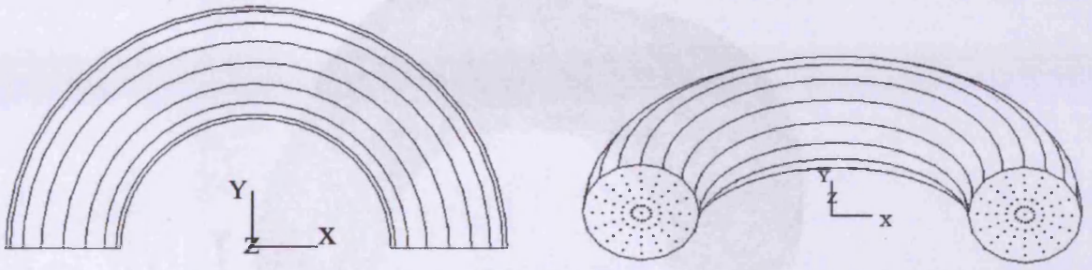


**Figure 5.34** Fibre arrangement in the half torus

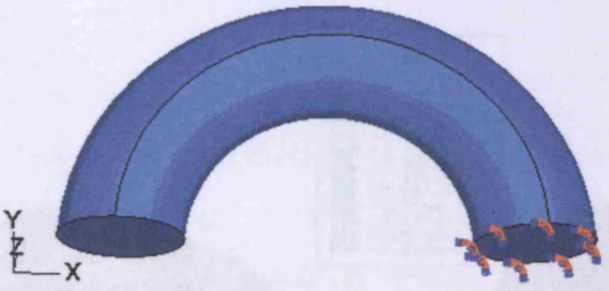


**Figure 5.35** Boundary condition on the half torus

In this example, two methods are used to simulate the fibre arrangement inside this half torus. In the first approach, the half torus is divided into two segments from the middle and the fibre direction in each segment is approximated by a single unchanged direction, as shown in Figure 5.36, where the green part represents one segment of the half torus, the grey part represents the other segment, and the red arrow lines represent the fibre direction

in each segment. The results from this method are presented in Figures 5.37 and 5.38.

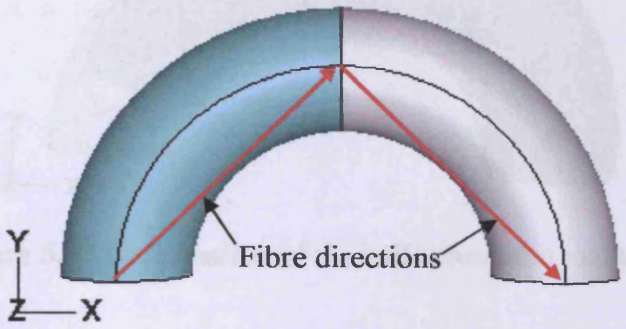


**Figure 5.36** Fibre directions in segments of the half torus (method 1)

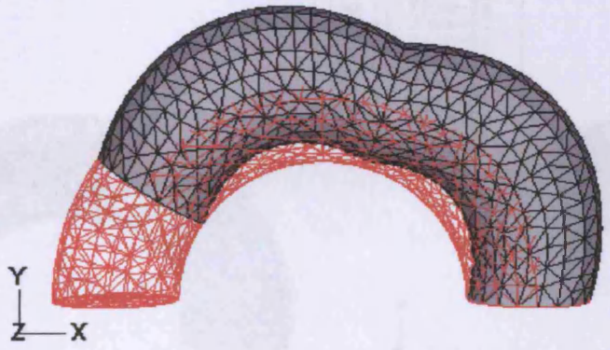


**Figure 5.37** Deformation of the half torus from method 1

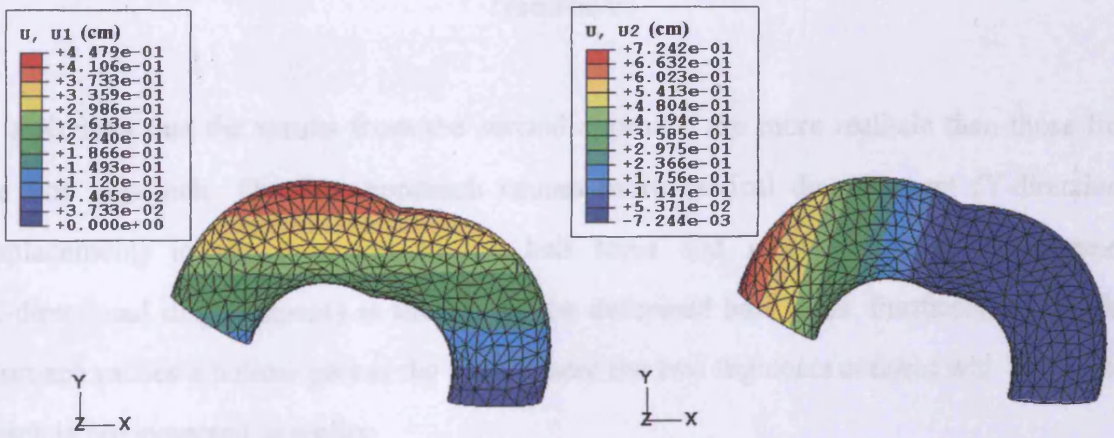


**Figure 5.38** X-directional and Y-directional displacement distribution in the half torus (method 1)

In the second approach, the fibre arrangement within the half torus is represented using the NURBS technique and the results from this method are presented in Figures 5.39 and 5.40.

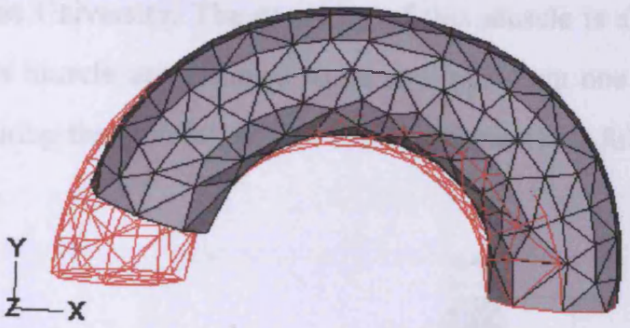


**Figure 5.39** Deformation of the half torus from method 2

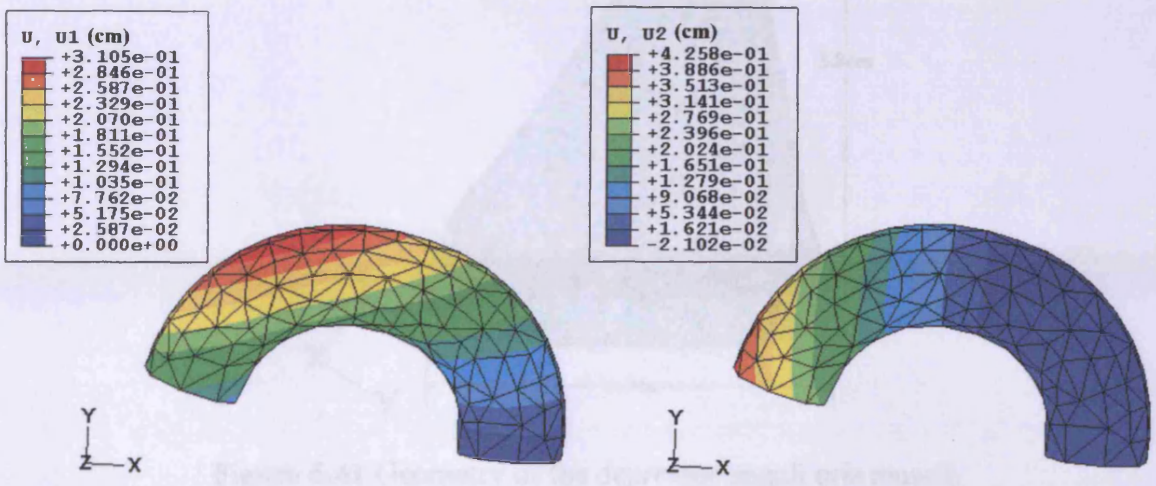


**Figure 5.40** X-directional and Y-directional displacement distribution in the half torus (method 2)

It is obvious that the results from the second approach are more realistic than those from the first approach. The first approach causes more vertical displacement (Y-directional displacement) in the free end of the half torus and more horizontal displacement (X-directional displacement) at the top of the deformed half torus. Furthermore, the first approach causes a hollow part at the place where the two segments connect with each other, which is not expected in reality.

## 5.6.5 Example five: contraction of the depressor anguli oris

In this demonstration, a human facial muscle is considered. The shape of the depressor anguli oris muscle is taken from the standardised forensic database provided by School of

Life Sciences, Dundee University. The geometry of this muscle is shown in Figure 5.41. The fibres within this muscle are assumed to be arranged from one end to the other end along Z-direction. During the simulation, one end of the muscle is fully fixed, as shown in Figure 5.42.

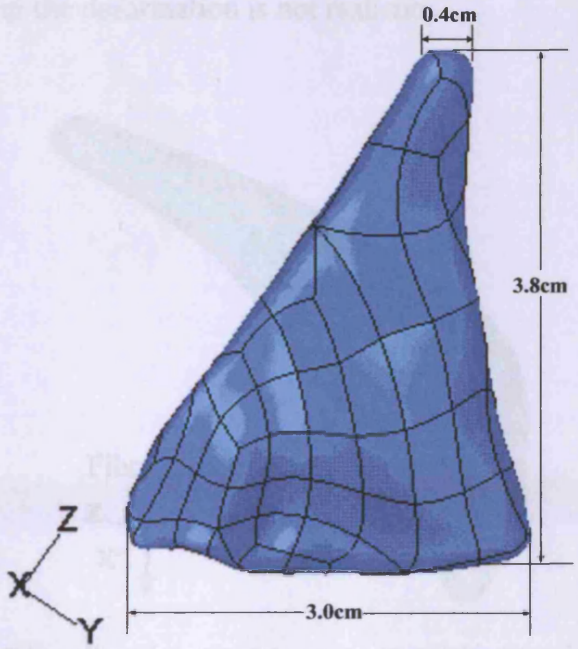


**Figure 5.41** Geometry of the depressor anguli oris muscle

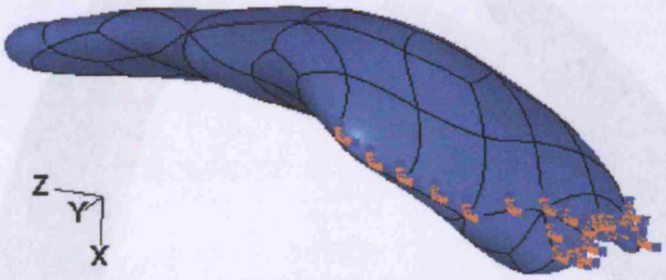


**Figure 5.42** Boundary condition on the depressor anguli oris muscle

Two approaches for simulating the fibre arrangement inside the depressor anguli oris muscle are performed here. In the first approach, the muscle is divided into two segments from the middle and the fibre directions in each segment are approximated by one single unchanged direction, as indicated by the red arrow lines in Figure 5.43. It should be noted

that this approach is widely used in most of the musculoskeletal human body systems where the muscles are represented by the line segments. The simulated muscle shape and the displacement distributions from this approach are presented in Figures 5.44 and 5.45, respectively. It can be seen that the free end has rotated away from the undeformed configuration, suggesting the deformation is not realistic.

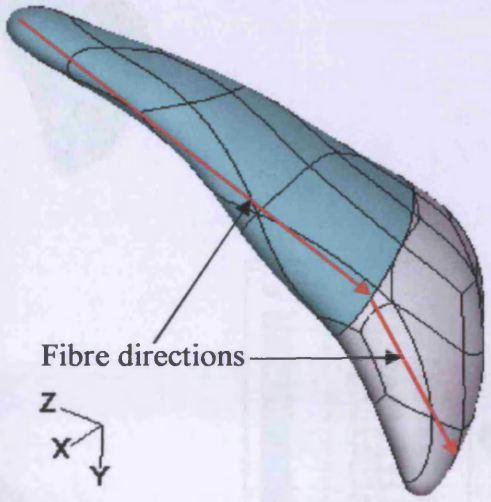


**Figure 5.43** Fibre directions in the segments of the muscle (method 1)

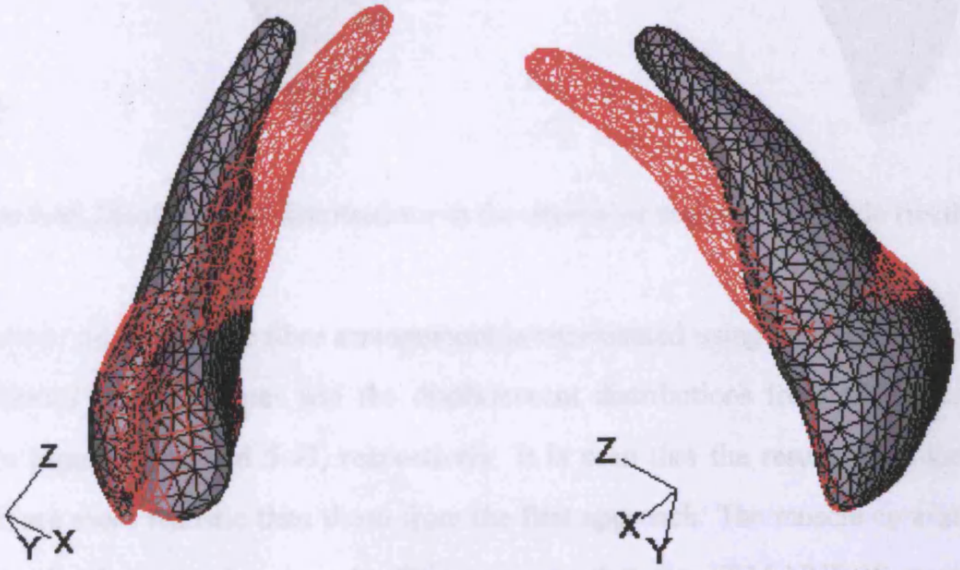


**Figure 5.44** Deformation of the depressor anguli oris muscle (method 1)

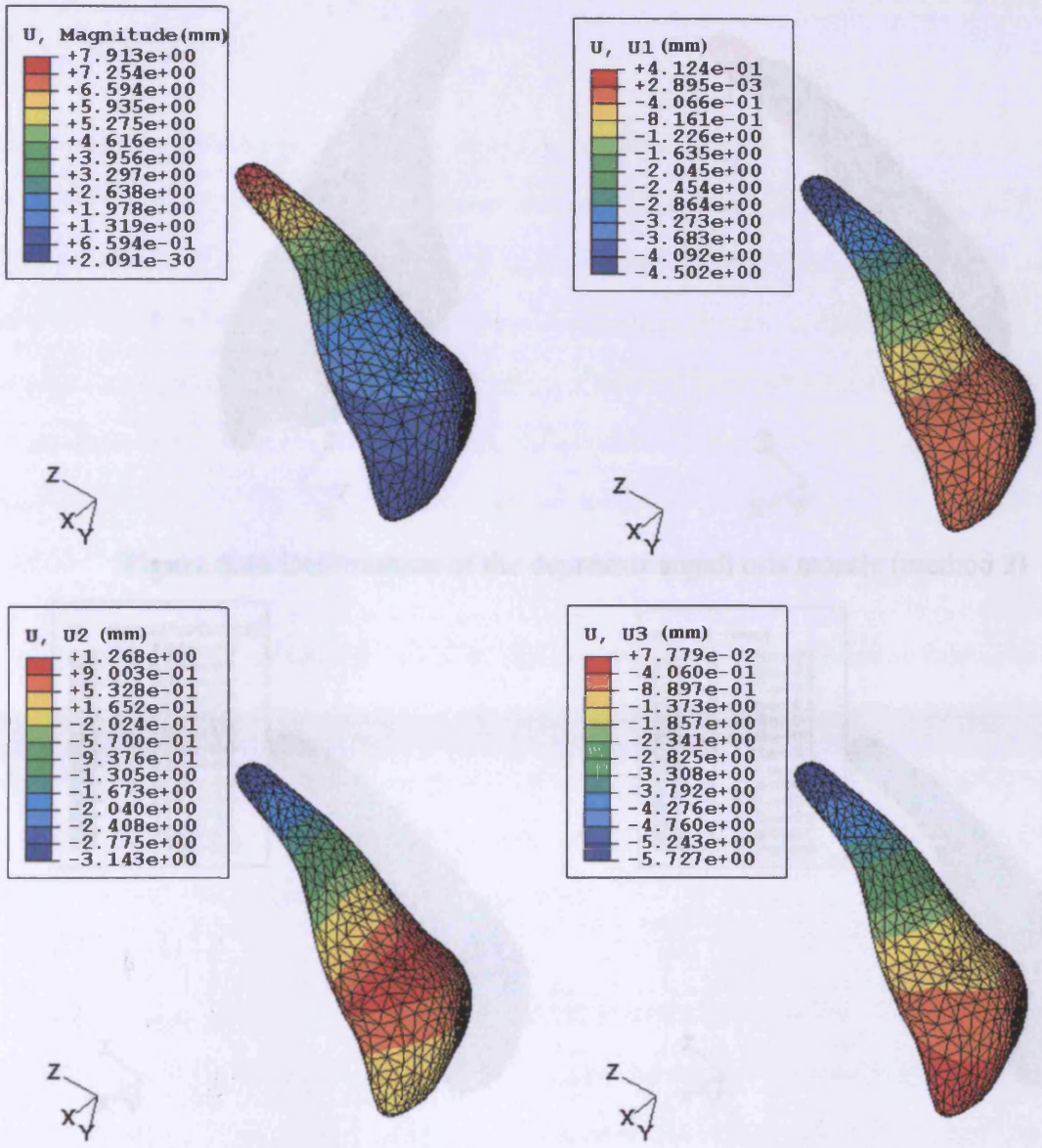


**Figure 5.45** Displacement distributions in the depressor anguli oris muscle (method 1)

In the second approach, the fibre arrangement is represented using the NURBS technique. The deformed muscle shapes and the displacement distributions from this approach are shown in Figures 5.46 and 5.47, respectively. It is seen that the results from the second approach are more realistic than those from the first approach. The muscle contracts along this shape in the second approach. This suggests that the FEM-NURBS technique is capable of simulating the fibre arrangement in an irregular muscle as long as the fibres within the muscle can be represented by the isocurves of a NURBS solid.

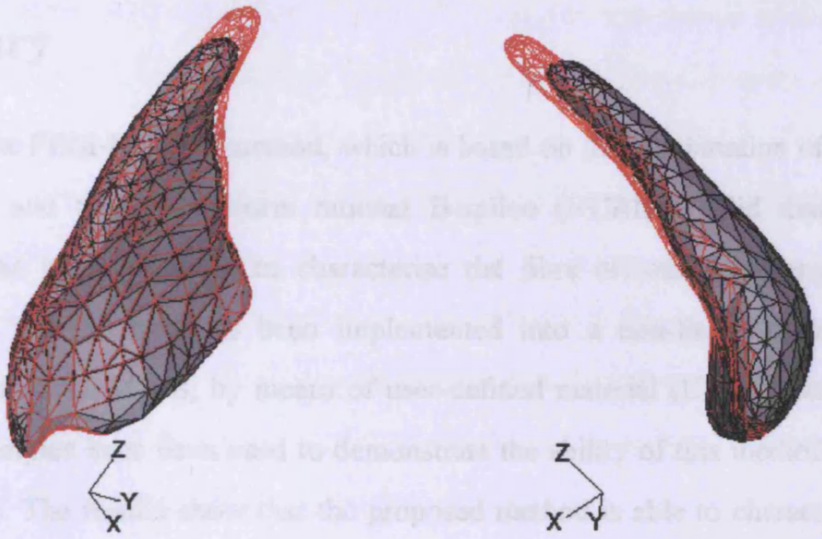


**Figure 5.46** Deformation of the depressor anguli oris muscle (method 2)

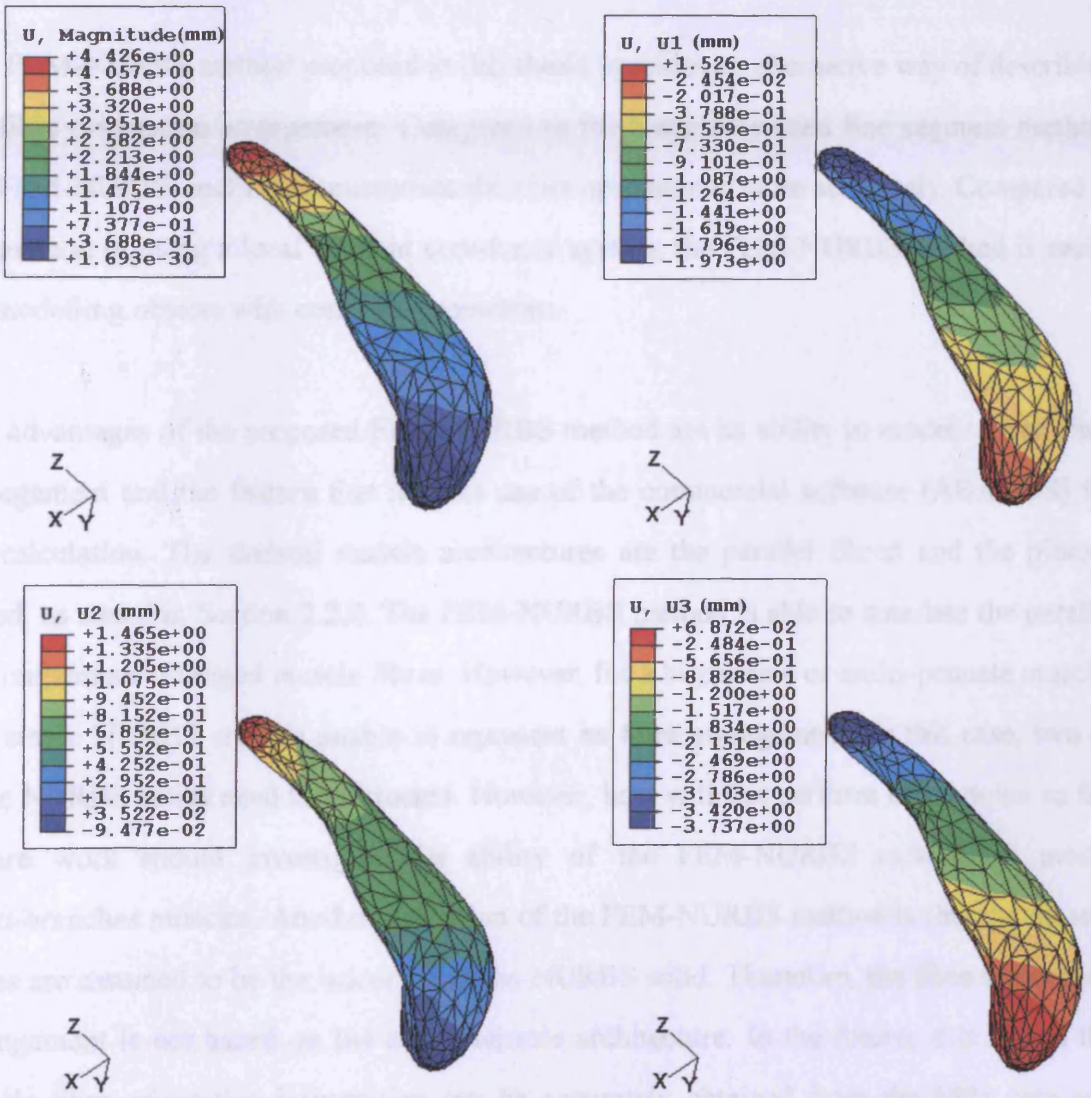


**Figure 5.47** Displacement distributions in the depressor anguli oris muscle (method 2)

## 5.7 Summary

In this chapter, the FEM-NURBS method, which is based on the combination of the finite element method and the non-uniform rational B-spline (NURBS) solid mathematical representation, has been proposed to characterise the fibre orientation arrangement of skeletal muscle. This method has been implemented into a non-linear finite element analysis programme, ABAQUS, by means of user-defined material (UMAT) subroutines. A number of examples have been used to demonstrate the ability of this method to model muscle structures. The results show that the proposed method is able to characterise both the fibre arrangement and the biomechanical response of skeletal muscle.

The FEM-NURBS method proposed in this thesis provides an alternative way of describing the fibre orientation arrangement. Compared to the commonly used line segment method, the FEM-NURBS method characterises the fibre orientations more accurately. Compared to the method of using a local element coordinate system, the FEM-NURBS method is easier for modelling objects with complex geometries.

The advantages of the proposed FEM-NURBS method are its ability to model curved fibre arrangement and the feature that it takes use of the commercial software (ABAQUS) for the calculation. The skeletal muscle architectures are the parallel fibred and the pinnate fibred, as stated in Section 2.2.2. The FEM-NURBS method is able to simulate the parallel and unipennate arranged muscle fibres. However, for a bi-pennate or multi-pennate muscle, one single NURBS solid is unable to represent its fibre arrangement. In this case, two or more NURBS solids need to be created. However, how will this perform is unknown so far. Future work should investigate the ability of the FEM-NURBS method to model multi-branches muscles. Another limitation of the FEM-NURBS method is that the muscle fibres are assumed to be the isocurves in the NURBS solid. Therefore, the fibre orientation arrangement is not based on the actual muscle architecture. In the future, it is hoped the muscle fibre orientation information can be accurately obtained from the MRI data and then input into the finite element model for the calculation.

It should be noted that the FEM-NURBS method developed in this chapter enables a more accurate simulation of the facial muscles. However, because of the limitation of the data that can be fetched to the LS-DYNA user subroutine interface, this FEM-NURBS method cannot be implemented into LS-DYNA at this stage. Therefore, this method has not been applied to the facial model developed in Chapter 4. In the future, as the development of LS-DYNA progresses, the implementation of the FEM-NURBS method will become achievable and this will permit a more accurate facial model. Furthermore, the muscle fibre orientation arrangements of the facial model could also be considered for investigation using the FEM-NURBS method developed in this chapter.

# Chapter 6

# Conclusions and Future Work

## 6.1 Summary and conclusions

This chapter summarises the general conclusions that are drawn from the present investigation and gives guidelines for future research. For specific conclusions and future research directions, readers are directed to these sections at the end of each chapter.

The research objectives of this thesis, as outlined in Chapter 1 - introduction, were to:

1. Develop reliable numerical facial soft tissue models
2. Develop a numerical facial model which can be used for the simulations of facial surgery and facial movement.

In respect to these objectives, the following research has been undertaken, which has led to the following conclusions being made:

### ● Skeletal muscle model development

A finite element skeletal muscle model has been developed to simulate the skeletal muscle mechanical behaviour which include the active, quasi-incompressible, fibre-reinforced and hyperelastic behaviour. This model is phenomenological and based on Hill's three-element model. The force-velocity and force-length relationships of the muscle are incorporated into the model. The model is implemented into a non-linear finite element analysis

programme LS-DYNA by means of user-defined material subroutines and validated by comparing the finite element analysis results with the published experimental data on the New Zealand white rabbit tibialis anterior muscle. It is shown that the model is able to capture the passive and active muscle behaviour during both the shortening and lengthening movements. This work is presented in Chapter 3.

The constitutive skeletal muscle model developed in Chapter 3 is able to capture the complex mechanical behaviour of skeletal muscle. However, in this model, it is assumed that the skeletal muscle fibres are distributed parallel and have a single direction. Thus, the model fails to capture the complex fibre arrangement within a skeletal muscle system. To overcome this problem, in Chapter 5, a FEM-NURBS method is proposed to model both the mechanical properties and the internal fibre arrangement of skeletal muscle. This method is implemented into the non-linear finite element analysis programme, ABAQUS by means of user defined material subroutines. A number of numerical examples have been carried out to demonstrate that the proposed method is able to capture both the biomechanical response and the fibre arrangement of skeletal muscle.

- **Finite element facial model development**

A finite element facial model has been developed which can be used for the simulation of facial surgery and facial movement. In this model, the facial skin and the skull structures are based on the patient specific CBCT data, and the muscle geometry is taken from a standardised forensic database. The subcutaneous tissue is created to fill the gap among the facial skin, the skull and the muscles. This facial model is first used to simulate cranio-facial surgical procedures. The results are compared with the patient's 6-month post-surgery data. Good agreement is achieved, suggesting that the finite element modelling technique can serve as a predictive tool for surgical procedures.

Apart from using the developed facial model for predicting a patient's post-surgical facial changes, simulations of human facial movement are also considered. In these simulations, a

novel approach is proposed. In this method, the facial muscles responsible for individual facial expressions are assigned with the constitutive muscle material model developed in Chapter 3. Thus, muscles can be activated and contracted to generate individual facial expressions. To test this method, firstly, two facial expressions (smile and disgust) are performed on the patient's pre- and post-surgical facial models. This is followed by the simulation of mouth opening process by activating the anterior digastric and mylohyoid muscles. The simulations of the aforementioned facial movements show promising results.

## 6.2 Directions for future work

As a consequence of the above conclusions, directions for future work are suggested in the following areas:

- **Finite element skeletal muscle model development**

Although, an active, quasi-incompressible, fibre-reinforced and hyperelastic finite element skeletal muscle model has been developed in this thesis, the development of the skeletal muscle model is still in its early stages. In order to consider some of the shortcomings, the model can be improved from the following perspectives:

(i) The skeletal muscle behaviour is known to be viscoelastic. It is shown that the skeletal muscle tissue stress-strain curves are affected by the loading rate (Myers, Wooley, Slotter et al., 1998). Therefore, when modelling the dynamic behaviour of the skeletal muscle, it is necessary to take the muscle strain rate effects into account.

(ii) The developed skeletal muscle model is based on Hill-type and is based at the macroscopic level. This model is able to describe the general macroscopic phenomenon of skeletal muscle, including the skeletal muscle force-velocity and force-length relationships. The shortcoming of this model is that it always involves many material constants, some of which do not have physical interpretations and cannot be measured from experiments. However, in the micro-structural Huxley-type model, most

parameters have a physical meaning and some of them can be measured directly. Besides, the Huxley-type model describes the muscular contraction dynamics at a micro-scale level, which is more reasonable when compared to the Hill-type model. However, the Huxley-type model increases the level of complexity due to the need of capturing data at the micro level. Future work here could be to develop a multi-scale skeletal muscle by combining the merits of Hill-type and Huxley-type models.

(iii) A FEM-NURBS method has been proposed and is able to characterise the fibre orientation arrangement of skeletal muscle. However, this method is unable to handle an arbitrary muscle fibre arrangement at present. When the muscle has multiple branches, this method loses its applicability. Further improvement could be carried out to deal with multi-branches muscles in the future.

- **Development of accurate finite element facial models**

Further to the developed finite element facial model for the simulations of facial surgery and facial movement, more studies are suggested in the following areas:

(i) In this thesis, a finite element facial model is constructed from the patient specific CBCT data of the facial bones and facial skin together with the adjusted generic facial muscles. As the development of MRI and image segmentation techniques and patient specific muscle data becoming available, more accurate simulation is possible. Here, in particular, patient specific muscle data instead of generic muscle data would provide enhanced results. In addition, MRI will provide detailed fibre orientation of each facial muscle. Inputting the fibre orientation information into the FE facial model will significantly increase the simulation accuracy.

(ii) Human skin is a complex tissue consisting of several distinct layers. The complex structure of the skin leads to complex mechanical behaviour. The skin shows a non-linear stress-strain relationship, time-dependent, incompressible, anisotropic and

inhomogeneous behaviour (Hendriks, Brokken, Eemeren, et al. 2003). Besides, wrinkling is a phenomenon common to all human skin. On the face, certain wrinkles are important for self-expression. Any model of skin should take the complex mechanical behaviour and skin wrinkling into consideration in order to make realistic predictions. Therefore, future work should look at developing better facial skin models instead of the linear elastic model used in this thesis.

(iii) In this thesis, the simulation of facial surgery using the finite element technique has only been validated by using one patient. Quantitative validation of the simulation should be considered in the future. On the other hand, in this thesis, simulations of two facial expressions and the mouth opening process have been performed. However, none of these results have been validated at present. In the future, both pre-surgery and post-surgery facial movement data could be collected and used for the validation of these simulated facial movements (facial expressions and mouth opening).

(iv) The FEM-NURBS technique developed in this thesis has been implemented into the ABAQUS system. Because of the restriction of the data passed into LS-DYNA user subroutines, the FEM-NURBS method cannot be implemented into LS-DYNA at present. However, the facial model is developed in LS-DYNA. Thus, the FEM-NURBS method cannot be applied into the developed facial model at the current stage. Further extension of the LS-DYNA code would allow the implementation of the proposed FEM-NURBS technique to the facial model. Then, the accuracy of the facial model with the muscle fibre orientation arrangement modelled by the method presented herein should be investigated.

(v) After the facial surgery, clinician and patient are interested in the expected facial contours and shape some months after the swelling has disappeared. During this healing period, the soft tissue changes due to not only reduced swelling but also ageing and growth. Therefore, incorporating of the soft tissue growth into the finite element facial

model will increase the accuracy of simulating the long-term post-surgery facial movements.

(vi) In addition, more work is needed before the proposed method can be used as a tool in the day-to-day planning of maxillofacial surgery, such as simplifying the process of creating the finite element facial model and the need of finding faster segmentation methods for facial muscles. More future challenging work could be to simulate speech and other facial actions.

# References

ABAQUS Standard User's Manual, Version 6.6, 2006. Hibbit, Karlsson and Sorensen Inc.

ANSA User's Manual, Version 13.0.2, 2009.Greece: BETA CAE Systems S.A.

Audu, M.L. and Davy, D.T. 1985. The influence of muscle model complexity in musculoskeletal modelling. *Journal of Biomechancial Engineering* 107, pp. 147-157.

Barbarino, G., Jabareen, M., Trzewik, J. and Mazza, E. 2008. *Physically Based Finite Element Model of the Face*. In: Bello, F. and Edwards, P.J. eds. Proceedings of the 4th International Symposium on Computational Models for Biomedical Simulation. London, UK: Springer-Verlag Berlin, pp. 1-10.

Barbarino, G.G., Jabareen, M., Trzewik, J., Nkengne, A., Stamatas, G. and Mazza, E. 2009. Development and Validation of a Three-Dimensional Finite Element Model of the Face. *Journal of Biomechanical Engineering* 131(4).

Bath-Balogh, M., Fehrenbach, M.J. and Thomas, P. 2006. *Illustrated Dental Embryology, Histology, and Anatomy*. W.B. Saunders Company.

Belytschko, T., Liu, W.K. and Moran, B. 2000. *Nonlinear finite elements for continua and structures*. New York: Wiley.

Berne, R.M. and Levy, M.N. 2000. *Principles of Physiology*. 3rd ed. Mosby.

Blemker, S.S. and Delp, S.L. 2005. Three-Dimensional Representation of Complex Muscle Architectures and Geometries. *Annals of Biomedical Engineering* 33(5), pp. 661-673.

Blemker, S.S., Pinsky, P.M. and Delp, S.L. 2005. A 3D model of muscle reveals the causes of nonuniform strains in the biceps brachii. *Journal of Biomechanics* 38, pp. 657-665.

Böl, M. and Reese, S. 2008. Micromechanical modelling of skeletal muscles based on the finite element method. *Computer methods in Biomechanics and Biomedical Engineering* 11(5), pp. 489-504.

Bosboom, E.M.H., Hesselink, M.K.C., Oomens, C.W.J., Bouten, C.V.C., Drost, M.R. and Baaijens, F.P.T. 2001. Passive transverse mechanical properties of skeletal muscle under in vivo compression. *Journal of Biomechanics* 34, pp. 1365-1368.

Bosboom, E.M.H., Thomassen, J.A.M., Oomens, C.W.J., Bouten, C.V.C. and Baaijens, F.P.T. 2001. *A numerical experimental approach to determine the transverse mechanical*

*properties of skeletal muscle*. In: Middleton, J. and Jones, M.L. et al. eds. Computer Methods in Biomechanics and Biomedical Engineering - 3. Lisbon: Gordon and Breach Sciences Publishers, pp. 187-192.

Carola, R., Wynsberghe, D.V. and Noback, C. 1995. *Human Anatomy and Physiology*. 3rd ed. McGraw-Hill Education.

Chabanas, M., Luboz, V. and Payan, Y. 2003. Patient specific finite element model of the face soft tissues for computer assisted maxillofacial surgery. *Medical Image Analysis* 7, pp. 131-151.

Chabanas, M., Marecaux, C., Chouly, F., Boutault, F. and Payan, Y. 2004. Evaluating soft tissue simulation in maxillofacial surgery using preoperative and postoperative CT scans. *International Congress Series* 1268, pp. 419-424.

Chabanas, M., Marecaux, C., Payan, Y. and Boutault, F. 2002. *Models for Planning and Simulation in Computer Assisted Orthognatic Surgery*. In: Dohi, T. and Kikinis, R. eds. Proceedings of the 5th International Conference on Medical Image Computing and Computer-Assisted Intervention - MICCAI 2002. Tokyo, Japan: Springer Berlin, pp. 315-322.

Chabanas, M. and Payan, Y. 2000. *A 3D Finite Element Model of the Face for Simulation in Plastic and Maxillo-Facial Surgery*. In: Delp, S.L. and DiGioia, A.M. et al. eds. Proceedings of the Third International Conference on Medical Image Computing and Computer Assisted Intervention. Pittsburgh, PA, USA: Springer-Verlag, pp. 1068-1075.

Chabanas, M., Payan, Y., Marecaux, C., Swider, P. and Boutault, F. 2004. *Comparison of Linear and Non-linear Soft Tissue Models*. In: Cotin, S. and Metaxas, D. eds. Proceedings of the International Symposium on Medical Simulation, ISMS 2004. Cambridge, MA, USA: Springer, pp. 19-27.

Chao, E.Y.S., Lynch, J.D. and Vanderploeg, M.J. 1993. Simulation and animation of musculoskeletal joint system. *Journal of Biomechanical Engineering* 115, pp. 562-568.

Chen, D.T. and Zeltzer, D. 1992. Pump it up: computer animation of a biomechanically based model of muscle using the finite element model. *Computer Graphics* 26(2), pp. 89-98.

Ciarlet, P.G. 1988. *Mathematical elasticity Volume 1: Three-Dimensional Elasticity*. Amsterdam: North-Holland.

Close, R. 1964. Dynamic properties of fast and slow skeletal muscle of the rat during development. *The Journal of Physiology* 173, pp. 74-95.

Criscione, J.C., Douglas, A.S. and Hunger, W.C. 2001. Physically based strain invariant set for materials exhibiting transversely isotropic behavior. *Journal of the Mechanics and Physics of Solids* 49, pp. 871-897.

Crowninshield, R.D. and Richard, A.B. 1981. A physiologically based criterion of muscle force prediction in locomotion. *Journal of Biomechanics* 14(11), pp. 793-801.

Davis, J., Kaufman, K.R. and Lieber, R.L. 2003. Correlation between active and passive isometric force and intramuscular pressure in the isolated rabbit tibialis anterior muscle. *Journal of Biomechanics* 36, pp. 505-512.

Delp, S.L., Loan, J.P., Hoy, M.G, Zajac, F.E., Topp, E.L. and Rosen, J.M. 1990. An interactive graphics-based model of the lower extremity to study orthopaedic surgical procedures. *IEEE Transactions on Biomedical Engineering* 37(8), pp. 757-767.

DiPaola, S. 1992. Extending the Range of Facial Types. *Journal of Visualisation and Computer Animation* 2(4), pp. 129-131.

Duck, F.A. 1990. *Physical Properties of Tissues: A Comprehensive Reference Book.* London: Academic Press.

Edman, K.A.P. 1966. The relation between sarcomere length and active tension in isolated semitendinosus fibres of the frog. *Journal of Physiology* 183(2), pp. 407-417.

Fehrenbach, M.J. and Herring, S.W. 2006. *Illustrated anatomy of the head and neck.* Third ed. Canada: Saunders-Elsevier.

Fenn, W.O. and Marsh, B.S. 1935. Muscular force at different speeds of shortening. *Journal of Physiology* 85, pp. 277-297.

Flory, P.J. 1961. Thermodynamic relations for high elastic materials. *Transactions of the Faraday Society* 57, pp. 829-838.

Fung, Y.C. 1973. Biorheology of soft tissues. *Biorhology* 10(2), pp. 139-155.

Fung, Y.C. 1981. *Biomechanics: Mechanical Properties of Living Tissues.* New York: Springer-Verlag.

Gareis, H., Moshe, S., Baratta, R. and Best, R. 1992. The isometric length-force properties of nine different skeletal muscles. *Journal of Biomechanics* 25, pp. 903-916.

Gatto, F. and Swannell, P. 1990. *Mathematical Descriptions of the Mechanical Properties of Skeletal Muscle: A Review.* University of Queensland: Department of Civil Engineering.

Geomagic Qualify 10 User's Manual, 2008.North Carolina, USA: Raindrop Geomagic, Inc.

Gibson, S. and Mirtich, B. 1997. *A survey of deformable modeling in computer graphics.* Cambridge, MA: Mitsubishi Electric Research Laboratories.

Gielen, A.W.J., Oomens, C.W.J., Bovendeerd, P.H.M., Arts, T. and Janssen, J.D. 2000. A finite element approach for skeletal muscle using a distributed moment model of contraction. *Computer Methods in Biomechanics and Biomedical Engineering* 3(2), pp. 231-244.

Gladilin, E. 2003. *Biomechanical Modeling of Soft Tissue and Facial Expressions for Craniofacial Surgery Planning. PhD Thesis.* Free University, Berlin.

Gladilin, E. and Ivanov, A. 2009. Computational modeling and optimization of soft tissue outcome in cranio-maxillofacial surgery planning. *Computer Methods in Biomechanics and Biomedical Engineering* 12(3), pp. 305-318.

Gladilin, E., Ivanov, A. and Roginsky, V. 2004. *A framework for biomechanical simulation of cranio-maxillofacial surgery interventions.* In: Cotin, S. and Metaxas, D. eds. Proceedings of the International Symposium on Medical Simulation, ISMS 2004. Cambridge, MA, USA: Springer, pp. 287-294.

Gladilin, E., Zachow, S., Deuflhard, P. and Hege, H.-C. 2002a. *Biomechanical Modeling of individual facial emotion expressions.* In: Villanueva, J.J. ed. Proceedings of Visualisation, Imaging and Image Processing. Marbella, Spain: ACTA Press, pp. 7-11.

Gladilin, E., Zachow, S., Deuflhard, P. and Hege, H.-C. 2002b. *Shape-based appraoch for the estimation of individual facial mimics in craniofacial surgery planning.* In: Mun, S.K. ed. Medical Imaging 2002: Visualisation, Image-Guided Procedures, and Display. San Diego, CA, USA, pp. 242-248.

Gladilin, E., Zachow, S., Deuflhard, P. and Hege, H.-C. 2003a. On constitutive modeling of soft tissue for the long-term prediction of cranio-maxillofacial surgery outcome. *International Congress Series* 1256, pp. 343-348.

Gladilin, E., Zachow, S., Deuflhard, P. and Hege, H.-C. 2003b. *Realistic prediction of individual facial emotion expressions for craniofacial surgery simulations.* In: Robert, L. and Galloway, J. eds. Medical Imaging 2003: Visualisation, Image-Guided Procedures, and Display. San Diego, CA, USA, pp. 520-527.

Gladilin, E., Zachow, S., Deuflhard, P. and Hege, H.-C. 2004. Anatomy and physics based facial animation for craniofacial surgery simulations. *Medical & Biological Engineering & Computing* 42(2), pp. 167-170.

Gordon, A. M., Huxley, A. F. and Julian, F. J. 1966. The variation in isometric tension with sarcomere length in vertebrate muscle fibres. *Journal of Physiology* 184, pp. 170-192.

Grieve, A.P. and Armstrong, C.G 1988. *Compressive properties of soft tissues.* In: deGroot, G and Hollander, A.P. et al. eds. Biomechanics XI-A, International Series on Biomechanics. Amsterdam: Free University Press, pp. 531-536.

Gurtin, M.E. 1981. *An Introduction to Continuum Mechanics.* New York: Academic Press.

Hawkins, D. and Bey, M. 1994. A comprehensive approach for studying muscle-tendon mechanic. *Journal of Biomechanical Engineering* 116, pp. 51-55.

Hawkins, D. and Bey, M. 1997. Muscle and tendon force-length properties and their interaction in vivo. *Journal of Biomechanics* 30, pp. 63-70.

Hedenstierna, S., Halldin, P. and Brolin, K. 2008. Evaluation of a combination of continuum and truss finite elements in a model of passive and active muscle tissue. *Computer methods in Biomechanics and Biomedical Engineering* 11(6), pp. 627-639.

Hendriks, F.M., Brokken, D. van Eemeren J.T.W.M., Oomens, C.W.J., Baaijens, F.P.T., Horsten, J.B.A.M. 2003. A numerical-experimental method to characterize the non-linear mechanical behavior of human skin. *Skin Research Technology* 9, pp. 274-283.

Herzog, W. 2000. *Skeletal muscle mechanics: from mechanisms to function.* Chichester: Wiley & Sons.

Herzog, W. and Keurs, H.E.D.J. 1988. Force-length relation of in-vivo human rectus femoris muscles. *Pflugers Archiv European Journal of Physiology* 411(6), pp. 642-647.

Hill, A.V. 1938. The heat of shortening and the dynamic constants of muscle. *Proceedings of the Royal Society of London. Series B, Biological Sciences* 126(843), pp. 136-195.

Hill, A.V. 1970. *First and last experiments in muscle mechanics.* Cambridge: Cambridge University Press.

Holzapfel, G.A. 2000. *Nonlinear Solid Mechanics: A Continuum Approach for Engineering* Chichester: John Wiley & Sons.

Hoschek, J. and Lasser, D. 1993. *Fundamentals of computer aided geometric design.* Natick, MA, USA: A.K.Peters, Ltd.

Hoy, M.G., Zajac, F.E. and Gordon, M.E. 1990. A musculoskeletal model of the human lower extremity: the effect of muscle, tendon, and moment arm on the moment-angle relationship of muscolotendon actuators at the hip, knee, and ankle. *Journal of*

*Biomechanics* 23(2), pp. 157-169.

Humphrey, J.D. and Yin, F.C.P. 1987. On constitutive relations and finite deformations of passive cardiac tissue: 1. A pseudostrain-energy function. *Journal of Biomechanical Engineering* 109, pp. 298-304.

Huxley, A.F. 1957. Muscle structure and theories of contraction. *Progress in Biophysics and Biophysical Chemistry* 7, pp. 257-318.

Huxley, A.F. 2000. Cross-bridge Action: Present Views, Prospects, and Unknowns. In: Herzog, W. ed. *Skeletal Muscle Mechanics: From Mechanisms to Function*. Chichester: Wiley.

Jensen, R.H. and Davy, D.T. 1975. An investigation of muscle lines of action about the hip: A centroid line approach vs. the straight line approach. *Journal of Biomechanics* 8, pp. 103-110.

Johansson, T., Meier, P. and Blickhan, R. 2000. A Finite-Element Model for the Mechanical Analysis of Skeletal Muscle. *Journal of Theoretical Biology* 206, pp. 131-149.

Kahler, K., Haber, J. and Seidel, H.-P. 2001. *Geometry-based Muscle Modeling for Facial Animation*. In: Moller, T. and Ware, C. eds. Proceedings of Graphics Interface. Ottawa, Ontario, Canada: A K Peters Ltd, pp. 37-46.

Kaipatur, N.R. and Flores-Mir, C. 2009. Accuracy of computer programs in predicting orthognathic surgery soft tissue response. *Journal of Oral and Maxillofacial Surgery* 67(4), pp. 751-759.

Kau, C.H., Cronin, A.J. and Richmond, S. 2007. A three-dimensional evaluation of postoperative swelling following orthognathic surgery at 6 months. Plastic and Reconstructive Surgery. 119(7). pp. 2192-2199.

Keeve, E., Girod, S. and Girod, B. 1996a. *Computer-aided Craniofacial Surgery*. In: Lemke, H.U. and Inamura, K.P.D. et al. eds. Proceedings of Computer Assisted Radiology CAR'96. Paris, France: Elsevier Science, pp. 757-762.

Keeve, E., Girod, S. and Girod, B. 1996b. *Craniofacial surgery simulation*. In: Hohne, K.H. and Kikinis, R. eds. Proceedings of the 4th International Conference on Visualisation in Biomedical Computing. Hamburg, Germany: Springer, pp. 541-546.

Keeve, E., Girod, S., Kikinis, R. and Girod, B. 1998. Deformable Modeling of Facial Tissue for Craniofacial Surgery Simulation. *Computer Aided Surgery* 3, pp. 228-238.

Koch, R.M. 2000. *Methods for Physics Based Facial Surgery Prediction. PhD thesis.* Swiss

Federal Institute of Technology.

Koch, R.M., Gross, M.H. and Bosshard, A.A. 1998. Emotion Editing Using Finite Elements. *Computer Graphics Forum* 17(3), pp. C295-C302.

Koch, R.M., Gross, M.H., Carls, F.R., Von Buren, D.F., Fankhauser, G. and Parish, Y.I.H. 1996. *Simulating Facial Surgery Using Finite Element Models*. In: Fujii, J. ed. Proceedings of the 23rd Annual Conference on Computer Graphics and Interactive Techniques. New Orleans, LA, USA: ACM Press New York, pp. 421-428.

Koch, R.M., Roth, S.H.M., Gross, M.H., Zimmermann, A.P. and Sailer, H.F. 2002. *A Framework for Facial Surgery Simulation*. In: Chalmers, A. ed. Proceedings of the 18th Spring Conference on Computer Graphics. Budmerice, Slovakia: ACM Press New York, pp. 33-42.

Kojic, M., Mijailovic, S. and Zdravkovic, N. 1998. Modeling of muscle behavior by the finite element method using Hill's three-element model. *International Journal for numerical methods in engineering* 43, pp. 941-953.

Lee, Y., Terzopoulos, D. and Walters, K. 1995. *Realistic Modeling for Facial Animation*. In: Mair, S.G. and Cook, R. eds. Proceedings of the 22nd International Conference on Computer Graphics and Interactive Techniques. Los Angeles, CA, USA: ACM Press New York, pp. 55-62.

Lee, Y., Terzopoulos, D. and Waters, K. 1993. *Constructing Physics-Based Facial Models of Individuals*. In: Proceedings of the Graphics Interface. Toronto, Canada: A K Peters, Ltd, pp. 1-8.

Lemos, R., Epstein, M., Herzog, W. and Wyvill, B. 2001. Realistic skeletal muscle deformation using finite element analysis. In: *14th Brazilian Symposium on Computer Graphics and Image*. Florianopolis, Brazil: IEEE Computer Society Press. pp. 192-199.

Li, J., Guo, X.J. and Kuang, Z.B. 2001. A nonlinear anisotropic model for porcine aortic heart valves. *Journal of Biomechanics* 34, pp. 1279-1289.

Liebgott, B. 2001. *The Anatomical Basis of Dentistry*. 2nd ed. Mosby.

Limbert, G. and Middleton, J. 2004. A transversely isotropic viscohyperelastic material: Application to the modelling of biological soft connective tissues. *International Journal of Solids and Structures* 41, pp. 4237-4260.

Limbert, G. and Taylor, M. 2002. On the constitutive modelling of biological soft connective tissues: A general theoretical framework and explicit forms of the tensors of elasticity for strongly anisotropic continuum fibre-reinforced composites at finite strain.

*International Journal of Solids and Structures* 39(8), pp. 2343-2358.

LS-DYNA Keyword User's Manual, Version 971, 2007. Livermore, California, USA: Livermore Software Technology Corporation (LSTC).

Luboz, V., Chabanas, M., Swider, P. and Payan, Y. 2005. Orbital and maxillofacial computer aided surgery: patient-specific finite element models to predict surgical outcomes. *Computer Methods in Biomechanics and Biomedical Engineering* 8(4), pp. 259-265.

Ma, D., Lin, F. and Chua, C.K. 2001. Rapid Prototyping Applications in Medicine. Part1: NURBS-Based Volume Modelling. *The International Journal of Advanced Manufacturing Technology* 18, pp. 103-117.

MaKinley, M. and O'Loughlin, V. 2005. *Human Anatomy*. 1st ed. McGraw-Hill Science/Engineering/Math.

Malvern, L.E. 1969. *Introduction to the Mechanics of a Continuous Medium*. Prentice Hall.

Marsden, J.E. and Hughes, T.J.R. 1994. *The Mathematical Foundations of Elasticity*. Dover.

Martini, F.H., Ober, W.C. and Garrison, C.W. 2006. *Fundamentals of Anatomy & Physiology*. 7th ed. Benjamin Cummings.

Martini, F.H., Timmons, M.J. and Tallitsch, R.B. 2008. *Human Anatomy*. 6th ed. Benjamin Cummings.

Martins, J.A.C., Pato, M.P.M. and Pires, E.B. 2006. A finite element model of skeletal muscles. *Virtual and Physical Prototyping* 1(3), pp. 159-170.

Martins, J.A.C., Pato, M.P.M., Pires, E.B., Jorge, R.M., Parente, M. and Mascarenhas, T. 2007. Finite element studies of the deformation of the pelvic floor. *Annals of the New York Academy of Sciences* 1101, pp.316-334.

Martins, J.A.C., Pires, E.B., Salvado, R. and Dinis, P.B. 1998. A numerical model of passive and active behavior of skeletal muscles. *Computer methods in Applied Mechanics and Engineering* 151, pp. 419-433.

Maurel, W., Wu, Y., Thalmann, N.M. and Thalmann, D. 1998. *Biomechanical Models for Soft Tissue Simulation*. Berlin: Springer.

McMahon, T.A. 1984. *Muscles, Reflexes and Locomotion*. Princeton, NJ: Princeton University Press.

Melbourne Dermatology. 2009. Skin Structure Diagram. [WWW] <http: // www. treatment-skincare.com/Glossary/Skin-Structure-Diagram.html> [Accessed 02 June 2010].

Meier, P. and Blickhan, R. 2000. FEM-Simulation of skeletal muscle: the influence of inertia during activation and deactivation. In: Herzog, W. ed. *Skeletal muscle mechanics: From Mechanisms to Function*. Chichester: Wiley, pp. 207-224.

Miller, G.S.P. 1988. The motion dynamics of snakes and worms. *Computer Graphics* 22(4), pp. 169-173.

Mollemans, W., Schutyser, F., Cleynenbreugel, J.V. and Suetens, P. 2003. *Tetrahedral Mass Spring Model for Fast Soft Tissue Deformation*. In: Goos, G and Hartmanis, J. et al. eds. Proceedings of the International Symposium on Surgery Simulation and Soft Tissue Modeling. Juan-Les-Pins, France: Springer-Verlag Berlin, pp. 145-154.

Mollemans, W., Schutyser, F., Cleynenbreugel, J.V. and Suetens, P. 2004. *Fast Soft Tissue Deformation with Tetrahedral Mass Spring Model for Maxillofacial Surgery Planning Systems*. In: Barillot, C. and Haynor, D.R. et al. eds. Proceedings of the International Conference on Medical Image Computing and Computer-Assisted Intervention. Saint-Malo, France: Springer, pp. 371-379.

Mollemans, W., Schutyser, F., Nadjmi, N., Maes, F. and Suetens, P. 2007. Predicting soft tissue deformations for a maxillofacial surgery planning system: From computational strategies to a complete clinical validation. *Medical Image Analysis* 11, pp. 282-301.

Mollemans, W., Schutyser, F., Nadjmi, N. and Suetens, P. 2005. Very fast soft tissue predictions with mass tensor model for maxillofacial surgery planning systems. *International Congress Series* 1281, pp. 491-496.

MSC/PATRAN User's Manual, 2008, California, USA: MSC.Software Corporation.

Muhl, Z.E. 1982. Active length-tension relation and the effect of muscle pinnation on fibre lengthening. *Journal of Morphology* 173(3), pp. 285-292.

Myers, B.S., Van Ee, C.A., Camacho, D.L.A., Woolley, C.T. and Best, T.M. 1995. On the structural and material properties of mammalian skeletal muscle and its relevance to human cervical impact dynamics. In: *Proceedings of the 39th Stapp Car Crash Conference*. San Francisco. CA. pp. 203-214.

Myers, B.S., Wooley, C.T., Slotter, T.L., Garrett, W.E. and Best, T.M. 1998. The influence of strain rate on the passive and stimulated engineeering stress-large strain behavior of the rabbit tibialis anterior muscle. *Journal of Biomechanical Engineering* 120(1), pp. 126-132.

Nedel, L.P. and Thalmann, D. 1998. Real time muscle deformation using mass-spring

systems. In: *Computer Graphics International*. Hannover, Germany.

Ng-Thow-Hing, V. 2001. *Anatomically-based models for physical and geometric reconstruction of humans and other animals. PhD Thesis.* University of Toronto.

Ng-Thow-Hing, V. and Fiume, E. 1997. Interactive display and animation of b-spline solids as muscle shape primitives. In: *Computer Animation and Simulation*. Budapest, Hungary.

Ng-Thow-Hing, V. and Fiume, E. 2002. Application-specific muscle representation. In: *Graphics Interface 2002*. Calgary, Alberta, Canada.

Oasys 9.3 PRIMER and D3PLOT User's Manual, 2009.Solihull, UK: Oasys Ltd & Arup.

Odland, G. 1991. Structure of the skin. In: Goldsmith, L.A. ed. *Physiology, biochemistry, and molecular biology of the skin*. Oxford: Oxford University Press.

Ogden, R.W. 1997. *Non-linear Elastic Deformations*. New York: Dover.

Oomens, C.W.J., Maenhout, M., van Oijen, C.H., Drost, M.R. and Baaijens, F.P. 2003. Finite element modelling of contracting skeletal muscle. *Philosophical Transactions of the Royal Society B: Biological Sciences* 358(1437), pp. 1453-1460.

Otten, E. 1987. A myocybernetic model of the jaw system of the rat. *Journal of Neuroscience Methods* 21, pp. 287-302.

Palevski, A., Glaich, I.I., Portnoy, S., Linder-Ganz, E. and Gefen, A. 2006. Stress relaxation of porcine gluteus muscle subjected to sudden transverse deformation as related to pressure sore modeling. *Journal of Biomechancial Engineering* 128(5), pp. 782-787.

Pandy, M.G, Zajac, F.E., Sim, E. and Levine, W.S. 1990. An optimal control model for maximum-heigth human jumping. *Journal of Biomechanics* 23(12), pp. 1185-1198.

Parke, F.I. 1982. Parameterized Models for Facial Animation. *Computer Graphics and Applications* 2(9), pp. 61-68.

Parke, F.I. and Waters, K. 2008. *Computer Facial Animation*. Second ed. A K Peters, Ltd.

Pinto, J.G. and Fung, Y.C. 1973. Mechanical properties of the heart muscle in the passive state. *Journal of Biomechanics* 6, pp. 597-616.

Pinto, J.G. and Patitucci, P.J. 1977. Creep in cardiac muscle. *American Journal of Physiology: Heart and Circulatory Physiology* 232(6), pp. 553-563.

Pitermann, M. and Munhall, K.G. 2001. An inverse dynamics approach to face animation.

*The Journal of the Acoustical Society of America* 110(3), pp. 1570-1580.

Platt, S.M. and Badler, N.I. 1981. Animating Facial Expressions. *Computer Graphics* 15(3), pp. 245-252.

Pocock, G. and Richards, C.D. 2004. *Human Physiology: The Basis of Medicine*. Oxford: Oxford University Press.

Pro/Engineer 2004. Getting Started with Pro/ENGINEER Wildfire 2.0. Parametric Technology Corp. (PTC).

Protsenko, D.E. and Wong, B.J.F. 2007. Laser assisted straightening of deformed cartilage: Numerical model. *Lasers in Surgery and Medicine* 39(3), pp. 245-255.

RAPIDFORM User's Manual 2006. Seoul, South Korea: INUS Technology Inc. & Rapidform Inc.

Richmond, S., Beldie, L., Lu, Y.T., Walker, B., Middleton, J. and Wilkinson, C. 2010. Predicting and managing surgical intervention in cranio-facial disharmony- a biomechanical perspective. In: Kau, C.H. and Richmond, S. eds. *Textbook of Three-Dimensional Imaging: The Face and Underlying Structures*. Chichester: Blackwell.

Rogers, D.F. 2001. *An introduction to NURBS: with historical perspective*. San Francisco, CA, USA: Morgan Kaufmann Publishers.

Roth, S.H.M. 2002. *Bernstein-Bezier Representations for Facial Surgery Simulation. PhD thesis.* Swiss Federal Institute of Technology.

Roth, S.H.M., Gross, M.H., Turello, S. and Carls, F.R. 1998. A Bernstein-Bezier Based Approach to Soft Tissue Simulation. *Computer Graphics Forum* 17(3), pp. 285-294.

Sarkar, S., Majumder, S. and Roychowdhury, A. 2004. Response of human head under static and dynamic load using finite element method. *Trends in Biomaterials and Artificial Organs* 17(2), pp. 130-134.

Sarti, A., Gori, R. and Lamberti, C. 1999. A physically based model to simulate maxillo-facial surgery from 3D CT images. *Future Generation Computer System* 15(2), pp. 217-221.

Schuenke, M., Schulte, E. amd Schumacher, U. 2007. *Thieme Atlas of Anatomy: Head and Neuroanatomy*. Thieme Publishing Group.

Shabana, A.A. 2008. *Computational Continuum Mechanics*. New York, USA: Cambridge University Press.

Silverthorn, D.U., Ober, W.C. and Garrison, C.W. 2009. *Human Physiology: An Integrated Approach*. 5th ed. Pearson Education.

Simo, J.C., Taylor, R.L. and Pister, K.S. 1985. Variational and projection methods for the volume constraint in finite deformation elastoplasticity. *Computer Methods in Applied Mechanics and Engineering* 51, pp. 177-208.

Simpleware $^{+}$ScanCAD, ScanIP and $^{+}$ScanFE User's Manual, version 3.1, 2008. Innovation Centre, University of Exeter, UK: Simpleware Ltd.

Spencer, A.J.M. 1984. *Continuum theory of the mechanics of fibre-reinforced composites.* New York: Springer-Verlag.

Stojanovic, B., Kojic, M., Rosic, M., Tsui, C.P. and Tang, C.Y. 2006. An extension of Hill's three-component model to include different fibre types in finite element modelling of muscle. *International Journal for Numerical Methods in Engineering* 71(7), pp. 801-817.

Swatland, H.J. 1995. Electronic Assessment of Muscle Quality. In: Jones, S.D.M. ed. *Quality and Grading of Carcasses of Meat Animals.* CRC Press.

Tang, C.Y., Stojanovic, B., Tsui, C.P. and Kojic, M. 2005. Modeling of muscle fatigue using Hill's model. *Bio-Medical Materials and Engineering* 15, pp. 341-348.

Tang, C.Y., Tsui, C.P., Stojanovic, B. and Kojic, M. 2007. Finite element modelling of skeletal muscle coupled with fatigue. *International Journal of Mechanical Sciences* 49, pp. 1179-1191.

Tang, C.Y., Zhang, G. and Tsui, C.P. 2009. A 3D skeletal muscle model coupled with active contraction of muscle fibres and hyperelastic behaviour. *Journal of Biomechanics* 43(7), pp. 865-872.

Teran, J., Blemker, S., Ng-Thow-Hign, V. and Fedkiw, R. 2003. Finite volume method for the simulation of skeletal muscle. In: *Proceedings of the 2003 SIGGRAPH/Eurographics Symposium on Computer Animation.* San Diego, California.

Terzopoulos, D. and Waters, K. 1990. Physically-Based Facial Modeling, Analysis, and Animation. *The Journal of Visualisation and Computer Animation* 1(2), pp. 73-80.

Teschner, M., Girod, S. and Girod, B. 1999. *Optimization Approaches for Soft-Tissue Prediction in Craniofacial Surgery Simulation.* In: Taylor, C.J. and Colchester, A.C.F. eds. The Second International Conference on Medical Image Computing and Computer-Assisted Intervention. Cambridge, UK: Springer-Verlag London, pp. 1183-1190.

Teschner, M., Girod, S. and Girod, B. 2000. *Direct Computation of Nonlinear Soft-Tissue Deformation.* In: Girod, B. and Greiner, G. et al. eds. Proceedings of Vision, modeling, and visualisation 2000. Saarbrucken, Germany: IOS Press, pp. 383-390.

Tortora, G.J. and Grabowski, S.R. 2002. *Principles of Anatomy and Physiology.* 10th ed. John Wiley & Sons.

Tran, H.V., Charleux, F., Rachik, M., Ehrlacher, A and Ho Ba Tho, M.C. 2007. In vivo characterisation of the mechanical properties of human skin derived from MRI and indentation techniques. *Computer methods in Biomechanics and Biomedical Engineering* 10(6), pp. 401-407.

Truesdell, C. and Noll, W. 1992. *The Non-linear Field Theories of Mechanics.* New York: Springer-Verlag.

Truesdell, C. and Noll, W. 2004. *The non-linear field theories of mechanics.* 3rd ed. Heidelberg: Springer-Verlag.

Vander, A.J., Sherman, J. and Luciano, D.S. 2003. *Human Physiology: The Mechanisms of Body Function.* 9Rev ed. McGraw-Hill Education.

Vandewalle, P., Schutyser, F., Cleynenbreugel, J.V. and Suetens, P. 2003. *Modeling of Facial soft tissue Growth for Maxillofacial Surgery Planning Environments.* In: Goos, G. and Hartmanis, J., et al. eds. Proceedings of the International Symposium on Surgery Simulation and Soft Tissue Modeling. Juan-Les-Pins, France: Springer-Verlag Berlin, pp. 27-37.

Van Leeuwen, J.L. 1991. Optimum power output and structural design of sarcomeres. *Journal of Theoretical Biology.* 149, pp. 229-256.

Van Loocke, M. 2007. *Passive mechanical properties of skeletal muscle in compression. PhD Thesis.* Trinity College Dublin.

Van Loocke, M., Lyons, C.G. and Simms, C.K. 2006. A validated model of passive muscle in compression. *Journal of Biomechanics* 39, pp. 2999-3009.

Van Loocke, M., Lyons, C.G. and Simms, C.K. 2008. Viscoelastic properties of passive skeletal muscle in compression: Stress-relaxation behavior and constitutive modelling. *Journal of Biomechanics* 41, pp. 1555-1566.

Vicente, G.S., Buchart, C., Borro, D. and Celigueta, J.T. 2009. Maxillofacial surgery simulation using a mass-spring model derived from continuum and the scaled displacement method. *International Journal of Computer Assisted Radiology and Surgery* 4(1), pp. 89-98.

Warwic, R. and Willems, P.L. 1973. *Gray's Anatomy*. 35th British ed. Philadelphia: W.B.Saunders.

Waters, K. 1987. *A muscle model for animation three-dimensional facial expression*. In: C., S.M. ed. Proceedings of the 14th annual conference on Computer graphics and interactive techniques. Anaheim, California, USA: ACM New York, pp. 17-24.

Weiss, J.A., Maker, B.N. and Govindjee, S. 1996. Finite element implementation of incompressible, transversely isotropic hyperelasticity. *Computer Methods in Applied Mechanics and Engineering* 135, pp. 107-128.

Widmaier, E.P., Raff, H. and Strang, K.T. 2005. *Vander's Human Physiology - The Mechanisms of body Function*. 10th ed. McGraw-Hill Higher Education.

Wilkinson, C., Rynn, C., Peters, H., Taister, M., Kau, H.C. and Richmond, S. 2006. A blind accuracy assessment of computer-modelled forensic facial reconstruction using computed tomography data from live subjects. *Forensic Science, Medicine, and Pathology*. 2(3), pp.179-187.

Winters, J.M. 1990. Hill-based muscle models: A systems engineering perspective. In: Winters, J.M. and Woo, S.Y. eds. *Multiple Muscle Systems: Biomechanics and Movement Organisation*. New York: Springer-Verlag, pp. 69-96.

Woledge, R.C., Curtin, N.A. and Homsher, E. 1985. Energetic Aspects of Muscle Contraction. *Monographs of the Physiological Society* 41, pp. 1-357.

Yu, H.S., Baik, H.S., Sung, S.J., Kim, K.D. and Cho, Y.S. 2007. Three-dimensional finite-element analysis of maxillary protraction with and without rapid palatal expansion. *The European Journal of Orthodontics* 29(2), pp. 118-125.

Zachow, S., Gladilin, E., Zeilhofer, H.F. and Sader, R. 2001. *Improved 3d osteotomy planning in cranio-maxillofacial surgery*. In: Niessen, W.J. and Viergever, M.A. eds. Medical Image Computing and Computer-Assisted Intervention - MICCAI 2001. Utrecht, Netherlands: Springer, pp. 473-481.

Zachow, S., Hege, H.C. and Deuflhard, P. 2006. Computer-Assisted Planning in Cranio-Maxillofacial Surgery. *Journal of Computing and Information Technology* 14(1), pp. 53-64.

Zahalak, G.I. 1981. A distribution moment approximation for kinetic theories of muscular contraction. *Mathematical Biosciences* 55, pp. 89-114.

Zahalak, G.I. and Ma, S.P. 1990. Muscle activation and contraction: constitutive relations

based directly on cross-bridge kinetics. *Journal of Biomechancial Engineering* 112, pp. 52-62.

Zajac, F.E. 1989. Muscle and tendon: Properties, models, scaling and application to biomechanics and motor control. *Critical Reviews in Biomedical Engineering* 17, pp. 359-411.

Zajac, F.E., Topp, E.L. and Stevenson, P.J. 1986. A dimensionless musculotendon model. In: *The 8th Annual Conference of IEEE Engineering in Medical and Biology Society.* Fort Worth, Texas USA.

Zhang, Y., Prakash, E.C. and Sung, E. 2004. A New Physical Model with Multilayer Architecture for Facial Expression Animation Using Dynamic Adaptive Mesh. *IEEE Transactions on Visualisation and Computer Graphics* 10(3), pp. 339-352.

Zhang, Y.P., Mak, A.F.T. and Lue, B. 1999. Objective assessment of limb tissue elasticity: Development of a manual indentation procedure. *Journal of Rehabilitation Research and Development* 36(2), pp. 71-85.

Zhou, X.L. and Lu, J. 2005. NURBS-Based Galerkin Method and Application to Skeletal Muscle Modeling. In: *ACM Symposium on Solid and Physical Modeling.* Cambridge, MA, USA.

Zhurov, A.I., Limbert, G, Aeschlimann, D.P. and Middleton, J. 2007. A Constitutive Model for the Periodontal Ligament as a Compressible Transversely Isotropic Visco-Hyperelastic Tissue. *Computer Methods in Biomechanics and Biomedical Engineering* 10(3), pp. 223-235.

# List of Publications

Below are the author's publications during his PhD study period.

## Journal papers

Lu, Y.T., Zhu, H.X., Richmond, S. and Middleton, J., 2010. A Visco-Hyperelastic Constitutive Skeletal Muscle Model. *Journal of Biomechanics.* (In press)

Lu, Y.T., Zhu, H.X., Richmond, S. and Middleton, J., 2010. Modelling skeletal muscle fibre orientation arrangement. *Computer Methods in Biomechanics and Biomedical Engineering* (In press).

Beldie, L., Walker, B., Lu, Y.T., Richmond, S. and Middleton, J., 2010. Finite element modelling of maxillofacial surgery and facial expressions. *International Journal of Medical Robotics and Computer Assisted Surgery.* (In press)

Lu, Y.T., Zhu, H.X., Richmond, S. and Middleton, J., 2010. Fibre-matrix interaction investigation for soft tissue under biaxial loadings. *International Journal for Numerical Methods in Biomedical Engineering.* (Under review)

Lu, Y.T., Beldie, L., Walker, B., Richmond, S. and Middleton, J., 2010. Parametric study of a Hill-type hyperelastic skeletal muscle model. *Proceedings of the IMechE, Part H: Journal of Engineering in Medicine.* (Under review)

## Conference papers

Lu, Y.T., Zhu, H.X., Richmond, S. and Middleton, J., 2010. Modelling the fibre orientation arrangement of skeletal muscles using FEM-NURBS method. In: *9th International Symposium on Computer Methods in Biomechanics and Biomedical Engineering.* February 24-27th, Valencia, Spain.

Lu, Y.T., Beldie, L., Zhu, H.X., Brian, W., Richmond, S. and Middleton, J., 2009. *Three Dimensional Skeletal Muscle Tissue Modelling.* In: Jorge, R.M.N. and Santos, S.M. et al. eds. *Proceedings of the first International Conference on Biodental Engineering.* June, 26-27th, Porto, Portugal: CRC Press, pp. 65-70.

Liu, X.H., Lu, Y.T. 2009. A discrete size optimization method for frame structures. In: Lecture notes in Decision Sciences – Global Optimization: Theory, Methods & Applications I. Hong Kong: Global-Link Publisher. 822-827.

# Appendix A — Abbreviations

| | |
|---|---|
| 1D | One-dimensional |
| 3D | Three-dimensional |
| 4D | Four-dimensional |
| ARCCA | Advanced Research Computing @ Cardiff |
| CAD | Computer-aided Design |
| CAM | Computer-aided Manufacturing |
| CBCT | Cone Beam Computerised Tomography |
| CE | Contractile element |
| CT | Computer Tomography |
| DM | Distributed moment |
| FE | Finite element |
| FEA | Finite Element Analysis |
| FEM | Finite Element Model |
| HPC | High-Performance Computing |
| MRI | Magnetic Resonance Imaging |
| MSD | Mass-Spring-Damper |
| MSM | Mass-Spring Model |
| MTM | Mass Tensor Model |
| NURBS | Non-uniform Rational Basis Spline |
| OS | Operating system |
| PE | Parallel element |
| SEE | Series elastic element |
| SMFE | Super-positioned muscle finite element |
| SR | Sarcoplasmatic reticulum |
| TA | Tibialis anterior |
| TMJ | Temporomandibular joint |
| UMAT | User-defined material |

# Appendix B — Notation

Boldface is used for tensors

## Chapter 2

| | |
|---|---|
| $\mathbf{a}$ | Outward unit vector in the current configuration |
| $\mathbf{A}$ | Outward unit vector in the reference configuration |
| $\mathbf{B}$ | Left Cauchy-Green deformation tensor |
| $\overline{\mathbf{B}}$ | Left Cauchy-Green tensor with the volume change eliminated |
| $B_y$ | A continuum body |
| $\mathbf{C}$ | Right Cauchy-Green deformation tensor |
| $\overline{\mathbf{C}}$ | Right Cauchy-Green tensor with the volume change eliminated |
| $\hat{\mathbf{C}}$ | Material version of the second elasticity tensor |
| $\tilde{\mathbf{C}}$ | Spatial version of the second elasticity tensor |
| $\mathbf{E}$ | Green strain tensor |
| $\mathbf{E}^i$ | Unit base vector components in the reference configuration |
| $\mathbf{e}^i$ | Unit base vector components in the current configuration |
| $\mathbf{F}$ | Deformation gradient |
| $\mathbf{F}_{vol}$ | Dilatational part of the deformation gradient |
| $\mathbf{F}_{dev}$ | Deviatoric part of the deformation gradient |
| $I_1, I_2, \ldots, I_5$ | Strain invariants |
| $\bar{I}_1, \bar{I}_2, \bar{I}_4, \bar{I}_5$ | Strain invariants with the volume change eliminated |
| $J$ | Jacobian determinant of the deformation gradient |
| $\mathbf{n}$ | Fibre direction in the deformed configuration |

| | |
|---|---|
| $\mathbf{N}$ | Fibre direction in the undeformed configuration |
| $\mathbf{P}$ | First Piola-Kirchhoff stress tensor |
| $P_t$ | A particle in the deformation configuration |
| $P_0$ | A particle in the undeformed configuration |
| $Q_t$ | A particle in the deformation configuration |
| $Q_0$ | A particle in the undeformed configuration |
| $\mathbf{S}$ | Second Piola-Kirchhoff stress tensor |
| $S_{vol}$ | Dilatational part of the deformation gradient |
| $S_{dev}$ | Deviatoric part of the deformation gradient |
| $\mathbf{t}$ | Cauchy traction vector |
| $\mathbf{t_0}$ | First Piola-Kirchhoff traction vector |
| $\mathrm{u}$ | Displacement of a material point |
| $u(\mathbf{X},t)$ | Displacement of material point X at time t |
| $W(\mathbf{C})$ | Strain energy function |
| $W_\alpha$ | Derivatives of strain energy function W with respect to $I_\alpha(\alpha = 1,2,\cdots)$ |
| $W_{vol}$ | Dilational part of the strain energy |
| $W_{dev}$ | Deviatoric part of the strain energy |
| $\mathbf{x}$ | Position vector of a material point in the current configuration |
| $x_i$ | Components of position vector in the current configuration |
| $\mathbf{X}$ | Position vector of a material point in the reference configuration |
| $X_I$ | Components of position vector in the reference configuration |
| $\lambda_f$ | Fibre stretch ratio in the direction of the undeformed fibre |
| $\lambda_1, \lambda_2, \lambda_3$ | Eigenvalues of the deformation gradient F |
| $\boldsymbol{\sigma}$ | Cauchy stress |

| | |
|---|---|
| $\Gamma_0$ | Boundaries in the reference configuration |
| $\Gamma_t$ | Boundaries in the current configuration |
| $\varphi(\mathbf{X},t)$ | Mapping function |
| $\psi(\mathbf{E})$ | Strain energy function |
| $\Omega_0$ | Reference configuration |
| $\Omega_t$ | Current configuration |

## Chapter 3

| | |
|---|---|
| $A$ | Material constants associated with PE |
| $b,c$ | Material constants associated with the isotropic matrix |
| $d$ | Offset of the eccentric part of force-velocity function |
| $D$ | Compressibility constant |
| $E$ | Young's modulus |
| $f(\xi)$ | Attachment rate function |
| $f_v$ | Muscle force-velocity function |
| $f_\lambda$ | Muscle force-length function |
| $f_t$ | Muscle activation function |
| $F_{CE}$ | Force generated in the contractile element of Hill's muscle model |
| $F_f$ | Total muscle force generated in Hill's muscle model |
| $F_{max}$ | Maximal isometric force |
| $F_{PE}$ | Force generated in the parallel element of Hill's muscle model |
| $F_{SEE}$ | Force generated in the series elastic element of Hill's muscle model |
| $g(\xi)$ | Detachment rate function |
| $G$ | Shear modulus |

| | |
|---|---|
| $\mathbf{I}$ | Second order unit tensor |
| $\bar{I}_1^C$ | First invariant of the right Cauchy-Green strain tensor with the volume change eliminated |
| $J$ | Jacobian of the deformation gradient |
| $K$ | Bulk modulus |
| $k_c, k_e$ | Shape parameters of the force-velocity curves |
| $\mathbf{L}$ | Symmetric fourth order unit tensor |
| $L_{PE}$ | Total muscle length |
| $L_{CE}$ | Muscle length component in the contractile element |
| $L_{SEE}$ | Muscle length component in the series elastic element |
| $\mathbf{N}$ | Fibre direction vector in the undeformed configuration |
| $\mathbf{n}$ | Fibre direction vector in the deformed configuration |
| n(x,t) | Distribution function |
| $n_1$ | Activation level before and after the activation |
| $n_2$ | Activation level during the activation |
| $Q_\theta$ | θ-th normalised moment of the bond distribution function |
| r | Activation factor |
| $S$ | Parameter related to the rate of the chemical process |
| $t_0$ | Activation time |
| $t_1$ | Deactivation time |
| u(t) | Scaled shortening velocity of a half sarcomere |
| $U$ | Total strain energy in the muscle |
| $U_f$ | Strain energy stored in the muscle fibre |
| $U_I$ | Strain energy stored in the isotropic matrix |

| | |
|---|---|
| $U_J$ | Strain energy associated with the volume change |
| $U_{PE}$ | Strain energy stored in the parallel element (PE) |
| $U_{SEE}$ | Strain energy stored in the series elastic element (SEE) |
| $\nu$ | Poisson's ratio |
| $\alpha_a$ | Fibre activation |
| $\alpha, \beta$ | Material constants associated with SEE |
| $\Delta\lambda_s$ | Fibre stretch increment in the series elastic element |
| $\xi^{CE}$ | A non-dimensional quantity proportional to the strain of CE |
| $\lambda$ | Extension ratio in the fibre direction |
| $\bar{\lambda}_f$ | Fibre stretch ratio with the volume change eliminated |
| $\lambda_s$ | Fibre stretch in the series elastic element |
| $\lambda_{opt}$ | Optimal fibre stretch |
| $\dot{\lambda}_m^{\min}$ | Minimum stretch rate |
| $\dot{\lambda}_m$ | Stretch rate in CE |
| $\boldsymbol{\sigma}$ | Cauchy stress produced in the whole muscle |
| $\sigma_0$ | Maximal isometric stress |
| $\sigma_a$ | Active stress generated by all cross-bridges |
| $\sigma_{CE}$ | Stress produced in the contractile element |
| $\boldsymbol{\sigma}_{fibre}$ | Stress produced in the muscle fibres |
| $\boldsymbol{\sigma}_{incomp}$ | Stress due to the volume change |
| $\boldsymbol{\sigma}_{matrix}$ | Stress produced in the surrounding matrix |
| $\boldsymbol{\sigma}_p$ | Passive stress produced in the muscle model |
| $\sigma_{PE}$ | Stress produced in the parallel element |
| $\sigma_{SEE}$ | Stress produced in the series elastic element |

| | |
|---|---|
| $\boldsymbol{\sigma}^{E}$ | Stress produced in the surrounding matrix |
| $\boldsymbol{\sigma}^{s}$ | Stress produced in the active muscle fibre |
| $\phi$ | Fraction of the muscle fibre |
| $\varphi$ | Fraction of participating myosin heads |

## Chapter 4

| | |
|---|---|
| $U$ | Strain energy density function |
| $I_1$ | First invariant of the strain tensor |
| $J$ | Jacobian of the deformation gradient |
| $C_{10}$ | Material parameter |
| $K$ | Material parameter |

## Chapter 5

| | |
|---|---|
| $\mathbf{B}_i$ | Control point position vectors for NURBS curve |
| $\mathbf{B}_{i,j}$ | Control point position vectors for NURBS surface |
| $\mathbf{B}_{i,j,k}$ | Control point position vectors for NURBS solid |
| $\mathbf{B}_{\mathbf{l}}^{\mathbf{h}}$ | Four-dimensional homogeneous control vertices |
| $\mathbf{B}_{i,j}^{h}$ | Four-dimensional homogeneous control net vertices |
| $\overline{\mathbf{B}}$ | Left Cauchy-Green strain tensor with the volume change eliminated |
| $b,c$ | Material constants associated with the isotropic matrix |
| $\overline{\mathbf{C}}$ | Right Cauchy-Green deformation tensor with the volume change eliminated |
| $\mathbf{D}_j$ | Control point vectors of the centreline |
| $D$ | Material constant associated with the volume change |
| $d$ | Offset of the eccentric force-velocity function |

| | |
|---|---|
| $\mathbf{E}$ | Green strain tensor |
| $\mathbf{F}$ | Deformation gradient tensor |
| $\mathbf{H}(u,v,w)$ | Rational B-spline solid representation |
| $\mathbf{H}$ | Material tangent stiffness tensor |
| $\mathbf{h}$ | Spatial form of the material tangent stiffness tensor |
| $\mathbf{I}$ | Second order unit tensor |
| $\bar{I}_1^C$ | First invariant of the right Cauchy-Green strain tensor with the volume change eliminated |
| $J$ | Jacobian of the deformation gradient |
| $k$ | Material constant, ratio of length of CE to that of SEE |
| $k_e$, $a_v$ | Shape parameters of hyperbolic force-velocity curve of contractile element |
| $\mathbf{L}$ | Symmetric fourth order unit tensor |
| $\mathbf{N}$ | Fibre direction vector in the undeformed configuration |
| $\mathbf{n}$ | Fibre direction vector in the deformed configuration |
| $N_{i,p}(u)$ | Non-rational B-spline basis functions |
| $\mathbf{P}(t)$ | B-spline curve representation |
| $\mathbf{Q}(u,v)$ | Cartesian product rational B-spline surface representation |
| $R_{i,p}(t)$ | Rational B-spline curve basis functions |
| $\mathbf{S}$ | Second Piola-Kirchhoff stress tensor |
| $S_{i,j}(u,v)$ | Rational B-spline surface basis function |
| $S_{i,j,k}(u,v,w)$ | Rational B-spline solid basis function |
| U | Total strain energy in the muscle |
| $U_I$ | Strain energy stored in the isotropic matrix |
| $U_f$ | Strain energy stored in the muscle fibre |

| | |
|---|---|
| $U_J$ | Strain energy associated with the volume change |
| $U_{PE}$ | Strain energy stored in the parallel element (PE) |
| $U_{SE}$ | Strain energy stored in the series elastic element (SEE) |
| $w_{i,j}$ | Weight factors |
| $\alpha_a$ | Activation function |
| $\alpha, \beta$ | Material constants associated with the series elastic element |
| $\Delta\lambda_s$ | Fibre stretch increment in the series elastic element |
| $\dot{\lambda}_{m0}$ | Strain rate corresponding to the maximum isometric tetanised force |
| $\bar{\lambda}_f$ | Fibre stretch ratio with the volume change eliminated |
| $\boldsymbol{\sigma}$ | Cauchy stress tensor |
| $\sigma_0$ | Material constant, the maximal isometric stress |
| $\sigma_{PE}$ | Stress produced in the parallel element (PE) |
| $\sigma_{SE}$ | Stress produced in the series elastic element (SEE) |

# Appendix C — Hill's Force-Velocity Equation

The most famous equation in muscle mechanics is Hill's equation (Hill, 1938). The equation refers to the property of a skeletal muscle in the tetanised condition. It has the form:

$$(v + p)(T + q) = p(T_0 + q) \qquad \text{(C.1)}$$

where $T$ represents the tension in a muscle; $v$ represents the velocity of contraction; $T_0$ is the maximum tension developed in the muscle under isometric condition; and $q$, $p$ are constants.

Hill's Equation (C.1) is an empirical equation based on the experimental data from the frog Sartorius muscle. During the experiment, the muscle was held under the isometric condition, i.e. its ends were clamped. Then the muscle was stimulated electrically at a very high voltage and frequency to generate the maximum tension. After this, the muscle was released suddenly to a new length. The tensile force $T$ corresponding to this new length was developed. $T$ is smaller than $T_0$. Immediately after the release, the contraction velocity was measured. The experimental data are plotted in Figure (C.1), where the circles represent the experimental data and the solid curve represents Hill's Equation (C.1) with $q$ = 357 gram/sq.cm; $q/T_0 = 0.22$; $p$ = 1.03 cm./sec.

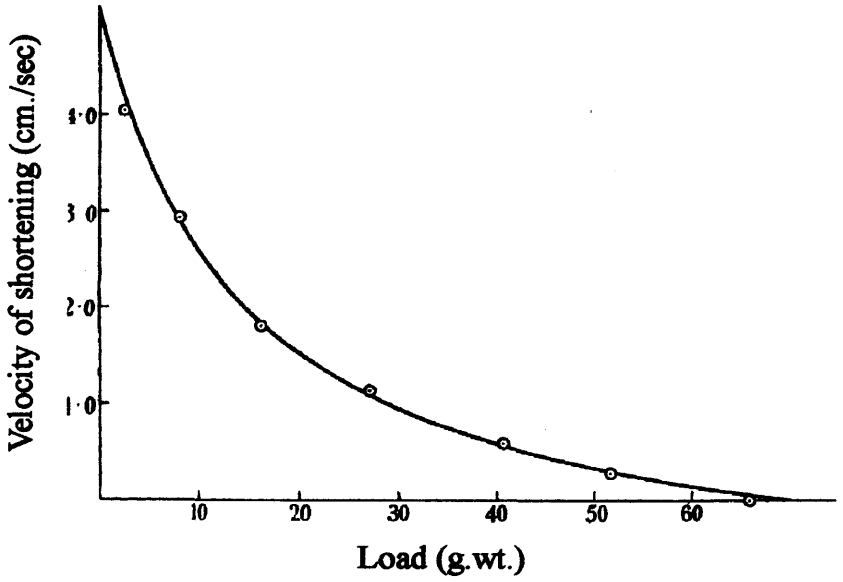


**Figure C.1.** Relation between load (g.wt.) and speed of shortening (cm./sec.) during isotonic contraction. (Hill, 1938)

From Figure C.1, it is seen that Hill's equation shows a hyperbolic relation between $T$ and $v$. The higher the contraction velocity, the lower is the tension; the slower the contraction velocity, the higher is the tension.

A non-dimensional form of Hill's equation is given as:

$$\frac{T}{T_0} = \frac{1-(v/v_0)}{1+k_q(v/v_0)} \tag{C.2}$$

Or

$$\frac{v}{v_0} = \frac{1-(T/T_0)}{1+k_q(T/T_0)} \tag{C.3}$$

where $k_q = T_0/q$ and the maximum velocity $v_0 = pT_0/q$. The constant $q$ is almost proportional to $T_0$. The value of $k_q$ for skeletal muscle is in the range of 1.2 to 4 (Fung 1981)

# Appendix D — Geometry Relation in Hill's Three-Element Model

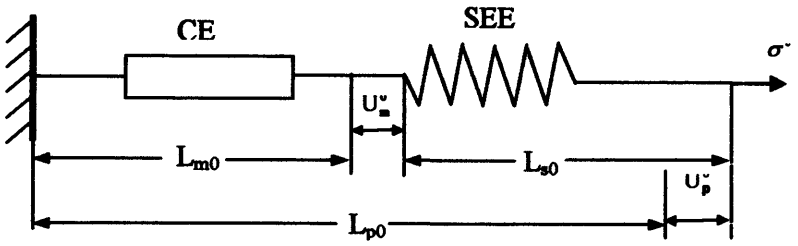


**Figure D.1** Geometry of Hill's Model (Kojic, Mijailovic and Zdravkovic, 1998)

When the Hill's three-element muscle is stretched without activation, the geometry relation among the three elements can be drawn in Figure D.1. The following relation can be obtained from this figure:

$$L_{p0} + U_p^0 = L_{m0} + U_m^0 + L_{s0} + U_s^0 \tag{D.1}$$

where $L_{p0}$ is the total initial length; $L_{m0}$ and $L_{s0}$ are the initial lengths of the contractile and series elastic elements respectively; $U_P^0$ is the total displacement, $U_m^0$ and $U_s^0$ are the displacements of the contractile and series elastic elements respectively. Since the muscle is passively elongated, the displacement in the series elastic element is zero, i.e. $U_s^0 = 0$, as illustrated in Figure D.1

Assuming the ratio of the length of contractile element to that of series elastic element as:

$$k = L_{s0} / L_{m0} \tag{D.2}$$

When the muscle has no deformation, the following relation holds:

$$L_{p0} = L_{m0} + L_{s0} \tag{D.3}$$

Dividing Equation (D.1) by $L_{m0}$ and using Equations (D.2) and (D.3), the following relation is obtained:

$$\Delta\lambda_m^0 = (1+k)\Delta\lambda_p^0 - k\Delta\lambda_s^0 \tag{D.4}$$

where $\Delta\lambda_m^0$, $\Delta\lambda_p^0$ and $\Delta\lambda_s^0$ are defined as: $\Delta\lambda_m^0 = \frac{U_m^0}{L_{m0}}, \Delta\lambda_p^0 = \frac{U_p^0}{L_{p0}}$ and $\Delta\lambda_s^0 = \frac{U_s^0}{L_{s0}}$. In the initial state, i.e. the muscle has no deformation, $\Delta\lambda_m^0 = 0, \Delta\lambda_p^0 = 0$ and $\Delta\lambda_s^0 = 0$

Now considering an arbitrary time $t$ state, the following equation can be obtained:

$${}^tL_p = L_{p0} + {}^tU = L_{m0} + U_m^0 + \int_{t_0}^{t} v_m dt + L_{s0} + {}^tU_s \tag{D.5}$$

where $v_m$ is the velocity of the contractile element contraction, and $t_0$ is the activation time. Dividing Equation (D.5) by $L_{m0}$, the following equation can be obtained:

$$(1+k)\,{}^t\lambda_p = \lambda_m^0 + \int_{t_a}^{t} \frac{v_m}{L_{m0}} dt + k\,{}^t\lambda_s \tag{D.6}$$

where ${}^t\lambda_s$, $\lambda_m^0$ and ${}^t\lambda_p$ are defined as: ${}^t\lambda_s = \frac{L_{s0} + {}^tU_s}{L_{s0}}$, $\lambda_m^0 = \frac{L_{m0} + U_m^0}{L_{m0}}$ and ${}^t\lambda_p = \frac{L_{p0} + {}^tU}{L_{p0}} = \frac{L_{p0}^t}{L_{p0}}$.

Further, Equation (D.6) can be written at the end of the time step as:

$$(1+k)^{t+\Delta t}\lambda_p = {}^t\lambda_m + \Delta\lambda_m + k\,{}^t\lambda_s + k\Delta\lambda_s \tag{D.7}$$

Then, the increment of stretch in the contractile element can be obtained as:

$$\Delta\lambda_m = \alpha_1 - k\Delta\lambda_s \tag{D.8}$$

where

$$\alpha_1 = (1+k)^{t+\Delta t}\lambda_p - {}^t\lambda_m - k\,{}^t\lambda_s \tag{D.9}$$

$\Delta\lambda_m$ is the stretch increment in the contractile element.

# Appendix E — Fortran Codefor the Skeletal Muscle Model

```
Subroutine umat43 (cm,eps,sig,epsp,hsv,dt1,capa,etype,time,temp,failel,crv)
c************************************************************************
c       LS-DYNA user defined routine for skeletal muscle constitutive model
c          Copyright: Yongtao Lu, School of Engineering, Cardiff University
c************************************************************************
c////////////////////  input variables explanation  ////////////////////////////////////////
c       cm(1) --- cm(32) = variables comes from the LS-DYNA keyword input deck
c   Cauchy stress components
c       sig(1) = local x Cauchy stress
c       sig(2) = local y Cauchy stress
c       sig(3) = local z Cauchy stress
c       sig(4) = local xy Cauchy stress
c       sig(5) = local yz Cauchy stress
c       sig(6) = local zx Cauchy stress
c   history variables
c       hsv(1) = 1st history variable
c       hsv(2) = 2nd history variable
c            .
c            .
c            .
c       hsv(n) = nth history variable
c   other variables
c       dt1 = current time step size
c       time = current time
c       temp = current temperature
      include 'nlqparm'
      include 'iounits.inc'
      common/bk06/idmmy,iaddp,ifil,maxsiz,ncycle,ctime(2,30)
      character*5 etype
      dimension cm(*),eps(*),hsv(*),crv(lq1,2,*),sig(*)
      logical faile

      DIMENSION GC(3,3),CBAR(3,3),GB(3,3),BBAR(3,3),AN0(3),ANN0(3,3),
        1 FN(3),AN1(3),ANN1(3,3),UNIT2(3,3),ST(3,3),DFGRD1(3,3),
        2 STI(3,3),STFPE(3,3),STFSE(3,3),STJ(3,3)

      PARAMETER (ONE=1.0D0,TWO=2.0D0,THREE=3.0D0,SIX=6.0D0)
```

```
      if (etype.eq.'solid') then
        b = cm(1)                ! b
        c = cm(2)                ! c
        TM0 = cm(3)        ! SIGMA0, maximum isometric stress
        D = cm(4)          ! D
        AK =  cm(5)        ! CONTANT K
        ALFA =  cm(6)          ! ALFA
        BETA =  cm(7)          ! BETA
        DDRSM0= cm(8)          ! anmdafm-zero-dot
        AC =  cm(9)            !  K-c
        AB =  cm(10)       ! K-e
        AD =  cm(11)       !  d
        Time0 = cm(14)         ! t0:the activation time
        Time1 = cm(15)         ! t1:the deactivation time
        Factor = cm(16)        ! S: the exponential factor
         APE  = cm(17)         ! material constant A
        aLevel1 = cm(18)       ! activation level before and after contraction,0.0
        aLevel2 = cm(19)       ! activation level during contraction, 1.0
        emda_opt = cm(20)      ! the optimal fibre stretch
c
c         calculate the intial fibre direction according to the two nodes' coordinates
c
      FX1 = cm(25); FY1 = cm(26); FZ1 = cm(27)
      FX2 = cm(28); FY2 = cm(29); FZ2 = cm(30)
      DIS = sqrt((FX2-FX1)**2+(FY2-FY1)**2+(FZ2-FZ1)**2)
      FX0 = (FX2-FX1)/DIS; FY0 = (FY2-FY1)/DIS; FZ0 = (FZ2-FZ1)/DIS
      AN0(1)=FX0; AN0(2)=FY0; AN0(3)=FZ0
c
c         NHV=8, thus,deformation gradient stored in hsv(9),...,hsv(17)
c         pass the deformation gradient to the matrix DFGRD(3,3)
c
      DFGRD1(1,1)=hsv(9); DFGRD1(1,2)=hsv(12); DFGRD1(1,3)=hsv(15);
      DFGRD1(2,1)=hsv(10); DFGRD1(2,2)=hsv(13); DFGRD1(2,3)=hsv(16);
      DFGRD1(3,1)=hsv(11); DFGRD1(3,2)=hsv(14); DFGRD1(3,3)=hsv(17);
c
c          compute the Jacobian
c
      DET = DFGRD1(1,1) * DFGRD1(2,2) * DFGRD1(3,3)
        2     + DFGRD1(1,2) * DFGRD1(2,3) * DFGRD1(3,1)
        3     + DFGRD1(1,3) * DFGRD1(3,2) * DFGRD1(2,1)
        4     - DFGRD1(1,2) * DFGRD1(2,1) * DFGRD1(3,3)
        5     - DFGRD1(1,3) * DFGRD1(3,1) * DFGRD1(2,2)
        6     - DFGRD1(2,3) * DFGRD1(3,2) * DFGRD1(1,1)
      SCALE1 = DET**(-ONE/THREE)
```

```
      SCALE2 = DET**(-TWO/THREE)
c
c         compute right Cauchy-Green tensor – GC(3,3)
c
      DO 200 I = 1,3
         DO 200 J = 1,3
            GC(I,J)= 0.0
            DO 200 K=1,3
               GC(I,J)= GC(I,J)+DFGRD1(K,I)*DFGRD1(K,J)
  200    continue
c
c         compute the right Cauchy-Green tensor with the volume change eliminated,
CBAR(3,3)
c
      DO 210 I=1,3
         DO 210 J=1,3
            CBAR(I,J) = GC(I,J)* SCALE2
  210 continue
c
c          compute left Cauchy-Green tensor -- GB(3,3)
c
      DO 220 I = 1,3
         DO 220 J = 1,3
            GB(I,J)= 0.0
            DO 220 K=1,3
                  GB(I,J)= GB(I,J)+DFGRD1(I,K)*DFGRD1(J,K)
  220 continue
c
c          compute the left Cauchy-Green tensor with the volume change eliminated,
BBAR(3,3)
c
      DO 230 I=1,3
         DO 230 J=1,3
            BBAR(I,J) = GB(I,J)* SCALE2
  230 continue
c
c             compute the first invariant with the volume change eliminated
c
      HIBARC1=CBAR(1,1)+CBAR(2,2)+CBAR(3,3)
c
c          compute the fibre stretch ratio in the undeformed configuration
c
      DO 240 I=1,3
         DO 240 J=1,3
```

```
            ANN0(I,J)=AN0(I)*AN0(J)
      240 continue

      ANMDF = 0.0
      DO 250 I=1,3
         DO 250 J=1,3
              ANMDF =ANMDF + CBAR(I,J)*ANN0(J,I)
      250 continue
      ANMDF = SQRT(ANMDF)
c
c        compute the current muscle fibre direction
c
      DO I=1,3
        FN(I) =0.0
         DO K=1,3
              FN(I) =FN(I)+DFGRD1(I,K)*AN0(K)
         END DO
              AN1(I) = SCALE1*FN(I)/ANMDF
       END DO
c
c        set the initial values for some variables
c
      RSS = hsv(5)                  !  stretch ratio in SEE, =Ls(t)/Ls(0)
      RSM = hsv(6)                  !  stretch ratio in CE, =Lm(t)/Lm(0)
      SIGM0 = hsv(7)                !  maximum stress of CE at initial time
      DRSM = hsv(8)                  !  stretch increment in CE, =Um(t)/Lm(0)

       AAA0=0.0
       DO I=5,8
         AAA0=AAA0+ABS(hsv(I))
       END DO
       IF (AAA0.EQ.0.) THEN          !    first iteration
            RSS = 1.0
            RSP = 1.0   !   stretch ratio in PE
            RSM = (1.0+AK)*RSP-AK   !  the stretch ratio in CE
           DRSM=0.0
           call ForceExten(RSP,emda_opt,ForceNor)
           SIGM0 = TM0*ForceNor
            goto 900     ! store the history variables and go to the next iteration
       ENDIF
       RSP=ANMDF
c
c        compute the activation level at time t
c
```

```
      ATIME=time
      if((ATIME.GT.Time0) .AND. (ATIME.LT.(Time1+0.1))) then
         call ActiLevel(ATIME,ALFAA,aLevel1,aLevel2,Time0,Time1,Factor)
      else                        !  the muscle is in the non-activation state
         SIGMS = 0.0              !  stress in CE and SE equals zero
         goto 800
      endif
c
c        computing the stress in CE at the previous time step
c
      EXPARS=EXP(ALFA*( RSS-1.0))
       SIGMS= BETA*(EXPARS-1.0)
c
c              compute the cofficient A1
c
       A1=(1.+AK)*RSP-RSM-AK*RSS
       DRSM0=DT1*DDRSM0

      IF (DRSM.GT.0.0) THEN            !lengthening case
            A2=(SIGMS+BETA)*(1.0-AB*AC*A1/DRSM0)
            A3=(SIGMS+BETA)*AB*AK*AC/DRSM0

A4=(AB*BETA*AC+SIGM0*ALFAA*(AD*AB*AC+AD-1.0))*AK/DRSM0
            A5= BETA+ SIGM0*ALFAA+
     1           (SIGM0*ALFAA*(1.0-AD-AD*AB*AC)-AB*BETA*AC)*A1/DRSM0
      ELSE                                 !shortening case
          A2=(SIGMS+BETA)*(1.0+AC*A1/DRSM0)
          A3=-(SIGMS+BETA)*AK*AC/DRSM0
          A4=(SIGM0*ALFAA-BETA*AC)*AK/DRSM0
          A5= BETA+SIGM0*ALFAA+(BETA*AC-SIGM0*ALFAA)*A1/DRSM0
      END IF
c
c        solve the unknown RSS by standard Newton's method
c
      DRSS=0.0
      CALL DNEWT(DRSS, A2,A3,A4,A5,ALFA,ncycle)
c
c          update the variables for the next step
c
c            update RSS and RSM
      RSS= RSS+DRSS
      DRSM=A1-AK*DRSS
      RSM=RSM+DRSM
c          calculate SIGMS at current time step
```

```
      EXPARS=EXP(ALFA*( RSS-1.0))
      SIGMS= BETA*(EXPARS-1.0)

800   IF(ANMDF.GT.1.0) THEN          !  muscle is stretched
          FPE = APE*(ANMDF-1.0)**2
      ELSE                           !  muscle is shortening, no force in PE
          FPE = 0.0
      END IF
c
c               calculate the strain energy
c
      U1PE=TM0*FPE
      U1SE = SIGMS
      U1F=U1PE+U1SE
      U1I=b*c*EXP(b*(HIBARC1-3.0))
      U1J=2.*(DET-1.0)/D
c
c       compute the Cauchy stress from the strain energy
c
      DO 260 I=1,3
          DO 260 J=1,3
              ANN1(I,J)=AN1(I)*AN1(J)
      260 continue

      DO I=1,3
        DO J=1,3
              UNIT2(I,J)=0.0
         END DO
              UNIT2(I,I)=1.0
      END DO

      DO 270 I=1,3
          DO 270 J=1,3
              STI(I,J) = (U1I*(2.0*BBAR(I,J)-2.0*HIBARC1*UNIT2(I,J)/3.0))/DET
      270 continue

      DO 280 I=1,3
          DO 280 J=1,3

STFPE(I,J)=(U1PE*(ANMDF*ANN1(I,J)-1.0*ANMDF*UNIT2(I,J)/3.0))/DET
      280 continue

      DO 290 I=1,3
          DO 290 J=1,3
```

```
      STFSE(I,J)=(U1SE*(ANMDF*ANN1(I,J)-1.0*ANMDF*UNIT2(I,J)/3.0))/DET
      290 continue
c
      DO 300 I=1,3
         DO 300 J=1,3
            STJ(I,J)=U1J*UNIT2(I,J)
      300 continue
c
      DO 310 I=1,3
         DO 310 J=1,3
            ST(I,J) = STI(I,J)+STFPE(I,J)+STFSE(I,J)+STJ(I,J)
      310 continue
c        stored as history variables for output purpose
      hsv(1)=STI(3,3)
      hsv(2)=STFPE(3,3)
      hsv(3)=STFSE(3,3)
      hsv(4)=STJ(3,3)
c
c        pass Cauchy stress
c
      sig(1)= ST(1,1); sig(2)= ST(2,2); sig(3)= ST(3,3)
      sig(4)= ST(1,2); sig(5)= ST(2,3); sig(6)= ST(1,3)
c
c            compute the muscle at time t
c
      Call ForceExten(RSP,emda_opt,ForceNor)
      SIGM0 = TM0*ForceNor
c
c        pass back the history varialbes for the next iteration
c
900   hsv(5) = RSS              !  rate of stretch in SEE
      hsv(6) = RSM              !  rate of stretch in CE
      hsv(7) = SIGM0     !  maximum stress of CE at time t+dt
      hsv(8) = DRSM             !  increment rate of stretch of CE
c
      else
         write (       *,20) etype
         write (iohsp,20) etype
         write (iomsg,20) etype
         call adios(2)
      endif
c
 20   FORMAT(/
```

```
     1 ' *** Error element type ',a,' can not be',
     2 '                run with the current material model.')
c
      RETURN
      END
c
c------------------------ Subroutines definition --------------------------------
c
SUBROUTINE ActiLevel(t,acti,aLevel1,aLevel2,Time0,Time1,Factor)
c**********************************************************************
*
c                        subroutine to define the activation function
c**********************************************************************
c/////////////////////////////////input parameters explanation ////////////////////////////////////////////////
c       t = the current time
c       alevel1 = the activation level before and after the activation
c       alevel2 = the activation level during the activation
c       Time0 = the activation time
c       Time1 = the deactivation time
c       Factor = the rate of the chemical process
c/////////////////////////////////output parameters explanation ////////////////////////////////////////////////
c       acti = the activation level corresponding to the current time t

        if(t .LT. Time0)   acti = aLevel1
        if((t .GE. Time0) .and. (t .LT. Time1)) then
            acti = aLevel1 + (aLevel2-aLevel1)*(1-exp(-factor*(t-Time0)))
        endif
        if(t .GT. Time1) then
            temp1 = (aLevel2-aLevel1)*(1-exp(-factor*(Time1-Time0)))
            acti = aLevel1 + temp1 - temp1*(1-exp(-factor*(t-Time1)))
        endif
    RETURN
    END

SUBROUTINE ForceExten(x,x1,y)
c**********************************************************************
c                        subroutine to define the force -- extension function
c**********************************************************************
c/////////////////////////////////input parameters explanation ////////////////////////////////////////////////
c       x = the current stretch
c       x1 = the optimal fibre stretch
c/////////////////////////////////output parameters explanation ////////////////////////////////////////////////
c       y = the normalised force corresponding to the current stretch
```

```
      tmp = x/x1
      if(tmp .LT. 0.4)   y=1.0e-4
      if((tmp .GE. 0.4) .and. (tmp .LT. 0.6))   y=9*(tmp-0.4)**2
      if((tmp .GE. 0.6) .and. (tmp .LT. 1.4))   y=1-4*(1-tmp)**2
      if((tmp .GE. 1.4) .and. (tmp .LT. 1.6))   y=9*(tmp-1.6)**2
      if(tmp .GT. 1.6) y=1.0e-4
    RETURN
    END

    SUBROUTINE FS(X,F,DY,A2,A3,A4,A5,ALFA)
c**************************************************************************
c                    subroutine to compute f(x)=F and df/dx=DY
c**************************************************************************
c////////////////////////////////input parameters explanation ////////////////////////////////////////////////
c       X = the independent variable
c       A2 – A5 = coefficient of the non-linear equation
c       ALFA = the material constant α
c////////////////////////////////output parameters explanation ////////////////////////////////////////////////
c       F = the value of the non-linear equation
c       DY = the Jacobian df/dx

        F = (A2+A3*X)*EXP(ALFA* X)-A4* X-A5
        DY=(A3+ ALFA *(A2+A3* X))* EXP(ALFA* X)-A4
    RETURN
    END

    SUBROUTINE DNEWT(X, A2,A3,A4,A5,ALFA,NITE)
c**************************************************************************
c                    subroutine for newton iteration method
c**************************************************************************
c////////////////////////////////input parameters explanation ////////////////////////////////////////////////
c       A2 – A5 = coefficient of the non-linear equation
c       ALFA = the material constant α
c       NITE = the current iteration number
c////////////////////////////////output parameters explanation ////////////////////////////////////////////////
c       X = the solution

      EPSS = 1.0E-6              ! used to control the solution precision
      L=60       ! the most iterative number to be given
      CALL FS(X,F,DY,A2,A3,A4,A5,ALFA)
30    IF ((ABS(DY)+1.0.EQ.1.0) .AND. NITE .GT. 0.0) THEN
        L=0
        WRITE(*,2000)
        RETURN
```

```
        END IF
        X1=X-F/DY
        CALL FS(X1,F,DY,A2,A3,A4,A5,ALFA)
        IF ((ABS(X1-X).GE.EPSS) .AND. (ABS(F).GE.EPSS)) THEN
            L=L-1
            X=X1
            IF (L.EQ.0) RETURN
            GOTO 30
        END IF
        X=X1
        if(NITE .EQ. 0) X=0.0
    RETURN
2000    FORMAT(1X,'   ERR')
    END
```

# Appendix F — Makefile for Building LS971.exe on WindowsXP

```
FC=ifort
FFLAGS=-c -W0 -WB -unroll -fp:precise -4Yportlib -assume:byterecl,buffered_io \
-Qfpp2 -DPCWIN -DINTEL -QxK

SMPS = -DOPENMP -Qopenmp
NSMPD= -DAUTODOUBLE -4R8 -4I8
SMPD = -DOPENMP -Qopenmp -DAUTODOUBLE -4R8 -4I8

FFLAGS = $(FFLAGS) $(SMPS)
LFLAGS = -F:4000000 -link -force -nodefaultlib:msvcrt.lib
OBJS= dyn21.obj dyn21b.obj umat43.obj
LIBS= libdyna.lib libansys.lib libguide.lib shell32.lib user32.lib comctl32.lib comdlg32.lib

ls971.exe: $(OBJS)
    $(FC) -w -q -o ls971.exe $(OBJS) $(LIBS) $(LFLAGS)

dyn21.obj: dyn21.F
    $(FC) $(FFLAGS) dyn21.F
dyn21b.obj: dyn21b.F
    $(FC) $(FFLAGS) dyn21b.F
umat43.obj: umat43.F
    $(FC) $(FFLAGS) umat43.F

clean:
    -if exist *.obj erase *.obj
    -if exist ls971.exe erase ls971.exe
```

# Appendix G — Fortran Code for NURBS Solid Representation and its Derivatives

```
      SUBROUTINE NURBSOLID(Vertex,OrderU,OrderV,NumPointU,
     1    NumPointV,VectorKnotU,VectorKnotV)
c**********************************************************************
c       Subroutine to calculate a Cartesian product rational B-spline Solid
c            using an open knot vector and write the derivatives into a file
c       Copyright: Yongtao Lu, School of Engineering, Cardiff University
c**********************************************************************
c//////////////////////////////input parameters explanation ////////////////////////////////////////////////
c       Vertex ()  = array containing the NURBS surface control net vertices
c            Vertex (:,1) contains the x component of the vertex
c            Vertex (:,2) contains the y component of the vertex
c            Vertex (:,3) contains the z component of the vertex
c            Vertex (:,4) contains the homogeneous weighting factor
c       OrderU  = order of the NURBS in u direction
c       OrderV  = order of the NURBS in v direction
c       NumPointU  = number of the control net vertices in u direction
c       NumPointV  = number of the control net vertices in v direction
c       VectorKnotU()       = open uniform knot vector in u direction
c       VectorKnotV()       = open uniform knot vector in v direction

      IMPLICIT DOUBLE PRECISION (A-H,O-Z)
      integer OrderU,OrderV,OrderW,iOutFile
      dimension    Point(3),PointCoordi(3),PointTemp(3),
     1    BasisU(NumPointU), BasisV(NumPointV), BasisW(2),
     2     Vertex(200,4),VertexTemp(200,4),
     3    VertexNet(NumPointU,NumPointV,2,4),
     4    VectorKnotU(200), VectorKnotV(200), VectorKnotW(4),
     5    BasisDU(NumPointU), BasisDV(NumPointV), BasisDW(2),
     6    DerU(3),DerV(3),DerW(3),ZBar(3),ZUBar(3),ZVBar(3),ZWBar(3)
      PARAMETER (ZERO=0.0D0,ONE=1.0D0,TWO=2.0D0,THREE=3.0D0)

c ////////////initialization part//////////
      OrderW = 2          ! order of the NURBS in w direction
      NumPointW = 2       ! number of control net vertices in w direction
      NumMeshU = 100          ! number of mesh in cylinder axial direction
```

```
      NumMeshV = 100          ! number of mesh in cylinder circumferential direction
      NumMeshW = 10           ! number of mesh in cylinder radius direction
      VertexTemp = 0.0        ! VertexTemp is a matrix
          ! calculate the number of knot vectors in each direction
      NumKnotU = NumPointU + OrderU
      NumKnotV = NumPointV + OrderV
      NumKnotW = NumPointW + OrderW
          ! assign the vector kont in w direction
      VectorKnotW = [0.0,0.0,1.0,1.0]
c//////////////end initialization part//////////
          ! open a file for output the results
      iOutFile = 20
      open(iOutFile,file="information.txt",status='Replace')
          ! calculate the total number of control points
      NumNode = (NumMeshU+1)*(NumMeshV+1)*(NumMeshW+1)
      write(iOutfile,*),NumNode
c----------part1   set up the control polygon vertex net-------------
          ! assign the exterior circle
      do i=1, NumPointU
          do j=1, NumPointV
              j1 = NumPointV*(i-1) + j
              VertexNet(i,j,1,1) = Vertex(j1,1)
              VertexNet(i,j,1,2) = Vertex(j1,2)
              VertexNet(i,j,1,3) = Vertex(j1,3)
              VertexNet(i,j,1,4) = Vertex(j1,4)
          enddo
      enddo
          ! calculate the interior circle and assign to the control net
      do i=1, NumPointU
          do j=1, NumPointV
              VertexTemp(i,1) = VertexTemp(i,1) + VertexNet(i,j,1,1)
              VertexTemp(i,2) = VertexTemp(i,2) + VertexNet(i,j,1,2)
              VertexTemp(i,3) = VertexTemp(i,3) + VertexNet(i,j,1,3)
              VertexTemp(i,4) = VertexTemp(i,4) + VertexNet(i,j,1,4)
          enddo
          do j=1, NumPointV
              VertexNet(i,j,2,1) = VertexTemp(i,1)/NumPointV
              VertexNet(i,j,2,2) = VertexTemp(i,2)/NumPointV
              VertexNet(i,j,2,3) = VertexTemp(i,3)/NumPointV
              VertexNet(i,j,2,4) = VertexTemp(i,4)/NumPointV
          enddo
      enddo
c-------------------end part1 ---------------------------------
```

```
c--------- part2   find the parametric lines in each direction ---------
      do u=VectorKnotU(1),VectorKnotU(NumKnotU),
     1                 abs(VectorKnotU(NumKnotU)-VectorKnotU(1))/NumMeshU
         call dbasisF(OrderU,u,NumPointU,VectorKnotU,BasisU,BasisDU)
        do v=VectorKnotV(1),VectorKnotV(NumKnotV),
     1                 abs(VectorKnotV(NumKnotV)-VectorKnotV(1))/NumMeshV
            call dbasisF(OrderV,v,NumPointV,VectorKnotV,BasisV,BasisDV)
           do w=VectorKnotW(1),VectorKnotW(NumKnotW),
     1                          VectorKnotW(NumKnotW)/NumMeshW
            call dbasisF(OrderW,w,NumPointW,VectorKnotW,BasisW,BasisDW)
               ! sum of basis function
           call sumrbas1(VertexNet,BasisU,BasisU,BasisW,NumPointU,
     1               NumPointU,NumPointW,sum)
               ! calculate the B-spline solid
           PointCoordi = 0.0     ! set the array to zero
           do i=1, NumPointU
              do j=1, NumPointV
                 do k=1,NumPointW
                    do m=1,3
                    qtemp = VertexNet(i,j,k,4)*VertexNet(i,j,k,m)
     1                       *BasisU(i)*BasisV(j)*BasisW(k)/sum
                    PointCoordi(m) = PointCoordi(m) + qtemp
                    enddo
                 enddo
              enddo
           enddo
           ! calculate the derivatives
        call sumrbas2(VertexNet,BasisU,BasisV,BasisW,NumPointU,
     1           NumPointV,NumPointW,ZBar)
        call sumrbas1(VertexNet,BasisU,BasisV,BasisW,NumPointU,
     1           NumPointV,NumPointW,DBar)
           ! 1. derivatives with respect to u
        call sumrbas2(VertexNet,BasisDU,BasisV,BasisW,NumPointU,
     1           NumPointV,NumPointW,ZUBar)
        call sumrbas1(VertexNet,BasisDU,BasisV,BasisW,NumPointU,
     1           NumPointV,NumPointW,DUBar)
        do k=1,3
            DerU(k) = ZUBar(k)/DBar-(DUBar/DBar**2)*ZBar(k)
        enddo
           ! 2. derivatives with respect to v
        call sumrbas2(VertexNet,BasisU,BasisDV,BasisW,NumPointU,
     1           NumPointV,NumPointW,ZVBar)
        call sumrbas1(VertexNet,BasisU,BasisDV,BasisW,NumPointU,
     1           NumPointV,NumPointW,DVBar)
```

```
        do k=1,3
            DerV(k) = ZVBar(k)/DBar-(DVBar/DBar**2)*ZBar(k)
        enddo
            ! 3. derivatives with respect to w
        call sumrbas2(VertexNet,BasisU,BasisV,BasisDW,NumPointU,
     1          NumPointV,NumPointW,ZWBar)
        call sumrbas1(VertexNet,BasisU,BasisV,BasisDW,NumPointU,
     1          NumPointV,NumPointW,DWBar)
            do k=1,3
            DerW(k) = ZWBar(k)/DBar-(DWBar/DBar**2)*ZBar(k)
        enddo

            ! calculate the normalised tangent vector of the isocurve with respect to u
        disance = sqrt(DerU(1)**2+DerU(2)**2+DerU(3)**2)
        DirectionX = DerU(1)/disance
        DirectionY = DerU(2)/disance
        DirectionZ = DerU(3)/disance

            ! write out the results, just write the u direction derivatives in this example
        write(iOutfile,100),PointCoordi(1),PointCoordi(2),PointCoordi(3),
     2          DirectionX,DirectionY,DirectionZ
100     format(F12.6,F12.6,F12.6,F12.6,F12.6,F12.6,F12.6,F12.6,F12.6)
          enddo
        enddo
    enddo
c---------------------- end   part2 -------------------------------

    RETURN
    END
C
c--------------------------------- subroutine definition ---------------------------------
c
    SUBROUTINE sumrbas1(VertexNet,BasisU,BasisV,BasisW,NumPointU,
    1   NumPointV,NumPointW,sum)
c**********************************************************************
c   subroutine to calculate the sum of the nonrational basis functions
c**********************************************************************
c////////////////////////// input parameters explanation ////////////////////////////////////////
c       VertexNet ()  = array containing the NURBS solid control net vertices
c           Vertex (:,:,:,1) contains the x component of the vertex
c           Vertex (:,:,:,2) contains the y component of the vertex
c           Vertex (:,:,:,3) contains the z component of the vertex
c           Vertex (:,:,:,4) contains the homogeneous weighting factor
c       BasisU()     = array containing the nonrational basis functions for u
```

```
c       BasisV()    = o array containing the nonrational basis functions for v
c       BasisW()    = o array containing the nonrational basis functions for w
c       NumPointU = number of the control net vertices in u direction
c       NumPointV = number of the control net vertices in v direction
c       NumPointW = number of the control net vertices in w direction
c////////////////////////////// output parameters explanation ////////////////////////////////////////
c       sum = sum of the nonrational basis functions

      IMPLICIT DOUBLE PRECISION (A-H,O-Z)
      dimension VertexNet(9,21,2,4),
     1   BasisU(NumPointU), BasisV(NumPointV), BasisW(NumPointW)

      sum = 0.0
      do i=1,NumPointU   !along the cylinder
         do j=1,NumPointV   ! cylinder circumferential direction
            do k=1,NumPointW        ! cylinder axial direction
               sum = sum + VertexNet(i,j,k,4)*BasisU(i)*BasisV(j)*BasisW(k)
            enddo
         enddo
      enddo

      RETURN
      END

      SUBROUTINE sumrbas2(VertexNet,BasisU,BasisV,BasisW,NumPointU,
     1   NumPointV,NumPointW,summ)
c*************************************************************************
c   subroutine to calculate the sum of the rational basis functions with vertex value
c*************************************************************************
c////////////////////////////// input parameters explanation ////////////////////////////////////////
c       same as those in subroutine sumrbas1
c////////////////////////////// output parameters explanation ////////////////////////////////////////
c       summ(:) = sum of the rational basis functions with vertex value

      IMPLICIT DOUBLE PRECISION (A-H,O-Z)
      dimension VertexNet(9,21,2,4),summ(3),
     1   BasisU(NumPointU), BasisV(NumPointV), BasisW(NumPointW)

      summ = 0.0
      do i=1,NumPointU   !along the cylinder
         do j=1,NumPointV   ! cylinder circumferential direction
            do k=1,NumPointW        ! cylinder axial direction
           summ(1) = summ(1) + VertexNet(i,j,k,1)*VertexNet(i,j,k,4)
     1                  *BasisU(i)*BasisV(j)*BasisW(k)
```

```
            summ(2) = summ(2) + VertexNet(i,j,k,2)*VertexNet(i,j,k,4)
     1                        *BasisU(i)*BasisV(j)*BasisW(k)
            summ(3) = summ(3) + VertexNet(i,j,k,3)*VertexNet(i,j,k,4)
     1                        *BasisU(i)*BasisV(j)*BasisW(k)
          enddo
        enddo
      enddo

      return
      end

      SUBROUTINE dbasisF(Order,t,NumPoint,VKnot,Basis,BasisD1)
c*****************************************************************
c     subroutine to generate B-spline basis functions and their derivatives
c                    for open knot vectors
c*****************************************************************
c////////////////////////////  input parameters explanation  ////////////////////////////////////////////
c          Order = order of the B-spline basis function
c          t = parameter value
c          NumPoint = number of control polygon vertices
c          VKnot() = knot vector
c////////////////////////////  output parameters explanation ////////////////////////////////////////////
c          Basis() = array containing the basis functions
c          BasisD1() = array containing the derivatives of the basis functions

      IMPLICIT DOUBLE PRECISION (A-H,O-Z)
      integer Order
      dimension temp(200), temp1(200), VKnot(NumPoint+Order),
     1     basis(NumPoint), basisD1(NumPoint)

      PARAMETER (ZERO=0.0D0,ONE=1.0D0,TWO=2.0D0,THREE=3.0D0)
      NumKnot = NumPoint + Order          ! number of knot values

      EPS = 1.0E-6
      temp = 0.0      !ARRAY
      temp1 = 0.0     !ARRAY

c     calculate the first-order basis functions n(i,1)
      do i=1, NumKnot-1
          if((t .ge. VKnot(i)) .and. t .lt. VKnot(i+1))  then
              temp(i) = 1
          else
              temp(i) =0
          end if
```

```
      enddo
          ! handle the end specially by setting the first-order basis functions
      if(abs(t-VKnot(NumKnot)) .lt. EPS)    temp(NumPoint) = 1

c     calculate the higher-order basis functions and their derivatives
      do k=2, Order
          do i=1, NumKnot-k
          !calculate basis function
                  !first term of the basis function
              if(temp(i) /= zero)     then
                  b1 = ((t-VKnot(i))*temp(i))/(VKnot(i+k-1)-VKnot(i))
              else
                  b1 = 0.0
              endif
                  !second term of the basis function
              if(temp(i+1) /= zero) then
                  b2 =((VKnot(i+k)-t)*temp(i+1))/(VKnot(i+k)-VKnot(i+1))
              else
                  b2 = 0.0
              endif
c         calculate first derivative
              if(temp(i) /= zero) then
                  f1 = temp(i)/(VKnot(i+k-1)-VKnot(i))
              else
                  f1 = 0
              endif
              if(temp(i+1) /= zero) then
                  f2 = -temp(i+1)/(VKnot(i+k)-VKnot(i+1))
              else
                  f2 = 0
              endif
              if(temp1(i) /= zero) then
                  f3 = (t-VKnot(i))*temp1(i)/(VKnot(i+k-1)-VKnot(i))
              else
                  f3 = 0
              endif
              if(temp1(i+1) /= zero) then
                  f4 = (VKnot(i+k)-t)*temp1(i+1)/(VKnot(i+k)-VKnot(i+1))
              else
                  f4 = 0
              endif

              temp(i) = b1 + b2
              temp1(i) = f1 + f2 + f3 + f4
```

```
        enddo
    enddo

c       pass the results back
    do i=1, NumPoint
        basis(i) = temp(i)
        basisd1(i) = temp1(i)
    enddo

    RETURN
    END
```